

VARIATION IN COAL COMPOSITION

A computational approach to study the mineral composition of individual coal particles

O. Charon, S. G. Kang, K. Graham, A. F. Sarofim and J. M. Beer

Department of Chemical Engineering
Massachusetts Institute of Technology
Cambridge, MA 02139 (U.S.A.)

Mineral matter transformations, and therefore fly ash evolution, during pulverized coal combustion depend on the amount, composition and spatial distribution of the inorganic matter within individual pulverized coal particles. Thus, it is necessary to have information on the mineral composition of individual particles, as well as that of the raw pulverized coal. A model has been developed to predict the variation of individual coal particle compositions. It uses CCSEM data for a given raw coal as input and randomly distributes the mineral inclusions in the coal volume. By random selection of monosize coal particles, it is possible to generate distributions of mineral content for any particle size distribution of coal. The model has been checked by comparing computed results with data on the compositional variations of narrowly size and density classified fractions of an Upper Freeport bituminous coal. The results for individual coal particle compositions are used to generate information on the variability of the composition of the fly ash generated during combustion.

1. INTRODUCTION

Understanding the processes that govern the size distribution and chemical composition of the ash within and at the exit of a pulverized coal fired combustor is important because the ash influences fouling, slagging, and heat transfer in boilers, as well as the downstream particulate control equipment. This understanding begins with not only a knowledge of the amount, composition, and spatial distribution of the mineral matter in the coal particles, but also with some knowledge of the variability of the mineral content of the coal particles.

In this paper a model is presented for calculating the distribution of mineral inclusions in pulverized coal of different size and density fractions from knowledge of the mineral inclusions in the parent coal. A test of the validity of the model is provided by comparing the model predictions of the variations in the composition of different size and density fractions of an Upper Freeport coal with computer controlled scanning electron microscopy (CCSEM) measurements of the mineral distributions. The results obtained for the Upper Freeport coal show good agreement between the CCSEM data and the model results, and also give information on the variation of individual coal particle compositions.

This study is part of a broader program on mineral matter transformations being funded by the DOE and coordinated by Physical Sciences Inc. The coal classification was done by Foster Wheeler and the CCSEM analysis by Huffman and Huggins at the University of Kentucky. The results of this study will be used as input into a model of char combustion which allows for coalescence of the mineral inclusions and fragmentation of the char in order to predict the composition and size of the fly ash.

2. EXPERIMENTAL

CCSEM analysis was performed on the Upper Freeport raw coal and several size and density fractions (63-105 μm , and less than 1.3, 1.3 - 1.8 , 1.8 - 2.85 , and greater than 2.85 g/cm^3) by Huffman and Huggins at the University of Kentucky. The CCSEM analysis provides the content and size distribution of each of the mineral species listed in Table 1. For details on the CCSEM analysis used to obtain these data, one can consult the publications of these two specialists [2][3][4], as well as other authors [5][6].

The main mineral species in the Upper Freeport raw coal are, by decreasing amount, Illite, Mixed silicates, Pyrite, Quartz and Kaolinite. All the other species occur in concentrations less than 2 wt%. The CCSEM gives the mineral inclusion size distribution for these five main mineral types and for the total minerals (Table 1). For the latter, all the sizes are equally represented in the range from 10 to 15%, except the largest size (greater than 40 μm) which reaches 36%.

The CCSEM data obtained for the Upper Freeport raw coal were used as input to the model. The CCSEM data obtained for the four size and density classified samples were compared with computed values in order to validate the model.

3. MODEL

The model has two objectives : first, it must simulate a raw coal volume with different types and sizes of mineral inclusions inside, and second, it must produce coal particles from this computed raw coal volume, sort them by density, and perform statistics on them. To accomplish these objectives two Fortran programs were created : Pr1 and Pr2.

The major difficulty in simulating the raw coal volume is storing the information about the mineral inclusions (type, size, location...) and about the coal particles (mineral composition, density...) during the run. In the case of the Upper Freeport coal, greater than five million inclusions must be stored in order to get at least one mineral inclusion for each type and size. Only a super computer has sufficient memory to handle all of this information. We used an IBM 3090-600E with 512 megabytes of real memory and 512 megabytes of expended storage.

3.1 Raw coal volume simulation (Pr1)

3.1.1 Definitions

The raw coal volume is cubic and divided into a cubic matrix with unit length of one micron. The mineral inclusions are assumed to be cubic and are assigned to occupy sites within the raw coal matrix. Eventually the coal matrix is divided into smaller cubes which are coal particles.

The model assumes 6 different possible mineral inclusion sizes, one average size for each size range given by the CCSEM analysis. These sizes are defined using an integer number I from 1 to 6 and the D (I) values are, respectively, 1, 4, 8, 16, 30, and 60 μm .

The model accounts for the five main mineral species of the Upper Freeport raw coal as defined by the CCSEM analysis [4] (see Table 1), and identifies them by an integer number J. To achieve a mineral mass balance, a sixth kind of mineral, called "Other", is defined. The "other" content, composition and size distribution are calculated to fit the total mineral inclusion analysis given by the CCSEM data :

$$f_m(6) = 1 - \sum_{J=1}^5 f_m(J) \quad \text{and}$$

$$f_{m,s}(6, I) = 1/f_m(6) \cdot [f_{m,s}(\text{All mineral}, I) - \sum_{J=1}^5 f_m(J) \cdot f_{m,s}(J, I)] \quad \text{with}$$

$$f_{m,s}(\text{All mineral}, I) = \sum_{J=1}^6 f_{m,s}(J, I)$$

where $f_m(J)$ is the mass fraction of the mineral J in all mineral
and $f_{m,s}(J, I)$ is the mass fraction of the size I for mineral J.

The last species to be defined is the mineral free coal (J=0). The density of this last species is an input data for the model and depends on the raw coal studied. A value of 1.2 g/cm³ was assumed for the Upper Freeport coal.

3.1.2 Random location of the mineral inclusions

An inclusion is defined by the location (X_i, Y_i, Z_i) of its closest point to the origin of the raw coal volume, and by its size $D(1)$. X_i, Y_i, Z_i are randomly computed between 0 and $L - D(1)$, where L is the size of the simulated raw coal cube.

In order to avoid overlap between two mineral inclusions, all of the sites used by a mineral inclusion are recorded. Then if a latter inclusion needs to use one of these recorded sites for its location, its location is randomly computed again. This test is necessary to avoid inclusion overlap, particularly for the Upper Freeport (20.5 wt% of mineral matter) where almost 10% of its sites are mineral sites, but at a cost of a significant increase in run time and memory requirement.

3.1.3 Mineral inclusion attribution to a coal particle

Knowing $L, X_i, Y_i, Z_i, D(1)$ and the coal particle size (N_{spart}) which is to be created from the raw coal volume, it is possible to attribute a given mineral inclusion to a coal particle. The coal particles and mineral inclusions are identified as a function of their location in the raw coal cube by a characteristic integer given as :

$$\text{Num} = \left[\sum_{k=1}^3 \text{INT} \left\{ (\text{Loc}(k) + D(1)/2) / N_{\text{spart}} \right\} \cdot N_{\text{step}}^k \right] + 1$$

where $\text{Loc}(k)$ for $k=1$ to 3 are $X_i, Y_i,$ and Z_i , respectively,
 $L = N_{\text{step}} \cdot N_{\text{spart}}$,
and $\text{INT}(\text{value})$ is the integer part of value.

All the inclusions within a coal particle will have the same identifying integer, Num, as the coal particle. A coal particle will be allowed to contain a mineral inclusion if its size is greater than the inclusion size, if it contains the gravity center of the inclusion, and if there is enough remaining space for the additional inclusion. If a mineral inclusion is not in a coal particle, it is a pure mineral particle, keeping the former inclusion size; however, this case was never encountered for the 84 μm Upper Freeport coal.

3.1.4 Running Pr1

All of the illustrations in this presentation are given for the Upper Freeport raw coal and its four well classified samples, previously described. Because the model is at this time only able to produce a monosize coal sample, the results from the model will be given for the size 84 μm , which is an average value for the experimental sample size range 63 - 105 μm . The input file for a run consists of the CCSEM data for a given raw coal, chosen coal particle size and chosen particle number. Typically, the Pr1 run time was 14'27" CPU, and 350 megabytes of virtual memory was used to produce 5 100 981 mineral inclusions randomly distributed in a raw coal volume 840 μm large. As shown in Table 2, for a small number of biggest inclusions (only 2 for the quartz) we obtain an increasing number of inclusions when the inclusion size decreases, to finally reach 4 994 227 inclusions of 1 μm (98% of the total number). This is a problem with this computation: i.e., the biggest mineral inclusion size is not statistically well-defined, and we are too close to the maximum of memory available, to increase the number of inclusions.

The number of inclusion (N_{inc}) for a given mineral type J and a size I is calculated as follows :

$$N_{\text{inc}}(J, I) = \text{INT} \left[(V(J, I) / D(1)^3) + 0.5 \right]$$

where $V(J, I)$ is the volume used in the raw coal cube by the mineral J , calculated from the CCSEM data. In this way the difference between the computed and the measured coal sample mineral composition is always less than 0.1 wt% and the total mineral content is exactly the desired value of 20.5 wt%.

3.2 Coal particle characterization (Pr2)

Each individual coal particle is identified by an integer number, Num. Pr2 then calculates, for all the computed inclusions, the amount of mineral inclusion J with the size I which falls in the coal particle Num. All this information is stored and used to calculate the mineral content and composition, mass or density of every individual

coal particle. A density classification is achieved and any kind of statistical analysis is possible for the whole computed coal sample or any well classified size and density fraction.

The mineral inclusion listing and a parameter listing (L, Nstep, Npart, D (I)...) generated by Pr1 are the two input files necessary to run Pr2. Typically the run time was 2'15" CPU and 160 megabytes of virtual memory was used to produce 1000 particles of 84 μm .

4 Results

4.1 Model validation

Comparison of experimental CCSEM data for density classified Upper Freeport coal to model predictions is shown in Figure 1. Figure 1 shows good agreement for the mass distribution between the four density ranges and for the total mineral content in each density range. The fourth density range, where .2 wt% of the whole sample and a total mineral content of 91.6 wt% was calculated, does not give satisfactory agreement, but the reason becomes clear from an examination of the particle statistics in each density range. Whereas 516, 399, and 84 coal particles were obtained in the first, second and third density ranges, respectively, only one ended up in the fourth density range. Thus, the current model is limited by the large amount of memory necessary for a run and the fourth density range sample is too small to give representative results.

Good agreement for the mineral composition in the first two density ranges was also obtained (Figure 1), but for the same reason the last two ranges show disagreements. Even though the agreement is not good in the last two density ranges, the results do agree with the CCSEM data that the pyrite is the main mineral in particle greater than 2.85 g/cm^3 . The mineral composition cannot be statistically well determined because the sample size of the simulated biggest mineral inclusions is too small.

A new statistical approach is currently under development to reduce the representation of the smallest inclusion size (currently 98 % of the memory used by Pr1).

4.2 Individual coal particle information

Assuming the model is validated, we can study the mineral composition variation in individual coal particles. The results, obtained for the Upper Freeport, show as expected that the density classification provides coal samples with small variations in the total mineral content of individual particles (Figure 2). From the whole sample, which contains 18.08 wt% mineral matter per particle with a standard deviation of 15.20 wt%, we obtain four density classified samples, which contain 10.16, 18.40, 64.40 and 91.60 wt% of mineral matter per particle but with a standard deviation always less than 5 wt% (only 1.47 % for the first density range).

From an examination of the mineral composition of an individual coal particle (Figure 3), it appears that the fraction of a given mineral varies greatly even through the mean value does not (32 wt% for illite); the standard deviation, more over increases when the particle density increases (8.93, 18.90, and 49.5 wt% for the first, second and third density ranges, respectively). Denser coal particles contain larger inclusions, which because of their size they represent most of the mineral mass of that coal particle. This is why the mineral composition approaches the limit of either 0 or 100 wt% for a given mineral, when the particle density increases. Table 3 shows variations in compositions of a given mineral in individual particles. For the first and second density ranges the variation ranges are around 40 and 70%, respectively.

We also observed that the classified sample that is most representative of the whole coal sample is in the second density range (1.3 to 1.8 g/cm^3).

5 conclusion

This new computational approach allows information to be obtained information on the mineral composition variation in individual coal particles, which can be useful for predicting the mineral transformations and the final fly ash size distribution during pulverized coal combustion. Without using sophisticated and expensive experiments, it is possible to obtain data on any classified samples and to compare them with fly ash composition. This information will be used as input to a model of coal particle combustion. This model can also be used to design a process for preparation of a well classified coal sample with a given mineral composition.

A future improvement of the model will be to develop a new statistical approach in which will increase the number of simulated big inclusions and reduced the memory required. This will allow for the characterization of the large particle composition variations as well.

Acknowledgement

We greatly acknowledge the support of DOE grant RA22-86PC90751 which made this work possible.

References

- [1] A. F. Sarofim , Polutant formation and destruction, Fundamental of the Physical-chemistry of pulverized coal combustion, J. Lahaye and G. Prado Ed., NATO ASI Series E, n°137,Nijhoff, 1987
- [2] G. P. Huffman and F. E. Huggins , Analysis of inorganic constituents in low rank coal, The Chemistry of Low Rank Coal, H. H. Schobert Ed., ACS Advances in Chemistry Series, American Chem. Soc., Washington D.C., pp 159-174, 1984
- [3] G. P. Huffman, F. E. Huggins and R. J. Lee, Scanning electron microscopy based automated analysis (SEM-AIA) and Mossbauer spectroscopy : Quantitative Characterization of Coal Minerals, Coal and Coal Products, Analytical Characterization Techniques, E. L. Fuller Jr, American Chem. Soc., ACS Symposium Series, Vol. 205, Washington D.C., pp 239-258, 1982
- [4] F. E. Huggins, D. A. Kosmack, G. P. Huffman and R. J. Lee, Coal Mineralogies by SEM Automated Image Analysis, Scanning Electron Microscopy, Vol. 1, pp 531-540, 1980
- [5] A. K. Moza, D. W. Sticker and L. G. Austin, Elemental analysis of Upper Freeport coal particles, Scanning Electron Microscopy, Vol. IV, pp 91-96, 1980
- [6] R. J. Lee and J. F. Kelly, overview of SEM-based automated image analysis, Scanning Electron Microscopy, Vol. 1, pp 303-310, 1980
- [7] H. Gan, S. P. Nandi and P. L. Walker, Nature of the porosity in american coal, Fuel, Vol. 51, pp 272-277, 1972
- [8] E. Raask, Mineral Impurities in Coal, Hemisphere Pub. Corp., 1985
- [9] O. P. Mahajan, Coal porosity, Coal Structure, R. A. Mayers Ed., Academic press, pp 51-86, 1982
- [10] J. J. Renton, Mineral matter in coal, Coal Structure, R. A. Mayers Ed., Academic press, pp 283-324, 1982

Table 1 : CCSEM data from J. Huffman and F. Huggins for the Upper Freeport raw coal

mineral	Wt% mineral matter	Size distribution (wt%)					
		<2.5µm	2.5-5µm	5-10µm	10-20µm	20-40µm	>40µm
Quartz	10	8	14	26	20	26	6
Kaolinite	7	15	9	15	25	19	16
Illite	35	10	10	13	11	12	44
Mix.il.	19	12	16	15	21	12	23
Pyrite	18	4	2	13	13	14	54
All mine.	100	9	10	15	15	14	36

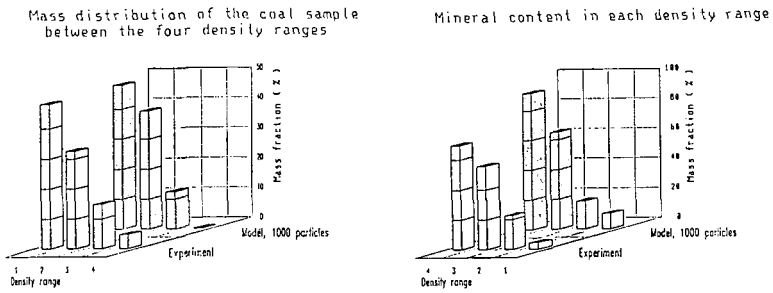
Table 2 : Number of mineral inclusion in 1 mm³ of the raw Upper Freeport coal based on an average size, in each CCSEM analysis size range

Mineral	Number of inclusions					
	1 µm	4 µm	8 µm	16 µm	30 µm	60 µm
Quartz	503988	13781	3199	308	61	2
Kaolinite	604460	5667	1181	246	28	3
Illite	2014867	31482	5116	541	90	41
Mix. sil.	1268790	26433	3098	542	47	12
Pyrite	240402	1878	1526	191	31	15
Others	361720	9304	1750	145	22	14

Table 3 : Particle by particle mineral composition variations for two density classified samples of an 84 µm Upper Freeport coal (wt%)

	Range 1 : less than 1.3 g/cm ³				Range 2 : 1.3 to 1.8 g/cm ³			
	Mean	St. dev.	Min.	Max.	Mean	St. dev.	Min.	Max.
Particle number	516	-	-	-	399	-	-	-
Total mineral content	10.2	1.5	6.3	13.0	18.41	4.85	12.1	38.2
Mineral composition								
Quartz	14.8	7.3	3.2	46.8	15.1	16.0	1.5	69.5
Kaolinite	9.1	6.8	2.2	38.8	9.1	12.4	0.5	76.4
Illite	32.1	8.9	12.9	59.1	30.8	18.9	5.3	79.4
Mixed silicates	25.5	9.3	7.2	57.6	21.9	16.7	3.2	75.3
Pyrite	9.4	7.2	1.3	38.9	14.7	17.2	0.5	82.0
Others	9.1	5.5	1.8	32.9	8.4	11.4	0.9	64.0

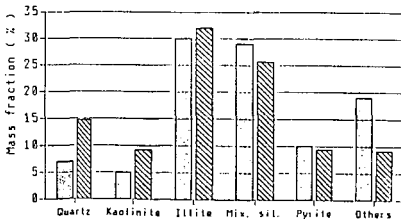
Figure 1: Comparison between experimental data and model results for an 84 μm Upper Freeport raw coal sample



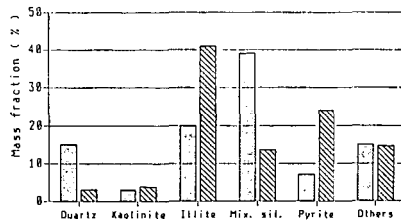
Density ranges (g/cm^3)

- 1 : less than 1.3
- 2 : 1.3 to 1.8
- 3 : 1.8 to 2.85
- 4 : greater than 2.85

Mineral composition for the first density range (less than 1.3 g/cm^3)



Mineral composition for the third density range (1.8 to 2.85 g/cm^3)



Experiment Model, 142 particles

Figure 2 : Model predictions of the total mineral content in different density classes for na 84 μm Upper Freeport coal sample

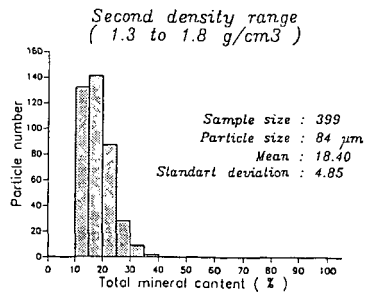
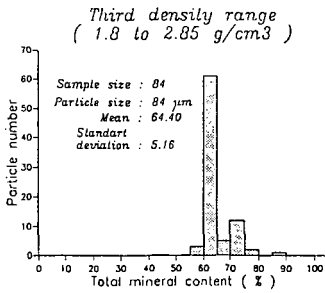
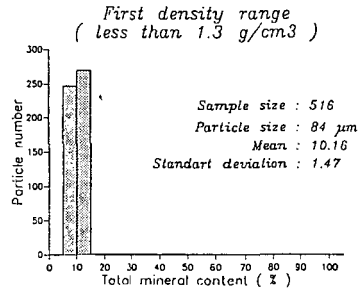
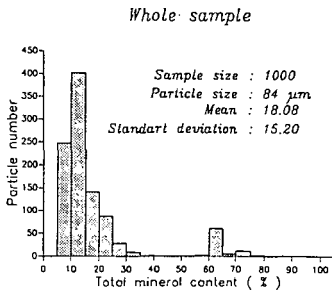
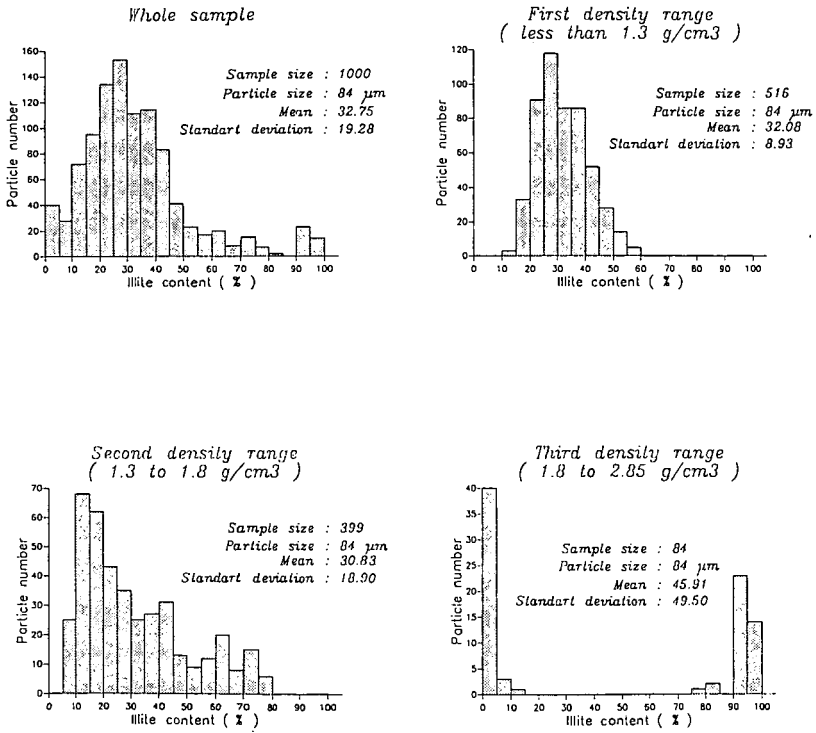


Figure 3: Model predictions of the illite content in different density classes for an 84 μm Upper Freeport coal sample



NEW TECHNIQUES FOR THERMOCHEMICAL PHASE EQUILIBRIUM PREDICTIONS IN COAL ASH SYSTEMS

M. Ramanathan, S. Ness, D. Kalmanovitch

University of North Dakota
Energy and Mineral Research Center
Grand Forks, North Dakota 58202

ABSTRACT

PHOEBE is a new computer code developed at UNDEMRC as a part of a long-term study of coal ash deposition phenomena in combustion systems. The task of developing a new code was undertaken to eliminate the various problems encountered with existing phase equilibrium codes such as SOLGASMIX and PACKAGE. These codes were not able to produce satisfactory comparisons with experimental data and the goal of PHOEBE was to apply better techniques to calculate the minimum Gibbs free energy at thermodynamic equilibrium. The new PHOEBE algorithm has been rigorously tested against standard mathematical functions and is currently being tested against experimental data on coal ash slags. This paper discusses the minimization and optimization techniques used in PHOEBE.

I. Introduction

Understanding the behavior of inorganic constituents during coal combustion is needed to predict the development of ash deposit formation, slagging, and fouling in a combustor. This requires information on the formation of the various mineralogical phases in the vapor, liquid, and solid states and their relationship to the relative amounts of the inorganic elements present in the raw coal and to the variations in combustion conditions. With this type of data, a better understanding of not only the deposition processes but their mitigational aspects as well may be achieved. The calculation of the equilibrium species and phase distributions provides a good starting point in approximating the requisite data.

The problem of obtaining the equilibrium values (x^*_1, \dots, x^*_n) of n distinct species comprising a thermodynamic system S at a fixed temperature and pressure has been extensively addressed in the past, and the utility of obtaining the equilibrium values by minimizing the Gibbs free energy of the system has also been thoroughly emphasized (1-10). A variety of numerical packages (HALTAFALL, SOLGASMIX, PACKAGE, SHIMPO-GOTO, NASA-CEC, etc.) related to this problem have been reported in the literature and their relative merits also discussed. Although the majority of these packages seem to perform adequately on many test cases, they sometimes also appear to produce quite erroneous results. (It must be pointed out that our experience with the above-mentioned packages is limited primarily to SOLGASMIX.) This is not unexpected, since conventionally, the calculations are simplified to the extent that the various interaction terms in the Gibbs free energy of the system are represented only by the 'free energy of mixing' terms, all other interactions being assumed minimal or nonexistent. It has been argued very convincingly that it is indeed valid to approximate the activities of the species by their respective mole fractions (11-13). Nonetheless, this minimality assumption has important consequences for the stability (and hence the existence) of various phases within the

system: even the introduction of a simple Lennard-Jones type potential in a non-interactive system, it may be recalled, lowers the energy of the system, favors the formation of the liquid phase, and would perhaps be more representative of the correct free energy of the system.

This in turn leads to the problem of the availability, or lack thereof, of thermochemical data. The most widely referred sources of thermodynamic data (16-18) often lack data for many of the typical products in coal combustion systems. It is to be also noted that the available thermodynamic tables are themselves extrapolated so that further extrapolations to unreferenced compounds may lead to additional sources of error.

The organization of the paper then is as follows. In Section II the mass constrained Gibbs free energy minimization problem is discussed in detail. A variety of standard numerical methods currently available and their relative merits are also briefly discussed. Section III describes PHOEBE, a Gibbs free energy minimization program currently under development at UNDEMRC.

II. Mass-Constrained Gibbs Free Energy Minimization

Let S be a multicomponent thermodynamic system at a given temperature T and pressure P comprising the species X^1, \dots, X^n and let G be Gibbs free energy of S . Let

$$A^{\alpha}_{aj} \chi^j_{\alpha} = b_a \quad 1)$$

be the mass constraint relations for S where

A^{α}_{aj} = stoichiometry coefficient of atom (or element) a in species j in phase α ,

χ^j_{α} = the number of moles of species j in phase α ,

b_a = the number of moles of atom (or element) a .

In Equation 1 the index α ranges from 1 through the number of phases N_p , the index j ranges from 1 through the number of species N_s , and the index a ranges from 1 through the number of atoms or elements N_a . The Einstein summation convention is used in Equation 1 and in the rest of the paper. Implicit in Equation 1 are the nonnegativity requirements,

$$\chi^j_{\alpha} \geq 0, \quad 1 \leq j \leq N_s, \quad 1 \leq \alpha \leq N_p, \quad 2)$$

that need to be satisfied by the molar amounts of the various species in the system. The Gibbs free energy of S is written as

$$G = \chi^j_{\alpha} \mu^{\alpha}_j \quad 3)$$

where the μ^{α}_j are the chemical potentials of the species which are in turn approximated as follows: let,

$$x_{\alpha} = \sum_{j=1}^{N_s} x_j^{\alpha} \quad 4)$$

be the total number of moles in phase α , and $(\mu_0)^{\alpha}_j$ the standard chemical potential of species j in phase α . μ^{α}_j is then given by

$$\mu^{\alpha}_j = \left\{ \begin{array}{ll} x_j^{\alpha}(\mu_0)^{\alpha}_j & , \text{ if } \alpha \text{ is a pure condensed phase} \\ x_j^{\alpha}(\mu_0)^{\alpha}_j + x_j^{\alpha} \ln \left[\frac{p x_j^{\alpha}}{x_{\alpha}} \right] & , \text{ if } \alpha \text{ is a gas phase} \\ x_j^{\alpha}(\mu_0)^{\alpha}_j + x_j^{\alpha} \ln \left[\frac{x_j^{\alpha}}{x_{\alpha}} \right] & , \text{ if } \alpha \text{ is a solid-liquid mixture} \end{array} \right\} \quad 5)$$

Note that, in Equation 5 the indices α and j are free indices and all implied summations over α and j are to be disabled.

Equations 3-5 approximating the Gibbs free energy of the system are for an assumed or *a priori* phase distribution. For the system S containing N_a distinct elements and N_p distinct phases the Gibbs phase rule may be written as

$$F = (N_a - r - 1) - N_p \quad 6)$$

with F denoting the number of degrees of freedom and r denoting the rank of the stoichiometry matrix A^{α}_{aj} . The nonnegativity requirement

$$F \geq 0 \quad 7)$$

on the degrees of freedom of the system then upper bounds the maximum number of extant phases at equilibrium according to

$$1 \leq N_p \leq N_a - r - 1, \quad 8)$$

and the system attains a free energy value G^* at equilibrium which is minimal with respect to both the possible phase distributions and the possible molar amounts of the species, the latter subject to the mass constraints in Equation 1. Hence, with \mathcal{P} denoting the set of all possible phase distributions, which in view of Equation 8 is finite, and $G^{(p)}$ denoting the Gibbs free energy of S for a particular phase distribution $p \in \mathcal{P}$, the mass constrained Gibbs free energy minimization problem takes the mathematical form

$$\text{Fin} \min_{p \in \mathcal{P}} \inf \{ G^{(p)}(x^1_1, \dots, x^{N_s}_{N_p}) \mid (x^1_1, \dots, x^{N_s}_{N_p}) \in \mathbb{R}^{N_s N_p}, A^{\alpha}_{aj} x^{\alpha}_j = b_a \}. \quad 9)$$

We wish to stress a couple of aspects regarding Equation 9. Firstly, it may be argued from purely physical considerations that there must exist a unique set x^{*1}, \dots, x^{*N_s} of molar values of the species that provides the correspondingly unique minimal of equilibrium value G^* of the free energy. At the mathematical level, the set

$$\Omega = \{(x^1_1, \dots, x^{N_s}_{N_p}) \in \mathbb{R}^{N_s N_p} \mid A^{\alpha_{aj}} x^j_\alpha = b_a, x^j_\alpha \geq 0, 1 \leq j \leq N_s, 1 \leq \alpha \leq N_p\} \quad (10)$$

is a compact (closed and bounded) convex subset of the $N_p N_s$ -dimensional real number space $\mathbb{R}^{N_s N_p}$. The Gibbs free energy G as approximated in Equations 3-5 is a concave, smooth (i.e., infinitely differentiable) function on the positive hyperoctant of $\mathbb{R}^{N_s N_p}$ and hence in the interior of Ω . A theorem of Kuhn and Tucker (19) then asserts that any local minimizer of Equation 9 is the global minimizer, i.e., that there exists one and only one minimizer for 9. Further, this unique minimizing point is given by (20-22)

$$x^{*j}_\alpha = \lim_{\lambda \rightarrow \infty} \frac{\int_{\Omega} x^j_\alpha e^{-\lambda G}}{\int_{\Omega} e^{-\lambda G}} \quad (11)$$

In physical terms, interpreting λ as time, Equation 11 merely expresses the fact that the equilibrium mole values of the species are given in the asymptotic limit $\lambda \rightarrow \infty$ of their expectation or average values.

The second aspect regarding Equation 9 that needs to be stressed is that of the minimization over the possible phase distributions. The total number of possible phase distributions or equivalently the cardinality $|P|$ of the set P is bounded above by

$$|P| \leq \sum_{N_p=1}^{N_a-r-1} \sum_{\substack{N_{k_1} + \dots + N_{k_t} \leq N_s \\ \binom{N_s}{N_{k_1}} \dots \binom{N_s}{N_{k_t}}}} \quad (12)$$

The estimate in Equation 12 is conservative and in practice the total number of phase distributions actually realized are considerably lower. Despite this, for a fairly large system ($N_s \geq 50, N_a \geq 10$), the phase distribution count grows very rapidly and the problem becomes computationally intractable. Various schemes are being studied and a few important results obtained in this regard. A report on these results will soon be appearing in a forth-coming paper (31). The perhaps most interesting trend that we have observed so far in our numerical studies is that the species appear to behave in the manner of 'bosons' preferring to occupy an already existing phase rather than 'creating' a new one. Our more recent studies are expected to shed further light on this rather intriguing aspect of the problem.

III. PHOEBE

A computer program called PHOEBE for calculating the equilibrium mole values and the Gibbs free energy of a given thermodynamic system has been developed implementing the ideas discussed above. PHOEBE is intended primarily for personal computer use and is fully menu driven. The user generates a specific thermodynamic system from a large database and the equilibrium evolution for the system as a function of temperature can be studied. The average run time for a system comprising approximately 50 species and 10 elements over a range of 10-12 temperatures is about 2 hours. There are no restrictions on the number of species or elements or phases except as dictated by available memory. A mainframe version of PHOEBE is currently under development.

The minimization algorithm adopted is a combination of the "variable metric" algorithms (23) and the projection gradient method (24). Given a point $x^{(0)}$ in the interior of the feasible region Ω , a sequence $\{x^{(n)} \mid n \in \mathbb{N}\}$ is generated converging to a local (and by convexity, to the global) minimum of G . If $M^{(k)}$ denotes the constraint matrix of the subset of constraints currently active at iteration step k , the idempotent projection matrix \mathbf{P} (superscript T denotes matrix transpose),

$$\mathbf{P} = \mathbf{I} - M^{(k)T} (M^{(k)}M^{(k)T})^{-1} M^{(k)} \quad (13)$$

is constructed to project the gradient of G into the orthogonal complement of the kernel of $M^{(k)}$. It may be observed that the projection matrix \mathbf{P} in Equation 13 reduces to the identity matrix when restricted to the kernel of $M^{(k)}$. It should also be observed that if the sequence of points so generated is a sequence of regular points (25) of Ω the first order optimality conditions are satisfied (26). If non-regular or degenerate points are encountered in the generation of the sequence leading to the so-called degeneracy or linear dependency problem, these degenerate points need to be appropriately 'sidestepped' (27),(28). (In any event, a generalized inverse of $M^{(k)}M^{(k)T}$ may be made use of to enter the orthogonal subspace of the kernel of $M^{(k)}$.) The convergence of the sequence is accelerated in its later stages by utilizing the Hessian of G , or if the problem is too large, by approximating the Hessian by a suitable symmetric positive definite matrix. The rate of convergence varies between being linear and superlinear.

In addition to the real Hermiticity of the active or binding constraint matrix $M^{(k)}M^{(k)T}$, its nonnegativity, meaning that each matrix element of $M^{(k)}M^{(k)T}$ is nonnegative, has some important consequences. The eigenvalues of $M^{(k)}M^{(k)T}$ are all real, and in view of the Perron-Frobenius theorems (29-30), the positive eigenvalues are all distinct with the largest positive eigenvalue bounded below by the minimum of the row sums and bounded above by the maximum of the row sums. Also, the existence of a nonnegative eigenvector with eigenvalue equal to the spectral radius of $M^{(k)}M^{(k)T}$ may be asserted. These remarks apply to the Hessian of G as well and are actively utilized in resolving the degeneracy problem if and when it arises.

IV. Conclusions

We have been able to develop a fairly satisfactory algorithm for obtaining numerical solutions to the mass-constrained Gibbs free energy minimization problem. PHOEBE performed quite satisfactorily in test runs on known binary and ternary systems. Some coal systems have also been analyzed and excellent results obtained. However, a few of the coal systems analyzed also produced unrealistic results which led directly to the identification and resolution of the degeneracy problem discussed earlier. Our current attempts are now directed towards representing the free energy of the system more accurately and towards accelerating the convergence of the iterative scheme. We expect to detail these extensions and include comparative studies of program output and experimental data in a forthcoming paper (31).

REFERENCES

- (1) Gibbs, J.W. (1961). *The Scientific Papers of J. Willard Gibbs*, Vol. 1, Dover, New York.
- (2) Bracken, J., and McCormick, G.P. (1968). *Selected Applications of Nonlinear Programming*, Wiley, New York.
- (3) Mylander, W.C., Holmes, R., and McCormick, G.P. (1971). *A guide to SUMT, Version 4*: The computer program implementing the sequential unconstrained minimization technique for nonlinear programming, RAC-P-63, McLean, Virginia.
- (4) Van Zeggeren, F., and Storey, S.H. (1970). *The Computation of Chemical Equilibria*, Cambridge U. Press, New York.
- (5) White, W.B., Johnson, S.M., and Dantzig, G.B. (1958). *J. Chem. Phys.*, **28** (751).
- (6) Oliver, R.C., Stephanou, S.E., and Baier, R.W. (1962). *Chem. Eng.* **69** (121).
- (7) Eriksson, G. (1971). *Acta Chem. Scand.* **25** (2651).
- (8) Eriksson, G. (1974). *Chemica Scripta*, **8** (193).
- (9) Eriksson, G., and Rosen, E. (1973). *Chemica Scripta*, **4** (193).
- (10) Stewart, G., Gruninger, J., Davidovits, P., Yousefian, V., Duff, J., and Weinberg, M. (1981). *Computer Modelling of Chemical Processes from Coal Conversion Streams and Related Experiments*, DOE/NC/11783-1849, Bedford, Maryland.
- (11) Hastie, J.N., Horton, W.S., Plante, E.R., and Bonnell, D.W. (1982a). *Thermodynamic Models of Alkali Vapor Transport in Silicate Systems, High Temp.- High Pressure*, **14** (669).
- (12) Hastie, J.N., Horton, W.S., Plante, E.R., and Bonnell, D.W. (1982b). *Alkali Vapor Transport in Coal Conversion Systems*, ACS Symp. Series, **172** (543).
- (13) Hastie, J.N., and Bonnell, D.W. (1984). *A predictive phase equilibrium model for multicomponent oxide mixtures, Part II: Oxides of Na-K-Ca-Mg-Al-Si*, *preprint*.

- (14) Friedman, H.L. (1985). *A Course in Statistical Mechanics*, Prentice-Hall, New Jersey.
- (15) McQuarrie, D.A. (1976). *Statistical Mechanics*, Harper and Row, New York.
- (16) Stull, D.R., and Prophet, H. (1971). JANAF Thermochemical Tables, National Bureau of Standards 37, 2nd ed.
- (17) Barin, I., and Knacke, O. (1977). *Thermochemical Properties of Inorganic Substances*, Springer-Verlag, Berlin.
- (18) Robie, R.A., Hemingway, B.S., and Fisher, J.R. (1978). *Thermodynamic Properties of Minerals*, United States Geological Survey Bulletin 1452, U.S. Govt. Printing Office, Washington, D.C.
- (19) Kuhn, H.W., and Tucker, A.W. (1951). Proc. Second Berkeley Symp. on Mathematical Statistics and Probability, U. of California Press, Berkeley.
- (20) Falk, J.E. (1969a). Lagrange multipliers and nonconvex programs, *SIAM J. Control*, 7 (534).
- (21) Falk, J.E. (1969b). Conditions for Global Optimality in Nonlinear Programming, Report No. 69-2, Series in Applied Mathematics, Northwestern U., Evanston, Illinois.
- (22) Pincus, M. (1968). A closed form solution of convex programming problems, *Letters to the Editor, Operat. Res.*, 16 (690).
- (23) Fletcher, R., and Powell, M.J.D. (1963). A rapidly convergent descent method for minimization, *Comput. J.*, 6 (163).
- (24) Rosen, J.B. (1960). The gradient projection method for nonlinear programming, Part I: Linear Constraints, *J. Soc. Ind. Appl. Math* 8 (181).
- (25) Rockafeller, R.T. (1976). Lagrange Multipliers in Optimization, *SIAM-AMS Proc.*, 9 (145).
- (26) Hestenes, M.R. (1966). *Calculus of Variations and Optimal Control Theory*, Wiley, New York.
- (27) Simmons, D.M. (1975). *Nonlinear Programming for Operations Research*, Prentice-Hall, New Jersey.
- (28) McCormick, G.P. (1983). *Nonlinear Programming: Theory, Algorithms, and Applications*, Wiley, New York.
- (29) Horn, R.A., and Johnson, C.A. (1985). *Matrix Analysis*, Cambridge U. Press, New York.
- (30) Lancaster, P., and Tismenetsky, M. (1985). *The Theory of Matrices*, 2nd ed., Academic Press, New York.
- (31) Ramanathan, M., Ness, S., and Kalmanovitch, D.P. (1988). Mass Constrained Gibbs Free Energy Minimization, UNDEMRC preprint.

DEPOSITION OF BEULAH ASH IN A DROP-TUBE FURNACE UNDER SLAGGING CONDITIONS

D.P. Kalmanovitch, C.J. Zygarlicke,
E.N. Steadman and S.A. Benson

Energy & Mineral Research Center
Box 8213, University Station
Grand Forks, ND 58202

INTRODUCTION

The deposition characteristics of coal ash in combustors is a major operational parameter when considering the applicability of a fuel for utilization in a given system. Recent research has shown that drop-tube combustion and deposition experiments can be effectively used to study ash-formation and deposition furnace behavior of coal under carefully controlled conditions (1,2,3). The drop-tube experiment has many advantages over the usual pilot-scale combustion system with respect to deposition studies. A small quantity of coal (400 grams) is needed to perform many tests and the coal feed rate can be carefully controlled. The flow pattern of the fly ash and products of combustion over the ash deposition surface can also be controlled as well as the temperature of the gases and the substrate, gas composition, and residence time. In order to best understand the processes involved in coal ash deposition detailed knowledge of the coal characteristics, combustion conditions, and temperature history of ash particles and deposit surfaces must be obtained. Furthermore, a detailed knowledge of the mineralogy of the various species within the coal allows comparison of the mineralogy of the ashes and deposits formed during combustion. This comparison can give valuable insight into the mechanism of ash formation and the processes involved in the growth and development of strength which lead to the problem of hard-bonded deposits on heat transfer surfaces in the boiler.

The coal chosen for study in this paper is a Beulah, North Dakota lignite. The lignite has been well-studied by a number of researchers and is considered to be somewhat characteristic of the Northern Plains lignite coal. The lignite has high moisture, low ash fusion temperatures, and high alkali - alkaline earth elements present in the ash. A benefit of the coal is the lower sulfur content on a sulfur per million Btu basis compared to eastern coals and high reactivity. The deposition characteristics of the coal are of particular interest as the fuel is known to cause heavy fouling deposits in utility boilers. Indeed, the boilers designed to burn the lignite are about 50% larger than comparable boilers designed to burn high ash-fusion eastern coals. The Beulah lignite is also of importance in ash deposition studies as the coal contains inorganic species both in the mineral phase as well as within the organic matrix of the coal. Extensive research at the University of North Dakota Energy and Minerals Research Center has shown the importance of the organically-bound species on the deposition characteristics in pilot-scale combustion testing (4). Techniques have been developed which can quantify the relative amount of an element which is organically bound or mineral bound. In general, the technique, called chemical fractionation, determines the amount of an inorganic species present in a series of leachates using water, ammonium acetate, and hydrochloric acid (5). The water removes the inorganic species which was loosely associated with the carbonaceous matrix. The ammonium acetate removes a portion of the inorganic constituents, by ion exchange; these constituents are chemically associated with the coal matrix, usually in the form of salts of carboxylic acids. The

hydrochloric acid dissolves the acid-soluble mineral grains such as carbonates, some oxides as well as sulfates and organically coordinated inorganic elements. By comparing the amount of inorganic constituents removed from the coal with the original composition, the amount of inorganics present as insoluble material can be calculated. The insoluble material usually includes inorganic elements associated with acid-insoluble discrete mineral phases such as quartz, pyrite, and clays. In the case of Beulah lignite, chemical fractionation shows that the bulk of the sodium and a large fraction of the calcium is organically bound. These data contrast with eastern coals, where most of the inorganic constituents tend to be associated with the acid-insoluble fraction.

The fate and behavior of the organically bound elements and their reactions with the mineral bound species are of great interest in relation to the deposition characteristics of the coal. Therefore, a detailed understanding of the processes that affect the deposition characteristics of Beulah lignite will give valuable insight into the fundamental aspects of coal ash deposition.

TABLE 1
DROP-TUBE FURNACE RUN CONDITIONS USED TO PRODUCE
INTERMEDIATE ASH FROM BEULAH COAL

Coal Size, μm	53-74
Coal Feed Rate, g/min	0.314
Primary Air, L/min	1.0
Secondary Air, L/min	3.0
Quench Gas, L/min	3.0
Temperature, $^{\circ}\text{C}$	
Secondary Air	930
Furnace Tube skin	1500
Gas Temperature at Inlet to Quench Probe	1450

EXPERIMENTAL PROCEDURE

A sample of Beulah lignite was characterized using chemical fractionation and computer controlled scanning electron microscopy (CCSEM). The latter technique provides the identification and size distribution of the coal minerals. Details of the technique can be found elsewhere (6). Pulverized coal samples were then burned under a range of combustion and deposition conditions in the EMRC drop-tube furnace facility. Details of the drop-tube facility can be found in other publications (1). However, for the purpose of this study, it is important to note that the drop tube furnace has the capability of studying the formation of ash intermediates as

TABLE 2
 DROP-TUBE FURNACE RUN CONDITIONS USED TO PRODUCE ASH DEPOSITS
 BEULAH DEPOSIT RUN

Feed Rate, g/min	0.272
Coal Size, μm	53-74
Primary Air, L/min	1.0
Secondary Air, L/min	3.0
Quench Air, L/min	8.0
Temperature, $^{\circ}\text{C}$	
Secondary Air	1000
Furnace Tube Skin	1501
Gas Temperature at Constrictor	1478
Substrate	475

• Distance from tip of injector

well as the formation of deposits over a wide range of temperature and residence times. In this study, the determination of intermediate species (entrained ash) and deposits formed under slagging (1450°C) conditions was defined by the gas temperature at the region of the probe and residence time (0.6 to 0.8 sec). The intermediate ash species were cooled with a gas quenching probe and collected using a six-stage multicyclone. Ash deposits were produced by accelerating the fly ash and products of combustion through a ceramic nozzle and impinged on an oxidized boiler steel substrate. In all cases where deposition was studied, the substrate consisted of pre-oxidized carbon steel and was controlled at a given temperature. The conditions used to produce the intermediate ash and deposits are summarized in Table 1 and 2, respectively.

In all cases the intermediate ash from each stage of the multicyclone and deposits were analyzed by x-ray diffraction, scanning electron microscopy and scanning electron microscopy point count (SEMP) techniques. The SEMPC technique was developed at the EMRC to quantify the various phases present in an ash sample. The technique involves the analysis of about 240 points on a polished section of a deposit or a dispersion of ash on cello tape using the electron microprobe facility of the electron microscope with a thin window energy dispersive detector. The compositions of each of the points are transferred to a Lotus[®] spreadsheet which classifies each analyzed point based on chemical composition. The range of classification includes a total of about 30 phases including coal mineral phases, derived mineral phases, crystalline phases, amorphous phases and unclassified phases. Full details of the technique can be found elsewhere (7). Major advantages of the technique include: quantification of the phases, chemical composition of the phases and chemical composition of the point analyzed. The latter is particularly useful for studies where there is insufficient material for bulk chemical analysis. Another important advantage is the ability to determine physical characteristics of each point based

on the chemical composition. For heterogeneous samples such as deposits and fly ash, the chemical composition of the points will be different. However, using the Urbain model of viscosity recently improved by Kalmanovitch and Frank (8), the chemical composition can be used to calculate the viscosity at a given temperature. From these calculations a distribution or population frequency of the viscosity can be determined. This has two advantages. The first is that it describes the heterogeneity of the sample with respect to a key parameter in the deposition process, namely the viscosity of the liquid phase. Second, it allows comparison of the viscosity distribution of specific areas with other areas from the same sample or other samples.

RESULTS AND DISCUSSION

Characterization of Coal

The chemical fractionation results for the coal, Table 3, shows that the bulk of the sodium, magnesium, and calcium are organically bound. The elements removed by HCl include significant amounts of aluminum, calcium, and iron. The extractability with HCl suggests that these elements are associated in the coal as carbonates, acid soluble oxides and organically coordinated elements. The elements remaining after the water, ammonia acetate, and HCl extractions consisted of portions of the aluminum, iron and most of the silicon. The aluminum is likely associated with clay minerals, the silicon with clay minerals and quartz, and the iron is associated as pyrite.

The mineral grains present in the 53-74 μ m sized fractions of coal were sized consistently with the multicyclone particle size controls. The results of the CCSEM mineralogical analysis of the 53-74 μ m sized fraction coal are listed in Table 4. The data shows that the major mineral phase present was aluminosilicate. The aluminosilicate is defined in the technique as mineral grains which contain predominantly Si and Al with no significant presence of another element. Oxygen is not detected by this technique. The aluminosilicate is found to be predominantly in the less than 11 micrometer size range. Only about 30 wt% of the mineral was observed to be larger than 11 microns. There was very little aluminosilicate observed in the size ranges below 2.1 microns. Quartz was also observed in the coal. The bulk of the quartz was in the 4.4-8.0 micron size range. There was very little quartz in the smaller size fractions (less than 2.1 microns) and little quartz above 11 microns. There was very little Fe-aluminosilicate or K-aluminosilicate detected in the coal sample. However, some Ca-aluminosilicate, that is mineral grains containing Si, Al, and Ca, was observed in the sample. The bulk of this phase was present in size ranges less than 4.4 microns. The other mineral phases which were observed in significant quantities were pyrite (Fe and S rich grains), barite (Ba and S rich grains), and gypsum (Ca and S rich grains). The pyrite was present in size ranges below 11.0 microns with the bulk observed in the 8.0-11.0 micron range. The barite was present in the sample both in the large size fractions, above 11.0 microns, and the smaller size fractions, between 1.2 and 8.0 microns. The gypsum was present in significant quantities between 2.1 and 11.0 microns. An important aspect of the mineralogy is that there was no mineral phase observed which contained sodium even though this element is present in the coal ash. Furthermore, the level of calcium present in the various mineral phases does not account for the total amount of calcium present in the coal ash. This data confirms the chemical fractionation data.

TABLE 3
CHEMICAL FRACTIONATION RESULTS FOR BEULAH (6.2% Ash)

	Initial ($\mu\text{g/g}$ mf coal)	Removed by H_2O (%)	Removed by NH_4OAc (%)	Removed by HCl (%)	Remaining (%)
Sodium	5,700	42	57	1	0
Magnesium	2,600	1	97	2	0
Aluminum	3,500	0	0	32	68
Silicon	7,230	1	4	2	93
Potassium	100	65	26	9	0
Calcium	9,700	0	74	26	0
Iron	3,500	0	2	83	15

TABLE 4
BEULAH CCSEM MINERAL COMPOSITION AND DISTRIBUTION
(Results expressed as wt% minerals)

Mineral types	SIZE CATEGORIES (MICRONS)						TOTAL WT. % TOTAL WT. %	
	<1.2	1.2-2.1	2.1-4.4	4.4-8.0	8.0-11.0	>11.0	MINERALS	MINERALS (Coal Basis)
QUARTZ	5.7	7.7	14.5	21.7	29.0	19.1	19.5	1.17
KAOLINITE	41.5	39.5	42.1	53.6	38.1	71.7	51.6	3.11
FE-ALUMINOSILICATE	2.4	1.3	0.3	0.7	0.0	0.0	0.4	0.03
K-ALUMINOSILICATE	0.0	0.0	2.3	0.0	0.0	0.0	0.5	0.03
CA-ALUMINOSILICATE	20.9	24.7	16.4	2.2	0.0	0.0	6.3	0.38
IRON OXIDE	3.6	0.5	0.7	3.9	0.0	0.0	1.6	0.09
PYRITE	4.4	2.1	7.2	1.1	15.3	0.0	4.5	0.26
GYPSUM/BARITE	1.5	5.4	0.4	0.0	0.0	0.0	0.5	0.03
CALCITE	0.0	0.0	0.7	0.0	0.0	0.0	0.1	0.01
BARITE	2.3	7.1	6.1	7.4	0.0	9.2	6.3	0.38
GYPSUM	0.0	0.5	2.8	6.6	12.4	0.0	4.5	0.28
UNKNOWN	17.7	10.5	6.5	2.8	5.2	0.0	4.1	0.24

Characterization of Intermediates

Table 5 lists the results of the SEMPC analysis of the various multicyclone fractions quenched at a gas temperature of 1450°C during the drop-tube combustion of the 53-74 μm Beulah lignite. The first five multicyclones contained various quantities of anorthite, $(\text{CaO}\cdot\text{Al}_2\text{O}_3\cdot(\text{SiO}_2)_2)$, quartz, melilite (a solid solution series between akermanite, $(\text{CaO})_2\text{MgO}\cdot(\text{SiO}_2)_2$ and gehlenite, $2\text{CaO}\cdot\text{Al}_2\text{O}_3\cdot\text{SiO}_2$), and kaolinite derived material. The anorthite and melilite are products of high temperature

recrystallization from a melt phase. The quartz is a residual coal mineral phase. The kaolinite derived material is defined as a point which has a Si/Al molar ratio corresponding to that of kaolinite but has extraneous elements associated with it. The kaolinite derived material and the unclassified material are assumed in our interpretation to be amorphous. In all cases where x-ray diffraction was performed on the same sample as analyzed by SEMPC the latter technique found more crystalline phases than the x-ray diffraction. The points which are overlaps of two adjacent phases may be unclassified. However, these are statistically rare and would not be expected to affect the interpretation of the data as amorphous phases. In general, the SEMPC data shows that the size fractions above 1.2 microns tend to aluminosilicate phases with little sulfate present. The presence of kaolinite derived, anorthite, and melilite phases, shows that there was significant melting and interaction between the Ca, derived from the organic matrix, and the aluminosilicate mineral phase (kaolinite). The relative amounts of quartz in the different size fractions follows the same trend as observed in the CCSEM analysis of the coal. The chemical composition of the material collected in the first five multicyclone filters contained very little sodium. The material in the final filter contained predominantly sodium-calcium sulfate, 76%. The data shows that the sodium and sulfate species tend to be present in, or associated with, the finely dispersed phase, that is, the phase below 1.2 microns.

TABLE 5
SEMPC RESULTS FOR BEULAH MULTICYCLONE SIZE FRACTIONS
(Results expressed as number %)

STAGE #	1	2	3	4	5	6
SIZE, μm	>11.0	8.0-11.0	4.4-8.0	2.1-4.4	1.2-2.1	<1.2
MASS, %	76.2	4.8	7.5	4.2	3.6	3.7
<hr/>						
Phase						
CaO	3	0	0	0	0	0
Fe-oxides	7.2	2.3	0	0.6	0	0
Kaolinite*	36.2	50.4	63.5	60.2	60.1	10
Anhydrite	0.4	0	0	0	0	5
Anorthite	5.1	3.1	2.9	6.4	1.2	0
Quartz	4.7	2.3	0.7	1.2	0.4	0
Melilite	1.7	2.3	5.8	1.2	1.2	0
Na-Ca-Sulfate	0	0	0	0	0	76
Unclassified	41.7	35.7	34.3	33.9	36.6	8

* kaolinite-derived

Characterization of Deposits

Figure 1 shows the general view of the slag droplet formed on the probe plate. There are two distinct regions, the sintered material near the base and the glassy droplet on the surface of the sintered material. The sintering material at the base of the deposit and slag droplet were each analyzed by the SEMPC technique. Table 6 compares the SEMPC data for the two samples.

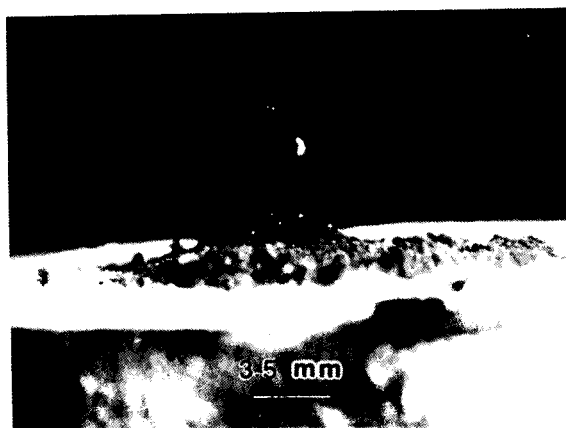


Figure 1. General view of slag formation on the probe plate.

TABLE 6

SEMPC DATA FOR SINTERED AND SLAG SAMPLES OF BEULAH ASH (1450°C)

PHASE, percent	SINTERED	SLAG
Calcium oxide	2.0	0.0
Montmorillonite-derived	0.5	1.3
Calcium silicate	1.0	0.0
Iron oxide	10.4	18.9
Kaolinite-derived	12.4	10.6
Anhydrite	1.5	0.4
Anorthite	1.5	1.3
Quartz	7.9	7.5
Melilite	0.5	0.0
Dicalcium silicate	0.5	0.0
Calcium derived	6.0	0.9
Unclassified	56.1	58.6

The results of the SEMPC analysis indicates that there are different phases present in the base of the deposit than in the slag at the top of the deposit. The SEMPC analysis of the base of the deposit corresponds very well with the analysis of the first stage of the multicyclone. All the phases observed in the first multicyclone stage were observed in the base of the deposit and the relative proportion of the phases are very similar. However, there was more calcium derived and less kaolinite derived material in the deposit base than was observed in the multicyclone. This is presumably due to the effect of residence time, milliseconds for the multicyclone sample compared to minutes for the deposit.

The slag deposit had similar phases to the base deposits. However, there were some significant differences. There was only one calcium aluminosilicate phase, that of anorthite, observed in the slag samples. This contrasts with the base where calcium silicate, dicalcium silicate, and melilite were observed in the base as well as the multicyclone samples. No calcium oxide was observed and the level of calcium-derived material was much lower in the slag as compared to the deposit base. The data indicates that the sample was approaching thermal equilibrium due to the long residence time and the higher temperature, approaching 1450°C. The composition of the material excluding quartz and iron oxide phases, would give a predominantly calcium aluminum silicate system. The normalized CaO-FeO-Al₂O₃-SiO₂ composition when plotted on the equilibrium phase diagram show that the composition lies in the primary phase of anorthite with a liquidus temperature of about 1400°C.

The SEMPC also gives data on the chemical composition of the sample studied. Table 7 compares the chemical composition of the sample base and slag deposit. Also included in Table 7 is the Si/Al molar ratio and the chemical composition of the unclassified points and the silicate phases observed in the two samples. The latter data is obtained by deleting the compositions of the quartz, iron oxide, calcium derived and anhydrite points from the data base and recalculating the average chemical composition.

The composition of the base was very different than the slag. Most notable differences were with the levels of SiO₂, Al₂O₃, CaO, and SO₃. The base had less SiO₂ and Al₂O₃ and greater CaO and SO₃ than the slag. This confirms the earlier observation that the initial deposit adhesion and growth is via a sulfate mechanism whereas the slag is via a silicate based matrix (9,10). The Si/Al molar ratio for the base and slag are relatively similar. This indicates that there is little change in the transport of silicate and aluminosilicate species to both types of deposit. The higher levels of CaO and SO₃ in the base of the deposit would suggest that there is a preferential deposition of the calcium-rich species on deposit surfaces still cooled by the probe. The level of SO₃ tends to indicate that the sulfation of the calcium occurred after the deposition of the calcium rich grains.

The CCSEM data on the coal and the chemical fractionation data indicated that there was relatively limited mineral bound calcium in the coal, the bulk was organically bound. This would tend to indicate that the transport of calcium would be as finely dispersed calcium oxide/calcium sulfate particles. However, the SEMPC data on the multicyclone samples indicate that significant calcium was associated with the large size fractions which were also rich in aluminum and silicon. It was also noted that the SEMPC data for the first multicyclone was very similar to the SEMPC data for the base of the deposit. This indicates that the major mass transport to the deposition probe is via the large size fractions. The presence of such a high level of calcium

TABLE 7
CHEMICAL COMPOSITION OF DEPOSITS (SEMPC)

<u>Wt. %</u>	<u>Base</u>	<u>Slag</u>
SiO ₂	25.5	39.8
Al ₂ O ₃	10.0	16.5
Fe ₂ O ₃	21.0	30.7
TiO ₂	0.7	0.4
P ₂ O ₅	0.0	0.0
CaO	31.3	9.8
MgO	2.0	0.3
Na ₂ O	0.2	0.8
K ₂ O	0.1	0.3
SO ₃	8.8	1.3
Si/Al molar ratio	2.05	2.17

CHEMICAL COMPOSITION OF UNCLASSIFIED AND SILICATE PHASES

<u>Wt. %</u>	<u>Base</u>	<u>Slag</u>
SiO ₂	24.9	50.6
Al ₂ O ₃	13.5	24.9
Fe ₂ O ₃	10.7	11.3
TiO ₂	1.0	0.6
P ₂ O ₅	0.0	0.0
CaO	37.6	13.1
MgO	2.6	0.4
Na ₂ O	0.1	1.1
K ₂ O	0.2	0.4
SO ₃	9.1	1.3

associated with the aluminosilicate species indicates that melting and assimilation occurred at the relatively high temperatures. The entrained ash would not be expected to see a temperature below the gas temperature of 1450°C. These high temperatures and relatively short residence times preclude the formation of sulfate species. However, calcium aluminosilicate phases, both liquid and crystalline, are stable at these temperatures. The reaction of calcium with the aluminosilicate

phases is evidenced by the presence of phases such as melilite, anorthite, calcium silicate, and dicalcium silicate in the multicyclone fractions. These phases are not the product of thermal decomposition of mineral phases but are products of recrystallization from a calcium rich melt phase.

The level of calcium in the multicyclone fractions precludes total reaction with the aluminosilicate phases, and once deposited, the calcium rich material will tend to react with sulfate at lower temperatures. This leads to the low level of calcium in the slag deposit. This process can be understood if one considers that the material which will form a melt phase at these temperatures will be the elements intimately associated with the aluminosilicate phases. Refractory oxides such as calcium oxide which have not reacted to any extent with the aluminosilicate will not be associated with the phase forming the liquid drop and will tend to be expelled from the surface of the droplet and removed by the scrubbing action of the gas stream. Substantiation of this process can be seen with the analysis of the relative levels of sodium in the two samples. The sodium was observed to be present predominantly in the final filter of the multicyclone along with calcium sulfate. The stability of sodium sulfate is less than that of calcium sulfate at 1450°C. Therefore, the low level of sodium in the base deposit is due to the fact that it was not transported along with the aluminosilicate phases. The relative enrichment in the slag is due to thermal dissociation of the sulfate species and reaction with the aluminosilicate phase. Sodium has a greater affinity for aluminosilicate melt phase than calcium at 1450°C. A large proportion of the sodium is present in the very small size fractions. Under the conditions used the bulk of the sodium must have been carried past the deposit probe along with the gaseous products of combustion. This shows why sodium is such a problem in the cooler regions of the boiler, i.e. the convective pass where conditions tend to increase the stability of sodium sulfate and other alkali-rich species.

CONCLUSIONS

The detailed analysis of a Beulah lignite sample and the deposits formed from the fuel in a drop tube furnace at a gas temperature of 1450°C has given valuable insight in the mechanisms of mass transport and deposit initiation and growth. The coal was shown by chemical fractionation and computer controlled scanning electron microscopy (CCSEM) to contain aluminosilicate species and organically bound calcium and sodium. The entrained ash, as sampled using a multicyclone, was shown, by using a novel technique called scanning electron microscopy point count (SEMPC), to contain high temperature calcium silicate and calcium aluminosilicate phases in the size fractions above 1.2 microns and calcium and sodium-calcium sulfate in the less than 1.2 micron range. The deposit formed from the coal ash with a probe surface temperature of 350°C and gas temperature of 1450°C was comprised of a small sintered base with a molten slag droplet on the surface; both sections were characterized using SEMPC. This technique showed that the deposit base had a similar chemical composition and phase assemblage as the largest multicyclone fraction, i.e. above 11.0 microns. The slag deposit however, had lower CaO and SO₃ than the base of the deposit and the calcium aluminosilicate phase observed was consistent with that expected for the melt phase from thermal equilibrium phase diagrams. Further analysis of the SEMPC data showed that the bulk of the material was transported to the probe surface with the aluminosilicate fraction. The different levels of CaO in the two sections of the deposit were consistent with the observed association of calcium with the aluminosilicate phases in the multicyclone samples and the known relative thermal stability of calcium aluminosilicates over calcium sulfate at 1450°C. The level of sodium was low in both samples of the deposit, and low in all multicyclone

samples except the final filter material. The low level of sodium in the deposit is consistent with the sodium being present in a finely dispersed form which was carried past the deposit with the combustion gases.

The study has shown the importance of detailed analysis of the coal, intermediates, and deposits in understanding the mechanisms and processes which affect deposit formation and growth in a drop-tube furnace. The results of this study can be summarized as follows:

- o Organically bound calcium will react with clay species to form calcium-rich aluminosilicates at short residence times.
- o The bulk of the calcium is transported via these calcium-rich aluminosilicates.
- o Sodium (organically bound) as sodium calcium sulfate was formed in the smallest size fractions.
- o The mass transport to the cooled metal surface tends to be that of the largest size fraction of the multicyclone (above 11 microns).
- o Sulfation of the calcium tends to occur after deposition and only in the cooler regions of the deposit (nearest the metal surface).
- o The matrix in the slag section of the deposit is predominantly calcium aluminosilicate and tends to approach thermal equilibrium.
- o The similarity in Si/Al molar ratio in the base and slag sections of the deposit indicates similar transport mechanisms throughout the deposit growth cycle.
- o Relatively low concentrations of Ca in the slag was indicated to be due to the poor assimilation of refractory calcium oxide rich regions into the melt phase.
- o Sodium enrichment in the slag relative to the base was consistent with the great affinity of sodium in silicate melts.
- o The low level of sodium in the deposit indicates that the sodium was entrained in the gas phase and passed over the probe and deposit under then slagging conditions.

ACKNOWLEDGMENTS

The collection and characterization of the intermediate ash material was performed under contract with the U.S. Department of Energy Pittsburgh Energy Technology Center. Philip Goldberg is the project manager. Formation and characterization of ash deposits was performed under contract with the Advanced Combustion Engineering Research Center, Brigham Young University, L. Douglas Smoot is the Project Manager. The authors would like to thank Mr. Goldberg and Dr. Smoot for their support of this work.

REFERENCES

1. Benson, S.A., E.N. Steadman, and D.P. Kalmanovitch, "Studies of the Formation of Alkali and Alkaline Earth Aluminosilicates During Combustion Using a Laboratory Scale Furnace," Presented at the EPRI Conference on Effects of Coal Quality on Power Plants, Atlanta, October 13-15, 1987.
2. Benson, S.A. and Austin, L.G., "Laboratory Ash Deposition Studies of a Gravity-fractionated Coal," 88-JPGC/Pwr-4.
3. Benson, S.A., W.H. Puffe, M.L. Jones, R.W. Borio, J.F. Durant, and A.K. Mehta, "Laboratory-scale Ash Deposition Studies of a Size and Gravity Fractionated Coal", Proceedings of the American Flame Research Committee 1988 Fall International Symposium, October 4-6, 1988.
4. Sondreal, E.A., Tufte, P.H., and Beckering, W. "Ash Fouling in the Combustion of Low Rank Western U.S. Coals", Combustion Science and Technology, Vol. 16, 95-110, 1977.
5. Benson, S.A. and P.L. Holm, "Comparison of Inorganic Constituents in Three Low-Rank Coals," Ind. Eng. Chem, Prod. Res. Dev., 24, 145-149, 1985.
6. Huggins, F.E., and D.A. Kosmack, 1980, Coal Mineralogies by SEM automatic image analysis: Scanning Electron Microscopy, 1980, I, AMF O'Hare (Chicago), IL 60666, p. 531-540.
7. Kalmanovitch, D.P., G.G. Montgomery and E.N. Steadman, ASME Paper Number 87-JPGC-FACT-4, 1987.
8. Kalmanovitch, D.P. and M. Frank, "An Effective Model of Viscosity for Ash Deposition Phenomena", presented at the conference on Mineral Matter and Ash Deposition from Coal, The Engineering Foundation, Santa Barbara, CA, February 21-26, 1988.
9. Benson, S.A. and L.G. Austin, "Study of Slag Deposit Initiation Using a Laboratory-Scale Furnace", Presented at the Conference on Mineral Matter and Ash Deposition from Coal, The Engineering Foundation, Santa Barbara, CA, February 21-26, 1988.
10. Jones, M.L. and S.A. Benson, "An Overview of Fouling and Slagging from Western Coals", Presented at the EPRI Conference on Effects of Coal Quality on Power Plants", Atlanta, GA, October 13-15, 1987.

A CLASSIFICATION OF COAL-FIRED BOILER DEPOSITS

Roderick M. Hatt
Island Creek Corporation
Lexington, KY 40579

Susan M. Rimmer
Department of Geological Sciences
University of Kentucky
Lexington, KY 40506

INTRODUCTION

Ash deposition in boilers has been studied by numerous investigators from virtually all areas of physical science. Several books (1) (2), and publications too numerous to reference have been published on this subject. Unfortunately the information flow between boiler operators and researchers has not always been ideal. In the absence of a workable classification system, valuable information concerning the nature and conditions of formation of boiler deposits may be lost. Field observations can greatly enhance information derived from laboratory study, and can lead to a more meaningful interpretation of the causes and, ultimately, to the solution of boiler deposits. As such, the system proposed here provides basic steps in the documentation of field observations together with a simple megascopic and microscopical classification scheme.

Whereas this system was designed to describe deposits from coal-fired steam generators, it may be applied to other environments or equipment with similar high-temperature mineral transformations. This system only addresses cooled deposits, as opposed to those that exist at the higher temperatures of boiler operation.

DEPOSITS IN BOILERS: FIELD OBSERVATIONS

Boiler Description

The type of boiler influences the properties and significance of the deposits (3). A simple description of the boiler and operating conditions provides information on processes and environments to which the coal and ash may have been exposed. This description should include, at a minimum, firing method (stoker, PC, cyclone), unit size including steam flow, heat input and plan area, and, if known, gas temperatures and velocities through out the system. All of these variables can influence deposit formation (4). Much of this information, in addition to the proximate, ultimate and heating values for the design fuel, is provided on the boiler manufacturers' performance sheet.

Fuel Description

Variations in ash content and composition of the feed coal can lead to a variety of boiler problems as discussed by Hatt (5). A

detailed description of the feed coal is important and could include, where available, proximate, HHV, total sulfur, sulfur forms, ash-fusion temperatures, and ash chemistry. Other, more detailed coal analyses can be helpful in determining coal quality impacts on deposit formation (6).

Location of Deposits

The physical appearance of the deposit should be given using the megascopic system presented below, together with location and extent of the deposit, preferably by providing a simple sketch of the boiler in a side and top sectional view (as shown in Figure 1). Photographic documentation is useful but can be difficult to obtain. The location of deposit samples taken during the boiler inspection can be documented on this sketch. Samples should be taken to represent the entire deposit. Guidelines on sampling can be found in the British Standard (7), and in a future publication (8).

MEGASCOPIIC CLASSIFICATION

Boiler deposits can be classified as either molten deposits (slags) or deposits bonded by sulfate salts (fouling deposits) (3). Each type of deposit has characteristics that can be used to describe the material and can provide clues about the conditions of formation. Figure 2 shows an outline of the megascopic system.

Slags or Molten Deposits

Slags or molten deposits can be classified into four basic types.

- Metallic - These slags have a metallic luster and are usually associated with the combustion of pyrite-rich coals under reducing conditions. The high specific gravity of the metal generally allows it to separate from the slag, and to remain isolated from any subsequent oxidizing atmospheres (Figure 3a).
- Amorphous - Amorphous slags are dark, solid, glassy, and generally show a conchoidal fracture. Amorphous slags are usually found in the higher temperature regions of the boiler (Figure 3b).
- Vesicular - Glassy slags with trapped bubbles (a sponge-like appearance) can be classified as vesicular. These are usually associated with higher temperature regions in the boilers. Trapped gas bubbles may be distorted due to viscous flow (Figure 3c).
- Sintered - Deposits that are composed of partially fused particles may be classified as sintered. These are gritty in texture, are typically found in

the upper furnace and convection passes, and may be associated with vesicular slags (Figure 3d).

Additional useful information could include physical characteristics such as tube imprints, gas flow direction, color, and size.

Fouling Deposits

Fouling deposits are differentiated from slags according to the type of bonding that occurs between particles. In slags, bonding is produced by melting or fusion of the ash particles; in fouling deposits, the ash particles are bound together by sulfate salts (3). Gas temperatures in furnace regions where fouling occurs are generally lower than those associated with slagging; there is, however, some overlap where both bonding mechanisms can occur. Fouling deposits are generally dull in luster, have a gritty or brick-like texture, and lack the glassy and vesicular textures observed in slags. Distinguishing features include color, shape, size, internal structures such as laminations, and strength. The location and orientation of the deposit with respect to the tubes and gas flow can provide additional information. Strength is one of the most important characteristics of fouling deposits, and may be categorized using the following relative index:

- Very Strong - Deposits are hard, and may be broken only with the aid of a hammer, chisel or other tool.
- Strong - Deposits can be broken by hand but do not crumble easily.
- Weak - Deposits crumble when handled.
- Unconsolidated - Deposits are not bonded and result from accumulations of material which settle out of the flue gas.

Although qualitative in nature, this strength rating provides an indication of the degree of bonding in the deposit, and can be used to determine the level of difficulty that removal of a deposit could present.

MICROSCOPIC CLASSIFICATION

Microscopic examination of ash deposits indicates the degree and nature of bonding. This microscopic classification system is designed to be used with both polarized-light and scanning electron microscopy. It is analogous to the megascopic system in that it differentiates between slagging and fouling deposits based on the presence or absence of sulfate salts. In many cases several phases may be discernible under the microscope, i.e. both amorphous and vesicular, or sintered with sulfate salts. This can make the categorization of some deposits problematic, and in these cases all of the appropriate descriptions should be noted. Figure 4 is an outline of the microscopic system.

Amorphous Slag Phases

Amorphous slags are usually alumino-silicate melts with varying amounts of basic (fluxing) elements. Using a polarizing microscope, crushed samples can be used to show the conchoidal fracture. Magnetic minerals can be identified by placing a magnet near the glass slide on which the crushed sample is mounted in oil or water. In thin section, amorphous slags do not exhibit any birefringence. Conchoidal fracture can also be observed using a scanning electron microscope. Quartz can be trapped inside of the slag as an inclusion; dendritic species can be formed during cooling of the deposit during unit shut down. Mullite needles are also present in some samples. (3) The presence of bubbles and their shape provides information on the viscosity and gas flow direction. Figures 5a & 5b shows several examples of amorphous slags viewed microscopically.

Partially Fused or Sintered Phases

Sintered phases are characterized by the presence of fused ash particles. The degree of fusion can vary within a single sample, and can tend towards complete fusion of the particles, i.e., the formation of an amorphous slag. The degree of fusion between particles has been correlated with the strength of the deposits (2) and with the chemical composition (7).

In the classification system presented here the degree of fusion between particles is not quantified; only the presence or absence of fusion is noted. If the ash exhibits no fusion or bonding, other classification systems, such as that proposed for fly ash by Fisher (8) or Roy (9) can be used. In addition, sintered deposits may contain non-bonded or slightly bonded particles, which add considerable bulk to the deposit. Figures 5c & 5d show examples of sintered ash particles.

Sulfate Salt Bonding

The presence of sulfate salt or similar bonding material is indicative of fouling mechanisms. The classification of these deposits is similar to that of slag, i.e. totally bonded versus partially bonded.

Total Bonding

When the individual fly-ash particles are bonded totally by sulfate salt, the deposit is generally hard and is representative of the classic fouling deposit. Another category of a totally bonded deposit occurs where sintered deposits are enveloped in a sulfate "glue." The combination of both sintered and fouling bond types makes these deposits particularly hard to remove. These dual-bonded deposits represent slagging and fouling at the same location, and possibly at the same time. Sulfate-salt bonding is not generally associated with amorphous slags. (Figure 6a & b)

Partial Bonding and Surface Crystals

Partial sulfate salt bonding and surface crystals can be observed in some deposits, with the degree of bonding increasing towards totally bonded types of deposits. The presence of this partial bonding can add strength to a sintered type slag. (Figures 6c & 6d)

CONCLUSIONS

The classification system presented here represents an initial attempt in the description of boiler deposits. The use of such a system should aid in communication about the nature of deposits encountered, allowing the engineer or operator to more precisely communicate his problem with the researcher.

REFERENCES

1. Vorres, K.S., Editor, "Mineral Matter and Ash in Coal," ACS Symposium Series 301. American Chemical Society, 1986.
2. Raask, E., "Mineral Impurities in Coal Combustion," Hemisphere Publishing Corp., New York, N.Y. 1985.
3. The Babcock and Wilcox Company, "Steam, Its Generation and Use," 38th Edition, 1975.
4. Hsu, L.L.; Kubarych, K.G.; Stetson, A.R.; and Metcalfe, A.G., "Mechanisms of Fouling, Slagging and Corrosion by Pulverized Coal Combustion," Final Report US DOE Contract No. DE-AC22-81PC40272, June, 1984.
5. Hatt, R.M., "Prediction and Evaluation of Coal Performance Based on Laboratory Analyses," from Proceedings of the 5th International Coal Testing Conf., February 11-13, 1986, Lexington, KY pp 79-87.
6. Borio, R.W. and Narciso, Jr., R.R., "The Use of Gravity Fractionation Techniques for Assessing Slagging and Fouling Potential of Coal Ash." Winter Annual Meeting of ASTM, December, 1978.
7. British Standard - BS2455: Methods of Sampling and Examining Deposits from Boilers and Associated Industrial Plant, Part 2, 1983.
8. Hatt, R.M., "Boiler Deposit Sampling Guidelines." To be published; available on request.
9. Hatt, R.M. and Bull, D.L., "Morphological and Chemical Relationships of Deposits Formed in a Full-Scale Steam Generator," Engineering Foundation Conference on Mineral Matter and Ash Deposition from Coal Santa Barbara, CA February 21-26, 1988.

10. Fisher, G.L., et al., "Physical and Morphological Studies of Size Classified Coal Fly Ash," Environmental Science and Technology V. 12 no. 4 p447-451, 178.
11. Roy, W.R., et al., Coal Fly Ash: A Review of the Literature and Proposed Classification System with Emphasis on Environmental Impacts, Illinois State Geological Survey, Environmental Geology notes 96, April, 1981.

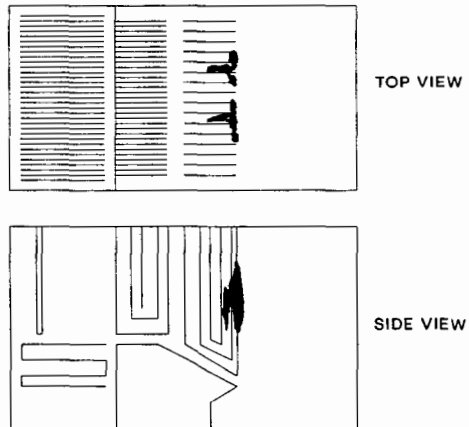


FIGURE 1. SIMPLE SKETCH OF BOILER

DEPOSIT	SLAG (FUSED DEPOSITS)	METALLIC	COMMONLY DERIVED FROM PYRITE DURING COMBUSTION UNDER REDUCING CONDITIONS
		AMORPHOUS	TYPICALLY FOUND IN HIGH- TEMP. ZONES OF BOILERS AND WITH LOW FUSION COAL
		VESICULAR	AMORPHOUS SLAG WITH BUBBLES
		SINTERED	PARTIALLY FUSED PARTICLES COMMONLY FOUND IN CONVECTION PASSES OF BOILERS
	FOULING (SULFATE SALTS)	VERY STRONG	CANNOT BE BROKEN WITH HANDS, YOU MUST USE A TOOL
		STRONG	CAN BE BROKEN WITH HANDS, BUT DOES NOT CRUMBLE
		WEAK	DEPOSITS CRUMBLE WHEN HANDLED
		UNCONSOLIDATED	DUST ACCUMULATIONS

FIGURE 2. MEGASCOPIC CLASSIFICATION SYSTEM

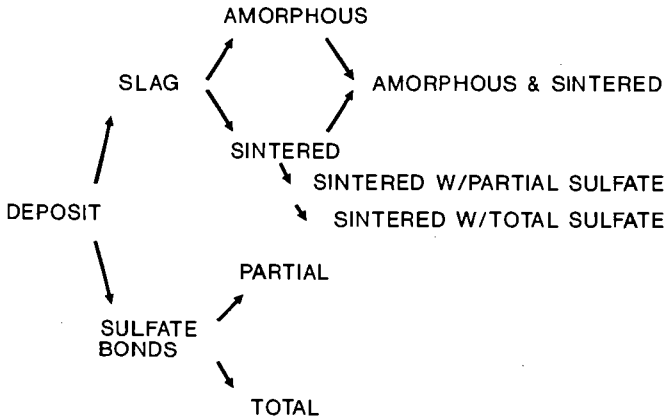
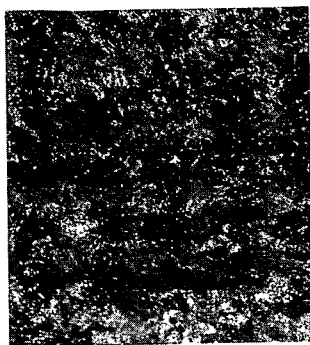
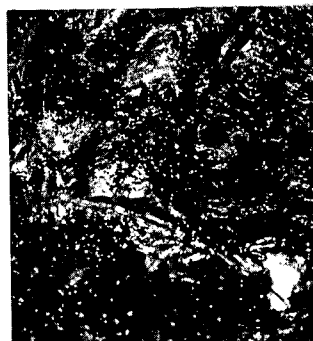


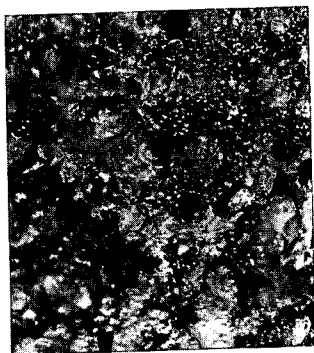
FIGURE 4. OUTLINE OF MICROSCOPIC SYSTEM



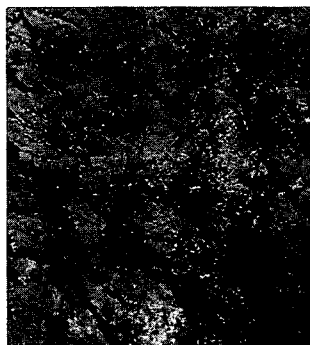
a



b



c



d

Figure 3, Examples of different types of slags: a, Metallic; b, Amorphous; c, Vesicular; d, Sintered.



a



b



c

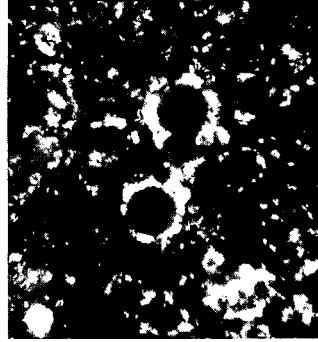


d

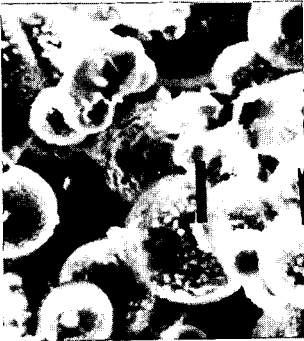
Figure 5. Microscopic view of slags: a, Dendritic crystals in amorphous slag (plain polarized light, thin section); b, Mullite crystals in vesicular slag (plain polarized light, thin section); c, Sintered slag with quartz crystal (PPL, thin section); d, Sintered slag (SEM, plain mount).



a



b



c



d

Figure 6. Microscopic view of Fouling Deposits: a, Total sulfate bonding (plain polarized light, crushed sample in oil); b, Total sulfate bonding (cross polars, thin section); c, Partial sulfate bonding of sintered deposit (SEM, plain mount); d, Surface crystals on sintered deposit (SEM, plain mount).

CALCULATIONS OF THE INFLUENCE OF ADDITIVES ON COAL COMBUSTION DEPOSITS

M. Blander, S. Sinha
Argonne National Laboratory
Argonne, Illinois 60439-4837

A. Pelton, G. Eriksson
Ecole Polytechnique de Montréal
Montréal, Québec, Canada H3C 3A7

INTRODUCTION

The complex chemistry of coal combustion involves hundreds of species in gaseous, solid, and liquid phases, with some of these being solution phases. We have developed new robust calculational techniques capable of defining the total chemistry of coal combustion and of the complex solid and liquid silicate and sulfate solutions involved.^{1,2} The results indicate that coal combustion chemistry is more complex than had been believed and that kinetic factors can enhance fouling and corrosion by liquid condensates. In this paper, we examine the changes in chemistry due to additions of CaCO_3 (to desulfurize the gaseous effluents) and of NaCl and CaCl_2 (which are recommended as deicers or to increase the conductivity of effluents in electrostatic precipitators).³ The results reveal the chemical changes due to these additives; these should be important in defining a strategy for making such additions. In addition, we also impose an expected kinetic constraint on the chemical reactions. Such constraints should, ultimately, prove to be very important in real systems. Ultimately, in order to take these into account in deducing the total chemistry of combustion, a coupled calculational-experimental study of combustion should be carried out to define the important kinetic factors.

CALCULATIONAL METHODS

A robust updated version of SOLGASMIX⁴ was used to perform these calculations using data on the large number of possible species in the F*A*C*T⁵ data base. In addition to the gaseous, solid, and liquid species in the data base, we incorporated a method for calculating the thermodynamic properties of liquid silicates^{6,7,8} and a method for calculations of the properties of sulfates using the data deduced in our analysis of the Na_2SO_4 - CaSO_4 - MgSO_4 ternary molten salt system and of the CaSO_4 - MgSO_4 and Na_2SO_4 - CaSO_4 - MgSO_4 solid solutions that crystallize from the sulfate melts. This analysis led to an assessed phase diagram for the ternary sulfate, which was necessary in order to define the chemical properties and the range of stability of the corrosive liquid sulfate phase that forms from the coal combustion condensates.

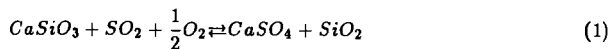
COMBUSTION OF ILLINOIS #6 COAL

We have previously examined the equilibrium combustion products of Illinois #6 coal and have imposed an expected kinetic constraint on the formation of $\text{NaAlSi}_3\text{O}_8$ and NaAlSiO_4 to illustrate the importance of kinetic factors.^{1,2} In this paper, we compare these constrained equilibrium calculations with calculations performed with the addition of CaCO_3 , NaCl , or CaCl_2 . These additions lead to changes in the total chemistry, and our results can be used to deduce strategies for making such additions. The overall composition of Illinois #6 coal is

given in Table I. In the calculations that follow, we combusted 100 grams of coal with an excess of oxygen (237 grams O₂ added as air). To this mixture, we added 6.25 grams of CaCO₃, or 0.4 grams of NaCl, or 0.4 grams of CaCl₂. The additives lead to complex changes in the total chemistry.

In Tables II, III, and IV, we present a selection of the results of our calculations of condensates with and without CaCO₃ addition that illustrate the important changes in chemistry brought about by the additive. In Table II, we give calculations for the composition of liquid silicates at temperatures where they are present. With no added CaCO₃, a molten silica-rich silicate exists down to about 1260 K, where a small amount of sulfate forms. With the addition of CaCO₃, the amount of molten silicate is increased significantly at the higher temperatures, mostly because of an increase in the CaO content. As a consequence, the liquid is not as silica rich and will be considerably less viscous than when no limestone is added. Because the activity coefficients of all the basic components of the slag are generally higher at low silica than at high silica contents, and also because of the high CaO concentration, this slag reacts more readily with SO₂ + $\frac{1}{2}$ O₂ (and SO₃) in the gas phase than does a high silica slag and forms a liquid sulfate phase between 1350 and 1400 K with CaCO₃ additions. This temperature is considerably higher than the temperature of first formation of liquid sulfate with no CaCO₃ addition, because the activities of the basic oxides (CaO, MgO, and Na₂O) in the silica saturated acid slag are significantly lower than in the less acid slags found with limestone addition and because the tendency to form sulfate increases with a decrease in temperature, i.e., the standard entropy of reaction of the oxides with gaseous SO₂ and O₂ is negative.

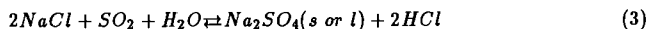
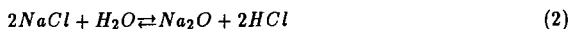
For the case with CaCO₃ addition, the decrease in the amount of slag at 1350 K (to 0.15 g) is accompanied by the appearance of a significant amount of sulfate, largely Na₂SO₄, as exhibited in Table III. These relative amounts remain essentially the same, at least down to 1300 K (Table III). The slag disappears by 1250 K (Table II) and somewhat more sulfate appears (Table III) at the expense of the slag constituents and CaSiO₃ (Table IV). The SO₃ (SO₂ + $\frac{1}{2}$ O₂) in the gas phase is a stronger "acid" at these temperatures than even SiO₂. Thus, one of the reactions that has taken place to a small extent between 1250 K and 1300 K is



with the product SiO₂ appearing as a new phase (Table IV). At yet lower temperatures, the liquid sulfate crystallizes to form two solid solutions and there is an increasing tendency for reactions of the remaining alkaline earth silicates or aluminosilicates with SO₂ + $\frac{1}{2}$ O₂ to form sulfates. Consequently, upon cooling, solid CaSiO₃ (wollastonite) disappears before 1150 K, and CaAl₂Si₂O₈ (anorthite) and CaMg(SiO₃)₂ (diopside) disappear before 1050 K, with a consequent increase in the amount of sulfate solid solutions and silica at both temperatures. Essentially, all of the alkali and alkaline earth oxides are thus converted to sulfate before 1050 K. This result holds with or without limestone additions because of the excess of oxides of sulfur in the gas. The total amount of sulfate is, of course, much larger with limestone additions because of an increased amount of CaSO₄ with a consequent decrease (relative to no limestone addition) in sulfur oxides of 68% at 1050 K and 1000 K. In real systems, kinetic factors could lead to desulfurization percentages less than this. The kinetics of reactions to form sulfates from solids such as CaAl₂Si₂O₈, CaSiO₃, or CaMg(SiO₃)₂ could be too slow to go to completion. If field data indicate this to be true, then our calculations can be used to define a strategy for improved

desulfurization. In addition, because a significant amount of SO_2 remains in the gas, greater desulfurization is possible in principle with larger additions of CaCO_3

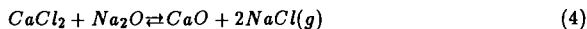
The addition of 0.4 grams of NaCl does not lead to large differences in the chemistry. NaCl is largely present in the vapor at high temperatures, which reacts at lower temperatures to form either the oxide or sulfate and HCl by the reactions



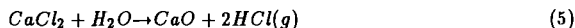
where the oxide in (2) could enter the slag or form a solid silicate. More HCl than NaCl is present in the vapor at 1300 K or lower with a liquid sulfate appearing between 1250 K and 1300 K.

For very large additions of NaCl (3.5 grams) to 100 grams of coal, the amount of Na_2O in the slag increases noticeably. However, most of the NaCl is in the vapor phase at the higher temperatures. In this case, the amount of HCl exceeds that of NaCl at 1250 K, at which temperature a liquid sulfate is also present. (There is no sulfate phase at 1300 K.)

With the addition of 0.4 grams of CaCl_2 , there is a significant decrease in the amount of slag (e.g., 0.49 grams at 1300 K), largely due to the formation of solid $\text{CaAl}_2\text{Si}_2\text{O}_8$ (anorthite) by the reactions



at high temperatures and



at low temperatures, where the CaO produced reacts with slag and aluminosilicates to form solid anorthite.

With no constraint on the formation of $\text{NaAlSi}_3\text{O}_8$ (albite), there is a similar effect on the amount of slag produced with NaCl additions. Removal of this constraint on albite formation with NaCl additions would be justified because albite forms at considerably higher temperatures with NaCl additions than without these additions, and the causes of the kinetic constraint would not hold at such temperatures. However, in order to explore this class of reactions more completely, we will have to perform analyses of alumina containing slag systems that are consistent with the liquidus temperatures of anorthite and albite and incorporate these analyses into our calculations. The possibility of reducing the amount of slag and the temperature range of liquid slag stability by suitable additives is important enough to expend an effort on the above analyses. Irrespective of the results of the above analyses, the volatility of sodium chloride and the increasing tendency of chlorides to form sulfates and HCl as temperature decreases partially controls the changes in the final products of combustion with chloride additives.

DISCUSSION

Our calculations provide information that could be useful for defining strategies for the use of additives. Two results of our calculations for limestone addition are clearly significant for desulfurization strategy. First, more slag is produced and it is considerably less viscous than those produced with no additives. Secondly, the CaO from the limestone forms silicates at high temperatures that react with sulfur oxides at lower temperatures to form sulfates. There is a good likelihood that this sulfate-forming reaction will not go to completion because of kinetic

barriers to reactions involving complex silicates. Consequently, addition of limestone at lower temperatures would avoid the complexity and kinetic problems involved in additions to the coal and if the additives can desulfurize effectively at temperatures of about 1200 K or below, the amount and temperature range of stability of the corrosive liquid sulfate would be minimized.

Additions of chlorides as deicers tend to produce gaseous HCl at low temperatures, and boiler designs and materials of construction should be chosen to minimize corrosion by this species. With large chloride additions, the stability and amount of molten slag produced will be very different from the case with no additions. Precise results require development of means to represent the slag chemistry with alumina as a constituent. Our calculations suggest that large additions of CaCl₂ and NaCl might decrease the amount and temperature range of stability of a liquid slag.

Further work is necessary to extend our slag model to incorporate alumina as a component to better define the total chemistry, especially for the case with chloride additions. In addition, a coupled experimental-calculational research program would help to define important kinetic factors to incorporate into our calculations as constraints and could ultimately permit us to define the total combustion chemistry of coal.

ACKNOWLEDGMENT

This work was supported by the U.S. Department of Energy, Office of Basic Energy Sciences, Division of Materials Sciences, under Contract No. W-31-109-ENG-38.

REFERENCES

1. S. Sinha, K. Natesan, and M. Blander, "A New Calculational Method for Deducing the Complex Chemistry of Coal Ash Deposits," Proceedings of the Conference on Mineral Matter and Ash Deposition from Coal, Santa Barbara, California, February 21-26, 1988, in press.
2. M. Blander, S. Sinha, A. Pelton, and G. Eriksson, "Calculations of the Chemistry of Coal Combustion Effluents," Proceedings American Flame Research Committee 1988 Fall Meeting, Pittsburgh, Pennsylvania, October 4-6, 1988, Paper No. 25.
3. J. E. Radway, "All You Ever Want to Know About Additive Application and Testing," Proceedings of the Conference on Mineral Matter and Ash Deposition from Coal, Santa Barbara, California, February 21-26, 1988, in press.
4. G. Eriksson, *Chemica Scripta*, **8**, 100-103 (1975).
5. W. T. Thompson, C. W. Bale, and A. D. Pelton, *F*A*C*T Users Guide*, McGill University, Ecole Polytechnique, Montreal (1988).
6. M. Blander and A. D. Pelton, "Computer Assisted Analysis of the Thermodynamic Properties of Slags in Coal Combustion Systems," ANL/FE-83-19, Argonne National Laboratory, Argonne IL (1983).
7. A. D. Pelton and M. Blander, *Metall. Trans.* **17B**, 805-815 (1986).
8. M. Blander and A. D. Pelton, *Geochim. et Cosmochim. Acta*, **51**, 85-95 (1987).

Table I. Composition of High-Sulfur Illinois #6 Coal Used for the Present Work

Coal Constituents		Ash Constituents	
Species	Wt %	Species	Wt %
C	60.15	SiO ₂	46.77
H	4.26	Fe ₂ O ₃	16.22
N	0.97	Al ₂ O ₃	18.47
S	3.41	CaO	6.91
Cl	0.05	MgO	1.28
H ₂ O	10.54	SO ₃	4.35
O	7.30	Na ₂ O	4.96
Ash	13.32	Unknown	1.04
TOTAL	100.00		100.00

Table II. Calculated Slag Compositions
(Weight Percent)

	Temperature (K)					
	1800	1700	1600	1500	1400	1300
<u>w/o CaCO₃</u>						
SiO ₂	57.47	65.63	74.63	77.27	78.62	78.08
FeO	23.57	16.15	7.41	1.92	0.32	0.06
CaO	10.27	6.65	3.61	2.22	1.03	0.51
Na ₂ O	7.07	9.43	11.71	15.81	18.98	20.87
MgO	1.63	2.13	2.64	2.79	1.04	0.48
wt (g)	9.78	7.45	6.02	4.46	3.72	3.38
<u>6.25 g CaCO₃ added</u>						
SiO ₂	42.16	44.11	45.90	46.65	47.56	71.27
FeO	19.41	9.86	4.63	1.88	0.64	0.06
CaO	31.46	36.40	38.48	40.13	34.97	4.49
Na ₂ O	5.63	7.85	8.97	9.26	13.74	23.91
MgO	1.34	1.80	2.03	2.09	3.10	0.27
wt (g)	11.87	8.85	7.84	7.62	5.14	0.16

Table III. Molten and Solid Sulfate Condensates
(Weight Percent)

	1350		1300		1250		1150		1050	
	Without CaCO ₃	With CaCO ₃								
<u>Liquid</u>										
Na ₂ SO ₄	--	94.77	--	91.10	96.65	80.73	--	--	--	--
CaSO ₄	--	5.22	--	8.89	3.25	19.25	--	--	--	--
MgSO ₄	--	0.01	--	0.01	0.10	0.21	--	--	--	--
wt (g)	--	1.61	--	1.68	1.67	2.04	--	--	--	--
<u>Solid</u>										
Na ₂ SO ₄	--	--	--	--	--	--	50.29	45.78	50.32	49.58
CaSO ₄	--	--	--	--	--	--	49.47	54.11	44.72	48.88
MgSO ₄	--	--	--	--	--	--	0.25	0.12	4.96	1.54
wt (g)	--	--	--	--	--	--	3.22	3.53	3.22	3.26
<u>Solid</u>										
CaSO ₄	--	--	--	--	--	--	--	99.77	87.86	96.62
MgSO ₄	--	--	--	--	--	--	--	0.23	12.14	3.38
wt (g)	--	--	--	--	--	--	--	5.01	1.14	9.66

Table IV. Solid Condensates (in grams)

	w/o CaCO ₃				w/CaCO ₃			
	1350	1250	1150	1050	1350	1250	1150	1050
CaAl ₂ Si ₂ O ₈	4.85	4.87	1.73	--	7.16	7.16	7.16	--
Fe ₂ O ₃	2.56	2.56	2.56	2.56	2.56	2.56	2.56	2.56
SiO ₂	1.25	3.82	4.50	5.02	0.00	0.21	3.10	5.05
Al ₆ Si ₂ O ₁₃	1.18	--	--	--	--	--	--	--
MgSiO ₃	0.33	0.40	0.39	0.15	--	--	--	0.08
Al ₂ SiO ₅	--	1.34	3.17	4.17	--	--	--	4.17
CaSiO ₃	--	--	--	--	5.78	5.55	--	--
CaMg(SiO ₃) ₂	--	--	--	--	0.85	0.85	0.83	--

**A PHYSICAL AND CHEMICAL BASIS FOR UNDERSTANDING INORGANIC MINERAL
TRANSFORMATIONS IN COALS BASED ON MODEL-MINERAL EXPERIMENTS**

S. Srinivasachar, J.J. Helble, and A.A. Boni
PSI Technology Company
Research Park, P.O.Box 3100
Andover, MA 01810

Abstract

Ash deposition depends on the size, surface composition and surface state of the transformed coal minerals. It is currently assumed that the minerals found in coals can be described in terms of their elemental chemical oxides. We hypothesize that each mineral represents a unique physico-chemical entity that undergoes a complex transformation as it is processed by the combustion environment and eventually reaches an oxidized state. We have performed drop-tube furnace experiments, with representative combustion conditions, on two important coal minerals: pyrite and illite. Comparison is made with an Eastern coal containing large quantities of the above minerals. There is evidence of exothermic and endothermic reactions, fragmentation, kinetic and transport-limited oxidation, and formation of both complex glasses and crystalline phases, at different stages in the mineral transformation process. These processes determine the final size, composition, and the surface state of the ash, which cannot be predicted by thermochemical methods alone.

INTRODUCTION

Ash deposition on heat transfer surfaces is the most severe problem associated with the combustion of coal. Besides lowering heat transfer rates, hence plant efficiencies, frequent maintenance and unscheduled shutdowns for removing these deposits substantially adds to the cost of power generation. It is therefore critical that for a given pulverized coal (p.c.) fired boiler, appropriate coals be selected and operating conditions be maintained to minimize ash deposition and its detrimental effects. Presently, empirical indices based on the elemental oxide composition are used to rank a coal's fireside behavior.^{1,2} These slagging and fouling "factors" are only applicable to very specific types of coal, coal ash and boiler units and extension of these factors to different coal/ash types or combustion conditions gives results which are uncertain at best. This can be attributed to the fact that different coals contain different amounts and species of minerals,³ and their specific physical and chemical transformations govern the state in which they arrive at a heat transfer surface and deposit. Slagging and fouling factors that are defined and used at present average out the expected behavior of the coal ash, i.e. they consider the coal and ash to be homogeneous and represented as a sum of individual elemental oxides. The detrimental deposition characteristics of ash resulting from some problematic individual minerals or their combinations is thus masked out. An understanding of the transformations of individual minerals in coal is therefore needed to develop a better predictor for ash deposition.

Iron and alkali-bearing minerals, for example, pyrite and illite respectively have long been recognized as a major source of wall slagging. The behavior of excluded pyrite particles under combustion conditions has been

reported by our group in detail previously^{4,5} and is only summarized here. The focus of this article is on transformations of illite under similar processing conditions. The stickiness characteristics of illite transformed in a combustion environment is also examined.

EXPERIMENTAL

All combustion and deposition experiments were performed in a resistance-heated entrained flow reactor, operated under laminar flow conditions. Schematics and detailed description of the reactor is given elsewhere⁶ and the deposit collection probe is shown in Figure 1. Samples of size-graded illite were entrained in an air stream and injected axially into the isothermal furnace via a water-cooled injector at a rate of about 0.3 gm/minute. Air was used as the furnace gas, and was injected separately through the top of the reactor. Gas temperature was held at 1500 K for the transformation experiments, but was varied for the stickiness determination experiments. For the former set of experiments, the particle residence time was varied from 0.8 to 2.5 seconds in the isothermal section, while it was held constant at 2.5 seconds for the stickiness tests.

The particles were collected via one of the following techniques:

1. isokinetic sampling, via a water-cooled, nitrogen-quenched probe. At the exit of the probe, all particles passed through a seven stage Pollution Systems Control Corp. cascade impactor, providing on-line size classification of all particles larger than 0.1 microns. Smaller particles were collected on a backup filter. In experiments where size classification was not required, a total filter was used.
2. deposition of a portion of the supermicron particles on a deposit collection probe. The capture efficiency is determined from the ratio of the mass of the deposit on the mullite tube to the mass of the particles that passed through the projected area of the substrate tubes. The gas temperatures at the deposition location, although intended to be the same as the furnace temperature, are 70 - 100 K lower.

Chemical Analysis of Illite

The illite examined in this study was a Cambrian shale from the Silver Hill formation, Jefferson Canyon, Montana. This illite has been characterized in detail by Hower et al.. The chemical composition (weight percent) of Silver Hill illite is as follows: SiO₂ (55.1), Al₂O₃ (22.0), K₂O (8.0), FeO (1.34),

Fe₂O₃ (5.3), MgO (2.8), Na₂O (0.08), H₂O- (1.0), H₂O+ (6.4). H₂O- represents the

weight loss at 110°C while H₂O+ is the weight loss on ignition. The composition of illite in various coals may be slightly different from each other, and therefore their behavior in the furnace may be somewhat different. One of the anticipated differences could be the fraction of the iron that is present in the ferrous state, as this will have significant impact on the its melting characteristics. However a study of Silver Hill illite can provide information as to the transformations undergone by "generic" illite in the combustion zone.

RESULTS AND DISCUSSION

Transformations of Illite

Samples of illite in the size range of 53 to 75 microns, exposed to high temperatures in the reactor for different residence times were examined by scanning electron microscopy (Figure 2). Illite particles in the feed are angular with an aspect ratio of about 1.5 to 2.0 for most particles. Upon exposure to 1500 K for a residence time of approximately 0.9 seconds, the color of the sample changed from a greenish gray to dark brown reflecting the oxidation of iron to the ferric state. Particles lose their angular form partially (Figure 2b) and vitrification is evident, although the overall morphology still resembles that of the original particle. Also isolated pore formation and gas evolution through these pores is evident. Examination of particles subjected to 1500 K for 2.5 seconds, shows that a much larger fraction had completely molten (Figure 2c). Several large pores are present on the particle surface, suggesting gas evolution and even some bloating as a result of trapped vapor trying to escape through a molten matrix. Gas evolution during heating consists of the release of the chemically bound hydroxyl groups. At slow heating rates, dehydroxylation does not occur until 600-700°C. At the high heating rates in our experiments, even higher particle temperatures would be reached before this step occurs. This endothermic step further delays the breakdown of the illite structure and its transformation into a glass.

The equilibrium behavior of illite can be determined from the $K_2O-Al_2O_3-SiO_2$ phase diagram. The phase diagram (Figure 3) shows that the minimum melting point appropriate to illite composition is 985°C.⁸ With addition of MgO and other components (particularly FeO, Fe_2O_3), a much lower eutectic melting point would be expected. The behavior of illite during the firing of ceramics was studied by Segnit and Anderson⁹ in an electric muffle furnace at heating rates of 100°C per hour and a soaking time of 4 hours. Clearly under these conditions one would be closer to equilibrium than in our experiments. They determined that glass formation started at 850°C, and vitrification was complete at 1000°C. Some pore formation was seen at 1050°C, and much more bloating and pore opening was evident at 1100°C. A comparison of the equilibrium behavior and the Segnit and Anderson work with our results shows that the transformations of illite under p.c. firing conditions would not approach the equilibrium condition, either during the heat-up stage or while cooling, for example when approaching a heat transfer surface after combustion has been completed. One would expect that under actual combustion temperatures which are higher than in our experiments (1500°C), and given that illite is associated with the coal during combustion (hence, even higher particle temperatures), illite will be completely molten before it arrives at a deposition surface. It then becomes important to describe the phase change kinetics and their impact on viscosity as the ash particle cools down. This transient viscosity variation will determine the deposition potential of the incoming ash particles.

Composition analysis of the raw and transformed illite particles was performed to determine if there was any preferential movement of potassium or iron to the particle surface. Surface analyses proved inconclusive since there was considerable compositional variation between different particles. A clearer picture of the selective mobilization of specific elements can only be obtained

by analyzing the particle cross-sections. We intend to do this as a next step. We also determined size distribution of the burnt illite particles using the cascade impactor. Data showed that all the particles were collected on the top stage of the impactor ($d_p > 8$ microns). This means that there is no vaporization of the illite (especially of the potassium) when it is not associated with carbon, nor any fragmentation into the 1 - 5 micron size range. Association with carbon would only mean that it would melt more quickly, thus impeding any fragmentation, although the higher temperatures might cause some vaporization.

Stickiness Behavior

Capture efficiencies of transformed illite particles were determined in the manner described in the experimental section. The capture efficiency is the fraction of the particles that both impact and stick. Impaction efficiency is determined from Stokes number considerations, and for the particle size (53-75 microns) and the velocity range used here, the impaction efficiency is unity. Figure 4 shows the capture efficiencies for different furnace temperatures and particle impaction velocities. When examined as a function of temperature, there is a dramatic increase in the rates of capture above 1400 K, except for the highest velocity. As the temperature is increased, the viscosity of the incoming particles decrease, and below a critical viscosity (approximately 10^7 poise) the particles are sufficiently deformable that the energy of impact is dissipated, and the particles stick without rebounding. One would normally expect that the capture efficiency would increase as the particle velocity increases - however, in our case the particles are large enough that all of them impact even at the lowest velocity. The observed reduction in the capture efficiency with increasing velocity must therefore be due to deposit erosion from the incoming particles. Microscopic observation of the deposit also showed that it was bonded at the higher temperatures, whereas at 1400 K, even though the capture efficiencies were high, the deposit was powdery and very friable. Quantitative analysis of these data will require consideration of both deposition and erosion.

Comparison of Illite and Pyrite Transformations

In a previous study,^{4,5} the transformations of pyrite were examined in the same entrained flow reactor setup. A comparison shows that the physical and chemical changes associated with the oxidation of pyrite is much more complex than for illite. Pyrite decomposed to pyrrhotite ($Fe_{0.877}S$), and this was followed by its oxidation to a molten sulfide-oxide mixture, subsequent crystallization of magnetite (Fe_3O_4) from the melt, and finally formation of hematite (Fe_2O_3). Particle temperature exceeds the gas temperature during this process due to the exothermic oxidation of sulfide. There was also a residence time region in which the particle remained molten. This constituted 80 percent of the total time for oxidation to magnetite. But, once magnetite formation was completed, the particle solidified, so that deposition was favored only as long as the pyrite was partially oxidized. Illite, on the other hand, does not exhibit such dramatic changes upon heating. Once the illite particle is molten, it is expected to remain as such until the gas, hence particle, temperature is lowered. Besides the formation of glass, the predominant reaction for illite seems to be the loss of the hydroxyl group, an endothermic reaction. Further analysis by EXAFS and Mossbauer techniques would reveal how the chemical

structure of iron and potassium in the illite-derived glass changes.

Based on limited data on the behavior of the minerals in coal,¹¹ the similarity with the behavior of the pure minerals is borne out. In Kentucky #11 coal, where the minerals are finely and uniformly dispersed through the coal matrix, examination of the ash size distribution showed that a large degree of coalescence was taking place. The final ash composition showed glasses with compositions ranging between illite, kaolinite, and silica, suggesting that the molten illite had incorporated the other minerals within its matrix. This data are also not inconsistent with little fragmentation seen with pure illite and that illite is expected to melt under combustion conditions. Mossbauer data on iron showed that only a small portion of the iron was in a glass, and the level of iron present as hematite increased as the oxygen level in the gas was raised.⁴ This is consistent with model calculations for oxidation of the pure mineral.

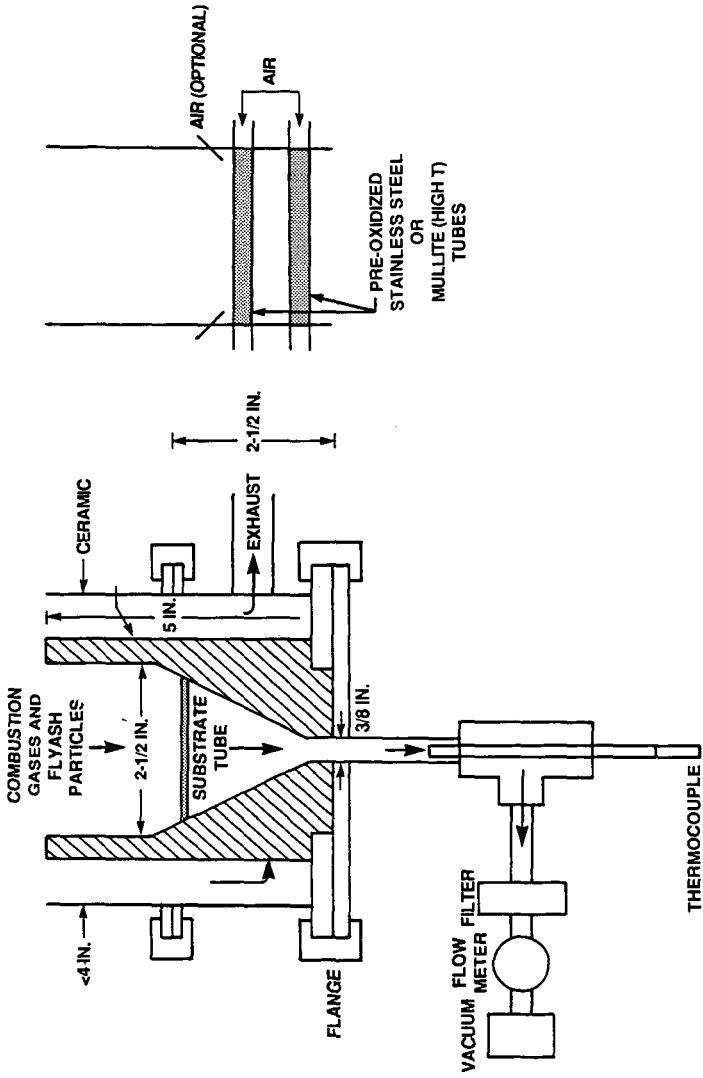
ACKNOWLEDGEMENTS

The authors thank the Department of Energy, Pittsburgh Energy Technology Centre for their support of this work under Contract No. DE-AC22-86PC90751

REFERENCES

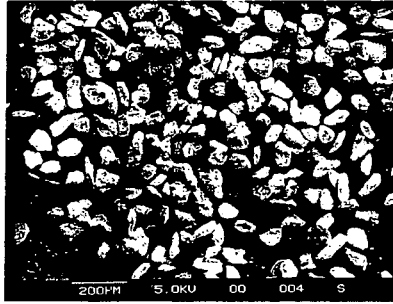
1. Winegartner, E.C., Coal Fouling and Slagging Parameters, American Society of Mechanical Engineers (1974).
2. Bryers, R.W., "An Overview of Slagging/Fouling Due to Impurities in Coal," Proceedings of EPRI Conference on Effects of Coal Quality on Power Plants, October (1987).
3. Boni, A.A., Flagan, R.C., Bryers, R.W., Sarofim, A.F., Beer, J.M., Peterson, T.W., Wendt, J.O.L., Huffman, G.P., Huggins, F.E., Helble, J.J., Srinivasachar, S., "Transformations of Inorganic Coal Constituents in Combustion Systems," Proceedings of DOE AR&TD Meeting, (1987).
4. Srinivasachar, S., and Boni, A.A., "A Kinetic Model for Pyrite Transformations in a Combustion Environment," Fuel (accepted) (1988).
5. Srinivasachar, S., Helble, J.J., Katz, C.B., Morency, J.R., and Boni, A.A., "Experimental and Modeling Study of Pyrite Transformations under Coal Combustion Conditions," Coal: Fuel for Today and for the Future, International Symposium, American Flame Research Committee, October (1988).
6. PSI Technology Company, "Transformations of Inorganic Coal Constituents in Combustion Systems," Quarterly Report No. 2, DOE Contract DE-AC22-86PC90751, April (1987).
7. Hower, J., and Mowatt, T.C., *Amer. Mineralogist* **51**, 825 (1966).
8. Levin, E.M., Robbins, C.R., and McMurdie, H.F., Phase Diagrams for Ceramists, The American Ceramic Society (1964).
9. Segnit, E.R., and Anderson, C.A., *Trans. Br. Ceram. Soc.* **71**, 85 (1972).
10. Srinivasachar, S., Helble, J.J., Katz, C.B., and Boni, A.A., "Transformations and Stickiness of Minerals During Pulverized Coal Combustion", Proceedings of the Engineering Foundation Conference on Mineral Matter and Ash Deposition in Coal (in press) (1988).
11. Helble, J.J., Srinivasachar, S., Katz, C.B., and Boni, A.A., "Mineral Transformations in Selected Coals-Size and Composition of the Ash", ACS Meeting, Dallas (to be presented) (1989)

STICKY PROBE

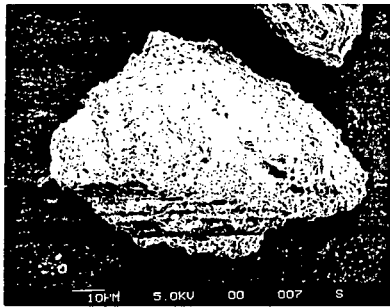


A-7398

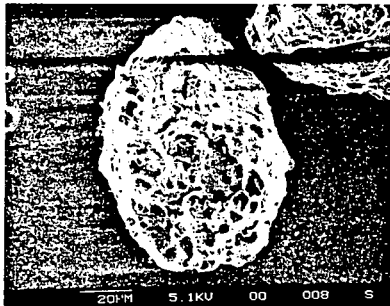
Figure 1. Schematic of the deposit collection probe



a)



b) Res. time ~0.9 seconds



c) Res. time ~2.5 seconds

Figure 2. Scanning Electron Micrographs of a) raw and b), c) Burnt Illite at Different Residence Times ($T_{\text{gas}} = 1500\text{K}$) for 53-75 Micron Particle Size Fraction

$K_2O-Al_2O_3-SiO_2$

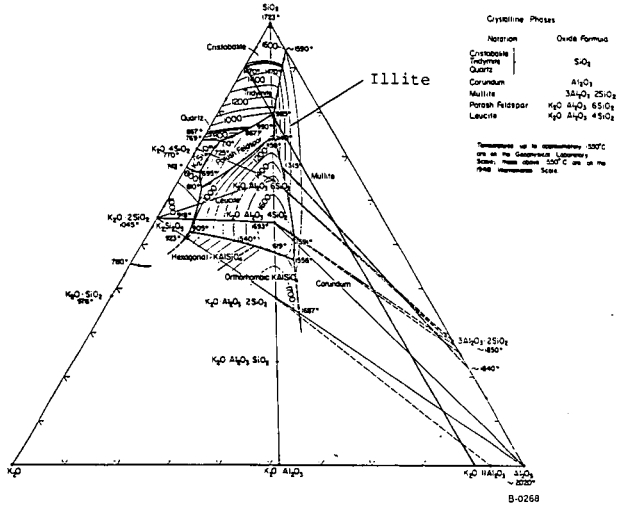


Figure 3. System $K_2O-Al_2O_3-SiO_2$; Composite. E.F. Osborn and Arnulf Muan, Revised and Redrawn "Phase Equilibrium Diagrams of Oxide Systems," Plate 5, Published by the American Ceramic Society and the Edward Orton Jr., Ceramic Foundation, 1960.

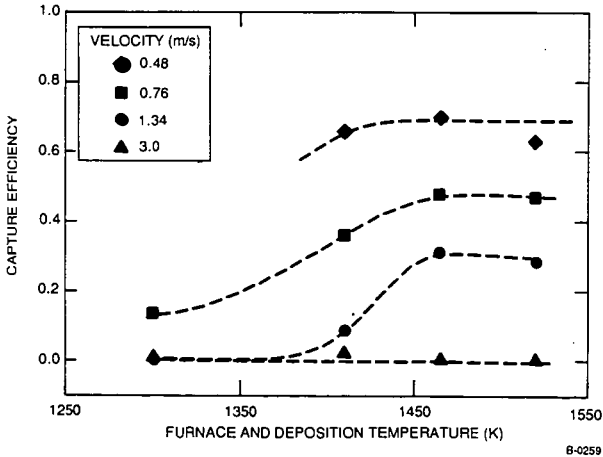


Figure 4. Capture Efficiencies (slagging probe) for Burnt Illite at Different Furnace Temperature and Particle Impaction Velocities

STUDIES OF TRANSFORMATIONS OF INORGANIC CONSTITUENTS IN A TEXAS LIGNITE DURING COMBUSTION

C.J. Zygarlicke, E.N. Steadman, S.A. Benson, and W.H. Puffe
University of North Dakota Energy and Mineral Research Center
Box 8213 University Station
Grand Forks, ND 58202.

INTRODUCTION

The effects of coal composition and combustion conditions on the mechanisms of ash formation are being investigated at the Energy and Mineral Research Center (EMRC). The objective of the study is to develop a unified understanding of formation of ash components during pulverized coal combustion. This understanding will aid in predicting the formation of ash deposits, erosion of boiler parts and formation of fine particulate that is difficult to collect.

The approach used to obtain a better understanding of inorganic transformations that take place during combustion of pulverized coals involves the following key elements: 1) an effective multidisciplinary means of characterizing the original coal for its inorganic content; 2) a controlled, small-scale combustion regime that can be quickly and easily manipulated to simulate the time and temperature profile in a full scale utility boiler; and 3) an effective means of characterizing the combustion products, such as fly ash generated in the small scale combustor. The abundance and mode of occurrence of inorganic components in coal are quantified using a combination of computer controlled scanning electron spectroscopy (CCSEM) and chemical fractionation techniques^{1,2,3,4}. The CCSEM is used to determine the size and abundance of mineral grains in the coals. Chemical fractionation is used to quantify the abundance of organically associated elements. Ash is produced under carefully controlled combustion conditions using an entrained flow reaction or drop tube furnace system which simulates full scale utility boiler regimes^{5,6,7,8}. The resulting ash is collected in a multicyclone which size-classifies the ash. The size segregated ash is characterized using a scanning electron microscope.

There are many methods of ash deposit and fly ash characterization which greatly enhance the ability of researchers to determine, with reasonable accuracy, the size distribution and composition of fly ash^{9,10,11}. This allows for inferences to be made concerning the crucial factors involved in the transformation of inorganic components and also allows for the direct comparison of original mineral material with fly ash. In this particular study the mechanisms of coal ash formation were investigated for Monticello lignite from Titus County, Texas. The Monticello lignite was carefully prepared, analyzed, and combusted. The resulting ash was analyzed and compared to the original inorganic components in the coal.

EXPERIMENTAL

Coal Characterization

Monticello coal was characterized using a variety of analytical techniques. Standard ASTM coal and coal ash analyses were performed. Chemical fractionation and computer-controlled scanning electron microscopy (CCSEM)^{6,8}

were used to ascertain abundance and distribution of inorganic components, as well as the size and type of mineral grains in the coal.

Chemical fractionation was used to selectively extract elements from the coal based on solubility, which reflects their association in the coal. Briefly, the technique involves extracting the coal with water to remove water-soluble elements. This is followed by extraction with 1M ammonium acetate to remove elements that are associated as salts of organic acids. The residue of ammonium acetate extraction is then extracted with 1M HCl to remove acid-soluble species in the form of hydroxides, oxides, carbonates, and organically coordinated species. The components which remain in the residue after all three extractions are assumed to be associated with the insoluble mineral species such as clays, quartz, and pyrite.

The CCSEM analysis was performed on a 53-74 μ m sized fraction of Monticello lignite. Approximately 1000 mineral grains were type-classified based on elemental compositions, and sized according to average diameter. The size categorization of the grains was selected to be consistent with multi-cyclone cutpoints used in size-classifying the fly ash produced from this same coal fraction in the drop tube furnace. The CCSEM technique tends to underestimate the true average diameters of the mineral grains. Since the coal sample that is analyzed is a cross-section, the mineral grains observed are also cross-sectioned. This means that a mineral that has been sliced exactly at its average diameter is rare. To verify the CCSEM sizing technique, the coal minerals were also sized using a coulter counter analysis of a low temperature ash sample.

Fly Ash Production and Characterization

Fly ash was produced using an entrained-flow tube furnace, also known as a drop-tube furnace. The drop-tube furnace is a laboratory scale furnace system that has the ability to mimic conditions of commercial combustors without the high cost associated with pilot-scale combustion testing. The combustion temperature, residence time, and gas cooling rate can be closely controlled and monitored. Table 1 gives the combustion parameters used to produce the ash. More specific details of the EMRC drop-tube furnace are described elsewhere³. Fly ash was cooled by means of a fly ash quenching probe and collected using a multicyclone. The multicyclone aerodynamically separates the fly ash into 6 stages or aerodynamic categories. Each of the fly ash samples collected from the 6 stages was mounted in a suitable SEM mount and characterized using scanning electron microscopy and electron microprobe analysis. A technique called scanning electron microscopy point (SEMP), which was developed at the EMRC, was employed to determine the relative abundance of phases present in the fly ash particles. The types of phases identified include: (1) phases that resemble the original components in the coal, (2) phases that have molar and weight ratios of elements that are consistent with known crystalline species, and (3) unclassified species that do not fit in the first two categories. This information is used to compare not only the compositional changes in the ash, but also the changes in phases as a function of particle size. Specific information regarding the SEMPC technique can be found elsewhere¹⁰.

RESULTS AND DISCUSSION

Coal Characterization

The chemical fractionation results for the Monticello coal are found in Table 2. The large percentage of aluminum, silicon, potassium, and titanium remaining after the extraction implies that these elements were mostly associated with insoluble minerals as clays, quartz, and possibly rutile (titanium oxide). The results suggest that significant amounts of the alkali and alkaline earth elements are associated in the coal as salts of organic acid groups. For example, most of the magnesium, calcium, and strontium were removed by the ammonium acetate extraction. Potassium appears to be associated with a clay mineral. The iron was distributed as roughly half acid-insoluble sulfides (probably pyrite) and half organically coordinated or acid soluble minerals.

The Monticello coal has a relatively high ash content of 15%. From the chemical fractionation analysis it was calculated that at least 77.8% of the ash or 11.7% of the coal consisted of discrete mineral phases. Table 3 shows the distribution of discrete mineral phases in the Monticello 53-74 μ m coal, as determined by CCSEM. Nine minerals were observed in this size fraction of Monticello coal including: quartz, kaolinite, Fe-aluminosilicate, K-aluminosilicate, Ca-aluminosilicate, iron oxide, pyrite, rutile, and an aluminosilicate-gypsum mixture. The Fe and Ca-aluminosilicates were probably a type of montmorillonite and the K-aluminosilicate was most likely illite. One limitation of the CCSEM technique is that it is difficult to accurately classify clay minerals, except for kaolinite and in some instances, illite. Quartz was the most abundant mineral and was the dominant phase in all of the size ranges except for the >8.0-11.0 μ m range where kaolinite was the major phase. Figure 1 shows the abundance of five important mineral types observed in the six size categories. Quartz and Ca-aluminosilicate (montmorillonite) show approximately 70% of their mass in the >11 μ m size range. All five minerals shown in Figure 1 have a slight increase in content in the 2.1-4.4 μ m size range. Kaolinite is evenly distributed in a 1.2-11.0 μ m size range.

Fly Ash Characterization

The results of the SEMPC analyses are listed Table 4. Hauyne, which is a sodium - calcium aluminosilicate with sulfur, was observed in all of the samples except the 2.1-4.4 μ m range. The highest content of hauyne was observed in the 1.2-2.1 μ m range. Calcium oxide (which refers to species such as CaCO₃ and CaO), montmorillonite-derived material, illite, and iron oxide were detected only in small amounts in all stages. All size categories contained significant quantities of kaolinite-derived materials with the highest level found in the 1.2-2.1 μ m range. Anhydrite was relatively enriched in the 8.0-11.0 μ m size fraction and on the final filter. Plagioclase in the form of solid solution phases between end members albite (NaAlSi₃O₈) and anorthite (CaAl₂Si₂O₈), was observed at low levels, with none observed in the sample from the 4.4-8.0 μ m size categories. The quartz content of the samples varied markedly between size categories. In the >11 μ m and 4.4-8.0 μ m size fractions, 25.4 and 31.8% quartz were detected, respectively. Melilite was present in all of the multicyclone stages except for the 2.1-4.4 μ m size range. The sample from the 4.4-8.0 μ m size category had the greatest number of unidentified phases (45.5%), whereas the 8.0-11.0 μ m and 2.1-4.4 μ m size ranges had the fewest unidentified phases (63.5 and 65.4%, respectively).

The chemical compositions (on an SO_3 -free basis) of each sample are listed in Table 4 along with the Si/Al molar ratio. The most striking result shown in Table 4 was the high level of Mg and Fe in the ash collected on the final filter. The very high Fe and Mg contents in the final filter suggests they may have vaporized and subsequently condensed to form submicron size particles, or that they were organically associated which can also produce very small particles during combustion. The chemical fractionation results suggest that approximately 53% of the iron is associated organically and/or as a carbonate mineral. The CCSEM data shows that a very low level of iron was observed in the form of iron oxide/carbonate minerals. In addition, no significant amount of pyrite was found.

The Si/Al molar ratios did not indicate any apparent trends between the multicyclone samples. The 4.4-8.0 size range had the highest value while the 1.2-2.1 μm range had the lowest. The data indicated that the >11 μm , 4.4-8.0 μm ranges were relatively enriched with silica (presumably quartz), whereas the 8.0-11.0 μm and 1.2-2.1 μm ranges were relatively depleted in silica.

The particle size distributions of the Monticello coal minerals, fly ash, and low temperature ash (LTA), as determined by CCSEM, multicyclone, and coulter counter analysis respectively, are shown in Figure 2. In all cases the majority of the mass was present in the larger size ranges. The minerals as determined by CCSEM show a bimodal distribution concentrated at the 2.1-4.4 μm and >11 μm ranges. The CCSEM technique tends to underestimate the average diameter of mineral grains in cross-section. The LTA distribution shows nearly the same amount of material at the 2.1-4.4 μm range as the CCSEM distribution, however, it has more particles with sizes in the 4.4-11.0 μm range and less particles in the >11 μm range. Two possible explanations for the differences between the LTA and CCSEM distributions are: 1) clay aggregates, which may be counted as only one particle in the CCSEM analysis, are usually broken up into smaller particles during the low temperature ashing process and 2) the LTA samples include mass from organically bound elements which are not quantified by CCSEM.

Figure 2 also shows that the fly ash distribution has very little mass in the lower size categories, but most of the particles are >11 μm . This is evidence for the process of coalescence and expansion whereby variously sized minerals and organically bound inorganics in a coal particle coalesce to form a larger fly ash particle. Further expansion may be due to the escape of gaseous or volatile matter.

Comparisons were made between the content of selected minerals in the original coal and their corresponding phases in the fly ash on a percent mass basis. The Monticello coal ash concentration was determined to be 15% on a dry basis. From the chemical fractionation analysis it was calculated that at least 78% of the ash or 12% of the coal consisted of true mineral phases (referred to as mineral matter here). When comparing the percentage of coal mineral phases to the inorganic phases present in the fly ash it must be remembered that the fly ash consists of both organically bound elements and mineral matter. The CCSEM analysis of coal minerals does not include the minute, organically bound inorganics. Therefore, to compare the coal mineral and fly ash data, the mineral data was multiplied by a correction factor of 0.78 to evenly weight the comparisons. The limits of experimental error for this comparison procedure are approximately 10-20%.

Comparison of the percent kaolinite in the coal to the percent kaolinite-derived in the fly ash revealed that the concentrations for corresponding size ranges were within 15% of each other except for the 8.0-11.0 μ m range (Figure 3). Kaolinite in the coal had lower concentration than the kaolinite-derived in the fly ash, excluding the <1.2 μ m and 8.0-11.0 μ m ranges. This suggests that a large percentage of the finer grained kaolinite in the coal collects extraneous inorganic matter during combustion which thereby increases its mass to a higher value than what was seen in the original coal. Sodium, magnesium, and calcium, most likely from organically bound cations, were the primary additions to the kaolinite-derived mass. The distribution of quartz, as shown in Figure 4, revealed a higher percentage of quartz in the coal than in the fly ash for all size ranges. Both curves have the same trends of slope when lines are drawn between the size ranges.

CONCLUSIONS

The Monticello 53-74 μ m coal and its corresponding drop tube furnace fly ash were characterized for their inorganic matter as a means of better understanding the inorganic transformations involved. The Monticello coal had a high ash content of 15% and approximately 78% of the inorganic constituents were determined to be mineral grains. The major mineral types identified included quartz, kaolinite, and Ca-aluminosilicate (montmorillonite). Major organically bound elements included sodium, magnesium, calcium, strontium, and barium. Iron content in the Monticello coal consisted of roughly half insoluble sulfides (pyrite) and half organically-coordinated or other acid soluble species. Although the CCSEM technique provides valuable data concerning the size and distribution of mineral phases, in its current stage of development the CCSEM technique appears to underestimate the total mass of minerals present. The CCSEM technique is best applied along with chemical fractionation; the combination of these two techniques provides a very complete picture of the form and nature of inorganic constituents present in a low-rank coal.

The particle size distribution of the Monticello minerals, as determined by CCSEM, had a bimodal distribution with over 60% of its mass >11 μ m. The LTA distribution had only 33% of its mass >11 μ m. The differences between the LTA and CCSEM distributions may be due to the breakup of clay aggregates during the low temperature ashing or the exclusion of organically bound elements in the CCSEM analysis. The size distribution of the fly ash showed 90.9% of its mass >11 μ m. Apparently, smaller mineral grains and organically bound inorganics are agglomerating or being assimilated into the melt phase of other material during combustion.

Analysis of the 6 multicyclone size fractions of fly ash using SEMPC identified 13 types of inorganic phases. The most abundant phases observed were hauyne, kaolinite, anhydrite, plagioclase, quartz, melilite, and unclassified material. Hauyne, a complex aluminosilicate containing sulfate, was mostly concentrated in the smaller size fractions. Kaolinite-derived phases had a fairly uniform distribution in all of the size ranges except for an anomalously low value in the final filter. The majority of the anhydrite was found in the final filter fraction probably due to deposition as gaseous or very fine particulate matter. Quartz content varied markedly between size ranges. Higher levels of Mg and Fe were noted in the smallest size fraction (<1.2 μ m). These values may be a result of how the Mg and Fe was associated in the coal; as a significant portion of both Mg and Fe are associated with the

organic fraction of the coal. Therefore, the relative sizes of the resulting ash particles containing these elements may be limited to a finer size fraction.

In comparing coal minerals to fly ash minerals and phases on a percent mass basis, several trends were noted. A large percentage of the finer-grained kaolinite in the coal appears to have combined with other minerals or extraneous inorganics during combustion. This was evidenced by the increase of non-crystalline kaolinite (kaolinite-derived) in the fly ash as compared to the original coal.

ACKNOWLEDGEMENTS

This work was performed under contract to the Department of Energy under the Cooperative Agreement No. DE-FC21-86MC-10637. The authors thank the Contracting Officers Technical Representative, Mr. Philip M. Goldberg, for permission to publish the results.

REFERENCES

1. Straszheim, W.E., Yousling, J.G., Younkin, K.A., and Markuszewski, R., 1988, Mineralogical characterization of lower rank coals by SEM-based automated image analysis and energy - dispersive x-ray spectrometry: *Fuel*, v. 62, August, p. 1042-1047.
2. Benson, S.A. and Holm, P.L., 1985, Comparison of Inorganic Constituents in three low-rank coals: *Ind. Eng. Chem. Prod. Res. Dev.*, 24, 145-149.
3. Huggins, F.E., Kosmack, D.A., Huffman, G.P., and Lee, R.J., 1980, Coal mineralogies by SEM automatic image analysis: *Scanning Electron Microscopy*, 1980, I, AMF O'Hare (Chicago), Illinois 60666, p. 531-540.
4. Russel, S.J. and Rimmer, S.M., 1979, Analysis of mineral matter in coal, coal gasification ash, and coal liquefaction residues by scanning electron microscopy and x-ray diffraction, in Karr, C., Jr., ed., *Analytical Methods for Coal and Coal Products*, v. III: Academic Press, p. 133-162.
5. Benson, S.A. and Austin, L.G., 1988, Study of slag deposit initiation using a laboratory-scale furnace: presented at the conference on mineral matter and ash deposition from coal, Engineering Foundation, Santa Barbara, California, February, 1988.
6. Sadakata, M., Mochizuki, H., Sakai, T., Okazaki, K., and Ono, M., 1988, Formation and behavior of submicron fly ash in pulverized coal combustion furnace: *Combustion and Flame*, v. 74, p. 71-80.
7. Abbot, M.F. and Austin, L.G., 1986, A study of slag deposit initiation in a drop-tube furnace: in *Mineral Matter and Ash in Coal*. Vorres, K.S., (ed.), ACS Symposium Series No. 301, Washington, D.C., p. 325.
8. Wibberley, L.J. and Wall, T.F., 1986, An investigation of factors affecting the physical characteristics of fly ash formed in a laboratory scale combustor: *Combustion Science and Technology*, v. 43, p. 177-190.

9. Furyua, K., Miyajima, Y., Chiba, T., and Kikuchi, T., 1987, Elemental Characterization of particle size - density separated coal fly ash by spectrophotometry, inductively coupled plasma emission spectrometry, and scanning electron microscopy - energy dispersive x-ray analysis: *Environmental Science Technology*, v. 21, no. 9, p. 898-903.
10. Kalmanovitch, D.P., Montgomery, G.G., and Steadman, E.N., 1987, Computer Controlled Scanning electron microscopic characterization of coal ash deposits: American Society of Mechanical Engineers, 87-JPGC-FACT-4, Presented at ASME/IEEE Power Generation Conference, Miami Beach, Florida - October 4-8, 1987.
11. Benson, S.A., Rindt, D.K., Montgomery, G.G., Sears, D.R., 1984, Microanalytical Characterization of North Dakota fly ash: *Ind. Eng. Chem. Prod. Res. Dev.*, 23, p. 252-256.
12. Rothenberg, S.J., Denee, P., and Holloway, P., 1980, Coal Combustion fly ash characterization: electron spectrascopy for chemical analysis, energy dispersive x-ray analysis, and scanning electron microscopy: *Applied Spectroscopy*, v. 34, no. 5, p. 549-555.
13. Benson, S.A., Sweeny, P.G., Abrahamson, H.B., Radonovich, L.J., Zygarlicke, C.J., Puffe, W.H., and Maldonado, M.E., 1988, Combustion Inorganic Transformation -- Final Technical Report, DOE, April (1988).

TABLE 1
DROP-TUBE FURNACE RUN CONDITIONS

<u>Monticello</u>	
Particle Size	53-74 μm
Primary Air	1.25 L/min
Sec. Air	4 L/min
Vacuum	15 L/min
Quench Gas	3 L/min
<u>Temperatures</u>	
Preheat Injector	1000°C
Furnace 1	
In	1500°C
Out	1315°C
Furnace 2	
Mid-Point	1280°C
Residence time	sec.

TABLE 2
CHEMICAL FRACTIONATION RESULTS FOR
MONTICELLO COAL

	Initial ($\mu\text{g/g}$ dry coal)	% Removed by H_2O	% Removed by NH_4OAc	% Removed by HCl	% Remaining
Na	315	31	31	0	18
Mg	1180	0	70	4	26
Al	9110	0	0	5	95
Si	23600	0	0	1	99
K	335	21	5	0	74
Ca	7320	0	77	13	10
Ti	395	0	0	15	85
Fe	2200	0	0	53	47
Sr	130	0	72	11	17
Ba	100	0	52	26	22

TABLE 3

CCSEM MINERAL COMPOSITION OF MONTICELLO COAL
(Weight Percent of Total Discrete Minerals)

Mineral	Size Categories (micrometers)						Total % Minerals	Total Wt% Minerals (Coal Basis)
	<1.2	1.2-2.1	2.1-4.4	4.4-8.0	8.0-11.0	>11.0		
Quartz	0.39	2.82	10.47	8.16	2.09	55.41	79.35	4.34
Kaolinite	0.11	0.61	2.13	1.6	2.65	0.0	7.09	0.39
Fe-Aluminosilicate	0.02	0.14	0.25	0.0	0.0	0.0	1.40	0.02
K-Aluminosilicate	0.03	0.27	1.26	1.05	0.0	0.0	3.04	0.17
Ca-Aluminosilicate	0.14	0.58	0.68	0.0	3.42	3.42	4.82	0.26
Iron Oxide/Carbonate	0.0	0.10	0.10	0.0	0.0	0.0	0.9	0.01
Rutile	0.03	0.12	0.32	0.0	0.0	0.0	0.48	0.03
Alum-Silic/Gypsum	0.03	0.13	0.07	0.37	0.0	2.73	3.34	0.18
Pyrite	0.0	0.06	0.07	0.0	0.0	0.0	0.13	0.01
Gypsum	0.0	0.0	0.0	0.0	0.0	0.0	0.0	0.00
Unknown	0.0	0.02	0.35	0.21	0.47	0.0	1.05	0.06
Coal								94.53
Total	2.75	4.89	15.77	11.40	5.63	61.56	100.0	100.00

TABLE 4
PHASES DETECTED BY SEMPC FOR MONTICELLO FLY ASH

	<u>Filter</u>	<u>Stage 5</u>	<u>Stage 4</u>	<u>Stage 3</u>	<u>Stage 2</u>	<u>Stage 1</u>
Particle Size Cutpoints (µm)	<1.2	1.2-2.1	2.1-4.4	4.4-8.0	8.0-11.0	>11.0
Percent Mass	2.0	2.4	1.1	1.6	2.0	90.9
<u>Phase (Number %)</u>						
Hauyne	1.6	11.2	1.0	0.0	2.9	0.5
Calcium Oxide	0.0	0.0	0.0	0.0	0.0	0.5
Montmorillonite +	0.0	0.7	1.0	0.0	0.0	1.5
Calcium Silicate	0.0	0.7	1.0	0.0	0.0	0.0
Illite	0.0	0.0	0.0	0.0	0.6	0.0
Iron Oxide	0.0	0.0	1.0	0.0	1.7	0.0
Kaolinite +	1.2	22.4	13.0	18.2	16.6	12.2
Anhydrite	28.0	1.4	0.0	2.3	6.3	0.5
Plagioclase	0.0	1.4	1.0	0.0	1.2	1.0
Quartz	0.0	2.1	16.3	31.8	6.3	25.4
Melilite	0.4	2.8	0.0	2.3	1.1	2.0
Pyroxene	0.8	0.0	0.0	0.0	0.0	0.0
Unclassified	67.9	56.6	65.4	45.5	63.5	56.3
<u>Average Composition, wt% (SO₃-Free)</u>						
SiO ₂	29.5	37.7	51.5	51.7	43.5	64.0
Al ₂ O ₃	10.2	18.2	15.2	11.6	17.5	15.1
Fe ₂ O ₃	26.0	6.7	5.7	4.6	5.8	2.6
TiO ₂	0.9	2.1	1.5	2.6	1.9	1.7
P ₂ O ₅	0.2	0.3	0.5	0.4	0.4	0.5
CaO	15.8	27.4	19.9	23.1	23.7	12.6
MgO	16.0	5.6	3.7	4.0	4.6	2.3
Na ₂ O	1.1	1.6	1.7	1.6	2.0	0.8
K ₂ O	0.1	0.3	0.3	0.3	0.4	0.4
(SO ₃)*	8.70	6.4	4.2	3.7	4.6	0.7
<u>Average Si/Al Molar Ratio</u>						
	2.5	1.8	2.9	3.8	2.1	3.6

*SO₃ added for comparison purposes.

+derived phases-resemble the original mineral in the coal.

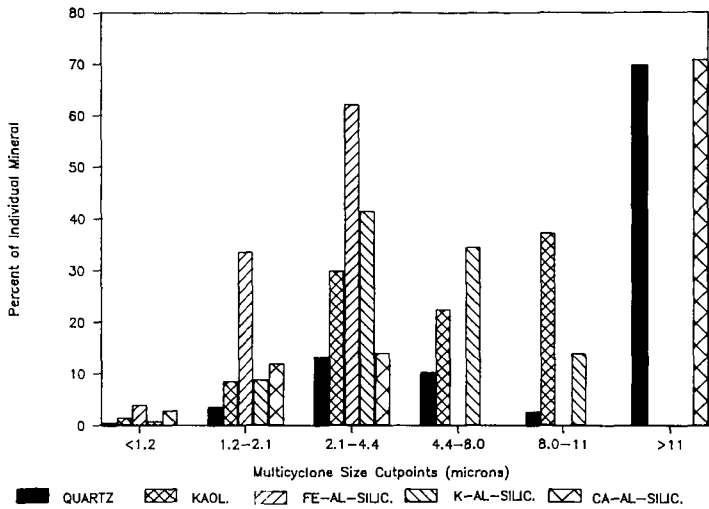


Figure 1. Size distribution of five individual mineral types in Monticello coal.

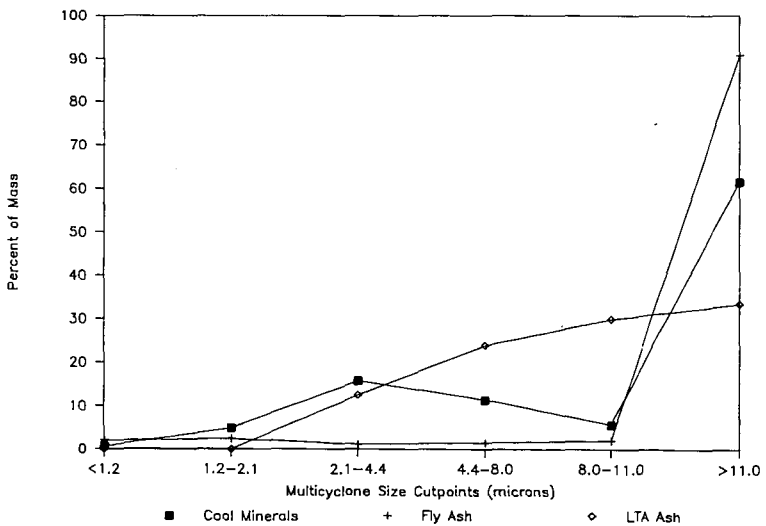


Figure 2. Particle size distribution of Monticello coal minerals, fly ash, and low temperature ash as determined by CCSEM, multicyclone, and coulter counter techniques, respectively.

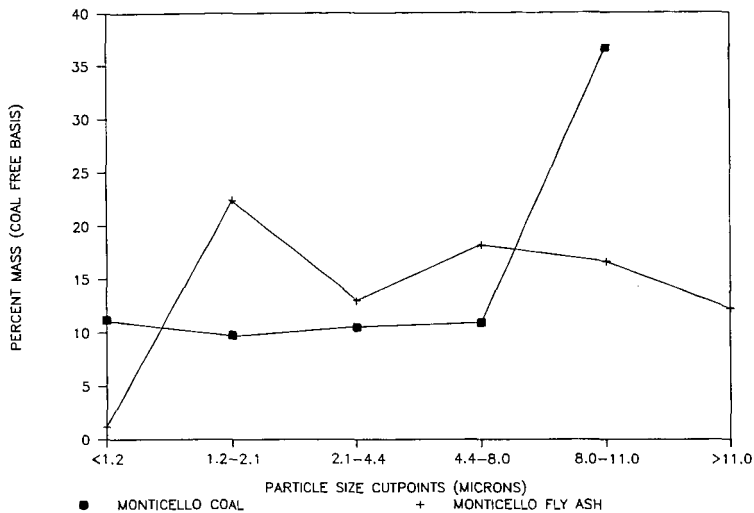


Figure 3. Distribution of Kaolinite in Monticello coal and Kaolinite-derived material in the Monticello Fly Ash.

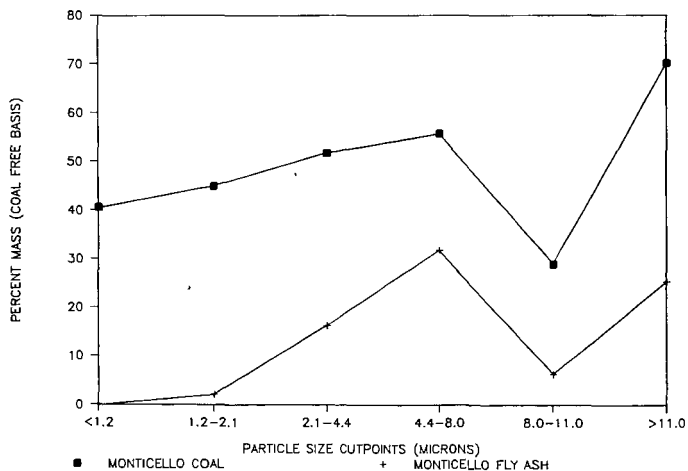


Figure 4. Distribution of Quartz in Monticello coal and Quartz-derived material in the Monticello Fly Ash.

BEHAVIOR OF BASIC ELEMENTS DURING COAL COMBUSTION

G. P. Huffman, F. E. Huggins, and Naresh Shah
CFFLS, University of Kentucky
233 Mining & Mineral Resource Building
Lexington, KY 40506-0107.

ABSTRACT

X-ray absorption fine structure (XAFS) spectroscopy, Mossbauer spectroscopy, and computer-controlled scanning electron microscopy (CCSEM) have been used to investigate the reactions of Ca, Fe, and alkalis in combustion systems. Ca may either transform to a CaO fume that reacts with SO_2 to form CaSO_4 , or may react with clays, quartz, and other minerals to form slag droplets, or flyash. Similarly, pyrite may devolatilize and oxidize exothermically to form molten or partially molten iron sulfide-iron oxide mixtures, or may react with other minerals to become part of the slag. Alkalies in lignites (principally Na) volatilize and may react with either SO_2 to form sulfates or with clay minerals (principally kaolinite) to form aluminosilicate slag droplets. K in bituminous coal is contained in illite which melts and becomes part of the slag phase. The calcium and alkali sulfates and the iron-rich species are observed to be concentrated in the initial layers of deposits, while the complex aluminosilicate slag droplets collect to form an outer glassy layer.

INTRODUCTION

The basic elements in coal ash (alkalies, Ca, Fe) exhibit an interesting dual behavior during combustion. Not surprisingly, this dual behavior is closely related to the way in which these elements are contained in the coal being burned. In this paper, some recent experimental results on the behavior of basic elements in combustion systems are reviewed and qualitative models of their combustion reactions are discussed.

EXPERIMENTAL PROCEDURES

Much of the data on which the current paper is based is summarized in detail in several recent and forthcoming publications.⁽¹⁻⁷⁾ Bituminous coals and lignites and a variety of combustion products obtained from both pilot scale combustion rigs and drop-tube furnaces have been investigated. The principal characterization techniques used were XAFS spectroscopy, Mossbauer spectroscopy, and computer-controlled scanning electron microscopy (CCSEM).

EXPERIMENTAL RESULTS

The principal experimental observations for the dominant basic elements are summarized below.

Calcium - In lignite, calcium is molecularly dispersed in the coal macerals and is bonded to the oxygen anions in carboxyl groups, while in bituminous coal it is predominantly contained in the discrete mineral, calcite. A systematic change from carboxyl-bound calcium to calcite is observed with increasing rank.⁽⁸⁾ During pyrolysis and gasification reactions the molecularly dispersed calcium in lignite is observed to agglomerate and, eventually, form CaO.⁽¹⁾

A recent XAFS study of the combustion products of a lignite and a bituminous coal detected two forms of Ca, Ca incorporated in aluminosilicate glass and CaSO₄.⁽⁵⁾ Solids rapidly extracted from within and above the flame contained all Ca in glass. In both superheater and waterwall deposits, glass was the dominant Ca-bearing phase in the outer (fireside) deposits, while CaSO₄ was dominant in the inner or initial deposits. In work currently underway, the forms of Ca in samples produced by combustion of Beulah lignite and other coals in drop-tube furnace studies are being investigated by CCSEM and XAFS spectroscopy. Typical results are shown by the ternary diagram in Figure 1. Here each point represents an ash particle identified by the CCSEM analysis as containing >80% Ca + Si + Al. The composition of each particle, normalized to three elements, is then plotted on the ternary diagram. It is seen that there are a substantial number of Ca-rich (principally CaO) particles, and aluminosilicate glass particles with a fairly broad range of Ca contents.

Iron - Pyrite and its oxidation products are the dominant iron-bearing phases in both low and high rank coals, although bituminous coals frequently contain substantial amounts of iron in clays and siderite.⁽⁹⁾ If pyrite is contained in a burning coal particle that also contains clay minerals and/or quartz, it is likely to react with these minerals to form an aluminosilicate slag droplet. Mossbauer spectroscopy has demonstrated that most of the iron in flyash samples quenched from within or above the flame of a pilot scale combustor, and most of the iron in the outer layers of deposits, is contained in aluminosilicate glass.^(3,4)

Pyrite particles that are isolated within a coal particle or that are liberated behave much differently. Recently, Mossbauer spectroscopy and CCSEM measurements were conducted to determine the transformation products formed from pyrite removed from coal in drop tube furnace tests at gas temperatures of 1311 to 1727 K and residence times from 0.07 to 1.2 seconds in a 95% N₂ - 5% O₂ atmosphere.⁽⁶⁾ Magnetite was the dominant oxide formed, while pyrrhotite (Fe_{1-x}S) was the dominant sulfide. CCSEM results show evidence of extensive melting, even at the lowest gas temperature. This is consistent with a thermodynamic model⁽¹⁰⁾ which yields particle temperatures significantly in excess of the gas temperature because of the exothermic oxidation of pyrrhotite. These results are also consistent with the observation of iron-rich initial layers observed in deposits^(3,4) that appear to have been formed from the impaction of highly viscous liquid droplets. The inner layer is

transformed to hematite over a period of time at the lower temperatures within the deposit near the waterwall or the superheater tubes.

Alkalies - The principal alkali species in lignite is Na, believed to be molecularly dispersed through the macerals and bonded to the oxygen anions in carboxyl groups. K is low in abundance but can be inserted into carboxyl bound sites in the coal macerals by cation exchange. In bituminous coals, K is the dominant alkali and it is contained almost exclusively in the clay mineral illite. Illite has a strikingly different XAFS spectrum from that of cation-exchanged K in lignite.⁽²⁾ Na in bituminous coals is usually contained as NaCl, frequently in solution in moisture adsorbed in coal pores and capillaries.⁽¹¹⁾

The behavior of alkalies during combustion is strongly dependent on their form in the coal. Carboxyl bound alkalies or alkalies in solution volatilize. Several volatile species are possible, but NaOH is the most likely for lignite.⁽¹²⁾ K in illite is likely to remain with the aluminosilicate particle and form a molten slag droplet. Partial melting occurs at 900-1000°C because of eutectic regions in the $K_2O - SiO_2 - Al_2O_3$ phase diagram.^(13,7) Volatile alkalies have a strong tendency to be absorbed by the aluminosilicates derived from clays^(7,12) and significantly lower the melting point of the resulting slag. This is illustrated by Figure 2 which shows the ternary Na - Si - Al diagram generated from CCSEM data on ash particles collected during combustion of Beulah lignite in a drop-tube furnace. Each data point indicates the normalized three-element composition of a particle identified in the CCSEM analysis as containing $\geq 80\%$ Na + Si + Al. The Ca - Si - Al diagram of Figure 1 is from the same sample. It is seen that the $NaO_2 - SiO_2 - Al_2O_3$ slag particles fall into a relatively small range of compositions.

When volatile alkalies reach the upper regions of the furnace they react with SO_2 to form molten alkali sulfates that react strongly with metal superheater tubes.⁽¹⁴⁾ In a limited set of experiments, we have used XAFS and CCSEM to determine that superheater deposits from a boiler firing North Dakota lignite contained a mixture of alkali sulfate and alkali-containing glass.⁽¹⁵⁾

SUMMARY AND DISCUSSION

On the basis of the results summarized above, qualitative models of the behavior of the major basic elements during combustion can be deduced. These models are indicated in the schematic diagrams of Figure 3.

Calcium in lignite is molecularly dispersed and bonded to carboxyl groups in the macerals. It rapidly agglomerates into Ca - O clusters and CaO, while the calcite in bituminous coal devolatilizes to form CaO. The CaO may be given off from the burning coal particles as a CaO fume or may remain with the particles and react with the clay, quartz or other minerals to form a molten aluminosilicate slag. The CaO fume apparently reacts with SO_2 to form $CaSO_4$ which is part of the initial, presumably sticky, layer in both superheater and waterwall deposits⁽⁵⁾.

Pyrite that is liberated or isolated alone in a coal particle devolatilizes to form pyrrhotite which undergoes exothermic oxidation that raises the particle temperature sufficiently far above the gas temperature to exceed the melting point of magnetite.^(6,10) The molten iron-rich particles impinging on the walls and tubes may be iron sulfide-iron oxide mixtures or magnetite, depending on residence time and temperature. Because of the high momentum of these particles, they readily impinge on the walls and tubes, forming a major part of the initial sticky layer for pyrite-rich coals. Those pyrite particles that are contained in coal particles containing clay, quartz and other minerals react to form molten aluminosilicate slag or flyash droplets which stick on top of the initial iron-rich, layer.

There is less good experimental data on alkalis in combustion systems. Nevertheless, some speculations can be made. It appears that Na is bound to carboxyl groups in lignite and readily volatilizes, presumably to NaOH, although other volatile species are certainly possible. Sodium reacts strongly with clay (mainly kaolinite in lignite) and quartz, both within the burning coal particle and in the vapor phase to form aluminosilicate slag droplets or flyash. The volatile NaOH also reacts with SO₂ to form NaSO₄ which has a low melting point (884°C) and becomes part of the initial sticky layer.

Finally, K in bituminous coal is contained in illite which melts and becomes part of the slag or flyash component of the ash stream.

While the simple diagrams of Figure 3 are consistent with the general trend of slagging and fouling behavior observed in coal combustion systems, it is clear that we have ignored many reactions and made a number of speculations for which there is no firm experimental proof. The current "model", therefore, should really be considered as a point of departure for future discussion and experimentation.

ACKNOWLEDGEMENT

This research was sponsored by the U.S. Department of Energy under DOE Contract No. DE-AC22-86PC90751.

REFERENCES

1. F. E. Huggins, N. Shah, G. P. Huffman, R. G. Jenkins, F. W. Lytle, and R. B. Gregor, *Fuel*, 67, 938-942 (1988).
2. G. P. Huffman, F. E. Huggins, and N. Shah, "EXAFS Spectroscopy: A New Technique for Investigating Impurity Elements in Coal that Control Slagging and Fouling Behavior," Engineering Foundation Conference on Mineral Matter and Ash in Coal, Santa Barbara, CA, 1988, Eds., K. S. Vorres and R. W. Bryers, to be published by Elsevier.
3. F. E. Huggins, G. P. Huffman, and A. A. Levasseur, "Ash Deposits from Raw and Washed Coals," *ibid.*
4. F. E. Huggins, G. P. Huffman, and A. A. Levasseur, ACS Division of Fuel

Chemistry Preprints, Vol. 33, No. 2, 73-80 (1988).

5. G. P. Huffman, F. E. Huggins, A. A. Levasseur, F. W. Lytle, and R. B. Greeger, "Investigation of the Atomic Structure of Calcium in Ash and Deposits Produced During the Combustion of Lignite and Bituminous Coal," Fuel, in press.
6. G. P. Huffman, F. E. Huggins, A. A. Levasseur, O. Chow, S. Srinivasachar, and A. Mehta, "Investigation of the Transformations of Pyrite in a Drop-Tube Furnace," Fuel, in press.
7. G. P. Huffman, F. E. Huggins, R. W. Shoenberger, J. S. Walker, F. W. Lytle, and R. B. Greeger, Fuel 65, 621-632 (1986).
8. G. P. Huffman and F. E. Huggins, in: Chemistry of Low-Rank Coals, ACS Symposium Series 264, Ed., H. H. Schobert, pp. 159-174, Amer. Chem. Soc., 1984.
9. G. P. Huffman and F. E. Huggins, Fuel 57, 592 (1978).
10. S. Srinivasachar and A. A. Boni, "A Kinetic Model for Pyrite Transformations in a Combustion Environment," Fuel, in press.
11. F. E. Huggins, G. P. Huffman, F. W. Lytle, and R. B. Greeger, "The Form of Occurrence of Chlorine in U. S. Coals: An XAFS Investigation," ACS Division of Fuel Chemistry Preprints, this volume.
12. L. J. Wiberly and T. F. Wall, Fouling and Slagging-Resulting from Impurities in Combustion Gases, R. W. Bryers Ed., Engineering Foundation, New York, NY, 1983; pp. 493-513.
13. E. M. Levin, H. F. McMurdie and H. P. Hall, Phase Diagrams for Ceramists, Amer. Ceramic Soc., Inc., Columbus, Ohio, 1964.
14. W. T. Reid "Coal Ash--Its Effect on Combustion Systems," pp. 1389-1446, Chemistry of Coal Utilization, M. A. Elliott, Ed., J. Wiley, 1981.
15. G. P. Huffman and F. E. Huggins, "Reactions and Transformations of Coal Mineral Matter at Elevated Temperatures," Amer. Chem. Soc. Symposium on Mineral Matter/Ash in Coal, Philadelphia, PA, 1984; ACS Symposium Series No. 301, pp. 100-113, 1986.

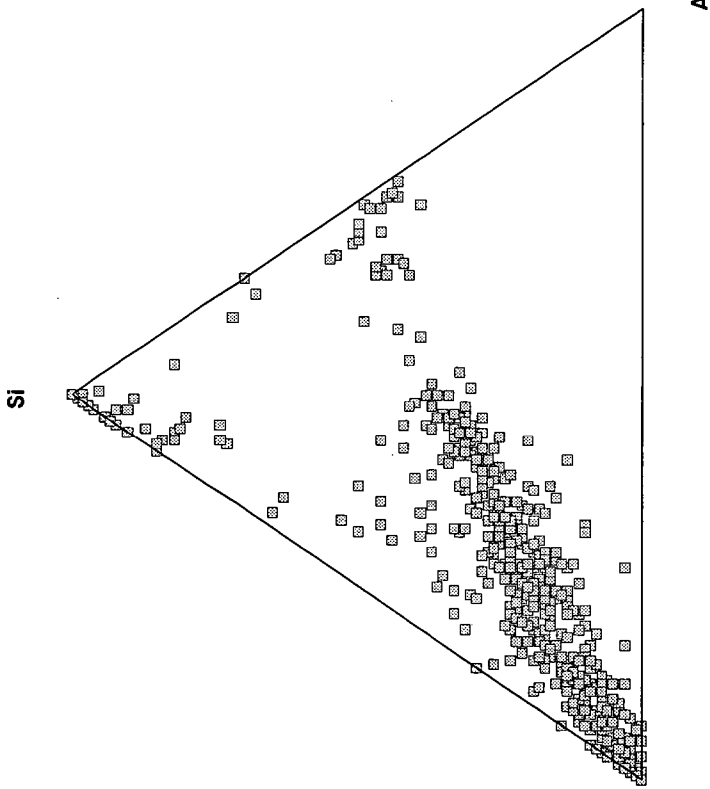


Figure 1. Ca - Si - Al diagram derived from CCSEM data for Beulah ash particles from a drop tube furnace combustion experiment.

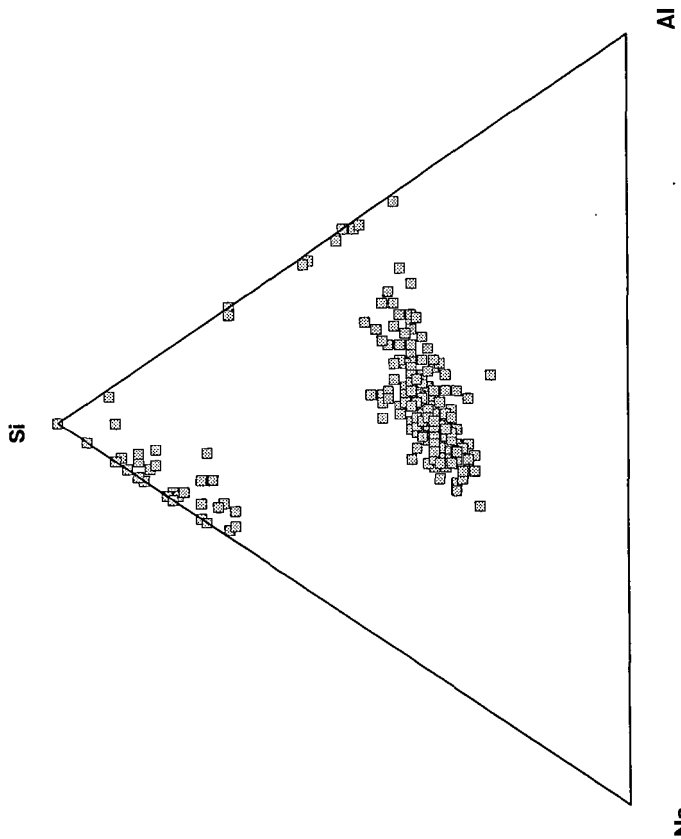


Figure 2. Na - Si - Al diagram derived from CCSEM data for Beulah ash particles from a drop tube furnace combustion experiment.

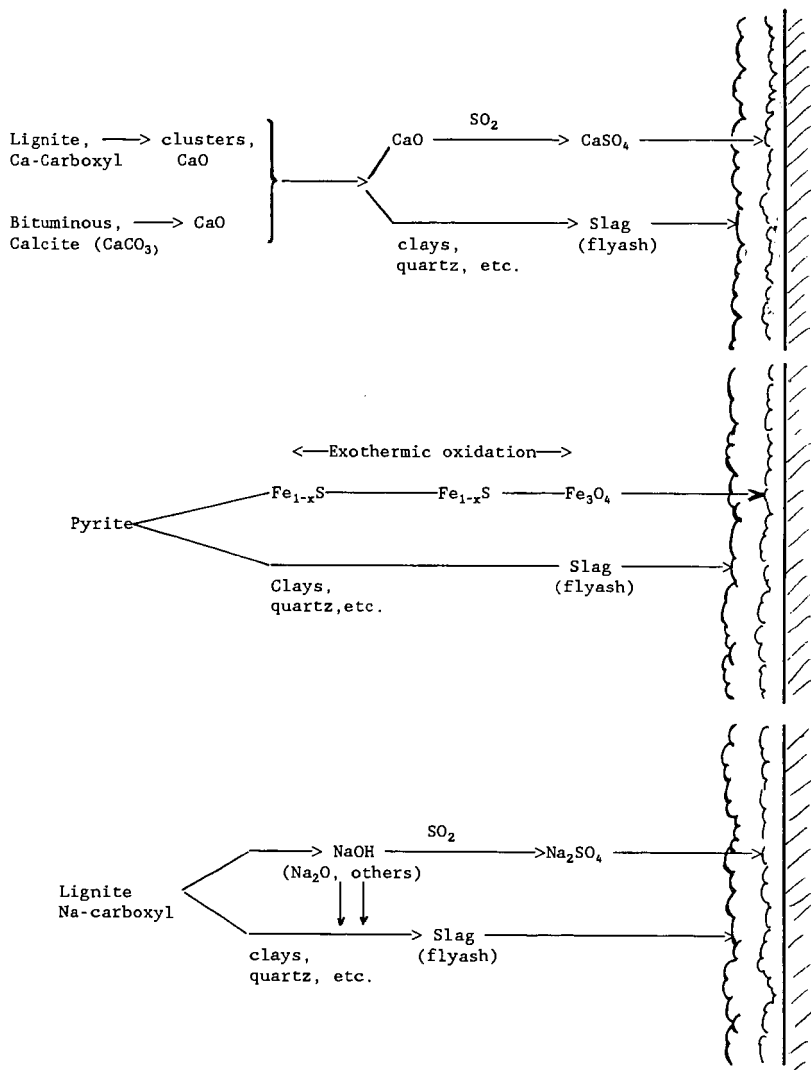


Figure 3. - Schematic diagram indicating the behavior of basic elements in combustion systems.

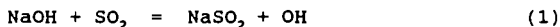
THE CHEMISTRY OF SODIUM WITH SULFUR IN FLAMES

Martin Steinberg and Keith Schofield
Quantum Institute
University of California
Santa Barbara, CA 93106

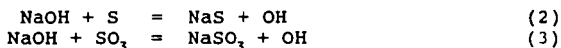
INTRODUCTION

The use of fuel/air systems contaminated with sodium and sulfur in combustion driven gas turbines is a source of turbine blade corrosion. Sodium sulfate, which deposits on turbine surfaces or is chemically formed there, has long been recognized as the active corrosive agent.^{1,2} There is very little chemical kinetic information for modeling this practical problem, and one is forced to invoke chemical equilibrium to attempt any quantitative treatment.

Sodium/sulfur chemistry has been addressed in a very few studies. Fenimore³ reported a decrease of Na with the addition of SO₂ to rich and lean H₂/Air flames which he attributed to the equilibration of Reaction (1).



Durie *et al*⁴, in a study in rich and lean C₃H₈/O₂/N₂ flames assigned the observed Na decay with sulfur addition to the equilibration of Reactions (2) and (3), respectively.



They also felt that Fenimore's data supported their model. In a mass spectrometric study in a lean CH₄/Air flame, Fryburg *et al*⁵ identified NaSO₂, NaSO₃, and Na₂SO₄ as gas phase products in lean methane-oxygen flames. They reported clogging of their sampler inlet orifice which limited their data gathering. In fact, it is not possible to conclude whether the observed species are homogeneous gas phase products, or are formed heterogeneously in the sample inlet probe.

The present study is an outgrowth of two previous efforts in this laboratory, sulfur chemistry⁶ and sodium oxidation chemistry⁷, in H₂/O₂/N₂ flames. Sodium/sulfur chemistry competes with the sodium oxidation chemistry and both are influenced by the flame radical/sulfur chemistry interaction. A brief overview follows.

The radicals H, O, and OH in the hot burnt gases of H₂/O₂/N₂ flames sharply overshoot their equilibrium levels through rapid bimolecular chain Reactions (4-6)



which are balanced due to their large kinetic fluxes in an otherwise non-equilibrated environment. Thus from measures of OH and temperature the concentrations of H, O, OH, and O₂ in rich or H₂ in lean flames

are calculable. The radicals recombine through slow 3-body reactions. With the addition of sulfur to these flames, radical recombination is catalyzed and in turn the radicals establish balances between SO_2 , SO , H_2S , SH , S_2 , and S . As with the flame radicals, the concentrations of these sulfur species also can be determined from measures of OH and T and the total sulfur content. SO_3 is formed in the slow termolecular Reaction 7.



It can be assumed to be in steady state through Reaction 7 followed by reactions of SO_3 with H and O regenerating SO_2 .

The oxidation of sodium in lean, sulfur free, $\text{H}_2/\text{O}_2/\text{N}_2$ flames was found to exhibit an interesting chemistry.⁷ The dominant oxidation path occurs through a fast 3-body process



and the NaO_2 then reacts with the radicals to produce overshoots in NaOH concentrations, which are balanced with small amounts of NaO. A kinetic model was developed for this system from which the concentration profiles of Na, NaO_2 , NaOH, and Na are determined from measures of OH and T and the total sodium concentration. The sodium/sulfur interaction is imbedded in this complex but reasonably understood environment.

EXPERIMENTAL CONDITIONS

Measurements are made in the laminar, premixed, one dimensional flow in the post flame gases above a Padley-Sugden⁸ burner of bundled hypodermic tubing with an overall diameter of 2.2 cm. Sodium is introduced as an aqueous NaNO_3 aerosol generated in an ultrasonic nebulizer⁹ and transported by a portion of the gas flow to the burner. Sulfur is added as H_2S and SO_2 to rich and lean flames, respectively, to minimize thermal contributions these additives make to flame properties. A schematic of the optical system is shown in Figure 1. Temperatures are measured using the sodium line reversal method. Sodium and OH are measured by laser induced fluorescence^{10,11} using a YAG pumped dye laser source beam passed through the flame parallel to the burner surface. The fluorescence, from a slice of the laser excited flame volume is collected by a 6 inch mirror, passed through an image rotator, and focused into the vertical entrance slit of the monochromator. The burner is mounted on a motor driven table programmed to collect data as a function of distance (and time) above the burner surface. The monochromator output is detected with a photomultiplier, the signal amplified, processed in a boxcar integrator, and recorded.

One line of the sodium doublet at 589.0 nm was pumped with fluorescence detection at 589.6 nm. Saturation excitation was employed to eliminate quenching uncertainties. The $\text{OH}(\text{A}^2\Sigma^+ - \text{X}^2\Pi)$ (1,0), $\text{R}_1(6)$ transition was excited at 281.14 nm and fluorescence detected at 314.69 nm from the (1,1), $\text{Q}_1(7)$ transition. The OH measurements are absolute values calibrated against a high temperature flame in which OH is at thermodynamic equilibrium.¹²

RESULTS

Measurements of temperature, OH, and Na have been made in 10-lean and 9-rich $H_2/O_2/N_2$ flames containing sodium with and without added sulfur. The flame matrix is listed in Table 1. Measured (Na) and (OH) profiles are plotted for a lean flame in Figure 2. It should be noted that the decreases in (Na) with added SO_2 result from two effects. The first may be the formation of some Na/S compound. The second, which is dominant in lean flames, is the increased sodium oxidation resulting from the sulfur catalyzed flame radical decay. It is this interaction that complicates the analysis.

KINETIC MODELING

The sodium experimental data has been scaled to refer to the same amount of total sodium in each flame. Sodium concentrations are the order of 10^{11} cm^{-3} , the radicals at least a few orders of magnitude greater, with total sulfur at the 1 to 2% level. Thus all species can influence (Na) but sodium has no effect on other species concentrations.

Checks on the balanced chemistry of Reactions (1-3), suggested by Fenimore³ and Durie *et al*⁴, indicated no such equilibrations. Plots of $\log K$ against T^{-1} for each of the reactions did not correlate the data. Apparently the chemistry is more complicated, requiring kinetic modeling.

With no sulfur present, the total sodium concentration, $(Na)_T$, is given by Equation 9, and with sulfur by Equation 10.

$$(Na)_T = (Na)_0 + (NaO_2)_0 + (NaOH)_0 + (NaO)_0 \quad (9)$$

$$(Na)_T = (Na)_s + (NaO_2)_s + (NaOH)_s + (NaO)_s + (NaX) \quad (10)$$

The subscript "s" indicates the presence of sulfur and (NaX) is a sodium/sulfur compound. To begin the analysis we will assume the formation of a single, dominant NaX. Eliminating $(Na)_T$, we obtain Equation (11)

$$(Na)_s = \frac{(1 + x + y + z)_0}{(1 + x + y + z + w)_s} (Na)_0 \quad (11)$$

where $x = (NaO_2)/(Na)$, $y = (NaOH)/(Na)$, $z = (NaO)/(Na)$, and $w = (NaX)/(Na)$. Equation (11) relates the sodium concentrations with and without sulfur at corresponding times in the profiles for a given flame. The parameter $(1 + x + y + z)_0$ is calculated using the oxidation model for the sulfur free flames. We have used Equation (11) to calculate the values for $(Na)_s$ from the experimental values for corresponding $(Na)_0$ in the sulfur free flames. The parameter $(1 + x + y + z + w)_s$ is modeled to achieve a comparison between the so calculated $(Na)_s$ values and those observed experimentally.

A list of possible reactions have been written for the production and consumption of $NaSO$, $NaSO_2$, $NaSO_3$, $NaSH$, NaS , and NaS_2 . At the sodium levels in this study there is little chance for the formation of any disodium compounds, such as Na_2SO_4 . Vibrational frequencies

and bond lengths have been estimated for calculating thermodynamic properties of the sodium/sulfur species.¹³ Estimates have been made for the gas kinetic collision rates of all the bimolecular reactions. Forward and reverse rate constants, related through the calculated equilibrium constants, have been formulated with the dissociation energy, $D_0(\text{NaX})$, for each of the assumed NaX products, as a parameter to be determined in the modeling program.

(NaO_2), (NaOH), (NaO), and (NaX) in the sulfur bearing flames were determined using a steady state analysis for these species. Three body rate constants for sodium with sulfur species were set initially equal to the rate constants for the sodium-oxygen analogs. Values for $D_0(\text{Na-X})$ and attenuating multipliers for each rate constant were then adjusted to achieve an optimal fit between calculated and experimental values for (Na)_s.

A reaction scheme for NaSO, added to the sodium oxidation model is seen in Figure 3. A comparison of the calculated and experimental profiles for (Na)_s are plotted in Figure 4. The optimal conditions required only reactions (21), (23), and (24) from Figure 3. All the remaining sodium/sulfur processes have negligible influence. NaSO and NaO_2 are isoelectronic and it was assumed that the termolecular formation rate constants for NaSO and NaO_2 are equal. The model yielded a value for $D_0(\text{Na-SO}) = 70$ kcal/mole. NaSO concentrations varied from about 1 to 24% of the total sodium in the rich flames with lower temperatures favoring the higher concentrations. NaOH concentrations ranged from about 1 to 16% with the higher concentrations favored in the high temperature flames. There appears to be little coupling of the sodium sulfidation and oxidation chemistries. Application of the NaSO model to the lean $\text{H}_2/\text{O}_2/\text{N}_2$ flames only made a small contribution to that chemistry.

Similar analyses have been conducted in the rich flames assuming NaS, NaS_2 , and NaSH as the primary sodium/sulfur product. NaS modeling does not quite approach the performance of the NaSO model. In addition the NaS optimal conditions require a value for $D_0(\text{Na-SO}) = 81$ kcal/mole, about 25 kcal/mole too large, ruling out NaS as a dominant product. NaSH and NaS_2 exhibit poorer accommodations to the experimental data.

Only NaSO, and NaSO_2 are possible candidates in the lean flames. NaSO_2 was ruled out as a meaningful product primarily due to the very low SO_2 steady state concentrations. NaSO_2 has been examined as a dominant product in both the rich and lean flames. Optimal rich flame conditions for NaSO, required $D_0(\text{Na-SO}) = 70$ kcal/mole. When applied to the lean flames this model consumed far too much sodium. Modeling NaSO_2 in the lean flames gave a very good approximation to the experimental data with a value for $D_0(\text{Na-SO}) = 46$ kcal/mole. The application to the lean flame data in Figure 2 is seen in Figure 5. In the lean flames NaSO levels reach a maximum of only about 0.5% of the total sodium. The higher values are favored in the richer and cooler flames. NaOH accounts for 8 to 70% of the total sodium with higher values in the leaner flames. It does appear, however, that there is some increased NaOH formation occurring through the small but effective NaSO₂ intermediate. In the rich flame this NaSO₂ model makes a small, almost negligible contribution.

CONCLUSIONS

The sodium/sulfur chemistry has been modeled in a series of rich and lean $H_2/O_2/N_2$ flames. It was found that simple equilibria identified in earlier studies can not account for the behavior exhibited in the present data. Kinetic modeling has been conducted assuming, as is often the case, that one sodium/sulfur product may dominate. To a good approximation this seems to be the situation in both the rich and lean flames. $NaSO$ appears to be the dominant sodium/sulfur product in the rich $H_2/O_2/N_2$ flames with $NaSO_2$ dominant in the lean flames.

The conclusions drawn for the lean flames are fairly firm. $NaSO_2$ is the only viable sodium/sulfur product in this oxidizing environment. However, we must view the rich flame discussion as provisional. It is possible that some combination of $NaSO$ with $NaSO_2$, or even NaS or $NaSH$ can provide a better description of the rich flame behavior. Currently, these combinations of contributing sodium/sulfur products are being examined.

ACKNOWLEDGEMENT

The support of this work by the Department of Energy, Morgantown Energy Technology Center under Grant DE-FG21-86MC23135 is gratefully acknowledged.

REFERENCES

1. E.L. Simons, G.V. Browning, and H.A. Liebhafsky, *Corrosion*, **11**, 505t (1955).
2. M.A. DeCrescente and N.S. Bornstein, *Corrosion*, **24**, 127 (1968).
3. C.P. Fenimore, *Symp. (Int.) on Combustion*, **14**, 955 (1973).
4. R.A. Durie, G.M. Johnson, and M.Y. Smith, *Symp. (Int.) on Combustion*, **15**, 1123 (1975).
5. G.C. Fryburg, R.A. Miller, C.A. Stearns, and F.J. Kohl, in "High Temperature Metal Halide Chemistry," D.L. Hildenbrand and D.D. Cubicciotti, Editors, p. 468, The Electrochemical Society Softbound Proceedings Volume 78-1, Princeton, NJ (1978); also NASA TM-73794 (1977).
6. C.H. Muller, K. Schofield, M. Steinberg, and H.P. Broida, *Symp. (Int.) on Combustion*, **17**, 867, (1979).
7. J.T. Hynes, M. Steinberg, and K. Schofield, *J. Chem. Phys.* **80**, 2585 (1984).
8. P.J. Padley and T.M. Sugden, *Proc. Roy. Soc. London Ser. A*, **248**, 248 (1958).
9. M.B. Denton and D.B. Swartz, *Rev. Sci. Instrum.* **45**, 81 (1974).
10. K. Schofield and M. Steinberg, *Opt. Eng.* **20**, 501 (1981).
11. J.T. Hynes, M. Steinberg, and K. Schofield, *J. Chem. Phys.* **80**, 2585 (1984).
12. C.H. Muller III, K. Schofield, and M. Steinberg, *ACS Symp. Series*, **134**, 103 (1980).
13. B.J. McBride and S. Gordon, "Fortran IV Program for Calculation of Thermodynamic Data," NASA TN D-4097, August, 1967 (Updated version).

Table 1. Experimental Hydrogen/Oxygen/Nitrogen Flame Matrix and Properties.

H ₂ /O ₂ /N ₂	Temperature (K)	[H ₂ O]	[O ₂] (molecules/cm ³)	[H ₂]	[OH]
0.6/1/1	1906-1929	1.0(18)	1.2(18)	---	3.8->0.7(16) ^a
1/1/2	2066-2100	9.9(17)	4.8(17)	---	3.8->1.1(16)
1/1/3	1667-1730	9.5(17)	4.7(17)	---	3.7->0.3(16)
1.4/1/3	2125-2197	9.8(17)	2.0(17)	---	3.5->1.4(16)
1.4/1/4	1810-1847	9.8(17)	2.1(17)	---	3.6->0.5(16)
1.4/1/5	1654-1669	9.3(17)	2.0(17)	---	3.6->0.3(16)
1.8/1/3	2280-2405	1.1(18)	5.9(16)	---	4.0->1.9(16)
1.8/1/4	2060-2228	9.8(17)	5.1(16)	---	3.6->1.4(16)
1.8/1/5	1825-1916	1.0(18)	5.3(16)	---	3.2->0.7(16)
1.8/1/6	1695-1726	9.6(17)	5.2(16)	---	3.1->0.4(16)
2.2/1/4	2160-2308	1.0(18)	---	1.1(17)	3.8->1.3(16)
2.2/1/5	1975-2106	9.7(17)	---	9.8(16)	2.7->0.8(16)
2.2/1/6	1780-1897	9.4(17)	---	9.4(16)	1.9->0.5(16)
3/1/4	2050-2167	9.7(17)	---	5.5(17)	2.4->0.3(16)
3/1/5	1883-2010	9.1(17)	---	4.6(17)	1.2->0.2(16)
3/1/6	1775-1857	8.8(17)	---	4.4(17)	1.1->0.2(16)
4/1/4	1898-2042	9.1(17)	---	9.1(17)	1.0->0.2(16)
4/1/5	1767-1900	8.6(17)	---	8.7(17)	0.6->0.1(16)
4/1/6	1650-1788	8.2(17)	---	8.2(17)	0.6->0.1(16)

^aConcentrations, read as 3.8×10^{16} near the flame reaction zone decaying downstream to 0.7×10^{16} at 4.0 ms.

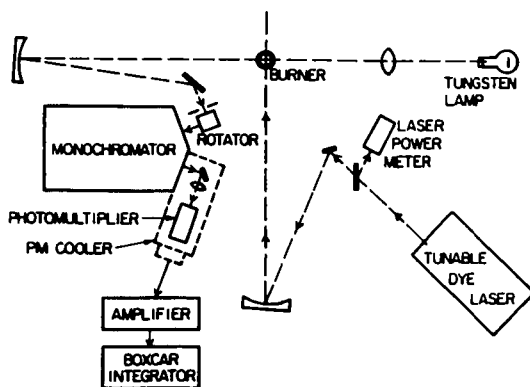


Figure 1. Optical Arrangement

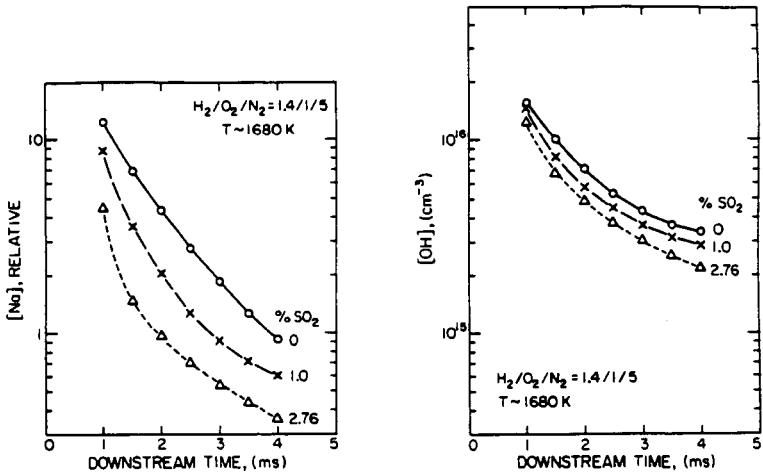


Figure 2. Measured (Na) and (OH) profiles in lean $H_2/O_2/N_2$ flames with varying amounts of SO_2 .

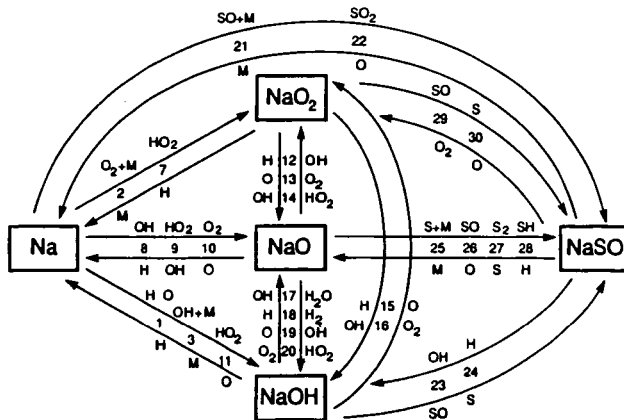


Figure 3. Sodium/sulfur reaction scheme assuming that $NaSO$ is the dominant sodium/sulfur product.

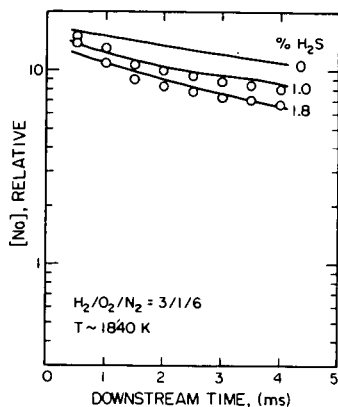


Figure 4. Comparison of measured and calculated sodium profiles in rich $H_2/O_2/N_2$ flames with varying H_2S and $NaSO$ the dominant sodium/sulfur product. Measured, —; calculated, O.

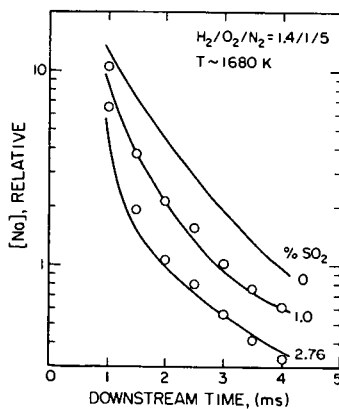


Figure 5. Comparison of measured and calculated sodium profiles in lean $H_2/O_2/N_2$ flames with varying SO_2 and $NaSO_2$ the dominant sodium/sulfur product. Measured, —; calculated, O.

**MINERAL TRANSFORMATIONS IN SELECTED COALS -
SIZE AND COMPOSITION OF THE ASH**

J.J. Helble, S. Srinivasachar, C.B. Katz, and A.A. Boni
PSI Technology Company
Research Park P.O. Box 3100
Andover MA 01810

ABSTRACT

The transformation of minerals during pulverized coal combustion has been examined by burning utility sized coals (70% < 200 mesh) in a laboratory-scale combustor. Experiments were conducted with several coals possessing different mineralogies, with particular attention paid to Kentucky #11 bituminous. Size and composition of the initial minerals and the resulting ash were measured by a variety of techniques, including computer controlled SEM, low temperature ashing, deposition on a cascade impactor, and optical (Malvern) particle size analysis. Results for the Kentucky #11 coal suggest a large degree of coalescence is occurring between illite, kaolinite, and quartz minerals, with occasional iron incorporation into the resulting glass. Partitioning of the acid-leachable potassium was found to split between incorporation into the glass and vaporization. For other coals, such as Beulah lignite, mineral fragmentation was inferred from the data, presumably due to large quantities of large (>40 microns) pyrite present.

BACKGROUND

Deposition of ash on heat transfer surfaces is the most costly problem associated with the combustion of pulverized coal. Although much research is currently focused toward obtaining a better understanding of the factors giving rise to deposition, current industry practice is to address the problem in an empirical manner which often proves unsatisfactory and inaccurate (1). In determining deposition indices, ash is treated as a homogeneous medium, possessing uniform properties. This neglects the fact that combustion generated ash is actually comprised of individual particles, of a wide variety of sizes and compositions. By treating the ash as disparate particles rather than as a homogeneous medium, it is possible that better deposition indices could be developed.

There are several components which must be addressed in determining the deposition behavior of an ash particle, and by extension, of a particular coal. Size, chemical composition and adhesive properties of the surface layers (i.e. stickiness) are all important considerations. The stickiness of ash particles has been addressed elsewhere (2,3); preliminary results of an experimental study of the factors giving rise to the observed size and composition distributions of ash are discussed herein. Several recent laboratory studies have utilized the size of the ash particles to infer the importance of various phenomena such as fragmentation, fines carry-over, and coalescence (4-9). Utilization of size information coupled with mineral and

ash compositional information for a particular coal to provide an overall picture of the important processes, is the focus of this study. Several U.S. coals and one Australian coal are being examined, with the results from one particular coal - Kentucky #11 bituminous - highlighted.

EXPERIMENTAL APPROACH

Combustion experiments were conducted in a laboratory scale drop-tube combustor which incorporates a gas-fired swirl-stabilized section on the front end to increase residence time and simulate particle concentrations present in an actual combustor. Details of this system are provided elsewhere (2). Ash particles were sampled isokinetically, quenched, and collected with a variety of techniques depending upon the desired information. Size distributions were obtained both by deposition on a Pollution Control Systems Mark III cascade impactor, and by filtration and subsequent sizing with a Malvern Instruments particle sizer. Chemical composition of coal minerals and individual ash particles was determined by computer controlled scanning electron microscopy (CCSEM) at the University of Kentucky.

RESULTS AND DISCUSSION

By comparing the initial distribution of minerals present in a pulverized coal with the final distribution of ash particles, it is possible to infer the major mechanisms of mineral transformation occurring. Kentucky #11 was chosen for this study, as it has finely disseminated minerals compared to other bituminous coals, with a relatively low degree of extraneous or excluded mineral matter. As it contains fairly large amounts of illite and kaolinite, it presents an ideal opportunity for examining the transformations undergone by clay minerals in the presence of carbon. The mineralogy of this coal is summarized in Table I.

TABLE I
Kentucky #11 Mineralogy and Ash Composition

<u>Fuel Analysis</u> *		<u>Ash Analysis</u>	
Fixed Carbon	41.9	SiO ₂	45.8
Volatile	33.8	Al ₂ O ₃	19.0
Ash	20.3	Fe ₂ O ₃	20.4
Moisture	4.0	CaO	4.4
		MgO	0.9
		K ₂ O	2.5
		Na ₂ O	0.3
		SO ₃	5.2
<u>Mineral Analysis</u>			
Quartz	19		
Kaolinite	8		
Illite	16		
Mix. Silicates	23		
Pyrite	24		

* for as-received coal

Mineral size distributions for this coal were obtained by two techniques: CCSEM analysis of the minerals in the utility grind coal, as well as Malvern analysis of a small sample of the low temperature ash. Results from these two measurements are compared in Fig. 1 with an ash particle size distribution, obtained upon combustion of the coal in 7% oxygen at 1500 K gas temperature. As the curves in the figure indicate, the mineral distributions agreed at small diameters, but varied somewhat at the larger mineral sizes. While the CCSEM indicates 80% by volume of the mineral matter to be < 13 microns in diameter, the low temperature ash measurement indicates that 80% of the mineral matter is less than 30 microns in size. As the two techniques measure size on a different basis (the CCSEM measures a cross-section and infers diameter, while the Malvern is a volume-based technique), this level of agreement is encouraging. Preliminary results with coals having a high percentage of extraneous mineral matter (Kentucky #9 bituminous and San Miguel Texas lignite) yields better agreement across the entire distribution.

Examination of the ash size distribution, measured by a combination of cascade impaction and Malvern techniques and also plotted in Fig. 1, reveals that upon combustion, a large degree of coalescence is taking place. This is evidenced by the uniform shift to larger particle diameters for the entire distribution. Although both char and mineral fragmentation may be occurring, the effects are lost when the utility grind coal is burned and the overall distribution examined. For this coal under these combustion conditions, mineral agglomeration and coalescence dominate.

Examination of the chemical composition of individual ash particles collected under these conditions also suggests that coalescence is the primary mechanism governing ash evolution. Figure 2 presents composition data for all ash particles containing potassium + silicon + aluminum in greater than 80% levels, excluding oxygen. Composition ranges for typical illite and kaolinite particles are also presented. Pure quartz can be assumed to occur at 100% Si on the diagram. Several conclusions can be drawn from this compositional information. First, it is evident that neither pure quartz, illite, nor kaolinite dominate the final ash. The resulting final ash composition is clearly a mixture of these three minerals. The compositions suggest that quartz is incorporated into both clay minerals, though the mixed silicates present in the initial coal are likely contributing as well. Analysis of the data on a particle by particle basis is currently under way to help resolve the effect of the mixed silicates. It is also interesting to note from the Figure that potassium levels do occasionally increase above the baseline present in the initial illite, but it is not a dramatic increase. This observation, coupled with fume measurements reported elsewhere (2), indicates that acid-leachable potassium present in the raw coal can vaporize in addition to being incorporated into the glassy ash particles.

The fate of the pyrite present in the coal can also be deduced from examination of the final ash composition. Mossbauer analyses of ash collected from combustion at two different oxygen levels are presented in Table II. It is evident that only a small portion of the iron is incorporated into a glassy phase under both oxygen levels. As anticipated, the level of iron present as hematite increases as the oxygen level is raised, due to an increase in the kinetically limited magnetite oxidation rate (10).

Table II
Kentucky #11 Mossbauer Results

<u>Conditions</u>	<u>Magnetite</u>	<u>Hematite</u>	<u>Glass</u>
5% O ₂ , 1500 K	70	21	9
21% O ₂ , 1500 K	57	33	10

Different behavior was noted in experiments conducted with a North Dakota Beulah lignite coal under this program. This coal was selected both for the large amount of large (>40 micron) pyrite minerals present, and the large amount of acid-leachable calcium. As the size distribution results presented in Fig. 3 indicate, combustion at both 7% and 21% oxygen levels yielded ash particles with distributions shifted toward smaller sizes relative to the initial minerals. What this suggests is that pure minerals may be fragmenting and influencing the distribution. It is anticipated that pyrite is the major species contributing to this observed behavior, as pyrite fragmentation has been noted in the literature under several conditions (11). Further experimentation with both the Beulah lignite and synthetic chars containing only pyrite is under way to test this hypothesis.

SUMMARY

Laboratory combustion experiments conducted with Kentucky #11 bituminous coal at low oxygen levels (7% oxygen in the bulk gas) demonstrate that agglomeration and coalescence of the included minerals is the dominant transformation mechanism occurring. Results suggest a large degree of coalescence is occurring between illite, kaolinite, and quartz minerals, with occasional iron incorporation into the resulting glass. Lack of iron incorporation was demonstrated by Mossbauer measurements, where approximately 10% of the iron was present as a glass under both oxygen levels studied. Acid-leachable potassium occasionally added to the glassy ash, as evidenced by relatively high potassium concentrations in some particles, though vaporization of the acid-leachable potassium was found to occur as well. For the second coal discussed in the study - Beulah lignite - mineral fragmentation was suggested by comparison of the ash distributions with initial mineral distributions measured by CCSEM. This presumably is due to large quantities of large (greater than 40 micron) pyrite present.

ACKNOWLEDGMENTS

The authors thank the Department of Energy Pittsburgh Energy Technology Center for their generous support of this work under contract number DE-AC22-86PC90751. Coal and ash analyses provided by R.W. Bryers of Foster Wheeler, and G.P. Huffman and F.E. Huggins of the University of Kentucky are also gratefully acknowledged.

REFERENCES

1. Bryers, R.W., "An Overview of Slagging/Fouling due to Impurities in Coal," Proceedings of EPRI Conference on Effects of Coal Quality on Power Plants, October (1987).
2. Srinivasachar, S. Helble, J.J., Katz, C.B., and Boni, A.A., "Transformations and Stickiness of Minerals During Pulverized Coal Combustion," Proceedings of the Engineering Foundation Conference on Mineral Matter and Ash Deposition from Coal (in press) (1988).
3. PSI Technology Company, "Transformations of Inorganic Coal Constituents in Combustion Systems," Quarterly Report No. 6, DOE Contract DE-AC22-86PC90751, April (1988).
4. Graham, K.A., Helble, J.J., Kang, S.G., Sarofim, A.F., and Beer, J.M., "Mechanisms of the Transformation of Mineral Matter to Ash in Coal and Model Chars," Proceedings of the Engineering Foundation Conference on Mineral Matter and Ash Deposition from Coal (in press) (1988).
5. Holve, D.J., Comb. Sci. and Tech. 44: 269 (1986).
6. Wibberley, L.J., and Wall, T.F., Comb. Sci. and Tech. 48: 177 (1986).
7. Helble, J.J., and Sarofim, A.F., "Influence of Char Fragmentation on Ash Particle Size Distributions," Comb. and Flame (in press) (1989).
8. Wall, T.F., Bailey, J.G., and Wibberley, L.J., "The Influence of Coal Properties and Combustion Conditions on the Size Distribution of Fly Ash," Proceedings of the Engineering Foundation Conference on Mineral Matter and Ash Deposition from Coal (in press) (1988).
9. Kang, S.G., Helble, J.J., Sarofim, A.F., and Beer, J.M., "Time-Resolved Evolution of Fly Ash During Pulverized Coal Combustion," 22nd Symposium (Int'l) on Combustion, Seattle (in press), August (1988).
10. Srinivasachar, S., and Boni, A.A., "A Kinetic Model for Pyrite Transformations in a Combustion Environment," Fuel (accepted) (1988).
11. Simpson, D.R., and Bond, R.M., "The Behavior of Pyrite and Its Reaction Products During Combustion," Proceedings of the Engineering Foundation Conference on Mineral Matter and Ash Deposition from Coal (in press) (1988).
12. Jorgensen, F.R.A., Trans. Instr. Min. Metall. Sect. C 90: 1 (1981).

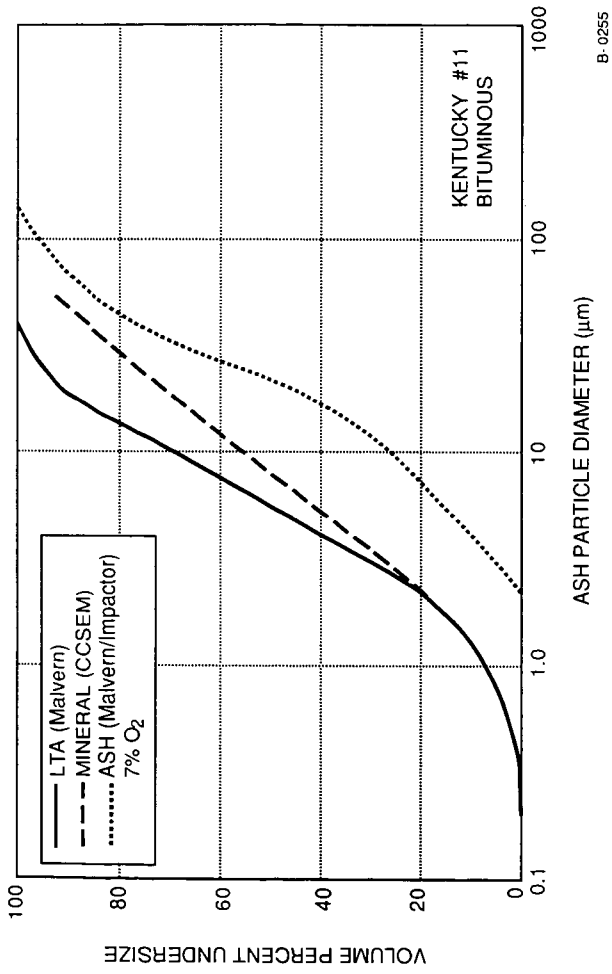
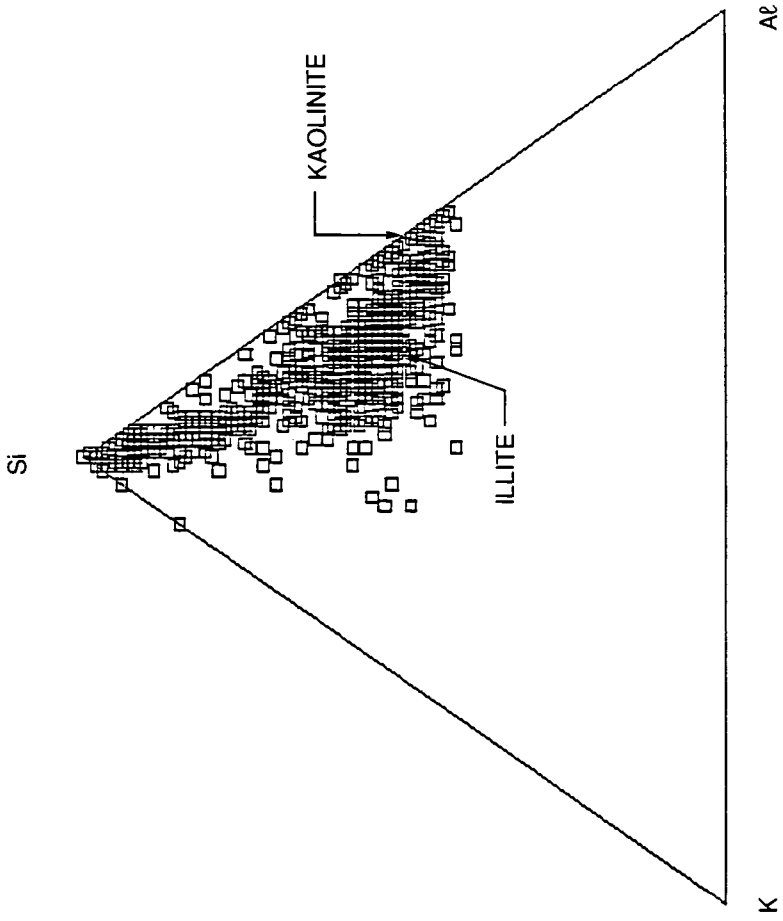
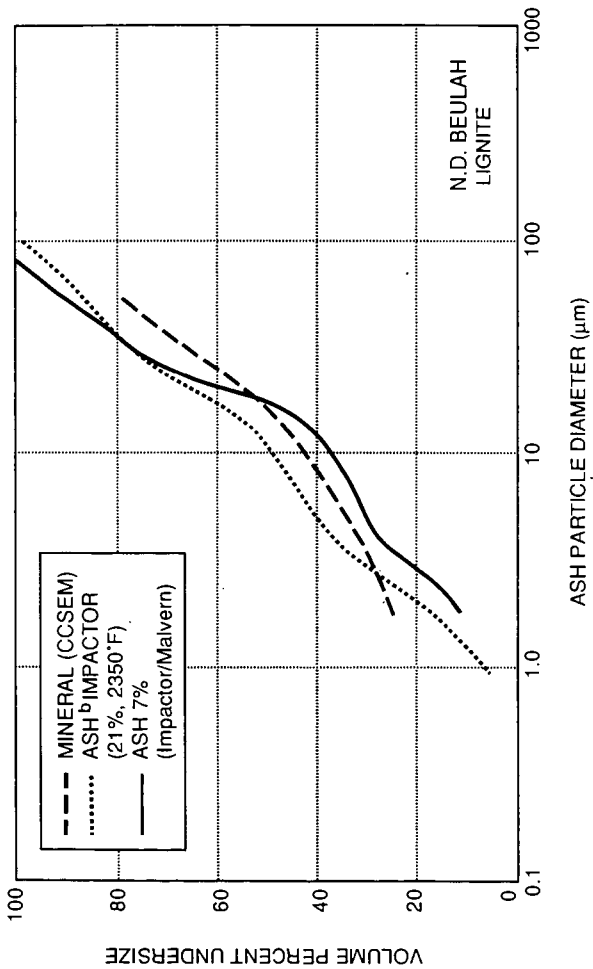


Figure 1: Mineral and Ash Particle Size Distributions - Kentucky #11



B-0258

Figure 2: Individual Particle Composition, $K+Al+Si > 80\%$, Kentucky #11



^bNORMALIZED TO 0% VAPORIZATION

B-0257

Figure 3: Mineral and Ash Particle Size Distributions - Beulah

A KINETIC DESCRIPTION OF ALKALI TRANSFORMATIONS
IN COAL COMBUSTION SYSTEMS

S. Srinivasachar, J.J. Helble, D.O. Ham, and G. Domazetis*
PSI Technology Company
Research Park, P.O. Box 3100
Andover, MA 01810

* State Electricity Commission of Victoria, Australia

ABSTRACT

A kinetic model was developed to predict concentrations of atomic and molecular sodium species existing in both flame and post-flame zones of pulverized coal combustors. To date, the model has successfully predicted measured literature values of sodium species in the Na/H₂/O₂/N₂ system. At all but the earliest conditions (< 1 ms) sodium hydroxide is predicted to be the dominant species. Atomic sodium levels decay rapidly, representing less than one percent of the total sodium species present at times greater than 5 milliseconds for lean hydrogen flames (H₂/O₂ = 0.6, temperature = 1650°C). Incorporation of sulfur chemistry into the model did not change this conclusion, as sodium hydroxide was still found to dominate. Further development, however, awaits determination as to whether alkali sulfation occurs in the vapor or the condensed phase, as well as the correct corresponding kinetics. Efforts in these areas are discussed.

BACKGROUND

The release of alkali species during the combustion of pulverized coal can seriously affect both deposition and corrosion of boiler components. Deposition can be affected as follows: Subsequent to combustion, vaporized alkali species will condense on, and possibly interact with, the fly ash particles present in the flue gas. Alkali species are known to reduce the viscosity of silica melts. If this interaction generates ash particles with reduced viscosity below the critical point for deformation and adhesion - a likely result - ash particle deposition may substantially increase, as results have shown that reduced particle viscosities generate increased sticking efficiencies (1,2). Direct condensation of alkali species on cooled tube surfaces may also affect deposition by generating a sticky layer on the tube surface, thereby increasing the sticking efficiency of impacting ash particles. Corrosion can also be directly affected by condensation of alkali species on the boiler tube surfaces. Clearly, the extent of influence the alkali species exert on the deposition and corrosion processes will depend upon the particular species present, as the various alkali compounds have different vapor pressures and hence will condense at different temperatures (locations) within a boiler.

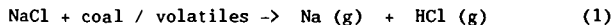
Although it is accepted that the atomic alkali species is the vaporizing species during combustion (except for coals with high sodium chloride

content, in which case it is also as the chloride), it is presently unclear when transformations to molecular oxide species occur, and at what point the assumption of equilibrium is valid. For this reason, a kinetics scheme was developed to follow the transformations of atomic sodium in a combustion environment. The model, which employs the CHEMKIN chemical kinetics code to solve the complex series of reactions, has been used to reproduce species profiles for $H_2/O_2/N_2/Na$ flames appearing in the literature. Modified species profiles resulting from addition of sulfur to the reaction chemistry, utilizing the preliminary sulfation kinetics scheme proposed by Domazetis and Campisi (3), have also been generated, and are discussed herein.

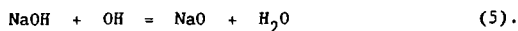
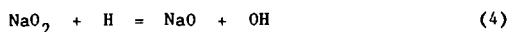
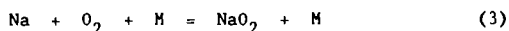
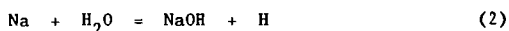
SODIUM VAPORIZATION

Sodium may occur in several forms within a given coal. It may be present as NaCl inclusions, less frequently as small Na_2SO_4 inclusions, or as organically bound material directly attached to the coal structure via carboxylic acid groups. Both of these forms readily vaporize under the high temperature environment of coal combustion, generating atomic sodium and/or NaCl in the vapor phase. Sodium also frequently appears as a component in the clay minerals such as plagioclase, $NaCaAlSi_3O_8$, contained in coals, though thermodynamic calculations have indicated that sodium has low activity in sodium - silica melts (4), thus suggesting that it may be relatively inert to vaporization in this form.

Vaporization of both the chloride and organic forms of sodium occurs rapidly at temperatures well below peak flame temperature, as measured by atomic absorption at SECV and shown in Fig. 1. Sodium carboxylates dissociate in the range 400 to 800°C, forming Na_2CO_3 , which subsequently decomposes further to form atomic Na at temperatures below 900°C. Sodium chloride also vaporizes rapidly under these conditions. Calculations indicate that in the temperature range 1000 - 1100°C, NaCl will completely vaporize in approximately 10 ms, and hence before char oxidation is fully under way. Vaporization of NaCl resulting from reduction to the volatile metallic form may compete with this process, via the reaction (3)



Upon vaporization, the atomic Na quickly encounters the complex chemical environment surrounding the reacting particle. Many species, including H, OH, CO, O, and H_2O are present in this environment, and may potentially affect the conversion of sodium to bound molecular states. Work in laboratory hydrogen flat flames has indicated this to be true, as experimental measurements of Na and OH coupled with kinetic modeling in lean flames demonstrated that Na profiles roughly track the decay of H atoms (5). In that study, the authors demonstrated that despite the existence of some twenty forward/reverse reactions affecting sodium species in their hydrogen flame, the complex sodium chemistry was dominated by just four reactions:

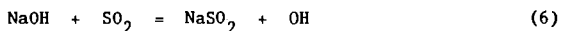


MODEL DEVELOPMENT AND RESULTS

By utilizing these four reactions in conjunction with a detailed hydrogen oxidation reaction sequence (6), CHEMKIN was used to determine species concentration levels for comparison to the data of reference (5). Note that the authors of reference (5) successfully modeled the kinetics in their study using measured OH as an input; in the model described and tested herein, OH is a predicted quantity. For typical lean flame data of $\text{H}_2/\text{O}_2/\text{N}_2$ equal to 0.6/1/1, corresponding to an average measured temperature of 1917 K (6), sodium levels are predicted to decay rapidly. As the curves in Figure 2 demonstrate, this decay parallels the rapid decrease in atomic hydrogen concentration. Sodium hydroxide is seen to be the dominant sodium compound at all times greater than 0.5 ms, as predicted by the measurements and calculations in reference 5.

Calculations were repeated under higher temperature conditions, where $\text{H}_2/\text{O}_2/\text{N}_2$ ratios of 1.8/1/3 yielded flame temperature of 2350 K. Under these conditions (results not shown), atomic sodium persisted for longer periods of time, and was present in levels comparable to NaOH. Again, the concentration profiles predicted here agree closely with those measured (OH and Na) and predicted by the investigators of the aforementioned study.

Calculations were also carried out subsequent to the incorporation of sulfur into the reaction matrix. Sodium-sulfur species are of prime interest in this study, as they are thought to play a major role in initiating deposition in the cooler regions of utility boilers. Although several studies have indicated the major sodium - sulfur reaction to be (7)



the entire sulfur reaction sequence, including all anticipated reactions with H, OH, and O was incorporated into the kinetic model discussed herein. Values for the reaction rate coefficients for this set of reactions were obtained from Domazetis and Campisi (3).

The effect of low levels of sulfur (0.4% by volume) on the sodium reaction chemistry can be seen by comparing species concentrations in Figure 2 with those presented in Figure 3, which includes sulfur. Temperature was assumed equal in both calculations, as the small amount of sulfur added will have a negligible effect. At 1917 K for the $\text{H}_2/\text{O}_2/\text{N}_2$ levels considered previously,

NaOH is still seen to be the dominant sodium species. Both NaSO_2 and NaO_2 are also predicted to occur, but at only 1% of the level of NaOH.

Although vapor phase Na_2SO_4 was considered in the reaction sequence, the calculations performed to date suggest that it will not form under these flame conditions. The possibility has not been excluded, however, as we have not yet identified a fundamental kinetic mechanism which permits the formation of Na_2SO_4 based upon collisions of gas phase species. This raises an interesting point as to the exact origin of sodium sulfate, as sodium sulfate is often identified in boiler deposits, and is frequently assumed to be the cause of initiation of convective pass fouling. The limited experimental data available to date indicate that vapor phase sodium sulfate may indeed form at flame conditions (not specified) (8), as determined by molecular beam mass spectrometry, though further evidence including a plausible kinetics scheme has not been presented. An independent set of calculations (3) suggest another mechanism for formation of Na_2SO_4 in the "vapor," as a result of complexing of species such as NaOH and NaSO_2 during condensation. This proposed non-elementary formation process has not been verified experimentally.

Efforts are currently under way on several fronts in the coal combustion community in an effort to conclusively determine the point (and phase) of alkali sulfation. Atomic sodium release and oxidation in coal systems is being studied through atomic laser-induced fluorescence (9), while at PSIT, techniques which permit direct measurement of alkali chloride and hydroxide in the vapor phase (10) are being employed in a combustion experiment to determine the location of sulfation. Traditional combustion experiments geared toward inducing preferential condensation of the sulfate are also under way at PSIT.

SUMMARY

In summary, a kinetic model utilizing sodium reaction sequences and rate coefficients from the literature has been incorporated into CHEMKIN. The model was able to successfully predict literature values of species concentrations in lean $\text{H}_2/\text{O}_2/\text{N}_2$ flames doped with sodium. Extension of the model to incorporate gas phase sulfur chemistry suggested that NaOH will still dominate under oxygen rich atmospheres, though NaO_2 and NaSO_2 will also form. The absence of vapor phase Na_2SO_4 suggests that Na_2SO_4 formation is a condensed phase reaction, though further mechanistic information is required before this can be conclusively determined. The possible existence of this species under other conditions is currently under investigation experimentally, as conclusive determination of the phase in which reaction to form alkali sulfate occurs remains to be accomplished.

ACKNOWLEDGMENTS

The authors gratefully acknowledge the financial support of the Department of Energy, Pittsburgh Energy Technology Center, through contract number DE-AC22-86PC90751. The authors also wish to thank the State Electricity

Commission of Victoria for generously providing funds which permitted Dr. Domazetis to interact with PSIT researchers during the course of this work.

REFERENCES

1. Srinivasachar, S., Helble, J.J., Katz, C.B., and Boni, A.A., "Transformations and Stickiness of Minerals During Pulverized Coal Combustion," Proceedings of the Engineering Foundation Conference on Mineral Matter and Ash Deposition from Coal (in press) (1988).
2. PSI Technology Company, "Transformations of Inorganic Coal Constituents in Combustion Systems," Quarterly Report Number 6, DOE Contract DE-AC22-86PC90751, April (1988).
3. Domazetis, G., and Campisi, A., "Chemical Kinetics of Coal Combustion and Pollution Formation," State Electricity Commission of Victoria, Report Number SO/86/104, Project No. 2403, NERDDP 933 (1986).
4. PSI Technology Company, "Transformations of Inorganic Coal Constituents in Combustion Systems," Quarterly Report Number 4, DOE Contract DE-AC22-86PC90751, October (1987).
5. Hynes, A.J., Steinberg, M., and Schofield, K., "The Chemical Kinetics and Thermodynamics of Sodium Species in Oxygen-Rich Hydrogen Flames," J. Chem. Phys. 80: 2585 (1984).
6. Muller, C.H., Schofield, K., Steinberg, M., and Broida, H.P., "Sulfur Chemistry in Flames," Seventeenth Symposium (Int'l) on Combustion, The Combustion Institute, Pittsburgh, p. 867 (1979).
7. Fenimore, C.P., "Two Modes of Interaction of NaOH and SO₂ in Gases From Fuel-Lean H₂-Air Flames," Fourteenth Symposium (Int'l) on Combustion, The Combustion Institute, Pittsburgh, p. 955 (1973).
8. Greene, F.T., and O'Donnell, J.E., "Investigation of Mechanisms of Ash Deposit Formation From Low-Rank Coal Combustion," Final Report of DOE Contract No. DE-AC21-81FC10287 by Midwest Research Institute, August (1987).
9. University of North Dakota Energy and Minerals Research Center, "Combustion Inorganic Transformations," Quarterly Report No. 8 under DOE Cooperative Agreement DE-FC21-86MC-10637, April (1988).
10. Oldenberg, R., "Optical Detection of Corrosive Compounds," paper presented at DOE AR&TD Direct Utilization and Instrumentation & Diagnostics Contractors' Review Meeting, Pittsburgh, September (1988).

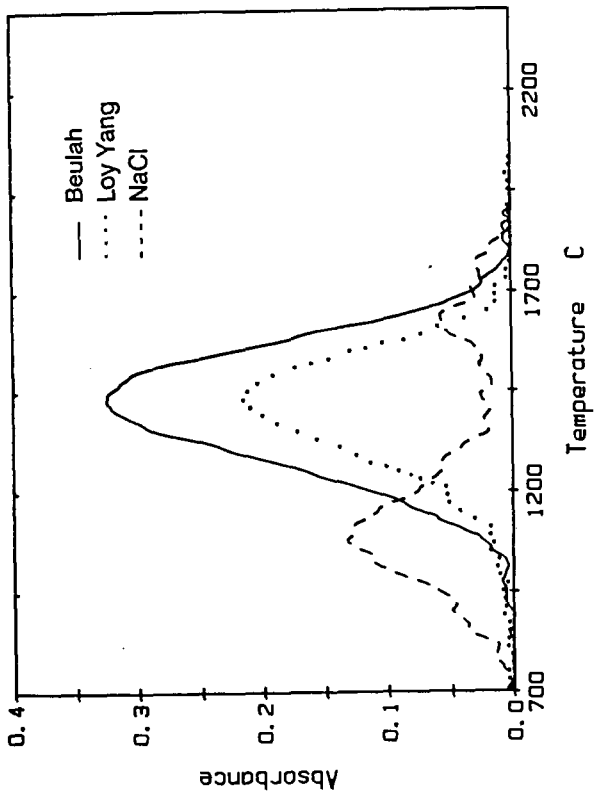
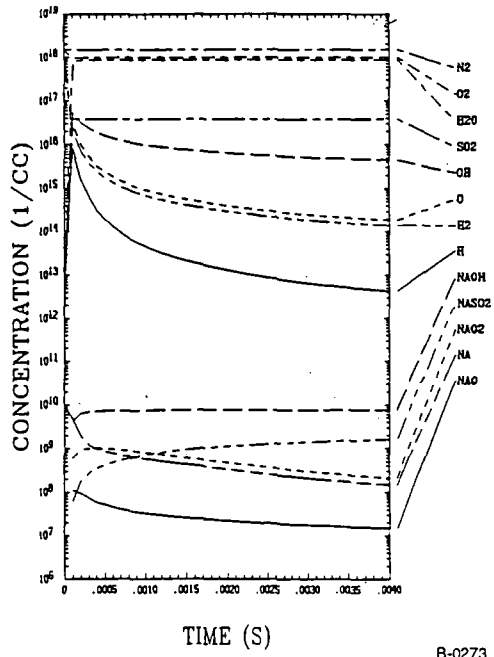


Figure 1 - Atomic Na formation profiles from Beulah and Loy Yang coals by AA

$H_2 / O_2 / N_2 / S$
0.6 / 1.0 / 1.0 / 0.01



B-0273

Figure 2 Model Predictions Without Sulfur

H₂ / O₂ / N₂ / S
0.6 / 1.0 / 1.0 / 0.00

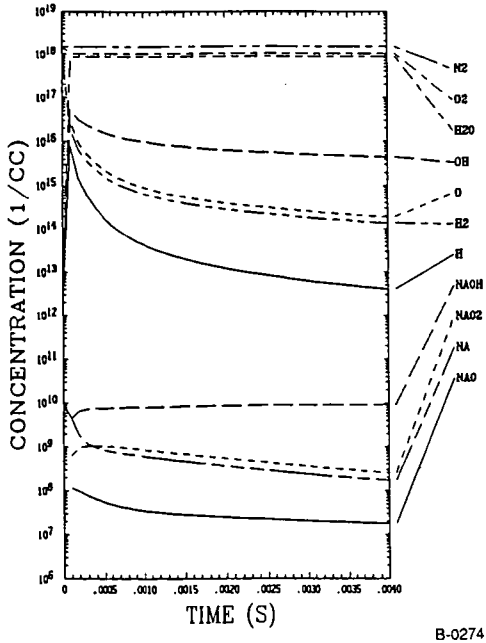


Figure 3: Model Predictions Incorporating Sulfur

CONTROL OF ASH DEPOSITION THROUGH THE HIGH TEMPERATURE ADSORPTION OF ALKALI VAPORS ON SOLID SORBENTS

Wayne A. Punjak, Mohit Uberoi and Farhang Shadman
Department of Chemical Engineering
University of Arizona
Tucson, AZ 85715

INTRODUCTION

Coal usually contains sodium and potassium minerals in various chemical and physical forms. During the combustion or gasification of coal, much of this alkali is released into the gas phase. This vapor is usually in the form of alkali chlorides. In the presence of sulfur, alkali sulfates are also formed. This alkali condenses on and reacts with ash to form low melting point phases that enhance fouling¹.

Cleaning of coal removes some of the alkali but is not effective enough to decrease the alkali concentration to acceptable levels. A promising technique for the removal of alkali from hot flue gases is by using materials (sorbents) that will adsorb and/or react with alkali vapors. In general, the sorbents can be used in two ways. One method is by passing the alkali-laden flue gas through a fixed bed of an appropriate sorbent. This process has been considered for alkali removal from flue gases in the combined-cycle power generation from coal^{2,3,4}. The second method is the injection of sorbents with coal for the in-situ capturing of alkali during pulverized coal combustion. This method has received much less attention⁵.

The choice of a suitable sorbent depends on the coal properties and the process operating conditions. In general, however, the important characteristics desired in a potential sorbent are high temperature compatibility, rapid rate of adsorption, high loading capacity, transformation of the alkali into a less corrosive form and irreversible adsorption to prevent the release of adsorbed alkali during process fluctuations.

Previous studies in this laboratory^{6,7} and those of other investigators^{2,3,4,8} have suggested that bauxite, kaolinite and emathlite are promising alkali vapor sorbents. The purpose of this study is to obtain fundamental information on the kinetics and the mechanism of alkali adsorption on these sorbents.

EXPERIMENTAL APPROACH

The composition of the sorbents used in this study are given in Table 1. These sorbents were used in the form of thin flakes with the approximate thickness of 0.5 mm. The flakes were devolatilized and then stored under vacuum until used.

The apparatus used in the sorption experiments consisted of a tubular quartz reactor, an electronic microbalance and a movable electric furnace. A detailed description of this system is given elsewhere^{6,9}. The experiments were performed in two groups. The first set of tests were made at a sorbent temperature of 800°C under a flowing simulated flue gas (SFG) atmosphere. The composition of the SFG was 80% N₂, 15% CO₂, 3% O₂ and 2% H₂O with a flowrate of 150 or 200 scfm, depending on the experiment involved. Crystalline NaCl was used as the alkali source. The alkali vapor concentration was varied between 50 and 230 ppmv, well below saturation to avoid physical condensation.

In these experiments, sorbent flakes were suspended from the microbalance directly above the alkali source which was placed in the bottom of the quartz reactor. The SFG was passed over the alkali source to vaporize and transport it toward the sorbent. A second SFG line, split from the first, entered the reactor a few cm above the first one and was used to dilute the alkali vapor to a desired concentration. A few cm above the sorbent the gases mixed with purging nitrogen coming down from the microbalance and went out an exhaust port. Thermocouples were placed on the outside of the reactor near the alkali source and the sorbent to monitor the temperature of each.

In the second set of tests the alkali source, either NaCl, KCl or K_2SO_4 , was allowed to saturate the simulated flue gas in the vicinity of the sorbent. The temperature in these experiments was varied from 750 to 1135°C. Thermodynamic calculations showed that for all of these experiments, essentially all of the alkali in the vapor phase remains in the form of the salt from which it was vaporized (i.e., NaCl, KCl or K_2SO_4).

EXPERIMENTAL RESULTS

Typical experimental weight gain profiles for the three sorbents tested in the first set of experiments are shown in Figure 1. The results indicate a decrease in adsorption rate with loading and a final alkali saturation limit. Bauxite is observed to have the highest initial rate, while kaolinite has the largest capacity. The effect of varying the alkali vapor concentration on the weight gain profiles for each sorbent was also tested. Typical profiles for kaolinite are shown in Figure 2. It can be seen that an increase in the alkali concentration results in an increase in the adsorption rate.

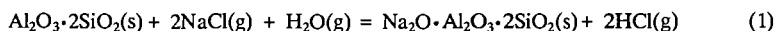
An important difference between the adsorption characteristics of the three sorbents is the reversibility of the adsorption process. After saturation, the reversibility of the alkali uptake was tested for each sorbent by reducing the alkali vapor concentration to zero. No desorption was observed for kaolinite and emathlite, but bauxite lost approximately 10% of its total initial weight gain. This suggests that the mechanism of adsorption is not the same for the three sorbents.

The fresh devolatilized and fully saturated sorbents were analyzed using various chemical analytical techniques to gain further insight into the mechanism of alkali sorption. Scanning Auger microscopy (SAM) was performed on the samples to determine elemental composition and alkali distribution. One important difference between the substrates revealed by these results is in the ratio of sodium to chlorine adsorbed. Chlorine, which has a peak at 176 eV, was not observed in the products of adsorption on emathlite and kaolinite. In contrast, chlorine was partially retained by bauxite.

The cross sections of partially converted samples were mapped for alkali using SAM to study the changes in the substrate during adsorption. The alkali content was observed to be largest near the outer edge of the flake, decreasing rapidly toward the flake center. Similar results were obtained for bauxite and emathlite, indicating that the sorption kinetics for all three sorbents are influenced by intraphase diffusion under the experimental conditions used. Additional details can be found in another publication¹³.

X-ray diffraction (XRD) spectra obtained for the sorbents prior to and after alkali adsorption indicate the formation of several reaction products. Kaolinite saturated with sodium from NaCl

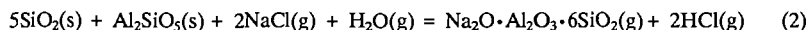
was found to contain primarily nephelite and carnegieite, sodium aluminosilicate polymorphs with the chemical formula $\text{Na}_2\text{O}\cdot\text{Al}_2\text{O}_3\cdot 2\text{SiO}_2$. In nephelite, which is thermodynamically favored at high temperatures, the sodium cation is octahedrally coordinated and in carnegieite it is tetrahedrally coordinated¹⁰. Based on this information and the absence of chlorine in the adsorption product, the following reaction scheme is proposed:



where metakaolinite ($\text{Al}_2\text{O}_3\cdot 2\text{SiO}_2$) is the dehydration product of kaolinite. The stoichiometry of this reaction suggests a 27.9% increase in sample weight on complete conversion. This is very close to the observed 26.6%. In addition, the alkali uptake determined by atomic emission analysis is very close to that predicted by Reaction 1. Kaliophilite ($\text{K}_2\text{O}\cdot\text{Al}_2\text{O}_3\cdot 2\text{SiO}_2$), the potassium analog of nephelite, was observed as the reaction product of KCl and K_2SO_4 with kaolinite. Other investigators^{10,11} also observed the formation of nephelite and kaliophilite when mixtures of sodium and potassium compounds, respectively, were heated with kaolinite to high temperatures. Due to the relatively high melting points of nephelite and kaliophilite, kaolinite would be a suitable sorbent for the in-situ capture of alkali at high temperatures. It is also an excellent choice for the downstream removal of alkali because of its high capacity.

The XRD spectra for the other sorbents indicate a more complicated process. The spectrum for as-received bauxite shows the presence of alpha-quartz, corundum and hematite. The XRD results for fully saturated bauxite indicate the formation of nephelite and carnegieite produced by a reaction similar to Reaction 1 in which NaCl was used as the alkali source. However, the amount of silica in bauxite is not sufficient for Reaction 1 to account for all the adsorbed alkali. Apparently, the rest of the alkali is present as glassy products or physisorbed chloride not detectable by XRD. Since chlorine is lost from the saturated bauxite during desorption, physisorbed NaCl might be the portion which is removed during the desorption experiments. The non-dissociative adsorption of alkali chlorides on alumina has been reported previously^{7,12}. Hematite, present both before and after adsorption, did not undergo any noticeable transformation.

The XRD results for emathlite show the presence of aluminosilicate (Al_2SiO_5), alpha quartz and cristobalite before adsorption. The sample fully saturated with sodium from NaCl consisted primarily of albite ($\text{Na}_2\text{O}\cdot\text{Al}_2\text{O}_3\cdot 6\text{SiO}_2$) together with smaller amounts of sodium calcium aluminate ($\text{NaCa}_4\text{Al}_3\text{O}_9$). Therefore, much of the sodium capture by emathlite can be described by the following overall reaction:



Since albite has a relatively low melting point (1000°C), it is more suited to downstream alkali removal where the flue gas temperature is lower.

MATHEMATICAL MODEL

A mathematical model was formulated to describe the simultaneous physical and chemical processes that occur during alkali sorption by solid sorbents. A brief description of the model is given here. Additional details are given in another publication¹³. In this formulation the alkali

compound, A, diffuses through the porous sorbent and is then adsorbed upon contact with the sorbent surface. The adsorption process is a combination of physical adsorption and reaction, the details of which depend on the alkali and substrate. Assuming a quasi-steady state for diffusion and reaction in a porous particle, the conservation equation for alkali vapor can be written as follows:

$$\nabla \cdot D_e \nabla C_A = R_A \quad (3)$$

where R_A is the molar rate of adsorption of alkali per unit bulk volume of sorbent. The boundary conditions used to solve Equation 3 are a zero concentration gradient at the flake center and an equation of fluxes at the flake surface. The local alkali loading or alkali concentration in the solid phase, C_s , is given by the following conservation equation:

$$(1 - \epsilon_0) \frac{\partial C_s}{\partial t} = R_A \quad (4)$$

in which ϵ_0 is the initial porosity. The initial condition used to solve Equation 4 is $C_s = 0$ at $t = 0$. It is assumed that the local rate of adsorption is given by the following rate expression:

$$R_A = (1 - \epsilon_0) k C_A \left(1 - \frac{C_s}{C_{sf}}\right) \quad (5)$$

in which k is the overall rate coefficient and C_{sf} is the alkali concentration in the solid phase at sorbent saturation. In this formulation the porosity is allowed to vary with conversion. Equation 3 was solved numerically using a variable-step central-difference technique. Equation 4 was solved simultaneously to obtain the solid conversion. The overall loading at any time is obtained by integrating C_s over the sorbent volume.

The model was first used to extract intrinsic kinetic information from the weight gain profiles. The overall rate constant, k , for each sorbent was obtained by fitting the model to the initial rate data. These rate constants together with the other parameters were then used to predict weight gain profiles for the other three sorbents at different alkali concentrations. The profiles and model predictions for emathlite are given in Figure 5.

The values of the rate coefficients estimated from the model are given in Table 2. The difference in the rate coefficients shows that the adsorption process is not a physical and nonselective process, but rather a chemical process which depends on the chemical nature of the sorbent. Under the experimental conditions used, this model suggests that sorbent particles smaller than $50 \mu\text{m}$ must be used for interphase and intraphase diffusional resistances to have a negligible influence on the observed sorption kinetics.

Evaluation of the experiments performed under saturated vapor conditions was more complicated. The data for these experiments are given in Table 3. Although no desorption of alkali was observed for kaolinite in the previous set of experiments, it was possible to desorb a portion of the alkali in the saturated vapor experiments. This suggests that in addition to chemical reaction, alkali was physically condensing on the sorbent. This can be explained by the Kelvin effect which predicts that the alkali vapor was supersaturated in the sorbent pores under the experimental conditions used. The model described above does not consider the physical condensation of alkali and therefore can not be used to evaluate the data in these runs. This model is currently being modified to allow for the physical condensation and chemical reaction of alkali.

CONCLUSIONS

It was found that kaolinite, bauxite and emathlite are suitable sorbents for the removal of alkali vapors from hot flue gases. However, kaolinite and bauxite are more suitable than emathlite at temperatures above 1000°C. The rate of adsorption was observed to decrease with alkali loading and drop to zero when a final saturation limit is achieved. This saturation limit is the highest for kaolinite. The adsorption of alkali chloride on kaolinite and emathlite is irreversible with the release of chlorine back to the gas phase as HCl vapor. The adsorption on bauxite is partially reversible and a portion of the chlorine is retained. Under the experimental conditions used it was found that interphase and intraphase diffusional resistances influence the kinetics of the adsorption process. The proposed theoretical model agrees with the experimental data and can be used for design and parametric studies if the alkali vapor concentration is well below saturation levels. Near saturation, a model must be used that allows for the physical condensation of alkali and reaction with the sorbent.

REFERENCES

1. Borio, R.W.; Levasseur, A.A., "Mineral Matter and Ash in Coal," Vorres, K.S. ed.; ACS Symposium Series, ISSN 0097-5156; 301; chapter 21 (1986).
2. Bachovchin, D.M.; Alvin, M.A.; DeZubay, E.A.; Mulik, P.R., "A Study of High Temperature Removal of Alkali in a Pressurized Gasification System," DOE-MC-20050-2226; Westinghouse Res. Dev. Center: Pittsburgh, PA (1986).
3. Jain, R.C.; Young, S.C., "Laboratory/Bench Scale Testing and Evaluation of A.P.T. Dry Plate Scrubber," DOE-ET-15492-2030; Air Pollution Technology, Inc.: San Diego, CA (1985).
4. Lee, S.H.D.; Johnson, I., *J. Eng. Power*, 102, 397 (1980).
5. Shadman, F.; Peterson, T.W.; Wendt, J.O.L.; Punjak, W.A.; Rizeq, R.G., "Mechanism of Surface Enrichment and Adhesion of Coal Combustion Particulates," second quarterly report; DE-FG22-86PC90505; US DOE (PETC) (1987).
6. Punjak, W.A.; Shadman, F., *Energy and Fuels*, 2 (5), 702 (1988).
7. Shadman, F.; Punjak, W.A., "Solid Adsorbents for the Control of Alkali in Combustion Systems," paper presented at the Fall meeting of Western States Section, Combustion Institute, Tucson, AZ (1986).
8. Lee, S.H.D.; Henry, R.F.; Myles, K.M., "Removal of Alkali Vapors by a Fixed Granular-Bed Sorber Using Activated Bauxite as a Sorbent," CON-8503513; Argonne National Laboratory: Argonne, IL (1985).
9. Punjak, W.A., "High Temperature Interactions of Alkali Vapors with Solids During Coal Combustion and Gasification," Ph.D. Dissertation, University of Arizona (1988).

11. Kuhn, L.; Plogmann, H., *Fuel*, **62**, 205 (1983).
12. Luthra, K.L.; LeBlanc, O.H., *J. Phys. Chem.*, **88**, 1896 (1984).
13. Punjak, W.A.; Uberoi, M.; Shadman, F., "High Temperature Adsorption of Alkali Vapors on Solid Sorbents," submitted for publication to *AIChE Journal* (1988).

Table 1
Composition of As-received Sorbents

<u>Component</u>	<u>Bauxite¹</u> <u>(wt%)</u>	<u>Kaolinite²</u> <u>(wt%)</u>	<u>Emathlite³</u> <u>(wt%)</u>
SiO ₂	11.0	52.1	73.4
Al ₂ O ₃	84.2	44.9	13.9
Fe ₂ O ₃	4.8	0.8	3.4
TiO ₂	----	2.2	0.4
CaO	----	----	5.0
MgO	----	----	2.6
K ₂ O	----	----	1.2
Na ₂ O	----	----	0.1

1. Alcoa (Paranam)
2. Burgess Pigment Company
3. Mid-Florida Mining Company

Table 2
Overall Rate Coefficients

<u>Rate Constant (units)</u>	<u>Bauxite</u>	<u>Kaolinite</u>	<u>Emathlite</u>
k [cm ³ gas/(cm ³ solid - h)]	6.1 x 10 ⁷	2.1 x 10 ⁷	5.9 x 10 ⁷
k _s [cm ³ gas/(cm ² surface area - h)]	28	9.4	37

Table 3

Initial Rate Data for Saturated Vapor Runs

Alkali	Sorbent	Alkali Vapor T (°C)	Initial Concentration ppmv	Rate (h ⁻¹)
NaCl	kaolinite	750	130	0.0349
NaCl	kaolinite	795	400	0.363
NaCl	kaolinite	875	1690	0.418
K ₂ SO ₄	kaolinite	985	5.5	0.0044
K ₂ SO ₄	kaolinite	1060	25	0.0088
K ₂ SO ₄	kaolinite	1135	270	0.0160
K ₂ SO ₄	bauxite	985	5.5	0.0073
K ₂ SO ₄	bauxite	1060	25	0.0205
K ₂ SO ₄	bauxite	1135	270	0.0403

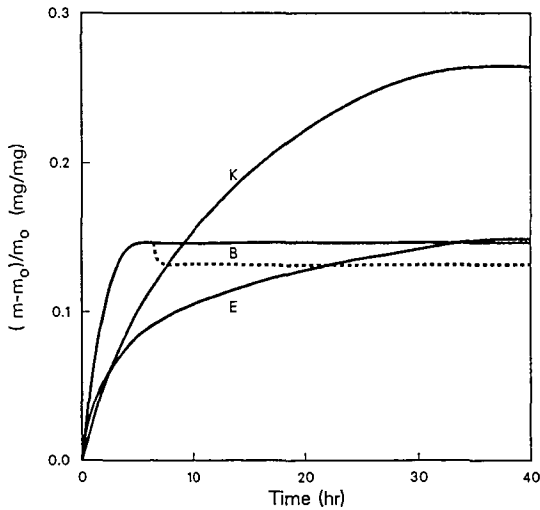


Figure 1. Temporal profile of NaCl adsorption on sorbents.
 K: kaolinite, 230 ppmv Na; B: bauxite, 185 ppmv Na;
 E: emathlite, 150 ppmv Na.

———— adsorption; - - - - - desorption.

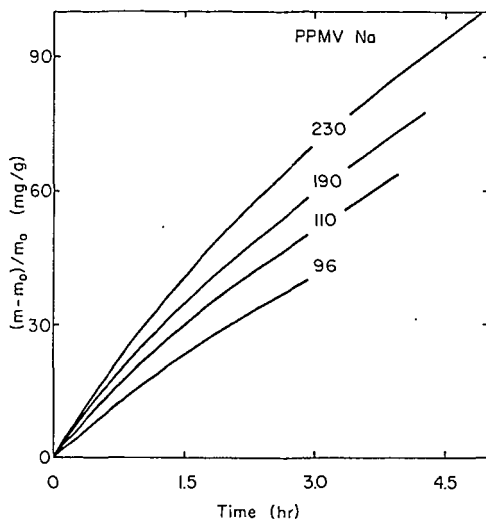


Figure 2. Temporal profile of NaCl adsorption on kaolinite.

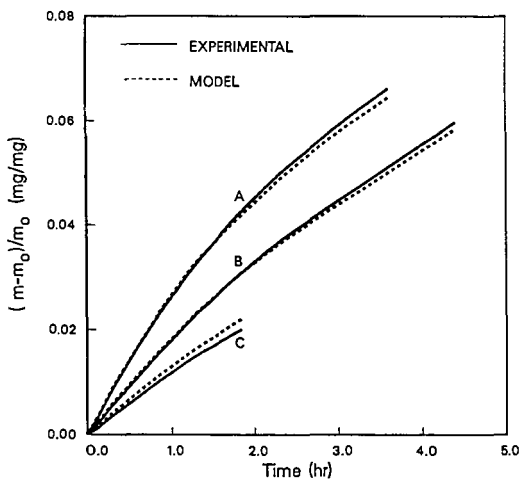


Figure 3. Comparison of model and data for NaCl adsorption on emathlite.

C_{Ab} is 125 ppmv for A, 80 ppmv for B and 65 ppmv for C.

DEPOSIT REMEDIATION IN COAL-FIRED GAS TURBINES THROUGH THE USE OF ADDITIVES

Clifford L. Spiro, C. C. Chen(*), S. Gene Kimura, Raymond G. Lavigne, and Paul W. Shields (**)

GE Corporate Research and Development Laboratory P.O.Box 8 Schenectady, NY 12345

(* Current address E.I. DuPont, Towanda, PA. (** Current address Arizona State Univ, Dept of Geology, Tempe, AZ.

ABSTRACT

Deposit formation represents a key impediment to the eventual commercialization of a direct coal-fired gas turbine engine. Deposits result from the thermal decomposition of coal-borne mineral matter followed by impact and adhesion along the hot gas pathway.

One strategy for deposit abatement is hot gas cleanup to remove particulate before entering the turbine. An alternative strategy, described in this Paper, is to modify the mineral matter/ash chemistry to render it non-adherent through the use of additives. In this way, the complexity and expense of hot gas cleanup is obviated. To date, alumina, boehmite, and a variety of kaolin clay additives have been tested in a coal-water mixture fired gas turbine simulator. A washed kaolin clay has proved to be most effective in reducing airfoil deposition. A mechanism involving in-situ slag decomposition, exsolution, and spontaneous spalling is proposed.

INTRODUCTION

A key objective of the Advanced Coal Fueled Gas Turbine Systems Program, a U.S. Department of Energy initiative, is to develop the technological basis necessary for subsequent commercial development of a direct-fired gas turbine power system. The system concept described in this paper uses a GE LM500 advanced aeroderivative gas turbine engine designed for direct firing of coal fuel. This system can be used in transportation and small stationary power applications. Components and systems required to achieve this objective in a cost-effective and environmentally sound manner are being developed.

Previous work Ref. 1-6, 9-16, reported in the open literature indicates that deposition represents a potential impediment to the commercialization of the coal-fueled gas turbine. Deposits reduce engine efficiency, and require potentially costly maintenance and down-time. Deposition is a prerequisite to hot corrosion (France, 1984).

In order to eliminate deposition, one or more of the key steps in deposition process must be interrupted. These steps are potentially system and fuel dependent, representing the complex interplay of fluid mechanics and thermochemistry.

In general, deposition can be considered as a sequence of events consisting of particle arrival and adherence. Potential mechanisms have been reviewed (Ref. 1). Applicable mechanisms for the in-line annular combustion system are the subject of this investigation, and are probably unrelated to off-board slagging systems (Ref. 2) which have distinctly different time/temperature/flow profiles, and where pre-expansion ash/slag removal is under investigation.

In order to minimize ash particle arrival rates, coal is micronized to comminute mineral matter deposit precursors, and is beneficiated to reduce the overall quantity of ash present in the system. Mineral matter occurs in coal as finely disseminated grains which melt during combustion. Presumably, if there is less mineral matter in the coal, there will be less to adhere. Complete de-ashing of the coal is not yet economically feasible. By micronizing the coal, mineral grains are also comminuted. Finer ash particles are more likely to follow hot gas path streamlines (Ref 16) and avoid impaction on the airfoils. Other mechanisms for deposition of fine particles are applicable (Ref. 8). Much of the ash remains weakly adhered to unburned char surfaces which results in larger effective Stokes diameters and impaction tendencies. To the extent that good atomization and

combustion efficiencies are achieved, this will be minimized.

Once the particles approach the airfoil surfaces, they can undergo collisional impact. To adhere, the particle kinetic energy must be at least partially dissipated, or it will not stick. By cooling the target, the molten slag which comprises the ash will freeze in the boundary layer, greatly reducing its stickiness and tendency for inelastic adhesion.

Unburned carbon will have a deleterious effect on the deposition tendency of the ash, reducing its melting point and also generating heat even after deposition. Unburned carbon has not been detected in deposits, but samples obtained by quenching combustion products (figure 1) reveal 10-40% of the combustion products consist of unburned carbon, even for combustion efficiencies in excess of 99.5%. Presumably final burnout takes place on the airfoil surface. In addition, carbon shell fragmentation may serve to dissipate particle translational energy. Improved burnout and reduced shell size are desirable, and are enhanced by improved atomization of slurry (Staub, 1988).

The condition of the target surface will also influence deposition. If it is cold and clean, there will be a limited tendency for inelastic collisions by the ash. If it is covered with a porous and fluffy surface, collisions may collapse the suprastructure and increase deposition. A very weak deposit may be eroded by incoming combustion products. A viscous liquid on the surface will very efficiently capture particles. In the event of extreme viscosity, the capture may be reduced as the surface may appear to be solid to the products of combustion.

Once deposited, the particles can be re-entrained by erosion, or may be sintered or even completely fused into a liquid. Kuczynski (Ref. 7) showed that sintering of glassy particles is governed by viscous flow. Deposit chemistry and temperature (Ref. 8) therefore determine sintering rate. A weakly sintered deposit initially develops which is subject to erosion or on-line abrasive cleaning, but eventually will fuse to a tenaciously adherent mass.

By understanding the chemistry and mechanism of deposition, the best means for deposit prevention or remediation may be identified.

EXPERIMENTAL

Coal-water mixture was provided as a 50% slurry by Otisca Industries. A summary of the slurry properties appears in Table 1. For the first four kaolin tests, an air classified kaolin was used in both a dry powder and a 70% slurry form. The dry powder was slurred with water and Colloid 211 sodium polyacrylate surfactant. Kaolin slurry was added slowly with stirring to pre-mixed coal slurry, and stirred for 1 hr. prior to combustion. The amount of kaolin was 0.8% by weight of dry coal. The kaolin contained mostly kaolinite with traces of anatase (TiO₂). Atomic absorption spectroscopy also revealed 1000ppm sodium on a slurry basis with comparable amounts of potassium anticipated.

Analytical data on deposits (vide infra) suggested that sodium was responsible for the more severe deposition. In order to limit its participation, a highly beneficiated kaolin, Satintone V* was used. It has a mean particle diameter of 0.8 microns and was mixed as a 46% slurry with Colloid 111 ammonium polyacrylate surfactant. Centrifugation of the slurry at 7000 rpm for 2 hr yielded a supernatant liquor with soluble sodium content of 2.8 ppm as determined by inductively coupled plasma emission spectroscopy. Thus the impact of alkali in such low concentrations could be minimized.

Alpha alumina, Alcan A16SG was also employed as an additive, with a primary particle size of 0.5 microns, and a surface area of 8.229 meters squared/gram. The alumina was dispersed with either Colloid 211 sodium polyacrylate, or Darvan C polyelectrolyte.

* Registered Trademark of Englehard Corporation

Boehmite has the formula $\text{AlO}(\text{OH})$, occurring in the gamma orthorhombic form. It has true density of 3 g/cc, and a hardness of 3.5-4 on Moh's scale, or roughly that of calcite. It is available in ultrapure form (no detectable alkali) as a byproduct of the Ziegler process for making alpha-olefins and fatty alcohols.

The actual boehmite used in the testing was Catapal A, a dry flowable powder which consists of 30-50 angstrom boehmite crystals which had been spray-dried to 30-50 micron granules. While complete dispersion of the crystals is possible under mildly acidic conditions, it was deemed undesirable since complete dispersions greater than 2% by weight will gel. On the other hand, the as-received grains were considered to be too coarse, representing a potential source of erosion in the event that sintering took place in the gas stream. However unlikely this might seem, precautionary comminution was performed in a mullite lined dry ball mill, using a charge of 50% volume 1" cylindrical alumina media for not less than 24 hrs. Sedimentation equivalent spherical diameter of the milled grains had a mean of 0.6 microns, considered to represent an acceptable risk of erosion, as was borne out.

Slurry was burned in the turbine simulator with no special measure taken to accommodate the presence of additives. Numerous combustion trials with doped slurry were made over a period of several months, with a typical test duration of 4-30 hr. Test conditions included the LM500 simulator, Figure 2, a 2000F firing temperature, a chamber pressure of 130 psig and the atomizing air pressure ratio maintained at 1.9. Oil assist was set at 10% to minimize complications due to combustion instability. In actuality, combustion instability did occur in the initial testing due to excessive atomizing air temperature, but this was corrected at the latter stages of testing.

Deposition rates are obtained on line through the determination of Normalized Nozzle Area Index Number (NAIN). NAIN is an indirect measure of the critical throat area between the airfoils. As deposits build up, the throat area is reduced, effectively reducing the mass flow at constant chamber pressure and temperature. By directly measuring these parameters, the NAIN can be calculated (Kimura, 1987).

RESULTS AND DISCUSSION

In the absence of additives, deposit formation is initially high, and after 25-40 hr, becomes catastrophic. (References) Figure 3 shows deposits from untreated Blue Gem coal after 20 and 45 hr respectively. In order to explore the concept of deposit remediation through ash modification in coal-fired gas turbines, several tests employing inorganic additives to Blue gem coal slurry were performed. The Blue Gem coal is highly slagging, dominated by the considerable presence of iron and calcium, Table 1.

ALUMINA ADDITIVES

Alumina, Alcan A16SG 0.5 micron mass mean diameter, was added to as an aqueous dispersion to the coal slurry in an amount sufficient to double the total ash content of the fuel. Considerable care was taken to ensure that the alumina was not agglomerated in the dispersion. Combustion of the alumina-doped slurry took place for 13 hrs in the turbine simulator. During the test, the NAIN actually increased by 2%, as compared to an anticipated reduction of 2-3% for an untreated coal. The obvious implication was that erosion was occurring which was opening the critical throat region.

The test was halted after 13 hr, and the airfoils were visually inspected. Pressure side and leading edge deposits were found to be considerably less than previously obtained despite the much higher ash loading. The deposits were whitish in appearance and were only slightly fused. Signs of erosion were apparent on both the airfoils and end walls. The vane trailing edge surface had become eroded to nearly a knife edge, and bare metal was obvious along the pressure side surface. The system was reassembled and refired on oil followed by nutshelling. The abrasive injection removed virtually all leading edge and pressure side deposits, confirming the efficacy of altering ash chemistry.

The system was refired on alumina-doped coal slurry for an additional 10 hours, with reduced alumina content, now 0.5 of the indigenous 0.8% ash content. The qualitative results were identical to those observed during the initial test segment.

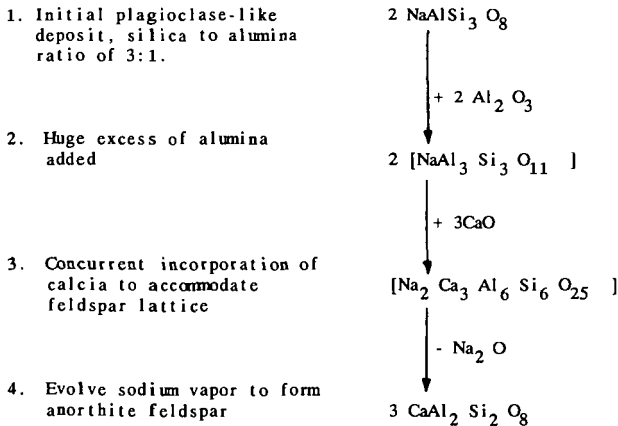
The conclusion from the alumina-added test was that indeed ash modification could take place by judicious addition of inorganic species, but that care must be taken to ensure that erosion did not occur.

BOEHMITE ADDITION

Based on the alumina test results, showing reduced ash adhesion accompanied by unacceptable erosion, boehmite was selected as an alternative. Boehmite is a hydrous alumina $\text{AlO}(\text{OH})$, isostructural with lepidochrosite. Its hardness is ca. 3.5 on Moh's scale, as compared to 9 for sapphire. Thus its erosive tendency should be greatly reduced. Further, it is available in extreme purity as a byproduct from the Ziegler process for alpha-olefin synthesis which employs triethylaluminum. The byproduct fume has an inherent particle size range in the tens of angstroms, and can be dispersed in acidic media. However, to avoid the potential for gelling, spray dried clusters 30 microns in diameter were obtained and dry-ball-milled to 0.6 microns. A slurry was prepared without dispersant, and was admixed with the coal slurry in sufficient quantity to equal the amount of indigenous ash in the coal.

The coal was burned, as usual, in the LM500 turbine simulator for a period of six hours. In contrast to the alumina test, deposition was observed with a NAIN reduction of over 1%. Large chunks formed in the transition section and on the leading edge of the airfoils, and a fine powdery adhered to the suction surfaces.

Analysis of the deposits revealed the usual complement of phases including anorthite, anhydrite, vuggy mullite crystals lining the pores, alpha alumina, hematite, and glass. Not anticipated was the presence of alkali sulfates, which we suggest arose from the following sequence:



The driving force for these reactions is to incorporate as much of the alumina into the feldspar lattice, which is also benefited by the evolution of alkali. The Si/Al ratio starts at 3/1 and ends at 1/1 as is observed. It is the evolution of alkali which results in alkali sulfate glue formation and deposition. In essence, the alumina reversed the gettingter process.

If this interpretation is correct, the use of alumina as a deposition control additive is fundamentally incorrect; it will exacerbate deposition in all but the most silica-rich deposits.

KAOLIN ADDITIVES

Kaolin clay was added, again in an amount sufficient to match the indigenous ash content of the coal. Four tests ranging from 6 to 15 hr in duration were performed using an air classified kaolin clay. Deposition on the airfoil surfaces was minimal, though upstream in the transition section leading to the

airfoils, chunks had formed which occasionally spalled and wedges in the turbine throats. Analysis of these deposits revealed a ten-fold enrichment of alkali metals in the deposit, presumably resulting from alkali impurities in the clay and the sodium polyacrylate surfactant. By using a highly beneficiated clay and an ammonium polyacrylate surfactant, the upstream deposition was considerably diminished. Comparison between deposits from the untreated coal (Figure 3) and the kaolin-treated coal (Figure 4) demonstrate clearly that it is the ash chemistry which dominates the deposition process, rather than the ash quantity.

In order to take full advantage of Kaolin for deposit mitigation, a method for eliminating formation of chunks of deposits which form in the transition piece must be identified. It is expected that through proper thermal and aerodynamic design, this will be accomplished.

It is speculated that the function of the kaolin is two-fold. First, it acts as a network extender, raising the viscosity and surface tension of the melt on the airfoils. Second, it shifts the composition of the melt from the anorthite phase field into the mullite phase field. Exsolution of the high density mullite results in pore formation, especially along the deposit/airfoil interface. The net effect is to reduce the contact area between the deposit and the airfoils so that the ash will either spontaneously spall or erode. Analytical and microscopic evidence supports this hypothesis.

SUMMARY

Deposit formation represents a key impediment to the commercialization of coal-fired gas turbines. It was determined that addition of judicious amounts of ash modifiers, especially inexpensive kaolin clays, is an effective means to render the ash non-adherent.

ACKNOWLEDGEMENTS

This work has been sponsored by the US Department of Energy, Morgantown Energy Technology Center, Contract DE-AC2186MC23168.

The authors acknowledge J. Myers of Meyers Chemical and Subash Lele of Englehard for providing additives.

REFERENCES

- [1] France, J.E., Grimm, U., Anderson, R.J., and Kovach, J.J., *DOE Report*, "Deposition and Corrosion in Gas Turbines Utilizing Coal or Coal-Derived Fuel", Report DOE/METC/84-14, 1984.
- [2] S.G.Kimura, C.L. Spiro, C.C. Chen, "Alkali Species Characterization for Coal-Fueled Gas Turbine", *Proceedings Third Annual Heat Engine Contractors Meeting*, F. Crouse, Ed., DE86001086, 92-103, 1986.
- [3] S.G.Kimura, C.L. Spiro, C.C. Chen, "Alkali Species Characterization for Coal-Fueled Gas Turbine", *Final Report*, DOE/MC/22164-2188, (1987), pp 1-39.
- [4] S.G. Kimura, C.L. Spiro and C.C. Chen, "Combustion and Deposition in Coal-Fired Gas Turbines", *ASME Journal for Engineering and Power*, Vol 109(3), 319-324 (1987). Also presented as paper 87-GT-266 at the Gas Turbine Conference and Exhibition, 5/31/87, Anaheim, CA.
- [5] S.G.Kimura, and C.L. Spiro, "Alkali Species Characterization for Coal-Fueled Gas Turbine", *Proceedings Fourth Annual Heat Engine and Gas Stream Cleanup Systems Contractors Review Meeting*, J. Byam, Jr and K.E. Markel, Jr, DE87001072, pp291-297 (1987).
- [6] F.W. Staub, S.G. Kimura, C.L. Spiro, and M.H. Horner, "Coal-Water Slurry Combustion in Gas Turbines", *Transactions of the ASME, Journal of Engineering for Gas Turbines and Power*, in

press (1988).

- [7] Kuczynski, G.C., "The Science of Sintering", *J. Scien. Sintering*, 9, 243(1977).
- [8] Raask, E., *Mineral Impurities in Coal Combustion*, Hemisphere Publishing, Washington, 1985.
- [9] K. Ross, S.G. Kimura and C.L. Spiro, *Final Report*, U.S. Department of Energy, Gas Turbine Components Screening, DoE/MC/21395-2298, (1987).
- [10] P.J. Schields, C.L. Spiro, and E. Koch, "Phase Characterization of Coal-Fueled Engine Deposits," in *Fly Ash and Coal Conversion Byproducts: Characterization, Utilization, and Disposal IV.*, edited by G.J. McCarthy, F.P. Glaser, and D.M. Roy, in press, (1988).
- [11] N. Rekos, ed., *Proceedings Sixth Annual Heat Engine Contractors Meeting*, 1988, in press.
- [12] C.L. Spiro, C.C. Chen, S.G. Kimura, "Alkali Species Characterization for Coal-Fueled Gas Turbine", *Proceedings Second Annual Heat Engine Contractors Meeting*, 149-156 (1985).
- [13] C.L. Spiro, C.C. Chen, J. Wong, S.G. Kimura, and R.B. Greeger, "Characterization of Products from a Direct Coal-Water Mixture Fired Gas Turbine Combustor", *Fuel*, 66(4), 563-567 (1987).
- [14] C.L. Spiro, S.G. Kimura, and C.C. Chen, "Ash Behavior During Combustion and Deposition in Coal Fueled Gas Turbines", *ASME Journal for Engineering and Power*, Vol 109(3), 325-330 (1987). Also presented as paper 87-GT-267 at the Gas Turbine Conference and Exhibition, 5/31/87, Anaheim, CA.
- [15] C.L. Spiro, S. G. Kimura, R.S. Lavigne, and P.J. Schields, "The Chemistry of Deposition in Coal-Fired Gas Turbines", in *Proceedings of the Mineral Matter and Ash From Coal Engineering Foundation Conference*, F. Bryers and K. Vorres, editors, in review, 1988.
- [16] Wenglarz, R.A., "Turbine Deposition, Erosion, and Corrosion Evaluations Using a Simplified Test Approach", ASME Paper 87-GT-214, Presented at the Gas Turbine Conference and Exhibition, Anaheim, CA, June, 1987.

Table 1- Properties of Otisca Coal-Water Mixture

PROXIMATE ANALYSIS (Dry Basis)		ASH ANALYSIS	
Ash Content %	0.90	SiO ₂	22.4
Total Sulfur %	0.80	Al ₂ O ₃	29.15
Volatile %	37.92	TiO ₂	1.80
Fixed Carbon %	61.18	Fe ₂ O ₃	28.54
Solids %	49.87	CaO	9.86
Viscosity cp (112/sec)	270	MgO	3.00
		K ₂ O	0.17
		Na ₂ O	0.54
		SO ₃	0.62
		P ₂ O ₅	0.33
		SrO	1.09
		BaO	0.67
		MnO	0.04

PARTICLE SIZE DISTRIBUTION

Diameter	Mass %
> 11.5	7.0
11.5	0.5
10.5	0.0
9.5	4.0
8.5	4.4
7.5	3.2
6.5	6.2
5.5	7.6
4.5	10.8
3.5	14.0
2.5	18.4
1.5	18.5
0.5	5.4

ASH FUSION DATA

	Reducing	Oxidizing
Initial Def	2215	2470
Softening	2415	2545
Hemispherical	2535	2605
Fluid	2655	2655

D50= 3.55 micron

Figure 1- Quench probe samples show char cenospheres, fume, and frozen slag spheres.

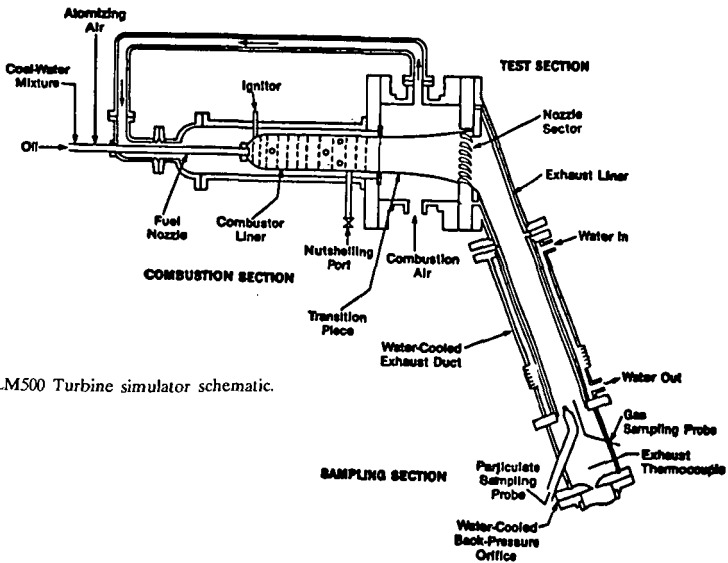
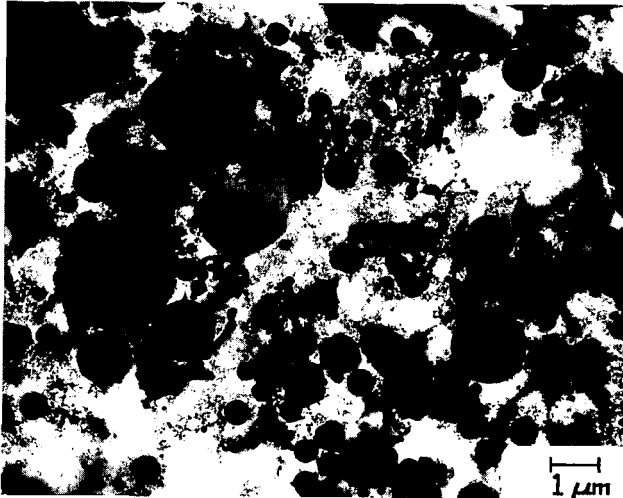


Figure 2- LM500 Turbine simulator schematic.

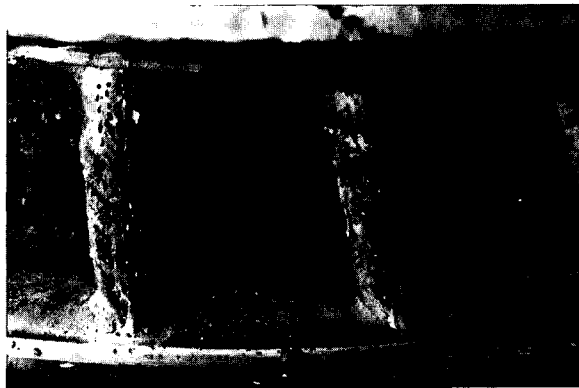


Figure 3- Comparison of deposition before and after treatment with kaolin additive.



A STUDY OF TECHNIQUES FOR REDUCING
ASH DEPOSITION IN COAL-FIRED GAS TURBINES

Ronald G. Logan, George A. Richards,
Charles T. Meyer, and Rodney J. Anderson
U.S. Department of Energy
Morgantown Energy Technology Center
Morgantown, WV 26505

INTRODUCTION

Corrosion and deposition on engine components are potential barriers to the utilization of coal and coal-derived fuels in heat engines. The U.S. Department of Energy has established a program to study mechanisms of ash deposition, with the goal of developing methods to alleviate deposition problems in coal-fired gas turbines. Ash deposits are formed in the turbines by the adherence of ash particles to the surfaces of stators and blades. During combustion, components of the coal ash become molten and thus readily adhere to metal surfaces in the turbine upon impaction (Figure 1) [1]. Deposit growth can be enhanced by the formation of a liquid layer on the surface of the ash particles, which may consist of alkali sulfates, aluminosilicates, or low-melting compounds of iron or calcium [2-5]. Typically, some fraction of the total amount of ash (denoted as the sticking coefficient [6,7]) actually sticks to turbine components forming a deposit.

The tendency of various coals to form ash deposits during combustion is a function of several variables including the ash chemistry, the gas temperature and pressure, the gas velocity, and the temperature of the turbine components. The objective of this work was to measure the sticking coefficient of various coals while studying the basic mechanisms of ash deposit formation to facilitate the development of techniques for preventing deposition in coal-fired gas turbines. Two methods of mitigating ash deposition were studied; active cooling of the deposition target, and the use of fuel additives. Surface cooling has been shown to be effective at reducing ash deposition in boilers [8] and in tests in gas turbine simulators [9]. Deposition reduction can also be accomplished by the use of fuel additives. The injection of additives which can promote spalling of weakly bonded ash has been used in boilers to reduce deposit strength [8]. It has been proposed that additives can act as getters for vapor phase alkali [10] to prevent the formation of low-melting alkali sulfates which can act as a glue to increase deposition. The additives may also contribute to the erosion of ash deposits. Spiro et al. [11] have reported the successful use of kaolin clay to reduce deposition problems in a gas turbine simulator.

EXPERIMENTAL

Experiments were performed in an electrically heated, laboratory scale drop-tube combustor designed to operate at temperatures up to 1500 C and pressures up to 12 atmospheres. This combustor, the combustion/deposition entrained reactor (CDER), is shown in Figure 2. The reaction zone in the CDER is 50.8 cm long and 5.1 cm in diameter. The residence time of coal particles in the reaction zone is approximately 500 ms. Approximately 3 grams per hour of -400 mesh pulverized coal was entrained in air from a circulating feeder, and injected into the reactor with a total air flow rate of 30 slpm. These fuel and air flow rates resulted in a relatively low equivalence ratio of 0.015, compared to overall

equivalence ratios of approximately 0.3 in gas turbines. However, deposition characteristics were shown to be independent of equivalence ratio for coal feed rates varied over an order of magnitude. The coal feed rate used in these experiments allowed longer sampling times which increased the ease and consistency of the measurements.

At the exit of the reaction zone the products of combustion were accelerated through a 3.2 mm diameter nozzle, creating a jet which impinged on a flat platinum disk at approximately 300 m/s, similar to the gas velocity expected in the first stage of a gas turbine. At this velocity, a stagnation flow configuration was created such that all particles greater than 0.5 microns in diameter impacted on the target, as would occur on the leading edge of a gas turbine blade. The 12.7 mm diameter platinum targets were positioned approximately 6 mm below the nozzle aperture. The nozzle and target configuration are shown in Figure 3. Platinum was used as a target material because of its inertness, thereby eliminating surface reactions peculiar to a specific blade material which could effect the experimental results. The target surface was cooled from the underside by introducing an opposing jet of cooling air. Thus the targets could be cooled over a range of temperatures by varying the cooling air flow rate. The target temperature was measured throughout each test via a two-color optical pyrometer monitoring the backside of the platinum target.

The reactor is equipped with three sets of optical access ports for use with a variety of nonintrusive diagnostic instrumentation that is currently under development. An on-line mass spectrometer was used to monitor the major components of the exhaust. A more detailed description of the CDER and its associated instrumentation has been presented previously [12].

Sticking coefficients were determined by first passing the jet of gas and ash particles through a filter to determine the total mass arrival rate. A vacuum pump was used to draw the gas through the filter, which was positioned in the same location as the target. Then a target of known weight was inserted in the jet and a deposit was collected for a specified period of time, usually 10 minutes. The sticking coefficient was calculated as the ratio of the weight gain of the target to the total mass arriving at the target (determined by the filter sample). The filter samples were quenched with cold air, resulting in unburned carbon in the samples. Since carbon was burned out of the deposits, filter samples were analyzed for carbon content to correct the ash arrival rate used to calculate the sticking coefficient.

The adhesion strength of the ash deposits was measured with an in situ adhesion strength meter (ASM). The ASM (shown in Figure 4) consists of a quartz load cell connected to a linear actuator. Attached to the linear actuator is a ceramic probe mounted on a rotational stage for precise control of the probe position. The entire unit is mounted on a precision translation stage, and the probe is coupled directly to the CDER for in situ measurements. When pressure is applied to an ash deposit via the probe, the load cell measures the shear force required to break the deposit free from the platinum target at the temperature of the reactor.

RESULTS

The baseline coal used in this study was Arkwright Pittsburgh bituminous. In addition, a highly-cleaned Kentucky Blue Gem bituminous coal was also studied.

Chemical analyses of the Arkwright and Blue Gem coals are shown in Table 1. All data reported here were collected at atmospheric pressure. Results from tests utilizing target cooling for ash deposition mitigation showed that at lower combustion (exhaust gas) temperatures (1100 C), target cooling had no effect on the sticking coefficient. However at higher combustion temperatures (1300 C), target cooling produced a significant reduction in the fraction of adhering ash (Figure 5). Sticking coefficients were higher at 1100 C and deposits were granular in character and easily removed. Deposits collected at 1300 C, although smaller, were tightly bonded to the target surface. Scanning electron microscope particle size analyses of ash samples collected at the two combustor temperatures showed that the high temperature combustion produced ash particles less than 20 microns in diameter, with a peak in the mass distribution of approximately 5 microns. Conversely, a large fraction of the low temperature ash was concentrated in the particle sizes between 10 and 40 microns. Only a small fraction of the ash was contained in particles smaller than 5 microns. It was proposed that target cooling was effective at reducing deposition at the higher combustion temperatures because the smaller particles were more easily cooled in the boundary layer above the cooled surface, which effectively froze the molten phases in the particles. The larger particles produced at the lower combustion temperature arrived at the target unaffected by the cooled surface. The data suggest that a proper combination of combustion history and hardware surface temperature can contribute to effective deposition mitigation if the combustion process is tailored to produce fine ash particles. A detailed discussion of these results has been presented elsewhere [13].

Three additives were tested; limestone and tricalcium silicate (potential sulfur sorbents), and kaolin. These additives were ground to -400 mesh and mixed with the coal prior to combustion in the CDER. Figures 6 and 7 show the effects of the addition of various amounts of kaolin on the sticking coefficient of Arkwright coal at 1100 and 1300 C, respectively. The data in Figure 6 show that the addition of kaolin had no effect at a reactor temperature of 1100 C until the amount of added kaolin roughly equaled the weight per cent of ash in the coal. Target surface cooling was ineffective at reducing the sticking coefficient at any percentage of kaolin addition for a reactor temperature of 1100 C, as was the case with the Arkwright coal alone. Figure 7 shows the results of similar tests conducted at a reactor temperature of 1300 C. At this temperature, the effectiveness of kaolin addition was more pronounced. Increasing percentages of kaolin decreased the sticking coefficient, and further, kaolin addition enhanced the mitigating effect of target cooling. In fact, the sticking coefficient measured with 7.5 percent kaolin addition and maximum target cooling was the lowest recorded for the Arkwright coal under any reactor conditions or with any other additive tested. This sticking coefficient was approximately an order of magnitude lower than that of the Arkwright coal alone with cooled targets and approximately two orders of magnitude lower than Arkwright alone with no cooling of the target surface.

Limestone addition reduced the sticking coefficient by an order of magnitude at a reactor temperature of 1100 C, and to a lesser degree at a temperature of 1300 C (Figures 8 and 9). However, cooling the deposition target had no effect on the sticking coefficient at either reactor temperature. This is in contrast to results of tests with Arkwright coal only, and Arkwright plus kaolin which showed an order of magnitude reduction in sticking with target cooling at a reactor temperature of 1300 C. Tests with tricalcium silicate produced results similar to those for the limestone tests. Tricalcium silicate was more effective at 1100 C (Figure 10). At a Ca/S ratio of 4, the sticking coefficient was

reduced approximately an order of magnitude, however there was no effect of target cooling. At a reactor temperature of 1300 C with Ca/S ratios less than 1.0, the deposition characteristics were similar to Arkwright coal only, showing an order of magnitude decrease with target cooling (Figure 11). However, mixtures with higher Ca/S ratios showed no reduction of sticking coefficient with target cooling.

The addition of kaolin substantially reduced the adhesion strength of the ash deposits. Many of the deposits collected during the kaolin tests fell off of the targets as they were removed from the CDER. Thus, the measure of the sticking coefficient alone may not adequately assess the effectiveness of kaolin addition for deposition reduction, since the fraction of ash that does adhere is easily removed. Kaolin may react chemically with components of the ash to produce a more friable deposit [10]. Deposits collected during limestone and tricalcium silicate addition lacked this feature, indicating that sticking coefficient reductions measured during these tests may have been due to deposit erosion.

CONCLUSIONS

In general, tricalcium silicate and limestone were marginally effective at reducing the sticking coefficient of the coal at the lower reactor temperature. Both additives tended to reduce the effectiveness of target cooling for lowering the sticking coefficient. Thus, while limestone addition lowered the sticking coefficient at 1300 C with no target cooling, the sticking coefficient was lower without the additive when the target was cooled. Kaolin was very effective at reducing both the sticking coefficient and the adhesion strength of the ash deposits, and produced the lowest sticking coefficient measured for the baseline coal. The data showed that the proper combination of gas temperature, surface temperature, and additive can be an effective means of minimizing the detrimental effects of ash deposition in coal-fired gas turbines.

REFERENCES

1. France, J. E., U. Grimm, and R. J. Anderson, "Deposition and Corrosion in Gas Turbines Utilizing Coal or Coal-Derived Fuels," DOE/METC/84-17 (DE84009290), (1984).
2. Cross, N. L., and R. G. Picknett, "Particle Adhesion in the Presence of a Liquid Film," The Mechanism of Corrosion by Fuel Impurities, H. R. Johnson and D. J. Littler. eds., Butterworths, London, pp. 383-390 (1963).
3. Wibberly, L. J., and T. F. Wall, "Alkali-Ash Reactions and Deposit Formation in Pulverized Coal-Fired Boilers: The Thermodynamic Aspects Involving Silica, Sodium, Sulfur, and Chlorine," Fuel, 61, 87-92 (1982).
4. Wibberly, L. J., and T. F. Wall, "Alkali-Ash Reactions and Deposit Formation in Pulverized Coal-Fired Boilers: Experimental Aspects of Sodium Silicate Formation and the Formation of Deposits," Fuel, 61, 93-99 (1982).
5. Wibberly, L. J., and T. F. Wall, "Deposit Formation and Sticky Particles from Alkali-Ash Reactions, Fouling and Slagging Resulting from Impurities in Combustion Gases, R. W. Breyers, ed., Engineering Foundation, New York, New York, pp. 493-513 (1983).

6. Rosner, D. E., and R. Nagarajan, "Toward a Mechanistic Theory of Net Deposit Growth from Ash-Laden Flowing Combustion Gases: Self-Regulated Sticking of Impacting Particles and Deposit Erosion in the Presence of Vapor Deposited or Submicron Mist 'Glue'," AIChE Symposium Series, Heat Transfer -- Pittsburgh, No. 257, 83, (1987).
7. Ross, J. S., and R. J. Anderson, "Effect of Sodium on Deposition in a Simulated Gas Turbine Environment," J. Energy & Fuels, 2, p. 282, (1988).
8. Raask, E., Mineral Impurities in Coal Combustion: Behavior, Problems, and Remedial Measures, Hemisphere Publishing Corporation, Washington, D.C., (1985).
9. Ahluwalia, R. K., K. H. Im, and R. A. Wenglarz, "Flyash Adhesion in Simulated Coal-Fired Gas Turbine Environment," ASME Paper GT-135 Presented at the Gas Turbine and Aeroengine Congress and Exposition, Amsterdam, The Netherlands, June 5-9, 1988.
10. Scandrett, L. A., and R. Clift, "The Thermodynamics of Alkali Removal from Coal-Derived Gases," Journal of the Institute of Energy, 391 (1984).
11. Spiro, C. L., C. C. Chen, S. G. Kimura, R. S. Lavigne, and P. J. Schields, "Deposit Remediation in Coal-Fired Gas Turbines Through the Use of Additives," To Be Presented at the 197th Annual Meeting of the American Chemical Society, Dallas, Texas, April 9-14, 1989.
12. Anderson, R. J., C. T. Meyer, and R. A. Dennis, "A Combustion/Deposition Entrained Reactor for High Temperature/Pressure Studies of Coal and Coal Minerals," To be presented at the 1988 Annual AIChE Meeting, Washington, D.C., November 1988.
13. Richards, G. A., R. G. Logan, C. T. Meyer, and R. J. Anderson, "Ash Deposition Temperature Effects," Submitted for publication in Transactions of the ASME, (1988).

Coal Rank	Arkwright Pittsburgh Bituminous	Blue Gem (Cleaned) Bituminous
% ASTM Ash	6.93	0.56
Ash Comp. (Wt%)		
SiO ₂	48.09	16.86
Al ₂ O ₃	25.07	22.75
Fe ₂ O ₃	10.95	29.57
TiO ₂	1.27	1.95
P ₂ O ₅	0.18	0.48
CaO	5.78	7.03
MgO	1.25	2.46
K ₂ O	1.16	0.53
Na ₂ O	0.90	1.54
SO ₂	5.34	8.07
Ash Fusion Temp. (C) (± 40)		
(ASTM, 1977)		
Initial Deformation	1,190	1,238
Softening	1,316	1,308
Hemispherical	1,356	1,371
Fluid	1,383	1,427

Table 1: Ash Characteristics

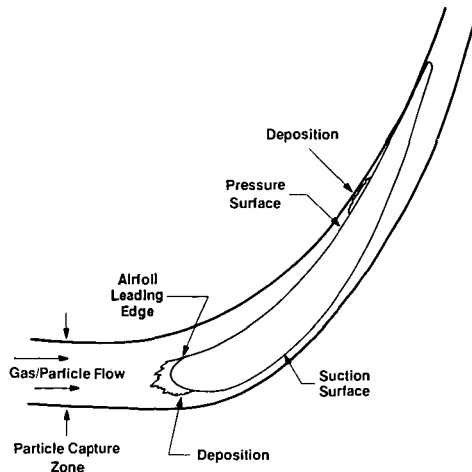


Figure 1: Particle Deposition on a Gas Turbine Vane

Item	Test Section
PRESSURE, ABSOLUTE, atm	1-12
FLOW RATE, scfh	25-700
VESSEL LENGTH, in	60
VESSEL OUTSIDE DIAMETER, in	24
WALL THICKNESS, in	1/4 (sch 40-304LSS)
PROCESS STREAM EXIT TEMPERATURE, °F	2,500
VESSEL SKIN TEMPERATURE, °F	< 300
ELEMENTAL TEMPERATURE (maximum), °F	3,000
HEATING ELEMENTS	KANTHAL SUPER 33 9/18
HEATER OUTPUT, watts	7,060
POWER SUPPLY, V/IA	35/350
EXHAUST FLOW COMPOSITION	DILUTE COAL POC/ FILTERED
EXHAUST FLOW PRESSURE/TEMPERATURE	< 2 atm; < 400°F

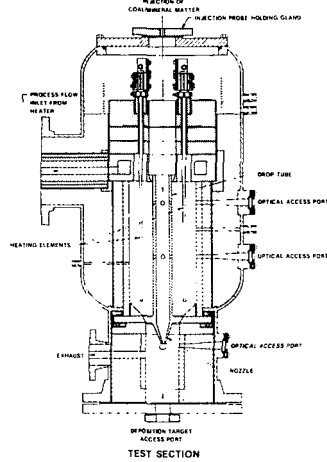


Figure 2: CDER System Design Specifications

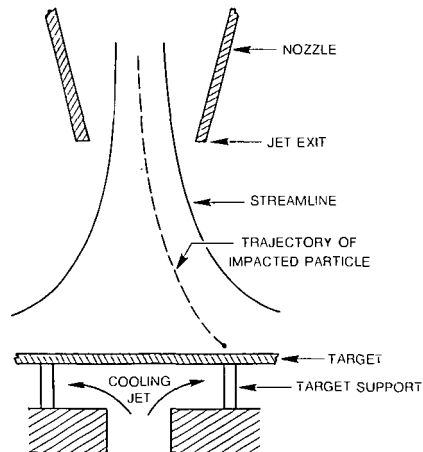


Figure 3: CDER Nozzle/Target Assembly

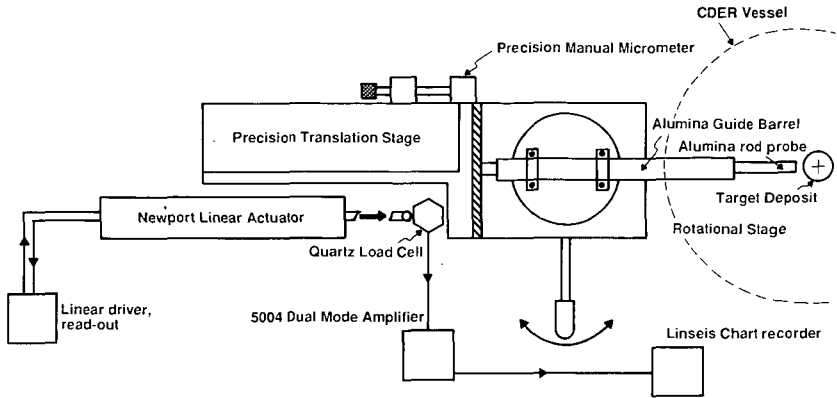


Figure 4: Adhesion Strength Meter (ASM)

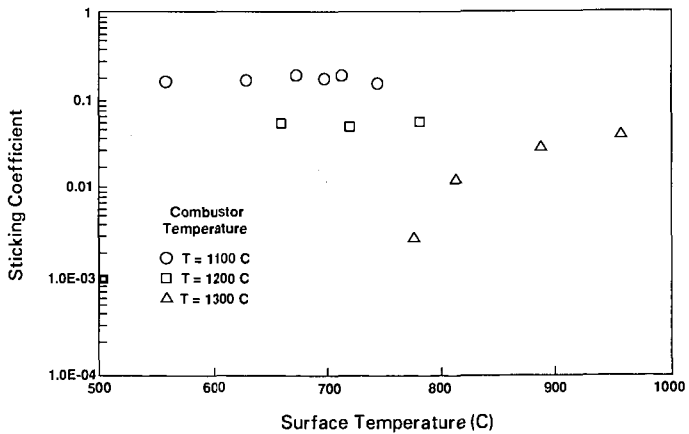


Figure 5: Effect of Target Cooling on Deposition; Arkwright Coal

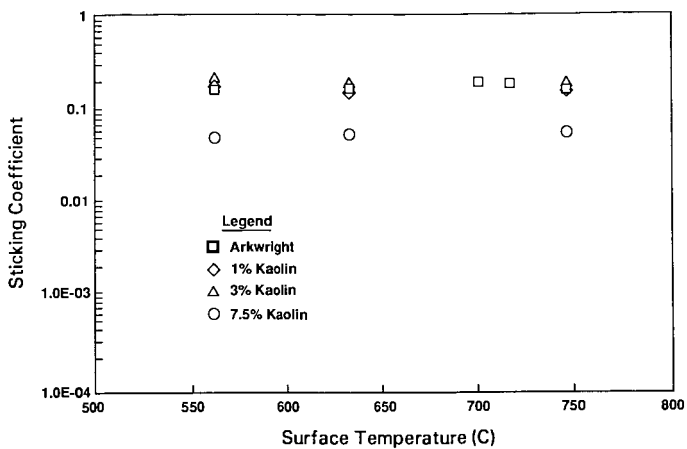


Figure 6: Effect of Target Cooling on Deposition; Arkwright Coal/Kaolin, T=1100 C

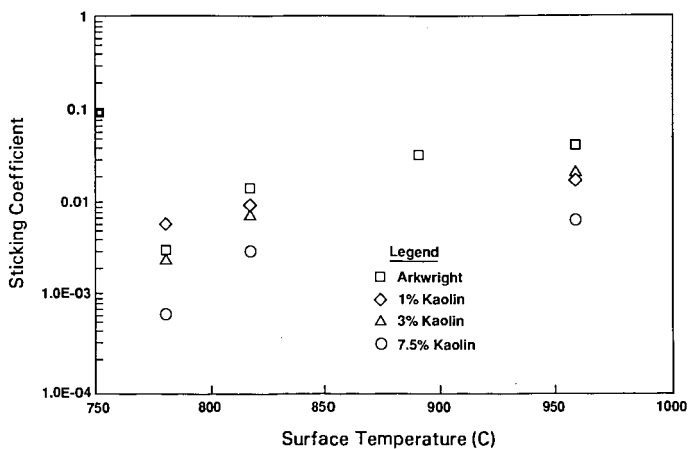


Figure 7: Effect of Target Cooling on Deposition; Arkwright Coal/Kaolin, T=1300 C

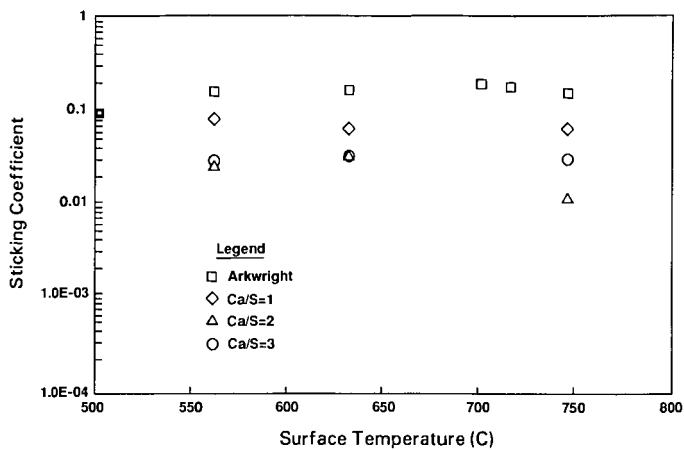


Figure 8: Effect of Target Cooling on Deposition; Arkwright/Limestone, T=1100 C

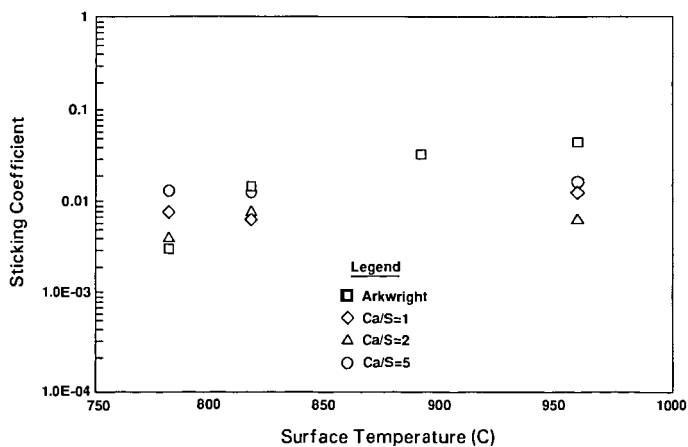


Figure 9: Effect of Target Cooling on Deposition; Arkwright/Limestone, T=1300 C

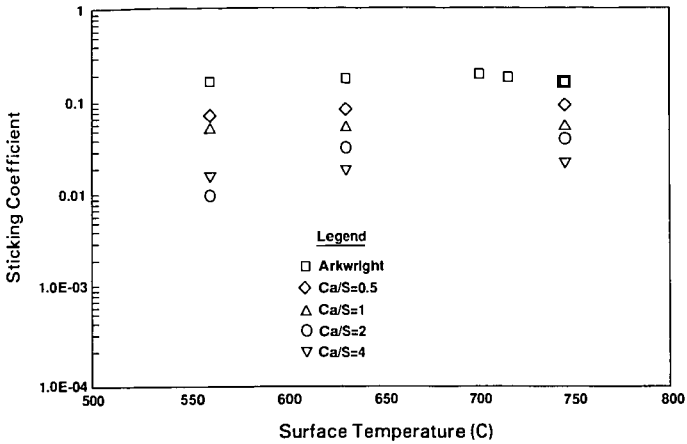


Figure 10: Effect of Target Cooling on Deposition; Arkwright/Tricalcium Silicate, T=1100 C

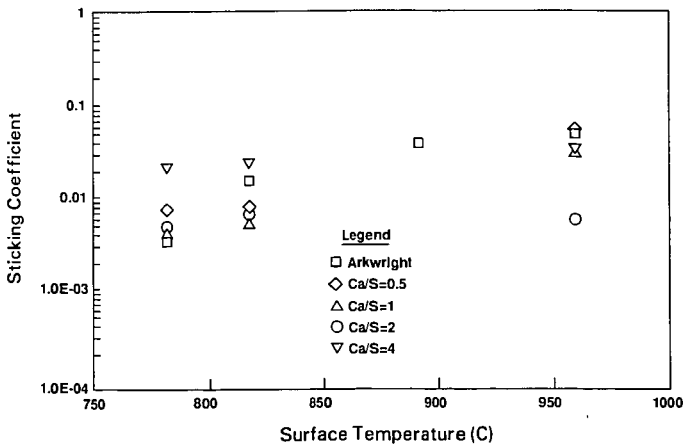


Figure 11: Effect of Target Cooling on Deposition; Arkwright/Tricalcium Silicate, T=1300 C

PHOTOPHORETIC CONTRIBUTION TO THE TRANSPORT OF ABSORBING PARTICLES ACROSS COMBUSTION GAS BOUNDARY LAYERS¹

Jose L. Castillo², Daniel W. Mackowski³, and Daniel E. Rosner⁴
Yale University, Department of Chemical Engineering
High Temperature Chemical Reaction Engineering Laboratory
New Haven, CT 06520, U.S.A

Abstract

Since radiation energy fluxes can be comparable to 'convective' (Fourier) fluxes in large fossil-fuel-fired power stations and furnaces, we have examined particle drift ('phoresis') induced by nonuniform photon-particle heating in a 'host' gas. Our analysis (Mackowski, 1988) of the photophoretic velocity includes the important 'slip-flow' regime, and the numerical results show that photophoresis is a significant transport mechanism for micron-sized absorbing particles in high radiative transfer combustion environments, with equivalent photophoretic diffusivities (dimensionless photophoretic velocities) being as large as 10 percent of the better-known thermophoretic diffusivity (Rosner, 1980, 1985). Since previous experimental results (Rosner and Kim, 1984) demonstrated that thermophoresis causes over a 3-decade increase in particle deposition rates by convective diffusion, clearly, for small, absorbing particles, photophoresis will also be an important contributor to observed deposition rates. Accordingly, we present mass transfer coefficients for particle transport across laminar gaseous boundary layers, including both particle thermophoresis and photophoresis.

Thermophoresis and Photophoresis

When both radiative and convective energy fluxes are present in a gas environment with a dilute amount of aerosol particles, the motion of these particles is affected by temperature gradients in two different ways.

Thermophoresis describes the phenomenon wherein small particles in a gas experience a force in the direction opposite to the thermal gradient in the gas. The thermophoretic velocity (*i.e.*, the terminal velocity reached for an isolated particle in a gas with a constant temperature gradient) is normally written in the form:

$$\vec{v}_{th} = \alpha_T \left[\frac{-(\text{grad } T)}{T} \right] \quad [1]$$

where α_T is a dimensionless thermal diffusion factor and D_p the diffusion coefficient of the particles. Actually, D_p is included here just to emphasize the similarity between \vec{v}_{th} and a diffusion

¹ Research supported, in part, by the U.S. DOE PETC under grant DE-FG22-86PC90756. To be presented to the 197th Annual ACS Mtg., Symposium on Ash Deposition, Dallas-TX, April 9-14. DER#171

² Professor and Head, Depto. Fisica Fundamental, U.N.E.D., Madrid, Spain

³ Postdoctoral Research Associate, Yale University, Chemical Engineering Dept., HTCRES Laboratory.

⁴ Professor of Chemical Engineering, Yale University, Chemical Engineering Dept.; Director, HTCRES Laboratory, to whom all inquiries concerning this research should be directed.

velocity, but the value of the thermophoretic diffusivity $\alpha_T D_p$ does not really depend on D_p (which, in fact, will be taken to be zero in our analysis). Talbot *et al.* (1980), presented an expression for $\alpha_T D_p$:

$$\alpha_{th} D_p = \frac{2c_s v \left(\frac{K_g}{K_p} + c_t \frac{l}{a} \right) \left[1 + \frac{l}{a} (A + B e^{-Ga/l}) \right]}{\left(1 + 3 c_m \frac{l}{a} \right) \left(1 + 2 \frac{K_g}{K_p} + 2c_t \frac{l}{a} \right)} \quad [2]$$

where K_g and K_p are the thermal conductivities of the gas and particle, respectively; l is the gas mean-free path, $l=2\bar{v}/\bar{c}$, with $\bar{c}=(8RT/\pi)^{1/2}$; a is the particle radius, $A=1.20$, $B=0.41$, $G=0.88$, and, for perfect accommodation between the particle and the gas molecules, $c_s=1.17$, $c_m=1.1$ and $c_t=2.18$; v is the gas kinematic viscosity.

Note that, in the limit of $K_p \geq K_g$ and $a \ll l$, Eq. [1.2] reduces to:

$$\alpha_{th} D_p \cong \frac{c_s v}{3c_m} (A + B) \cong 0.56 v$$

(the numerical factor in Waldmann's theory, 1961, is 0.54). This simple limiting case provides a first approximation for the magnitude of $\alpha_{th} D_p$, and motivates our introduction of $\alpha \equiv \alpha_{th} D_p / v$ in the analysis and examples which follow.

On the other hand, photophoresis takes into account the particle motion induced by the temperature gradient upon the particle surface originating from the nonuniform absorption of the radiant energy within the particle. The correspondent photophoretic velocity for an isolated particle can be written as

$$\vec{v}_{ph} = \alpha_{ph} D_p \frac{\vec{q}_R}{K_g T} \quad [3]$$

where $\alpha_{ph} D_{ph}$ is the photophoretic diffusivity and \vec{q}_R the radiative heat flux. Mackowski (1988) obtained an expression for \vec{v}_{ph} in the slip flow regime, resulting in

$$\alpha_{ph} D_p = -\frac{2c_s v \bar{J}_1}{3} \frac{1 + \frac{l}{a} (A + B e^{-Ga/l})}{\left(1 + 3 c_m \frac{l}{a} \right) \left(1 + 2c_t \frac{l}{a} + 2 \frac{K_g}{K_p} \right)} \quad [4]$$

whereas in the free molecular limit

$$\alpha_{ph} D_p = -0.14 v \bar{J}_1 \frac{a}{l} \quad [5]$$

\bar{J}_1 is the thermophoretic asymmetry factor and represents a weighted integration of the absorption of radiant energy over the particle volume. For spherical, homogeneous particles and monochromatic radiation, \bar{J}_1 can be obtained from Lorenz-Mie theory as a function of the particle radiative size parameter $\chi=2\pi a/\lambda$, where λ is the radiation wavelength, and the complex index of refraction $m=n+ik$. An exact, series-expansion expressions for \bar{J}_1 has been derived which is analogous to the expressions for the radiative cross sections (Mackowski, 1988). For spectrally-distributed radiation, \bar{J}_1 is obtained from integration over the wavelength distribution.

Realize that \bar{J}_1 can be positive or negative, leading to \bar{v}_{ph} directed either against or with the incident radiation direction. For radiation absorbed entirely on the particle surface, \bar{J}_1 attains a minimum value of -0.5 .

Underlying Assumptions

To simplify the problem without losing its essential features, the following defensible assumptions will be made:

- A1. The flow within the BL is steady and laminar. The usual BL approximations will be used and self-similarity will be assumed (see, *e.g.*, Schlichting, 1968).
- A2. The aerosol particles are very dilute so that the prevailing velocity and temperature field are not affected by their presence.
- A3. All thermophysical properties of the gas will be considered constant and equal to the values for the carrier gas at mainstream conditions. Transport properties for the dispersed aerosol will also be taken to be constant. Lastly, the system will be considered effectively incompressible, *i.e.*, the density will be assumed to be constant.
- A4. Aerosol particles do not appreciably Brownian diffuse. Therefore, at each position, the velocity of the particles is taken to be the gas velocity plus the thermophoretic and photophoretic velocities, with these velocities being those corresponding to an isolated particle in a uniform gas with the same temperature gradient and radiant energy flux. The direction of the radiative flux will be taken along the normal to the solid collecting surface.

We consider the two-dimensional stagnation point (Hiemenz) flow. This corresponds to a steady flow which arrives from the y -axis, impinges on a flat solid wall placed at $y=0$, where it divides into two streams near the wall, leaving in both (\pm) directions. The external (inviscid) velocity distribution in the neighborhood of the symmetrical forward stagnation "point" (at $x=y=0$) is given by (*e.g.* Schlichting, 1968):

$$u_e(x) = \left(\frac{du_e}{dx} \right)_{x=0} \cdot x \tag{6}$$

In the immediate vicinity of the solid wall, viscous (momentum diffusion) effects become important and, for a Newtonian fluid, the velocity field must satisfy the well-known two-dimensional BL equations:

$$u \frac{\partial u}{\partial x} + v \frac{\partial u}{\partial y} = u_e \frac{\partial u_e}{\partial x} + \nu \frac{\partial^2 u}{\partial y^2} \tag{7}$$

and

$$\frac{\partial u}{\partial x} + \frac{\partial v}{\partial y} = 0 \tag{8}$$

with boundary conditions: $u=0$ (no slip) and $v=0$ (no blowing) at $y=0$ and $u = u_e(x)$ at $y=\infty$.

Introducing the "stretched" dimensionless coordinate

$$\eta \equiv y \left[\frac{1}{\nu} \left(\frac{du_e}{dx} \right)_{x=0} \right]^{1/2} \quad [9]$$

and a stream function given by

$$\psi(x, y) = \left[\nu \left(\frac{du_e}{dx} \right)_{x=0} \right]^{1/2} \cdot f(\eta) \cdot x \quad [10]$$

the equation of local mass conservation [8] is automatically satisfied and the velocity components become

$$u = \frac{\partial \psi}{\partial y} = u_e(x) \cdot f'(\eta) \quad [11]$$

and

$$v = -\frac{\partial \psi}{\partial x} = - \left[\nu \left(\frac{du_e}{dx} \right)_{x=0} \right]^{1/2} \cdot f(\eta) \quad [12]$$

where above, and in what follows, primes denote differentiation with respect to η . Introducing these expressions into the x-momentum balance, equation [7], the following well-known nonlinear third-order (Blasius) ODE for $f(\eta)$ is obtained:

$$f''' + ff'' + [1 - (f')^2] = 0 \quad [13]$$

with the boundary conditions:

$$f = f' = 0 \quad @ \quad \eta = 0 \quad [14]$$

$$f' = 1 \quad @ \quad \eta = \infty \quad [15]$$

Notice that our assumptions of constant thermophysical properties and low mass loading allow $f(\eta)$ to be determined independently of the temperature and mass-fraction fields discussed below. Indeed, we will make use of the previous numerical computations of this well-known (Blasius) function (Schlichting, 1968).

Temperature Field

In the steady state, using laminar BL approximations A1, the PDE which governs the temperature distribution $T(x, y)$ is

$$u \frac{\partial T}{\partial x} + v \frac{\partial T}{\partial y} = \alpha_h \frac{\partial^2 T}{\partial y^2} \quad [16]$$

α_h being the heat (thermal) diffusivity. Defining

$$\theta \equiv \frac{T}{T_\infty} \quad [17]$$

when the wall temperature, T_w , is held constant, the ODE for $\theta(\eta)$ becomes

$$\theta'' + \text{Pr} \cdot f(\eta) \cdot \theta' = 0 \quad [18]$$

subject to the boundary conditions

$$\theta(\zeta) \equiv \theta_w = \frac{T_w}{T_\infty}, \quad \theta(\infty) = 1 \quad [19]$$

where Pr is the host gas Prandtl number, v/α_h . The solution can be written in the following quadrature form (e.g. Spalding & Evans, 1961):

$$\theta(\eta) = \theta_w + (1 - \theta_w) \cdot \frac{1}{\delta_T} \int_0^\eta \exp\left[-\text{Pr} \int_0^\xi f(\xi) d\xi\right] d\phi \quad [20]$$

where $f(\eta)$ is defined by [13]-[15] and

$$\delta_T \equiv \int_0^\infty \exp\left[-\text{Pr} \int_0^\xi f(\xi) d\xi\right] d\phi \quad [21]$$

For a description of the computation of δ_T see, for example, Castillo & Rosner (1988), Section 3.1. For $\text{Pr}=0.7$ (e.g. air) we find $\delta_T=2.01669$.

Particle Number Density

Now consider that in the mainstream there are $N_{p,\infty}$ particles per unit volume, each with the same radius⁵, a_∞ . In the absence of particle coagulation or break-up, the number density of particles N_p satisfies the equation

$$\text{div}(\vec{v}_p N_p) = 0 \quad [22]$$

Under assumption A4., the local particle velocity is given by

$$\vec{v}_p = \vec{v} + \vec{v}_{ph} + \vec{v}_{th} \quad [23]$$

with \vec{v}_{ph} and \vec{v}_{th} given by Eq.[3] and Eq.[1], respectively. Defining $n \equiv N_p/N_{p,\infty}$, the first ODE for n takes the simple form

$$A \frac{dn}{d\eta} + Bn = 0 \quad [24]$$

where we have introduced the dimensionless functions

$$A(\eta) \equiv f(\eta) + \frac{1}{\theta} \left(\beta + \alpha \frac{d\theta}{d\eta} \right) \quad [25]$$

$$B(\eta) \equiv \frac{d}{d\eta} \left(\frac{1}{\theta} \left(\beta + \alpha \frac{d\theta}{d\eta} \right) \right) \quad [26]$$

with

$$\alpha \equiv \frac{\alpha_{th} D_p}{v} \quad [27]$$

$$\beta \equiv -\frac{\alpha_{ph} D_p q R}{K_g T_\infty} \left[\left(\frac{du_e}{dx} \right)_{x=0} v \right]^{-1/2} \quad [28]$$

⁵ This assumption may easily be relaxed in order to deal with a distribution of particle sizes in the main stream.

The solution of Eq.[24], with boundary condition $n=1$ @ $\eta=\infty$, can be written in the form of a quadrature

$$n = \exp \left[\int_{\eta}^{\infty} \frac{B(\varphi)}{A(\varphi)} d\varphi \right] \quad [29]$$

The normal velocity of particles within the boundary layer is given by

$$v_p = v + v_{th} + v_{ph} = - \left[v \left(\frac{du_c}{dx} \right)_{x=0} \right]^{1/2} \left[f + \alpha \left(\frac{d \ln \theta}{d \eta} \right) + \frac{\beta}{\theta} \right] \quad [30]$$

which is negative for particles approaching the wall.

Under some circumstances, the particles do not arrive to the wall and a dust free region appears inside the boundary layer (Goren, 1977). The separation line between the region with particles and the dust free zone is located at the value of η where $v_p=0$; that is

$$A = f + \frac{1}{\theta} \left(\beta + \alpha \frac{d\theta}{d\eta} \right) = 0$$

When thermophoresis and photophoresis both push the particles away from the wall, that is, when $\theta_w > 1$ and $\beta < 0$, the dust free zone will exist for any value of β and θ_w and particles will not be collected by the solid surface. On the other hand, when both transport mechanisms compete in bringing particles towards the wall, the dust free zone exists only when

$$-\beta \geq \frac{\alpha}{\delta} (1 - \theta_w) \quad \text{for } \beta < 0 \quad \text{and } \theta_w < 1$$

or

$$\frac{\alpha}{\delta} (\theta_w - 1) \geq \beta \quad \text{for } \beta > 0 \quad \text{and } \theta_w > 1$$

Note that when both transport velocities oppose each other and are exactly equal, in modulus, at the wall (i.e., when the equal sign is verified in the above inequalities), the separation line coincides with the wall; that is, the deposition of particles vanishes even when the particles are everywhere inside the boundary layer. In this very particular case, however, some deposition will occur due to Brownian diffusion.

Anyway, here we are mainly interested in the cases when none of the above inequalities holds and deposition of particles takes place. When the particles arrive to the wall, the deposition rate of particles is given by

$$-N_w v_{p,w} = \left[v \left(\frac{du_c}{dx} \right)_{x=0} \right]^{1/2} N_{\infty} \frac{n_w}{\theta_w} \left[\beta + \frac{\alpha}{\delta} (1 - \theta_w) \right] \quad [31]$$

Thus, the dimensionless capture fraction, S , of particles will be

$$S \equiv \frac{-N_w v_{p,w}}{N_{\infty} \left[v \left(\frac{du_c}{dx} \right)_{x=0} \right]^{1/2}} = \frac{n_w}{\theta_w} \left[\beta + \frac{\alpha}{\delta} (1 - \theta_w) \right] \quad [32]$$

When we are interested in mass deposition rate instead of particle deposition, the relevant parameter is

$$J_m = \frac{1}{\rho \omega_\infty} \left[v \left(\frac{du_x}{dx} \right)_{x=0} \right]^{1/2} (-j_{m,w}) \quad [33]$$

where ω_∞ is the mass fraction of particles at mainstream and $(-j_{m,w})$ is the mass deposition rate at the wall. It is easy to see that $J_m=S$. When we consider the more practical case of a distribution of particle sizes at mainstream, the definition [33] is still valid, now with ω_∞ and $j_{m,w}$ taking into account the contribution of the different sizes. In that case, it results in

$$J_m = \frac{\int N_\infty(a) a^3 S(a) da}{\int N_\infty(a) a^3 da} \quad [34]$$

with $S(a)$ given by [32] and n_w , β and α being functions of the particle radius a .

Results for Simultaneous Photophoresis and Thermophoresis

Figure 1 represents the dimensionless capture fraction, S , as a function of the ratio T_w/T_∞ , for particles having a thermophoretic coefficient $\alpha=0.5$ (a value close to the free molecular limit). The line for $\beta=0$ corresponds to pure thermophoretic deposition with negligible photophoretic transport. In that case, particles are captured only by cold surfaces (*i.e.* when $T_w/T_\infty < 1$) and the deposition rate increases as the wall temperature decreases. When photophoresis helps to bring the particles towards the surface (*i.e.* when $\beta > 0$), it produces two effects: on one hand, it allows the capture of particles even for moderate hot surface ($T_w/T_\infty > 1$) and on the other hand it considerably increases the value of S for a given value of the ratio T_w/T_∞ . The opposite is true for negative values of β , the range of temperatures over which deposition occurs is diminished as well as the deposition rate for a given temperature. Analogous results are obtained for $\alpha=0.1$ (Figure 2) although the relative importance of photophoresis is higher. Thus, for $\beta=-10^{-1}$, no deposition occurs for the entire range of temperatures considered.

From Eq.[28], it can be seen that

$$\beta = \frac{1 - \theta_w}{\delta} \left(\frac{q_R}{q_F} \right) \alpha F^c$$

where q_F is the conductive (Fourier) heat flux at the solid surface, and F is the ratio v_{ph}/v_{th} computed for equal q_R and q_F . For particles in the slip-flow regime ($l/a < 1$), F can be expressed by

$$F = \frac{\bar{J}_1 K_g}{3 K_p \left(\frac{K_g}{K_p} + c_1 \frac{l}{a} \right)}$$

Numerical results of F for carbonaceous char and fly-ash particles exposed to a black body radiation spectrum at $T_{\text{Rad}}=1800\text{K}$ have been presented by Mackowski (1988) and are reproduced in Fig.3.

By using the above expression for β together with the values of F indicated in Fig.3, the deposition rate of char particles has been obtained and it is represented in Figure 4 for a fixed value of $T_w/T_\infty=0.7$ and different ratios of q_R/q_F . For vanishing radiative fluxes the larger char particles are more efficiently captured due to their larger thermophoretic coefficient α (obtained from Eq.[2]). When the radiative heat flux is directed from the solid surface towards the bulk (*i.e.*, when $q_R<0$), the char particles are rejected by photophoresis and the deposition rate decreases. For very large radiative fluxes, photophoresis precludes the capture of char particles larger than a given size.

It is evident from these illustrative examples that the combination of photophoresis and thermophoresis induces a change in the size distribution in the mainstream through the dependence of α and β on particle size. By an appropriate combination of radiative and conductive fluxes, particle sizes larger than a given value can be avoided in the deposit and, for particles which present an extremal in the function $F(a/l)$ (as it is the case for fly ash particles) only a narrow width of particle sizes can be selected to deposit.

References

- Castillo J.L., & Rosner D.E. (1988), "Theory of Surface Deposition from a Unary Dilute Vapor Containing Stream Allowing for Condensation within the Laminar Boundary Layer", *Chemical Engineering Science* (in press)
- Goren S.L. (1977), "Thermophoresis of Aerosol Particles into Laminar Boundary Layer on a Flat Plate", *J. Colloid Interface Science* **61**, pp.77-85
- Mackowski D.W. (1988), "Photophoresis of Aerosol Particles in the Free Molecular and Slip-Flow Regimes", *Int'l J. Heat Mass Transfer* (in press)
- Rosner D.E. (1980), "Thermal (Soret) Diffusion Effects on Interfacial Mass Transport Rates", *J. PhysicoChemical Hydrodynamics* **1**, pp.159-185
- Rosner D.E. (1985), "Mass Transfer across Gas Thermal Boundary Layers — Power Production and Materials Processing Implications", in *Heat Transfer in Fire and Combustion Systems*, HTD 45 (Law C.K. *et al.* eds.) ASME, N.Y.-N.Y., pp.3-8
- Rosner D.E. & Kim S.S. (1984), "Optical Experiments on Thermophoretically Augmented Submicron Particle Deposition from 'Dusty' High Temperature Gas Flows", *The Chemical Engineering J.* **29**, No.3, pp.147-157
- Schlichting H. (1968), *Boundary Layer Theory*, McGraw-Hill (6th ed.)
- Spalding D.B. & Evans M.L. (1961), "Mass Transfer through Laminar Boundary Layers — 3", *Int'l J. Heat Mass Transfer* **2**, pp.314-341
- Talbot L., Cheng R.K., Schefer R.W. & Willis D.R. (1980), "Thermophoresis of Particles in a Heated Boundary Layer", *J. Fluid Mechanics* **101**, pp.737-758
- Waldmann L. (1961), in *Rarefied Gas Dynamics* (Talbot L., ed.) Academic Press p.323

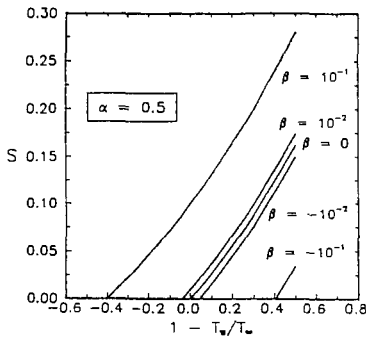


Figure 1. Dimensionless deposition rates S of particles as a function of $1-T_w/T_\infty$, for a constant thermophoretic coefficient $\alpha=0.5$ and different values of the photophoretic coefficient β .

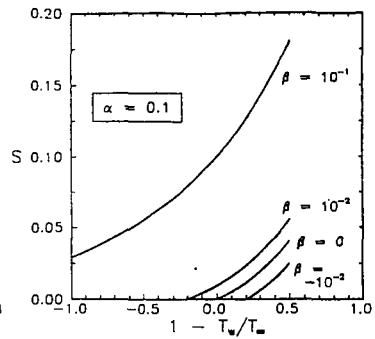


Figure 2. Dimensionless deposition rates S of particles as a function of $1-T_w/T_\infty$, for a constant thermophoretic coefficient $\alpha=0.1$ and different values of the photophoretic coefficient β .

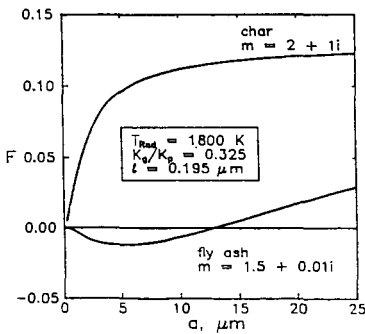


Figure 3. Photophoretic to thermophoretic velocity ratio for equal radiative and conductive heat flux, F , for carbonaceous char and fly-ash particles, as a function of particle radius. Radiation temperature $T_{Rad}=1800K$.

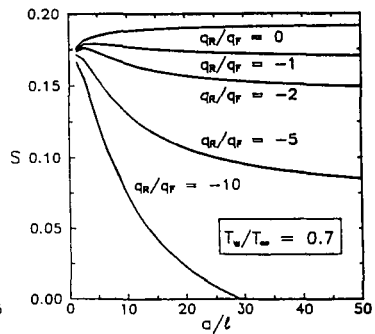


Figure 4. Dimensionless deposition rates S of char particles as a function of a/ℓ , for $T_w/T_\infty=0.7$ and different ratios of the radiative to conductive heat flux at the surface.

CHEMICAL AND ENERGETIC ASPECTS OF CVD DIAMOND GROWTH

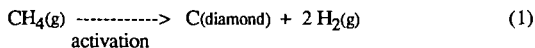
Karl E. Spear
Ceramic Science and Engineering
The Pennsylvania State University
University Park, PA 16802

INTRODUCTION

Excitement has emerged in both the scientific and industrial communities with the development of techniques for creating crystalline diamond films and coatings using low pressure gases rather than the high pressures and temperatures previously considered essential.(1) These developments have opened a new era in diamond technology and offer the potential for exploiting diamond's unique properties in applications ranging from coatings for cutting tools, to free standing windows and lense coatings for visible and infrared transmission, to thin films for high temperature, high power semiconductor devices.

Applications requiring advanced materials can uniquely utilize diamond because it (i) is the hardest known material, (ii) has the highest room temperature thermal conductivity of any material, (iii) is resistant to heat, acids, and radiation, (iv) is a good electrical insulator, but can be doped to produce either p-type or n-type semiconductors, (v) has a small dielectric constant, (vi) has a large hole mobility, and (vii) is transparent to visible and infrared radiation.(1) The high pressure-high temperature (HPHT) synthetic diamonds developed by General Electric in the 1950's (2) are now commonplace in cutting, grinding, and polishing, but many potential applications of diamond require thin films or coatings which cannot be produced from either natural or HPHT synthetic diamonds.

The diamond coating process which has generated the recent excitement utilizes temperature and pressure conditions under which graphite is clearly the stable form of carbon. However, kinetic factors allow crystalline diamond to be produced by a net chemical reaction of:



In addition to methane, a wide variety of carbon containing reactant gases can be used. The typical process consists of a reactant gas at less than atmospheric pressure which contains >95% hydrogen and is activated by passing it through a plasma or past an ~2000°C filament before contacting an 800-1000°C substrate on which the diamond is deposited.

Many questions must be answered concerning this deceptively simple looking "metastable" process before the potential of the new coating technology can be realized. Our understanding of the basic science must be extended far beyond our present knowledge, a challenge currently being met by laboratories around the world. The aim of this article is to summarize our current understanding of the chemical and energetic aspects of the growth processes for crystalline diamond.

CHEMICAL OBSERVATIONS

Many experimental observations concerning the activated vapor deposition of crystalline diamond have been made, particularly by Russian scientists Derjaguin, Fedoseev, Spitsyn, and co-workers. They have developed an extensive experimental base of chemical and kinetic information, and have proposed global kinetic theories for diamond growth based on nucleation theory, Langmuir adsorption-desorption kinetics, and equilibrium. Recent reviews in English give excellent summaries of this work.(1,3-5)

A major problem in growing high-quality diamond films is the co-deposition of graphitic-like carbon. Derjaguin and co-workers experimentally determined that the addition of excess hydrogen to the hydrocarbon precursor gas led to less graphite co-deposition with crystalline diamond, and that "activating"

the precursor gas prior to deposition increased the diamond growth rates from Å/hour to μm/hour. They activated the gas using either an electric discharge in the system, or a hot tungsten filament over which the gas flowed before encountering the lower temperature deposition region. A manifestation of the competition between the growth of diamond and graphite is the temperature dependence of the diamond growth rate which exhibits a maximum near 1000°C.

Derjaguin and Fedoseev(6) made a major breakthrough in determining that atomic hydrogen is critical to achieving appreciable growth rates for crystalline diamond, and proposed that a super-equilibrium concentration of atomic hydrogen at the growth surface is responsible for the major reduction in graphite co-deposition. They argue that atomic hydrogen behaves like a 'solvent' for graphite. Their studies of the relative etching rates of diamond and graphite showed that the removal of graphite by 'activated' hydrogen was orders of magnitude faster than diamond. Setaka(7) recently reported etching rates of graphite, glassy carbon, and diamond in a hydrogen plasma under typical diamond growth conditions. In units of mg/cm²-hr, his values are 0.13 for graphite, 0.11 for glassy carbon, and 0.006 for diamond. Saito et al.(8) also showed much greater etching rates for graphite than diamond when subjecting the materials to microwave plasmas of either hydrogen, or hydrogen-1.6% water mixtures.

Derjaguin and co-workers also observed that the nature of the precursor hydrocarbon gas had little effect on the deposition behavior. Sato et al.(9) have grown diamond from gaseous mixtures of various hydrocarbons and hydrogen by plasma-assisted deposition and found similar results. Both saturated and unsaturated hydrocarbons were used, and similar growth features were noted for all the hydrocarbons when comparisons were made as a function of the C/H ratio in the input gas. The density of nucleation and the growth rates were found to be essentially the same as those observed with the more commonly used methane. Crystalline diamond has been grown using aliphatic and aromatic hydrocarbons as well as alcohols and ketones. Small amounts of O₂ added to the precursor gas accelerates the growth rate of diamond films. Diamond can also be grown from hydrogen / hydrocarbon gas mixtures which contain larger amounts of oxygen (as in an oxygen-acetylene flame).

The relative independence of diamond growth on the nature of the input hydrocarbon species is consistent with the fact that most hydrocarbon sources tend to chemically transform to common product species (such as acetylene, one of the most stable of such gaseous products) under harsh environments such as those found in high temperature pyrolysis(10,11), combustion(12), plasmas(13), and the other typical methods used for activating precursor gases in diamond deposition. Good quality diamond films have been produced under a variety of different activation methods: microwave-, rf-, uv-, laser-, and hot-filament activated gas mixtures.(1) Approximately the same growth conditions (temperature, pressure, concentrations of precursors) are needed for crystalline diamond growth, regardless of the method of activation. The method of activation influences the rate of diamond growth, but not the general structure of the deposited crystallites.

A number of ongoing spectroscopic studies of activated methane-hydrogen gas mixtures under diamond film growth conditions indicate a predominance of acetylene and methyl radical growth species. One such study by Celii et al.(14) reported *in situ* infrared diode laser absorption spectroscopy results obtained from examinations of gas phase species present during hot-filament assisted deposition of diamond films; another by Harris et al.(15) reported mass spectra investigations in a hot-filament assisted diamond growth system as a function of filament-to-substrate distance. The initial analysis of these latter authors suggests that diamond growth comes mainly from acetylene and/or methyl radical precursors, but contributions from methane and ethylene cannot be ruled out.

ENERGETICS OF GAS-SOLID GROWTH INTERFACE

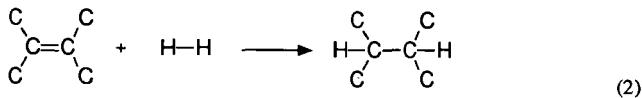
The pressure vs. temperature phase diagram for carbon given in Figure 1 clearly shows that graphite is the stable form of carbon under the conditions used for vapor depositing crystalline diamond. Why is it then possible to grow diamond at 750-1100°C and less than atmospheric pressure?

Although an established mechanistic answer is not yet available for the above question, one that is consistent with reported experimental facts can be given(16). The heart of this hypothesis on "metastable" diamond growth rests on the fact that the diamond growth process occurs at the gas-solid interface in the carbon-hydrogen system. The vapor growth process does not involve just elemental carbon, the one component which is represented on the phase diagram, but it also involves hydrogen. A diamond carbon surface saturated with sp^3 C-H bonds is more stable than a carbon surface free of hydrogen. Once a surface carbon is covered by another diamond growth layer, then that covered carbon possessing four sp^3 C-C bonds is metastable with respect to a graphitic carbon. Thus, an upper temperature limit for the vapor growth of diamond is determined by the kinetics of the diamond-to-graphite solid state transformation (and how these kinetics are influenced by structural imperfections).

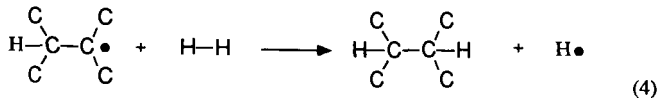
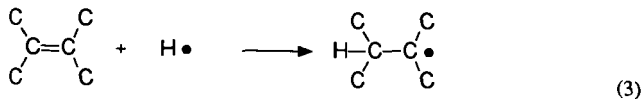
The close relationship between the diamond and graphite crystal structures is depicted in Figure 2. The puckered {111} planes of diamond are shaded to emphasize their relationship to the {001} planes of graphite. Hydrogen atoms are shown as satisfying the "dangling sp^3 bonds" of the carbons on the top diamond plane. Without the hydrogens maintaining the sp^3 character of these surface carbons, it is easy to imagine the {111} diamond planes collapsing into the more stable planar graphite structure during the growth process. In fact, in the absence of hydrogen, it is well known that the surface atoms on cleaned bulk diamond crystals will reconstruct from their bulk-related surface sites at about 900-1000°C. However, in hydrogen, the surface sp^3 bonds are satisfied by C-H bonding.(17-20)

The question then arises as to why earlier thermal CVD studies utilizing hydrogen-methane mixtures for epitaxial growth on diamond surfaces were of very limited success [see, for example, Angus et al.(21)]. The pressure-temperature-composition conditions used by these earlier researchers were quite similar to those currently used for the successful activated vapor growth of crystalline diamond, but the primary deposition product was always graphitic-like carbon in these early studies.

The net saturation of a C=C double bond with hydrogen



yields a favorable negative enthalpy change, $\Delta H^0(\text{reaction}) = -126$ kJ. However, an activation energy to produce either a carbon or a hydrogen radical will be required to get the net reaction to proceed at a significant rate. Likely mechanistic radical reactions are



where a hydrogen radical attacks the C=C double bond to produce a carbon radical, which then reacts with a hydrogen molecule to complete the saturation and regenerate a hydrogen radical. This is in agreement with the fact that only when gas activated deposition methods were first employed in the 1970's did the growth rates of crystalline diamond become large enough to be of technological interest.

As was mentioned in the section on the chemistry of diamond growth, atomic hydrogen etches sp^2 graphitic carbon at a much higher rate than it etches sp^3 diamond carbons. Thus, the source of hydrogen

atoms can serve the dual role of hindering graphite growth as well as etching away any that does nucleate on the growing diamond surface.

The thermodynamics of the deposition process may place a lower limit on the deposition temperature for a given total pressures and gas concentration. Without some type of surface activation such as bombardment, the surface reactions for deposition may approach their thermal equilibrium limits. The fact that faceted diamond crystals are produced during deposition is a typical indication that surface mobilities are large enough for surface reactions to reach equilibrium. Which reactions reach their equilibrium limits, and which ones are kinetically limited is still an open question, but it is still of value to consider the thermodynamic limits for the deposition process.

Two plots of the output of equilibrium calculations are shown in Figure 3 to illustrate how the deposition limits depend on experimental parameters.(16) Such calculations have also been made by Bichler et al.(22) and Sommer et al.(23) The fraction of carbon deposited from methane-hydrogen mixtures is plotted versus temperature for several pressures and compositions. Two important observations can be made:

- (1) The fraction of carbon deposited changes from practically zero at lower temperatures to close to 100% over two hundred degrees.
- (2) High pressures and/or low methane concentrations increase the lower temperature limit required to obtain any deposit.

Thus, thermodynamic considerations set a lower temperature limit on diamond growth of about 400 – 600°C, depending on specific pressure–composition conditions, unless “non–equilibrium” bombardment techniques are used. These latter techniques always produce some diamond-like carbon (DLC), or similar highly defective form of carbon, along with crystalline or microcrystalline diamond.

Not shown on the above plots is the fact that the elemental gaseous carbon species of C, C₃, C₅, etc. have negligible partial pressures at about 2000°C and lower. Also, at 2000°C, a typical temperature for the filament in the hot-filament-activated systems, the quantity of atomic hydrogen in equilibrium with about 10 torr of molecular hydrogen is close to 7 at. %, an appreciable amount to interact at the 800–1000°C substrate temperature.

CONCLUDING REMARKS

Under the temperature-pressure conditions used for the growth of diamond from the vapor, graphite is clearly the most stable form of carbon. However, the energy differences between depositing diamond and graphite are quite small, so kinetic factors will determine which solid phase is deposited in the carbon-hydrogen system. Even so, energetic arguments are still important in explaining the experimental observations.

At the solid-gas interface where the diamond nucleation and growth processes are occurring, a diamond surface with hydrogens satisfying the “dangling” sp³ carbon bonds is energetically more favorable than a graphite surface. If diamond forms during deposition, and its surface is adequately saturated with sp³ C-H bonds, then graphite can subsequently form only through a solid state transformation, which is kinetically unfavorable until temperatures greater than ~1600°C are reached. If graphite forms during the deposition process, atomic hydrogen can saturate the C=C double bonds to produce a diamond surface with sp³ carbons, or it can preferentially remove the graphite through a chemical etching process. Without the presence of atomic hydrogen, the rates of saturating surface C=C bonds and the rates of graphite etching are slow compared to the solid carbon deposition, so graphitic-like carbon may dominate the process. This delicate balance between deposition rate and the concentration of atomic hydrogen has not yet been quantitatively measured.

The role of atomic hydrogen in the etching of graphitic-like carbon may be shifted to oxygen in systems containing appreciable amounts of this element, such as in the growth of diamonds from flames.

However, oxygen will probably not be important in stabilizing a diamond surface by saturating the "dangling" sp^3 carbon bonds on such a surface. The experimental and theoretical expertise which has evolved over the years in the area of combustion chemistry is clearly needed to develop quantitative models for the growth of diamond from C-H-O vapor systems.

ACKNOWLEDGMENTS

This research was sponsored by the Office of Naval Research, contracts #N00014-86-K-0283 and #N00014-86-K-0443.

REFERENCES

- (1) Karl E. Spear, *J. Am. Cer. Soc.* (review article to be published Feb. 1989)
- (2) F.P. Bundy, H.T. Hall, H.M. Strong, and R.J. Wentorf, Jr. *Nature*, **1955**, 176, 51.
- (3) D.V. Fedoseev, V.P. Varnin, and B.V. Derjaguin, "Synthesis of Diamond in Its Thermodynamic Metastability Region," *Russ. Chem. Rev.*, **1984**, 53(5), 435.
- (4) A.R. Badzian and R.C. DeVries, *Mat. Res. Bull.*, **1988**, 23, 385.
- (5) J.C. Angus and C.C. Hayman, *Science*, **1988**, 241, 913.
- (6) B.V. Derjaguin and D.V. Fedoseev, *Growth of Diamond and Graphite from the Gas Phase*, Izd. Nauka, Moscow (1977).
- (7) N. Setaka, *Chemical Vapor Deposition 1987*, Proc. Tenth Internat. Conf. on Chemical Vapor Deposition (G.W. Cullen and J. Blocher, Jr., eds.) Electrochem. Soc., Pennington, NJ, (1987), p. 1156.
- (8) Y. Saito, K. Sato, H. Tanaka, K. Fujita, and S. Matsuda, *J. Mater. Sci.*, **1988**, 23, 842.
- (9) Y. Sato, M. Kamo, and N. Setaka, *Proc. 8th Internat. Sympos. Plasma Chem.* Vol. 1 (K. Akashi and A. Kinbara, eds.), Tokyo, Aug. 31-Sept. 4, 1987, p. 2446.
- (10) R.E. Duff and S.H. Bauer, *J. Chem. Phys.*, **1962**, 36, 1754.
- (11) S.C. Khandelwal and G.B. Skinner, in *Shock Waves in Chemistry* (A. Lifshitz, ed.) Marcell Dekker, NY (1981), p. 1.
- (12) I. Glassman, *Combustion*, 2nd ed., Academic Press, NY (1987).
- (13) H.V. Boenig, Chapt. 4 in *Plasma Science and Technology*, Cornell University Press, Ithaca, NY (1982), p. 75.
- (14) F.G. Celii, P.E. Pehrsson, H.T. Wang and J.E. Butler, *Appl. Phys. Lett.*, **1988**, 52(24), 2043.
- (15) S.J. Harris, A.M. Weiner, and T.A. Perry, *Appl. Phys. Lett.*, **1988**, 53, 1605.
- (16) K.E. Spear, M. Frenklach, A. Badzian, T. Badzian, and R. Messier, *Ceram. Eng. Sci. Proc.*, **1988**, 9(9-10), 1095.
- (17) A.R. Badzian, in *Advances in X-Ray Analysis*, Vol. 31 (C.S. Barrett, J.V. Gilfrich, R. Jenkins, J.C. Russ, J.W. Richardson, and P.K. Predecki, eds.) Plenum Publishing Corp. New York (1988), p. 113.
- (18) J.M. Thomas, in *The Properties of Diamond*, (J.E. Field, ed.) Academic Press, New York, (1979), p. 211.
- (19) K.C. Pandey, *Phys. Rev.*, **1982**, B25, 4338.
- (20) B.B. Pate, *Surface Science*, **1986**, 165, 83.
- (21) J.C. Angus, H.A. Will, and W.S. Stanko, *J. Appl. Phys.*, **1968**, 39, 2915.
- (22) R. Bichler, R. Haubner, and B. Lux, *Proc. 6th European CVD Conf.*, Jerusalem (1987), p. 413.
- (23) M. Sommer, K. Mui, and F.W. Smith, presented at the *SDIO/IST - ONR Diamond Technology Initiative Symposium*, Crystal City, VA, July 12-14, 1988.

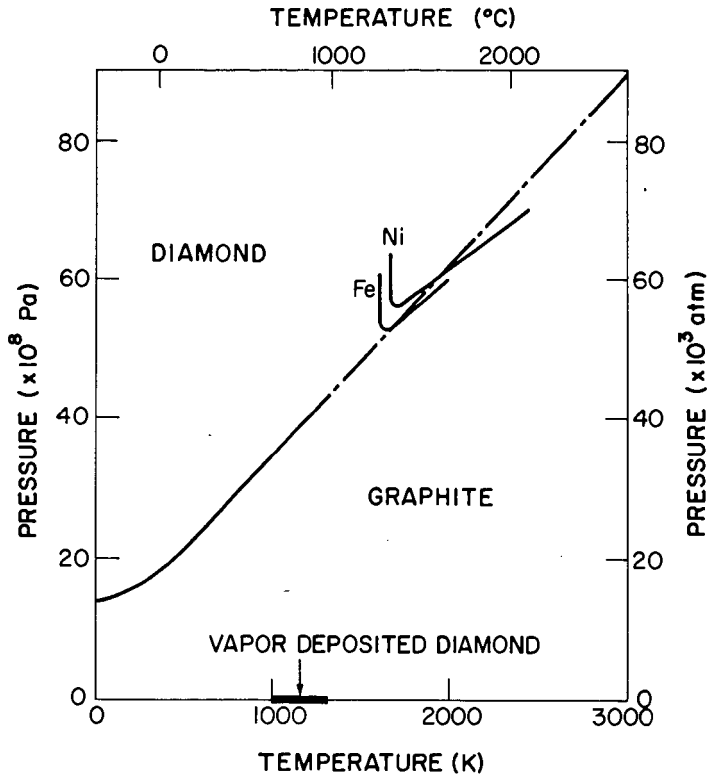
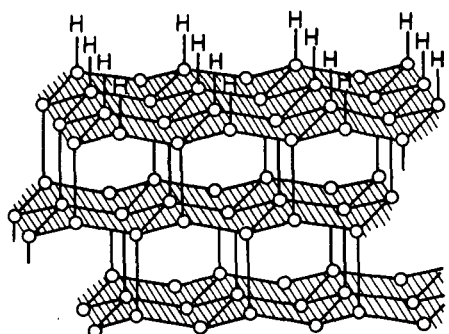
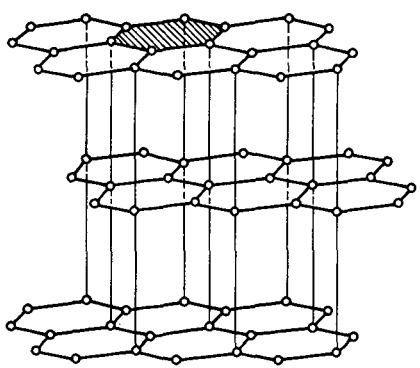


Figure 1: Pressure vs Temperature Phase Diagram for Carbon . The lines labeled with metallic elements denote the high pressure-high temperature (HPHT) conditions utilized for diamond growth using metallic solvents.



DIAMOND



GRAPHITE

Figure 2: Schematic Diagrams Showing the Similarities in the Crystal Structures of Diamond and Graphite. The hydrogen atoms bonded to the surface carbons depict their role in stabilizing the diamond surface structure.

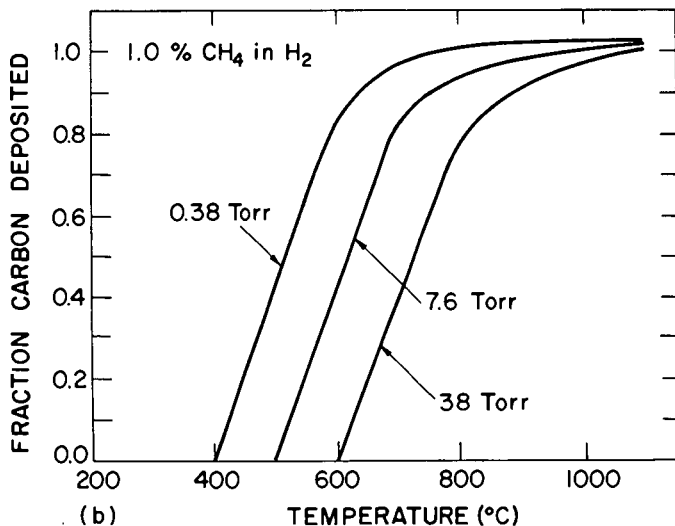
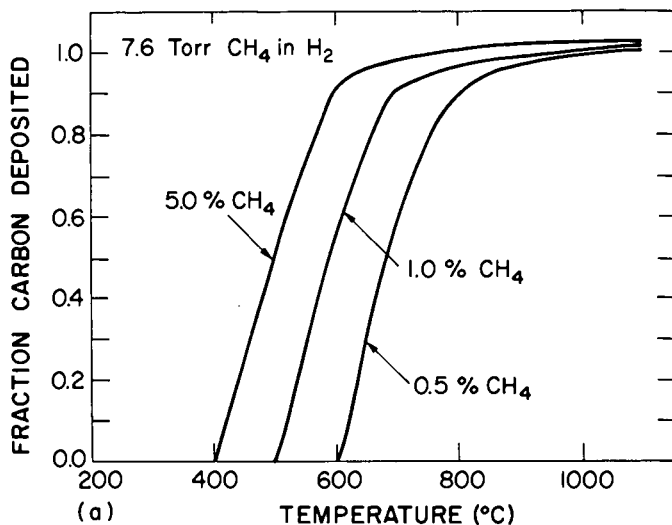


Figure 3: Equilibrium Plots of the Fraction Carbon Deposited from Methane/Hydrogen Mixtures as a Function of Temperature. (a) Constant total pressure, varying CH₄ content in reactant gas (b) Constant CH₄ content, varying total pressure.

DIAMOND SYNTHESIS IN FLAMES

L. M. Hanssen, W. A. Carrington*,
D. Oakes^A, J. E. Butler^T, and K. A. Snail
Code 6522, Optical Sciences Division
Naval Research Laboratory
Washington, D.C. 20375-5000

INTRODUCTION

The synthesis of diamond in an atmospheric pressure flame was first reported by Hirose and Kondo¹ in March, 1988. The conditions leading to diamond growth were given as an oxygen/acetylene flow ratio of 1.5/2, a substrate temperature of 1000°C, and a Si substrate positioned in the 'inner' or acetylene feather region of the flame. Slower diamond growth was also observed in a hydrogen-methane flame with a filament. More recently, Hirose and Mitsuizumi² have reported growing diamond with acetylene, ethylene, methane, propane, methanol and ethanol gases burned in air when mixed with either hydrogen or oxygen. Growth was achieved on Si, SiC, Al₂O₃, W, WC, and Mo substrates in an oxygen-acetylene flame, and maximum growth rates of 200 μm/hr for particles² and 100-150 μm/hr for films³ were reported. The effects of varying key parameters on diamond growth were not discussed in these reports.

In the U.S., Hanssen et al.⁴ studied the effect of substrate position, fuel/oxidizer gas flow ratio, and substrate temperature on diamond growth in a premixed oxygen-acetylene flame, and observed growth on Si(100), Si(111), BN, Mo(100), Nb(100), TiC(100), Ta and Cu. Carrington et al.⁵ reported diamond growth on Si(100) in an oxygen-ethylene flame. Yarbrough⁶ confirmed the growth of diamond in an oxygen-acetylene flame at atmospheric pressure. Snail et al.⁷ observed diamond growth in an oxygen-ethane flame, studied the uniformity of diamond crystallite growth as a function of position in an oxygen-acetylene flame, and reported that adding hydrogen to an oxygen-acetylene flame increased the ratio of the (diamond / amorphous carbon) Raman peaks. Recently Yarbrough observed diamond growth in a low pressure (25 torr) oxygen-acetylene flame.⁸

The next section of this paper discusses the experimental apparatus used at the Naval Research Laboratory (NRL) to study diamond synthesis in flames. Following that, a partial review of the results obtained at NRL on the flame synthesis of diamond is given. The results of several other studies currently in progress will be presented at the meeting.

EXPERIMENTAL SETUP

An oxygen-acetylene brazing torch (see Fig. 1) fitted with a .89 mm orifice tip was used to deposit diamond crystallites and films. The torch was mounted on an xyz translation stage and the gas flow rates were adjusted with mass flow controllers. Substrates were mounted on a water cooled copper block and a two color near infrared pyrometer was used to monitor the peak substrate temperature from 650°C to 1200°C. A more detailed description of this setup can be found in Ref. 4.

Most of the depositions reported on in this paper were grown on Si(100) substrates which were prepared by scratching with 5-6 micron diamond paste, and ultrasonic cleaning in acetone and methanol. A typical deposition lasted for 10-15 minutes. During depositions the torch was operated in a fuel rich mode and the substrates were positioned in the first diffusion flame (or 'acetylene feather') beyond the premixed flame front.

The substrate temperature distribution was monitored during depositions with a thermal (8-12 μm) imaging camera having a spatial resolution on the substrate of $\sim 1/3$ mm (3 mrad). During several long (2-4 hours) depositions, a zoom microscope (10-70x) with a video camera attachment was used to record the changes in crystallite morphology with time. Square faced (100) diamond crystallites with up to 350 micron sized edges have been grown during these longer depositions, using an oxygen-acetylene flame.

RESULTS AND DISCUSSION

In the first subsection of this section, the oxygen/acetylene flow ratios and substrate temperatures which lead to the growth of faceted diamond crystallites, micro-crystalline graphite and amorphous carbon (a-C) are reviewed. Adding hydrogen to an oxygen-acetylene flame is then discussed in terms of its effect on the a-C contributions to the crystallite's Raman spectra and the crystallite morphology. Finally, the variation in diamond crystallite growth with position in a premixed oxygen-acetylene flame is analyzed.

Process parameters - material property relationships

A detailed mapping of the type of material deposited versus the substrate temperature and fuel/oxidizer flow ratio has been performed for an oxygen-acetylene flame. The ($\text{O}_2/\text{C}_2\text{H}_2$) flow ratio, R, was varied from 0.8 to 1.5; this corresponds to a range of equivalence ratios⁹ of 3.13 - 1.67, respectively. The total gas flow rate was ~ 2.3 slm and the substrate was positioned 1-2 mm below the inner flame tip. The substrate temperature was varied from 650°C to 1200°C. The deposited material was analyzed with an optical microscope, a field emission scanning electron microscope (SEM), and also by x-ray diffraction (XRD) and Raman spectroscopy. Raman spectra were taken with a 5145 Å laser excitation and ~ 30 mm spot size. The Raman data discussed in the next two subsections were taken with ~ 1 mm spot size using a micro-Raman accessory.

As in the case of the low pressure CVD processes, well faceted crystallite growth occurs when the substrate is near 900°C. For the torch nozzle and total flow rates used, these studies indicate that for flow ratios less than 0.9, ball-like structures (see Fig. 2a, Ref. 4) grow at all substrate temperatures. For values of R between 0.9 and 1.2, well faceted crystallites grow (see Fig 2b, Ref. 4). The temperature range for which crystallite growth occurs expands from near 900°C at R = 0.9 to 650°C - 1050°C at R = 1.2. Above and below this temperature range, ball-like structure growth occurs. For R greater than 1.15, the growth rate decreases rapidly with increasing values of R so that at R = 1.2 the growth rate is very low and at 1.3 and 1.4 growth does not occur.

The variation of material morphology with substrate temperature and oxygen/acetylene ratio encompasses three distinct regions corresponding to the growth of faceted crystallites and ball-like structures, and no growth. The boundary between the ball-like structure and crystallite regions exhibits a gradual transition in particle morphology from faceted crystallites to ball-like particles. For an example of a transitional structure see Fig. 2d of Ref. 4. The diamond Raman peak at 1332 cm^{-1} is seen in the spectra of some ball-like structures and indicates that the ball-like structures can contain diamond. This suggests that measurements of the growth rates of different materials (diamond, graphite, a-C) versus the substrate temperature and oxygen/acetylene flow ratio are needed. The Raman spectra of both ball-like structures and faceted crystallites grown in an oxygen-ethylene flame also exhibited coexisting peaks due to different forms of carbon⁵.

The ball-like structures grown with R > 0.9 at substrate temperatures above those delineating the ball-crystallite boundary exhibited strong Raman peaks at 1355 cm^{-1} and 1575 cm^{-1} associated with micro-crystalline and crystalline graphite, respectively¹⁰. These peaks were also observed for ball-like structures grown at R < 0.9. Ball-like structures grown with R > 0.9 at substrate temperatures below those delineating the crystallite-ball boundary exhibited a high fluorescence background. This suggests that the region of ball-like growth may have to be further subdivided.

Hydrogen-oxygen-acetylene flames

The effect on diamond growth of adding hydrogen to an oxygen-acetylene flame was studied for two cases: first, with the $(\text{O}_2/\text{C}_2\text{H}_2)$ flow ratio fixed at 1.12, and hydrogen added to the flame, and second, with the $[\text{O}_2/(\text{C}_2\text{H}_2 + \text{H}_2)]$ flow ratio fixed at 1.12, and hydrogen substituted for acetylene. In both cases the oxygen flow rate was fixed at 1.7 slm. The total flow rate for the hydrogen addition study ranged from 3.2 slm to 4.0 slm. In the case where the $(\text{O}_2/\text{C}_2\text{H}_2)$ flow ratio was fixed, hydrogen was added so that the $(\text{H}_2/\text{C}_2\text{H}_2)$ flow ratio equalled 0.0-0.50. Most samples had an annular region of heavy crystallite nucleation; Raman spectra were taken at the inner and outer edges of the annuli, and growth center of each sample.

The ratio of the diamond to the amorphous carbon Raman peaks (R_{DC}) of individual crystallites is plotted in Figure 2 versus the $(\text{H}_2/\text{C}_2\text{H}_2)$ flow ratio for the three different positions on the samples. The R_{DC} ratio is essentially constant for crystallites located in the same local region of the sample. These results show a nearly linear increase in R_{DC} with increasing hydrogen flow rate, although the diamond growth rate decreased significantly as the $(\text{H}_2/\text{C}_2\text{H}_2)$ flow ratio exceeded 0.25. For a $(\text{H}_2/\text{C}_2\text{H}_2)$ flow ratio equal to 0.45, no growth is observed. When the $[\text{O}_2/(\text{H}_2 + \text{C}_2\text{H}_2)]$ flow ratio is fixed, substituting hydrogen for acetylene leads to an increase in R_{DC} for $(\text{H}_2/\text{C}_2\text{H}_2)$ flow ratios up to 0.02. No diamond growth is observed for $(\text{H}_2/\text{C}_2\text{H}_2)$ flow ratios equal to or greater than 5/95. This data suggests that oxygen is preferentially burning with acetylene, rather than hydrogen.

Variation of growth with position in flame

The nucleation density of crystallites deposited in an oxygen-acetylene flame was frequently higher within an annular region, and lower in other regions on the substrate. The causes of this nonuniform growth include both temperature inhomogeneities and species concentration variations. A thermal (8-12 μm) imaging camera having a spatial resolution on the substrate of $\sim 1/3$ mm (3 mrad) was used to measure substrate temperature profiles. During a typical deposition on a Si substrate in an oxygen-acetylene flame the substrate temperature profile exhibited large decrease with increasing distance from the center of the growth. For a substrate to flame front distance (D) of 4.5 mm, the temperature decrease observed from the center to edge of the diamond growth region was approximately 250°C.

The variation in diamond growth with position in the acetylene diffusion flame was studied with an oxygen flow rate of 1.7 slm and an acetylene flow rate of 1.5 slm, and is illustrated in Figure 3. When the distance (D) from the substrate to the oxygen-acetylene flame front was 3.0-4.5 (± 0.5) mm, the resulting nucleation density of diamond crystallites was low directly beneath the flame axis and significantly higher within an annulus centered on the flame axis. The outer edge of this annulus occurred where the edge of the acetylene diffusion flame intersected the substrate. As D was increased to 7.5 mm, the nucleation density increased on the region of the substrate directly under the flame axis and the annular pattern of crystallites disappeared. Growth areal density was estimated by counting crystallites in 3600 mm^2 areas using an 800X optical microscope. A weighting factor was assigned for crystallites less than 50% of the mean size in a region; the typical crystallite size ranged from 1-11 microns.

An SEM and micro-Raman study of the spatial variation of diamond crystallite quality was performed on a sample grown in an oxygen-acetylene-hydrogen flame. For this sample, the $(\text{O}_2/\text{C}_2\text{H}_2)$ flow ratio was equal to 1.12, the $(\text{H}_2/\text{C}_2\text{H}_2)$ flow ratio was set at 0.10, and the peak substrate temperature ranged from 910-960°C. The substrate was positioned 4.5 mm below the premixed flame front. Individual crystallites showed a significant decrease in the ratio (R_{DC}) of the 1332 cm^{-1} diamond Raman peak to the 1510 cm^{-1} amorphous carbon peak with increasing distance from the growth center. This variation is exhibited in Figure 4. Crystallites outside of the annular region (extending from 0.7-2.7 mm) exhibited a small increase in R_{DC} compared to those in the annulus. Electron and optical microscope analyses showed a correlation of the decrease of R_{DC} across the annular growth region with the degree of secondary growth observed on the diamond crystallite faces. Significant secondary growth was observed on crystallites in the annular growth region while 'cleaner' better formed crystallites were observed inside and outside of the annulus.

The Raman spectra of all crystallites exhibited a fluorescent background signal level which increased with the wavelength shift up to 1650 cm^{-1} , which was the limit of the measurements; this background level increased as the crystallites' distance from the growth center increased.

CONCLUSIONS AND FUTURE DIRECTIONS

These results demonstrate that diamond can be grown at atmospheric pressure in premixed oxygen-hydrocarbon flames on a variety of substrates. Growth in oxygen-acetylene flames occurs throughout the first diffusion flame beyond the premixed flame front, for acetylene rich flames. The type of material grown (diamond, graphite, a-C) in an oxygen-acetylene flame depends on the substrate temperature and oxygen/acetylene flow ratio. The ranges of the parameters found to lead to diamond crystallite growth are: 1) substrate temperatures, $T = 650$ to 1050°C , and 2) gas flow ratios, $R = 0.9$ to 1.2 for a total flow rate of ~ 2 - 3 slm (the appropriate flow rate is strongly dependent on the nozzle used). The "cleanest" crystallites were grown at $T = 950^\circ\text{C}$, and $R = 1.13$.

The addition of hydrogen to an oxygen-acetylene flame produces significant improvements in the diamond to amorphous carbon Raman peak ratio of the deposited crystallites. For an initial ($\text{O}_2/\text{C}_2\text{H}_2$) flow ratio of 1.12, a significant decrease in crystallite growth rate occurs for ($\text{H}_2/\text{C}_2\text{H}_2$) flow ratios greater than 0.24 when hydrogen is added to the flame, and 0.02 when hydrogen is substituted for acetylene. For flames from a single orifice, the diamond crystallite growth density and quality can vary significantly with the position of the substrate in the flame. These variations are probably caused by variations in chemical species, which are known to vary significantly with position in 2d flames.

Several techniques for controlling and reducing the nonuniformities in the substrate temperature are currently under investigation. These include a mount with both heating and cooling capabilities, and using liquid metals to improve the thermal contact between the substrate and the mount. A microtube flat flame burner is currently being fabricated¹¹. This burner is expected to produce flame temperatures that are uniform to $\pm 50^\circ\text{C}$ over a 1 cm diameter disk. Several other 2d and 1d burner designs are also being studied. The nonuniform flame structure associated with single orifice flames offers an opportunity to identify the chemical species responsible for diamond growth.

* Dept. of Electrical Engineering, Thornton Hall, University of Virginia, Charlottesville, VA. 22906

^ Office of Naval Technology Postdoctoral Fellow

† Chemistry Division, Code 6174, Naval Research Laboratory, Washington, DC 20375-5000

- 1 Y. Hirose and N. Kondo, Program and Book of Abstracts, Japan Applied Physics Spring 1988 meeting, March 29, 1988, p. 434
- 2 Y. Hirose and M. Mitsuizumi, *New Diamond* 4, 34 (1988).
- 3 Y. Hirose, "Synthesis of diamond using combustion flame in the atmosphere", Program and Abstracts Book, 1st Intl. Conf. on New Diamond Science and Tech., Oct. 24-26, 1988 (Tokyo), p. 38.
- 4 L. M. Hanssen, W. A. Carrington, J. E. Butler and K. A. Snail, "Diamond synthesis using an oxygen-acetylene torch", to be published in *Mats. Ltrs.*, Dec. 1988 or Jan. 1989.
- 5 W. A. Carrington, L. M. Hanssen, K. A. Snail, D. B. Oakes, and J. E. Butler, "Diamond growth in $\text{O}_2 + \text{C}_2\text{H}_4$ and $\text{O}_2 + \text{C}_2\text{H}_2$ flames", accepted for publication in *Metal. Trans. A*, Sept., 1988.
- 6 W. Yarbrough, presentation at the Conf. on High Performance Inorganic Thin Film Coatings, Gorham Inst. for Adv. Mats., Monterey Beach, Monterey, CA., (Oct. 1988).

⁷K. A. Snail, L. M. Hanssen, W. A. Carrington, D. B. Oakes, and J. E. Butler, "Diamond growth in combustion flames", Program and Abstracts Book, 1st Intl. Conf. on New Diamond Science and Tech., Oct. 24-26, 1988 (Tokyo), p. 142.

⁸Personal communication with W. Yarbrough, December 1988.

⁹The equivalence ratio is defined as the actual fuel:oxidizer ratio divided by the fuel:oxidizer ratio corresponding to complete combustion to carbon dioxide and water.

¹⁰F. Tuinstra and J. L. Koenig, J. Chem. Phys. **53**, 1126 (1970).

¹¹Research Technologies, P.O. Box 384, Pleasanton, CA. 94566

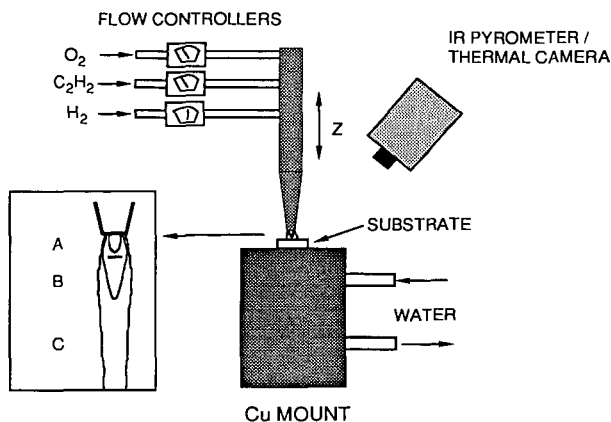


Figure 1: Schematic of the oxy-acetylene torch deposition experiment. The inset is an expanded view of the oxygen-acetylene flame. The three regions described in the text are: A) the inner cone, B) the acetylene feather, and C) the outer flame. For diamond growth, the substrate is positioned inside the acetylene feather region.

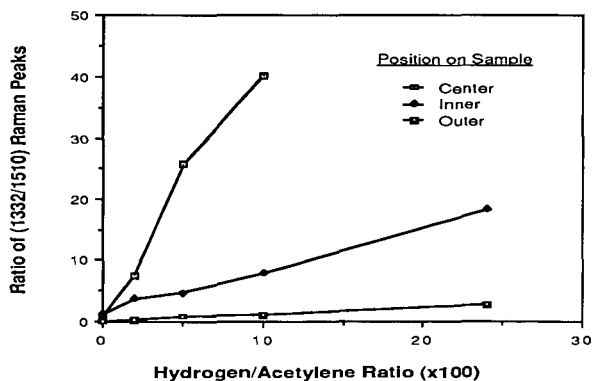


Figure 2: Ratio of the diamond Raman peak (1332 cm^{-1}) to the amorphous carbon peak (1510 cm^{-1}), for different hydrogen flow rates added to an oxygen-acetylene flame with $R = 1.12$. Data for the growth center of the sample, and the inner and outer edges of the growth annulus are shown. Note the monotonic increase in crystal quality with increasing hydrogen flow rate.

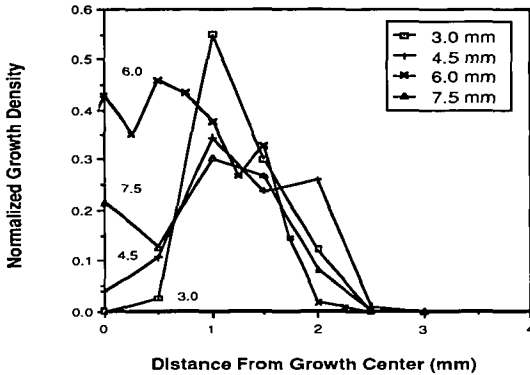


Figure 3: Normalized diamond growth density versus position on the substrate, for different flame-substrate separations (D) and the growth conditions described in the text. Note the transition from annular growth patterns to disk type patterns with increasing D .

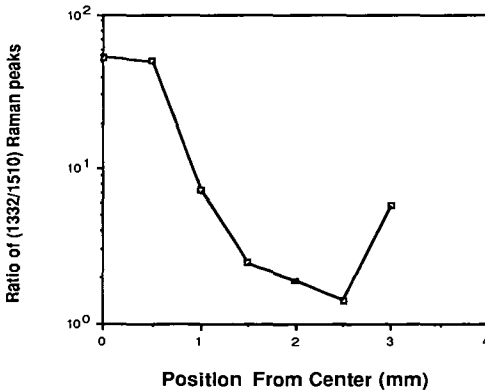


Figure 4. Ratio of the diamond Raman peak (1332 cm^{-1}) to the amorphous carbon peak (1510 cm^{-1}), versus radial distance on the substrate for the conditions described in the text. The increase at large distances is associated with positions outside of the annular growth region. SEM analysis has correlated this increase with a decrease in secondary growth on the crystallite faces.

KINETICS OF METHANE PYROLYSIS IN HOT-FILAMENT REACTOR: EFFECT OF HYDROGEN

Michael Frenklach

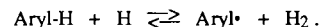
Fuel Science Program
Department of Materials Science and Engineering
The Pennsylvania State University
University Park, PA 16802

INTRODUCTION

A major breakthrough in low-pressure diamond deposition technology, that has led to micron-a-minute growth rates, began with the addition of molecular hydrogen to the reactive hydrocarbon mixtures [1-7]. Several factors have been suggested to explain the effect of the hydrogen dilution. First, and the most important one, is the preferential etching of graphite over diamond by hydrogen atoms [1,3,4,7-10]. This theory assumes that graphite and diamond are formed simultaneously but graphite (or, more generally, graphitic phase) is destroyed by reactions with H atoms whereas diamond is not, or at least not to the same extent. Deryagin and co-workers [1,3,4,8] argued that hydrogen atoms should be in a superequilibrium state for a successful growth of diamond. The requirement of the H superequilibrium (as opposite to just a high concentration of hydrogen atoms, which, for example, can be in partial equilibrium with H₂) was rationalized by Frenklach and Spear [11] suggesting that a reversible H-atom abstraction reaction is the rate limiting step of the diamond surface growth. In a following work, using quantum mechanical methods, Huang *et al.* [12] computed that this reaction has a substantial energy barrier whereas subsequent steps of the diamond growth reaction sequence, acetylene addition to the surface radicals, have no energy barriers at all.

The second most frequently discussed [3,4,7] effect of hydrogen is to satisfy the dangling bonds of surface carbon atoms, thus keeping them in the *sp*³ configuration and preventing the diamond surface from reconstruction into graphitic *sp*² (or carbynic *sp*) structures. Other possible roles of atomic hydrogen suggested are: to promote the production of acetylene, which was proposed to be the main monomer for diamond growth, in the gas phase [11]; to promote the *sp*³ configuration of the gaseous radical precursors and surface clusters [13]; and to remove oxygen chemisorbed on the substrate [13].

The hydrogen effect was also attributed to the molecular hydrogen. Fedoseev *et al.* [3] suggested that "the addition of hydrogen to the initial hydrocarbon lowers its rate of decomposition, and therefore also the rate of formation of the solid phase." A recent computational study [14] examining the formation of polycyclic aromatic hydrocarbons (PAHs) in carbon-rich circumstellar envelopes revealed that the formation of aromatic structures, thought to be the precursors of carbonaceous solid phases [15-17], is entirely suppressed in the atmosphere of H₂ at high temperatures — temperatures that otherwise exhibit high growth rates of soot (and other forms of solid-phase carbon [18]) in fossil fuel air combustion [15] and argon-diluted pyrolysis [19]. The suppression phenomenon is explained [20-22] by the increase in the rate of the reverse direction of the abstraction reactions



It is predicted [14,22] that at lower temperatures this reaction is no longer rate-limiting and PAH growth is controlled by the rate of acetylene additions to aryl radicals. Under these conditions polycyclic aromatic hydrocarbons and solid carbon phases begin to appear.

There is an analogy between the conditions of PAH and carbon grain formation in circumstellar envelopes of carbon-rich stars [14,16,17] and CVD diamond deposition in hot-filament [23-25] and plasma-assisted [6,26] CVD reactors. In both processes the reaction takes place in hydrogen atmosphere; it is initiated by an intensive flux of energy, thermal or plasma; the reaction develops under the decrease in gas temperature; and the formation of the high molecular weight products, PAHs or diamond, occur at about the same temperatures, 800 – 1000 °C. The above theoretical considerations suggest that this analogy is not circumstantial. The results of the present computational study, aimed at the analysis of the effect of hydrogen on gaseous species under the conditions of diamond formation, demonstrate the similarity in gas-phase chemistry of the two processes, and suggest that the suppression of PAH production by molecular hydrogen plays the key role in diamond growth.

COMPUTATIONAL MODEL

The model assumed for simulation of the gas-phase chemistry is a constant pressure, constant flow rate plug-flow reactor with an imposed temperature profile. This choice is based on the following considerations. First, diamond deposition characteristics obtained in experimental reactors of different geometries and energy sources are very similar [6] and, hence, it is more logical to begin modeling the process with a simplest case, hot-filament reactor, where gas activation can be assumed to be thermal. It will be argued elsewhere that the results obtained with this assumption are also applicable to plasma-assisted CVD reactors. Second, the idealization of the gas flow is a practical necessity as neither flow characteristics, which are required for development of the gas-dynamic model, nor species profiles, that can be used to test the model predictions, have been established experimentally. Finally, and most importantly, the objective of the present simulations is to study *qualitative* trends in the computed chemical species profiles, for which the numerical accuracy of the results is not critical.

The chemical reaction mechanism used here is based on the mechanism developed for the study of PAH production in carbon-rich circumstellar envelopes [14]. It is applicable to wide ranges of temperatures, 700 – 3000 K, and pressures, up to 10^{-10} atm. The latter is compiled of 112 reactions and 39 species that describe, beginning with acetylene, the formation of benzene and its further growth to an infinitely large sized PAHs; this mechanism was adopted here without change. The 112 reactions of this mechanism were augmented with 19 reactions (adding 6 new species) describing the initial stages of methane pyrolysis: formation of CH_3 and CH_2 radicals and their subsequent reactions producing C_2H_6 , C_2H_5 , C_2H_4 and C_2H_3 , the last two being the precursors of C_2H_2 . The added reaction subset, along with the associated rate parameters, will be reported elsewhere.

The initial conditions for the "reference" case were assumed based on recent experiments of Harris *et al.* [25]: 0.3% CH_4 – H_2 mixture, pressure 20 torr, and the initial (inlet) reaction temperature 2600 K, which decreases linearly in time with the rate of 1400 K/s. Such a cooling rate means that the gas reaches the temperature of diamond deposition, ~ 1000 °C [26], within about 1 second. The computer simulations were carried until the temperature dropped to about 650 °C, well below the deposition conditions. The numerical integration of the differential equations describing the time-dependent species concentrations were performed with a constant-pressure kinetic code on a IBM 370–3090 computer at the Pennsylvania State University Computer Center using the LSODE integrator of Hindmarsh [27]. The relative error (parameter RTOL) was kept at 1×10^{-4} and the absolute error (parameter ATOL) was set well below the concentration of the principal PAH species.

RESULTS AND DISCUSSION

The concentration profiles of major species computed for the "reference" case are similar to those obtained in constant-temperature computations of Harris *et al.* [25] and in plasma simulations of

Kline and co-workers [28]. These results indicate that C_2H_2 is the major hydrocarbon species at the temperatures of diamond deposition. However, if the reaction time scale is decreased from 1 to 1×10^{-3} s (i.e., the temperature rate is changed from 1.4×10^3 K/s to 1.4×10^6 K/s), CH_4 and CH_3 become the predominant species. The residence times on the order of 1 ms have been reported by Yarbrough and Roy [23]. These authors modified the hot-filament reactor replacing the filament by bringing the gas to the substrate surface through a small-diameter tantalum tube which is heated by a surrounding wire coil to the hot-filament temperatures. Under such conditions the reaction mixture remains in contact with the hot tube for a relatively long period of time, on the order of milliseconds. As a result, the methane pyrolysis and hydrogen decomposition are accelerated by heterogeneous processes on the surface of the tube and the equilibrium between H and H_2 is likely to establish before the gas leaves the tube. A gas-phase kinetic simulation with the "reference" case but assuming the initial concentration of hydrogen atoms to be $[H]_{t=0} = ([H_2]/K_h)^{1/2}$, where K_h is the equilibrium constant of reaction $H + H = H_2$, indicated that the concentration of C_2H_2 reaches and supercedes that of CH_3 at about 100 μ s. Thus, we conclude that under thermal activation of the gas phase acetylene should be the predominant hydrocarbon species at the conditions of diamond deposition, as initially suggested by Frenklach and Spear [11] and verified in recent optical [24] and mass-spectrometric [25] measurements.

To investigate the effect of hydrogen addition, a computer simulation was performed similar to the "reference" case but with argon instead of hydrogen as diluent. The numerical results obtained in these two cases are compared in Figs. 1 through 4. The H concentration is larger by about an order of magnitude in the H_2 environment compared to that in the case of Ar (Fig. 1), which may support the H atom etching theory. The same information displayed in the form of H supersaturation, defined as

$$f = \frac{[H]}{[H]_{eq}} = \frac{[H]}{[H_2]/K_h},$$

shows that practically the same values of f are computed in the both cases. This result indicates that the H supersaturation itself is not a critical parameter. This is understandable since the f values are extremely large ($\sim 10^7$ at 1000 °C), so that the kinetics of H atom reactions (e.g., etching) or of the following steps (e.g., acetylene addition) rather than their thermodynamics should be the controlling factors [22].

The concentration of CH_3 is computed to be significantly larger in H_2 than in Ar (Fig. 2), whereas the concentration of C_2H_2 is practically the same in the both cases (Fig. 3). At first glance, these results may support the proposal of Tsuda *et al.* [29] that CH_3 and not C_2H_2 is the main "building block" for diamond film growth. Further computational tests, that will be discussed elsewhere, clarify this point. Now it is pertinent to note that since acetylene is the main reaction product of methane pyrolysis, the proximity in C_2H_2 profiles computed in H_2 and Ar environments (Fig. 3) demonstrates that the abundance of H_2 does not lower the rate of methane decomposition. However, as seen in Fig. 4, the presence of H_2 does pronouncedly suppresses the production of aromatic hydrocarbons. It is this suppression phenomenon that is proposed here to play the critical role in the hydrogen effect on diamond growth. Aromatic species formed in the gas phase condense on the (diamond) surface, i.e., collide with the surface and held there by van der Waals forces. Their further growth leads to the formation of graphitic layers, which competes with and thus prevents the growth of diamond.

ACKNOWLEDGEMENT

The work was supported in part by the Office of Naval Research, Contracts No. N00014-86-K-0283 and N00014-86-K-0443.

REFERENCES

1. B. V. Spitsyn, L. L. Bouilov, B. V. Derjaguin, *J. Crystal Growth* **52**, 219 (1981).
2. S. Matsumoto, Y. Sato, M. Kamo, and N. Setaka, *Jpn. J. Appl. Phys.* **21**, L183 (1982).
3. D. V. Fedoseev, V. P. Varnin, and B. V. Deryagin, *Russ. Chem. Rev.* **53**, 435 (1984).
4. D. V. Fedoseev, B. V. Deryagin, I. G. Varshavskaya, and A. S. Semenova-Tyan-Shanskaya, *Crystallization of Diamond* (Nauka, Moscow, 1984, in Russian).
5. R. C. DeVries, *Ann. Rev. Mater. Sci.* **150**, 161 (1987).
6. R. Messier, A. R. Badzian, T. Badzian, K. E. Spear, P. Bachmann, and R. Roy, *Thin Solid Films*, **153**, 1 (1987).
7. J. H. Angus and C. C. Hayman, *Science* **241**, 913 (1988).
8. B. V. Spitsyn and L. L. Bouilov, in *Extended Abstracts. Diamond and Diamond-Like Materials Synthesis*, edited by G. H. Johnson, A. R. Badzian, and M. W. Geis (Materials Research Society, Pittsburgh, 1988), p. 3.
9. J. C. Angus, H. A. Will, and W. S. Stanko, *J. Appl. Phys.* **39**, 2915 (1968).
10. S. P. Chauhan, J. C. Angus, and N. C. Gardner, *J. Appl. Phys.* **47**, 4746 (1976).
11. M. Frenklach and K. E. Spear, *J. Mater. Res.* **3**, 133 (1988).
12. D. Huang, M. Frenklach, and M. Maroncelli, *J. Phys. Chem.* **92**, 6379 (1988).
13. E. S. Machlin, *J. Mater. Res.* **3**, 958 (1988).
14. M. Frenklach and E. D. Feigelson, *Astrophys. J.*, in press.
15. B. S. Haynes and H. Gg. Wagner, *Prog. Energy Combust. Sci.* **7**, 229 (1981).
16. M. Frenklach, M., in *Carbon in the Galaxy: Studies from Earth and Space*, edited by J. Tarter (NASA CP, 1988) in press.
17. A. G. Tielens, in *Carbon in the Galaxy: Studies from Earth and Space*, edited by J. Tarter (NASA CP, 1988) in press.
18. M. Frenklach, J. P. Hsu, D. L. Miller, and R. A. Matula, *Combust. Flame* **64**, 141 (1986).
19. M. Frenklach, S. Taki, M. B. Durgaprasad, and R. A. Matula, *Combust. Flame* **54**, 81 (1983).
20. M. Frenklach, D. W. Clary, W. C. Gardiner, Jr., S. E. Stein, *Twentieth Symposium (International) on Combustion* (The Combustion Institute, Pittsburgh, 1985), p. 887.
21. M. Frenklach, T. Yuan, and M. K. Ramachandra, *Energy & Fuels* **2**, 462 (1988).
22. M. Frenklach, *Twenty-Second Symposium (International) on Combustion* (The Combustion Institute, Pittsburgh, 1989), in press.
23. W. A. Yarbrough and R. Roy, in *Extended Abstracts. Diamond and Diamond-Like Materials Synthesis*, edited by G. H. Johnson, A. R. Badzian, and M. W. Geis (Materials Research Society, Pittsburgh, 1988), p. 33.
24. F. G. Celii, P. E. Pehrsson, H. T. Wang, and J. E. Butler, *Appl. Phys. Lett.* **52**, 2045 (1988).
25. S. J. Harris, A. M. Weiner, and T. A. Perry, *Appl. Phys. Lett.* **53**, 1605 (1988).
26. A. R. Badzian and T. Badzian, in *Extended Abstracts. Diamond and Diamond-Like Materials Synthesis*, edited by G. H. Johnson, A. R. Badzian, and M. W. Geis (Materials Research Society, Pittsburgh, 1988), p. 27.
27. A. C. Hindmarsh, "Towards a Systematic Collection of ODE Solvers," 10th IMACS World Congress on Systems Simulation and Scientific Computation (Montreal, 1982); also Lawrence Livermore Laboratory Preprint No. UCRL-87465, March 1982.
28. L. E. Kline, W. D. Partlow, and W. E. Bies, *Proc. Electrochem. Soc. Symp. on Plasma Processing* (ECS, Pennington, N.J., 1987); also *J. Appl. Phys.* (1988), to appear.
29. M. Tsuda, M. Nakajima, M., and S. Oikawa, S., *Jpn. J. Appl. Phys.* **108**, 5780 (1987).

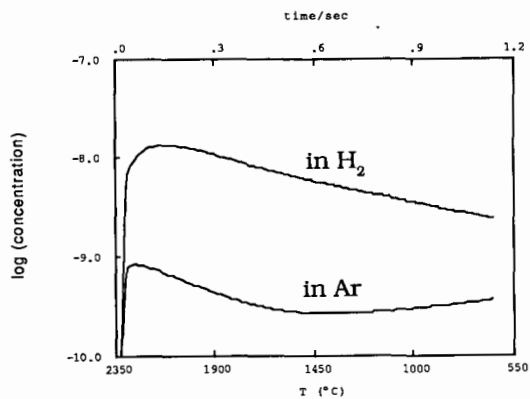


Fig. 1. Concentration of H

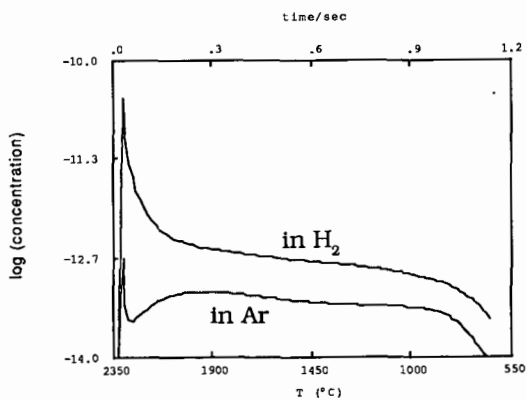


Fig. 2. Concentration of CH₃

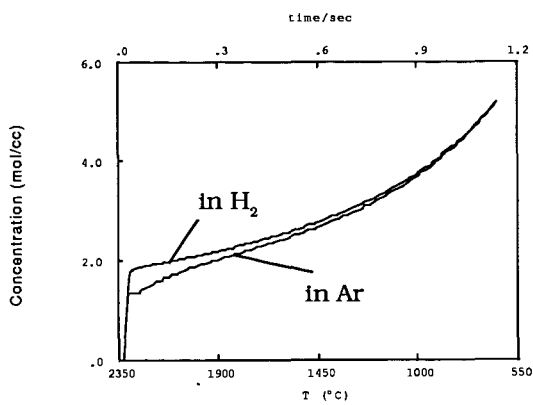


Fig. 3. Concentration of C_2H_2

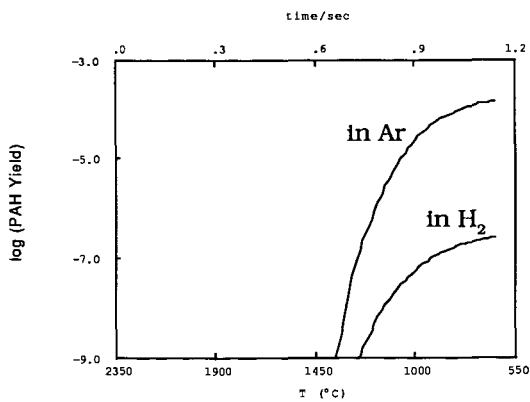


Fig. 4. Concentration of PAHs

SUPERSONIC BEAM STUDIES OF CARBON CONDENSATION

R. E. Smalley
Rice Quantum Institute and Department of Chemistry
Rice University
Houston, Texas 77251

INTRODUCTION

In the course of the current rage of fascination with how diamond growth may be nucleated and controlled, it is probably wise to consider in some detail the nature of the beast with which diamond growth must compete. The beast in this case is the growth of graphite either in its perfect crystalline form, or more typically in one of its less flat, often more tortuous morphologies. After all graphite is the most stable form of carbon under moderate pressure conditions, and diamond growth can dominate only as a result of some kinetic trick. Unfortunately, this will have to be a very powerful trick indeed, since it turns out that the kinetics of nucleation and growth of graphitic type objects are sensationally facile.

This short paper considers some of the newest evidence of just how formidable this graphitic beast is. Strangely, much of this new evidence has come from the rarified and esoteric environment of supersonic beams and laser spectroscopy. Advances in laser and supersonic molecular beam techniques over the past 5-10 years have produced a flood of new results and insights as to the nature of small clusters. Within the sub-field of strongly bound (non van der Waals) clusters, certainly one of the most active and intellectually exciting areas has been the study of carbon. Although many of these new experiments are still in the process of verification, extension, and further interpretation, a remarkable new picture is beginning to emerge as to some of the dominant processes of carbon condensation and the nature of the (largely graphitic) species involved.

Perhaps the most concise way to summarize this subject is simply to list some of the key features of the emerging new view of the small clusters of carbon.

- (1) Carbon nucleates to form small clusters far more readily than any other element in the periodic table (including such refractory metals as tungsten and tantalum or the semiconductors silicon, germanium, and gallium arsenide).
- (2) The smallest clusters (C_2 through C_{29}) are essentially one-dimensional: they are most stable in the form of linear chains or monocyclic rings (depending on the charge state and temperature).
- (3) Even-numbered clusters in the 32-100+ atom size range often take the form of entirely closed, hollow spheroidal

shells (the "fullerenes") made up of catacondensed networks of 5- and 6-membered rings. All such fullerenes contain exactly twelve 5-membered rings. Under certain conditions it is possible to trap any of a wide range of metal atoms inside the hollow cavity of these fullerene shells. This includes such metals as sodium, potassium, cesium, calcium, barium, strontium, lanthanum, and actinides such as uranium.

(4) Odd-numbered clusters in the 33-101+ atom size range often take the form of nearly-closed spheroidal shells (the "semifullerenes") also made up of 5- and 6-membered rings.

(5) The prototypical fullerene, C_{60} ("buckminsterfullerene"), prefers the shape of a truncated icosahedron. Because of its size and perfect symmetry, it is extremely stable (chemically, thermodynamically, photophysically). The strain of closure of the fullerenes tends to concentrate at the vertices of the pentagons. Only for C_{60} -- and only when it takes the perfectly icosahedral form -- is this strain uniformly distributed over all carbon centers. It is this symmetry-derived absence of concentrated strain that gives C_{60} its unique stability.

(6) The fullerenes appear to be made whenever carbon condenses, including sooting flames where they are the most abundant ions present above 300 amu.

(7) A spiraling shell is an interesting model for the active nucleus involved in carbon grain growth in space, and soot formation in combustion environments here on earth. It is sensible that this is the most likely graphitic growth form possible in condensing carbon vapors. In this view the fullerenes are best interpreted as side products (dead ends) in a growth process that ultimately produces macroscopic particles.

When compared to the view prevalent in the carbon literature only a few years ago, these 7 points (with the possible exception of the first two or three) are quite divergent -- perhaps even wildly divergent. Nonetheless, my colleagues and I have found the new experimental evidence compelling. To our knowledge this picture is the only one consistent with all experimental results, both new and old.

Within the scope of this short paper it is unreasonable to attempt a full review of the various experiments and lines of argument that have led to this new view. My colleagues and I have published extensively as this work has proceeded from the original experiments of Rohlfing, Cox, and Kaldor (1), and our subsequent realization that C_{60} is supremely special and probably spherical (2). Two fairly comprehensive and up-to-date reviews have recently appeared as articles in the journal Science (3,4). These serve well as both a summary of current evidence and beliefs (at

least as perceived the principal proponents), and as pointers to the relevant literature.

Instead, I will take this opportunity to dwell a bit on one central point of this story that is often misunderstood: the mechanism we have come to suspect is responsible for the facile formation of C_{60} and the other fullerenes. Like most mechanisms offered to explain chemical reactions, this one is highly conjectural. But it does offer a simple explanation for why hollow, spheroidal objects form with such facility. I bring it up in the context of this symposium on diamond growth since the conditions used in most of the current diamond film research are also those where such spheroidal, basically graphitic objects as the fullerenes would be expected to form as well. The thrust of the argument is that this fullerene formation mechanism may either be the "beast" himself, or at least a close associate.

A NEW GROWTH SENARIO FOR THE FULLERENES AND GRAPHITIC SOOT

To most observers the most unbelievable aspect of the buckminsterfullerene story was not that C_{60} may prefer the soccerball geometry. It was clear from the outset that this was a perfectly kosher bonding network for carbon which solved the problem of tying up all dangling bonds with beautiful symmetry and structural integrity. In fact it had been predicted to be stable, and its synthesis had been undertaken years before the supersonic cluster beam experiments were even conceived of at Rice University. What seemed truly incredible was the notion that such a huge, highly symmetric structure could pop full-formed out of something so simple and mindless as a carbon vapor. Particularly vexing was the question of why any molecule would naturally form with a such a huge vacuous cavity in the center. Whatever happened to Nature's supposed abhorrence of a vacuum?

Confronted with the clear fact that, regardless of intuition, C_{60} and the fullerenes are produced readily, and the compelling evidence that they did have the spheroidal cage structure, we searched for a rational growth mechanism. The growth senario we began to advocate was first sketched briefly in a few paragraphs of a short paper we submitted late in 1985 (5).

It seemed clear that the key topological event must involve some inherent tendency of a growing polycyclic aromatic net to curl. We are accustomed to think of aromatic carbon nets as rigid, flat plates. Certainly the vast majority of known polycyclic aromatic compounds are indeed flat (at least at absolute zero). More insidiously, the molecular model kits used to teach modern chemistry have engendered this notion of rigid, flat sp^2 carbon frameworks as though it were a central dogma of structural chemistry. This is a great model for ordinary closed shell aromatic molecules, but that is certainly not what one is dealing with when a pure carbon vapor condenses. Carbon networks growing at high temperature in the absence of hydrogen will have a

large number of dangling bonds, so it is by no means clear that perfect sp^2 hybridization should apply.

Instead we noted that simply by incorporating a pentagonal ring in the periphery of a growing hexagonal net, at least one good new carbon-carbon bond will always be formed from what was previously two dangling bonds. This pentagon causes the net to curl out of plane, the added strain of curvature being offset by the increased bonding.

Following along on this notion that curvature in a growing graphitic net would be a natural consequence of a local incentive to minimize dangling bonds, we supposed that if one pentagon was good, two would be better. But as a second-order consideration it should be noted that two adjacent pentagonal carbon rings is hardly ever encountered as a stable aromatic structure in ordinary polycyclic compounds (it is an antiaromatic cycle, and it concentrates strain). One should therefore expect a tendency for the growing graphitic sheet to incorporate pentagons offset from one another by intervening hexagons on the leading edge of the growth front.

That is basically all there is to the mechanism. There is a simple local tendency to minimize dangling bonds by incorporating pentagons on the growth front, and a weaker tendency to have these pentagons spaced by an intervening hexagon. Note that if followed perfectly, this simple growth rule forms a net which closes perfectly on itself -- it makes a C_{60} soccerball!

Under rapid growth conditions, with insufficient time and/or energy to anneal out mistakes and adhere slavishly to the lowest energy path, this mechanism would predict a wide range of fullerenes to form. Once formed, the absence of dangling bonds on these fullerenes effectively removes them from subsequent direct growth reactions. They can participate further in the condensation process only by adhering to each other, or by becoming sufficiently excited to break open at a site where strains have concentrated, thereby producing a point for further chemical attack and growth.

As we argued in the original paper (5), it seems likely that a rapidly growing graphitic net tying up dangling bonds by this simple rule will most typically fail to close. Instead it is easy to visualize one growth front curling over and burying the opposite edge inside to form the first turn of a 3-dimensional spiral. Once an edge is buried, there is no opportunity for the growth to stop, the spiral simply continuing to grow turn by turn until a macroscopic spherical carbon particle is produced. In fact such particles have been seen before with scanning electron microscopes (6). Such spherical carbon particles formed from pure condensing carbon we prefer to call "graphitic soot". Their ready formation is an unavoidable prediction of the fullerene growth mechanism.

CARBON GROWTH IN A HYDROGEN-RICH ENVIRONMENT

More relevant to the formation of ordinary soot in combustion environments -- and to the conditions where diamond film growth is sought in the experiments discussed in this symposium -- is the circumstance where there is an abundance of hydrogen. Since the fullerene growth mechanism we've been discussing is driven by the presence of dangling bonds, it's not immediately clear how it could apply when there is plenty of hydrogen around to tie up these dangling bonds. With enough hydrogen, one can make any graphitic sheet into a perfectly stable polycyclic aromatic hydrocarbon (PAH), and the most stable of these are always flat.

But at sufficiently high temperatures, hydrogen does not effectively tie up dangling bonds on carbon. Only another carbon atom can do that. Elementary chemical thermodynamics shows that most hydrocarbons are uphill with respect to graphite + H_2 even at room temperature. At the elevated temperatures encountered in flames this is even true for such species as methane and acetylene. The driving force for this is not so much the strength of the carbon-carbon bond in graphite. Instead it is primarily due to the high entropy of gaseous H_2 . Thermodynamically, that's why soot forms.

At elevated temperatures where a significant concentration of hydrogen atoms are present, the carbon-hydrogen bonds on the periphery of a PAH are not safe. Hydrogen abstraction reactions will proceed to generate a free H_2 molecule; leaving behind a bare, dangling bond on the now partially hydrogen terminated graphitic network. Under sufficiently intense H atom attack, therefore, the fullerene growth mechanism discussed above should come into play. The only way such a molecule can tie up its dangling bonds is to use carbon. It will do this until it forms a stable fullerene, or if it misses the fullerene stage, it would be expected to spiral its way to a microscopic soot particle.

So it is conceivable that the fullerenes and spiral graphitic soot particles may be formed in sooting flames. Indeed Homann and his group have found C_{60} and the fullerenes to be very abundant as positive ions in flames (7). In my opinion this is a singularly vital experiment to be repeated and explored by other groups. Although currently the vast majority of the combustion community appears to disagree, to my reading the current evidence supports the notion that the fullerene growth mechanism is so facile in flames that it may be the mechanism responsible for the nucleation and early stages of soot growth in flames. Homann and his associates seem to have at least the beginnings of a method to give a critical test to this notion, but as yet there is no proof one way or the other.

FULLERENES UNDER DIAMOND GROWTH CONDITIONS

More relevantly to this symposium, it seems likely that fullerenes and the related graphitic spirals may be important species under diamond growth conditions. The conventional wisdom in the diamond film growth business is that graphitic (or "amorphous") carbon is constantly being nucleated as well as diamond on the growth surface, but that H atoms etch the non-diamond phases preferentially. The mechanism of this etching process is quite unclear, but there is little doubt that it is essential.

One obvious question is whether the etch process requires attack at an edge of a graphitic sheet. If it does, the presence of fullerenes will be a problem: they have no edges. In fact this suggests that an interesting line of research would be to study the susceptibility of large fullerenes to H atom attack. This turns out to be a vital issue in astrophysics as well. We have argued (2-4) that C_{60} in particular, and the fullerenes in general are likely to be made in vast quantities in the outer regions of carbon-rich red giant stars. Their abundance there, and their subsequent viability in space as they are driven from the star by photon pressure and the stellar wind will depend strongly on the ability to withstand H atom attack. It seems likely that there will be only a mild barrier to attaching a single H atom on one of the surface carbon atoms. But it may be a fairly weak bond, and do little to weaken the structural integrity of the fullerene cage. The lowest thermal dissociation process of such a H-fullerene would most likely be just a simple desorption of the H atom.

Beyond this question of getting rid of the fullerenes once formed, it is sobering consider the great efficiency of this fullerene condensation mechanism for carbon. Even in the absence of hydrogen, all the bare clusters of carbon starting from C_2 , extending through the last of the linear chains and monocyclic rings, to the curling polycyclic graphitic nets, to the fullerenes and the spiraling soot particles ... all of these species are abnormally strongly bound molecules. Unlike any other element, these species are formed almost instantly in a laser-produced vapor, and the final end point, graphite, is one of the most refractory species known.

The fullerene growth mechanism when it defaults to the formation of a spiral graphitic soot particle quickly generates an almost perfect graphite particle. It is mostly edgeless: if it forms optimally, its only edges are found on the last turn of the spiral, and on the innermost turn where the initial edge was buried. Since each layer of the spiral contains only 12 pentagons, the vast majority of the carbon atoms in such a structure are involved in hexagonal rings with only a tiny deviation from planarity. Remarkably, it turns out that the most perfect and symmetrical of these spiral soot particles (the one

that starts with an aborted C_{60} truncated icosahedron, and proceeds to a second layer of 240 atoms, a third of 540 atoms, etc.) naturally has each layer spaced from those above and below by 3.6 angstroms. This is almost exactly the normal interplanar spacing of bulk graphite. In other words, these spiral graphitic particles are macromolecular (but still microscopic) forms of graphite. They may be expected to form with extraordinary speed, and be highly stable. For diamond film growers this is a beast that, once conjured up, may be rather difficult to slay.

ACKNOWLEDGEMENT

The author wishes to acknowledge Robert Curl, Harry Kroto, and Jim Heath for extensive, expansive discussions; and David Nelson who stimulated these thoughts toward diamond. Supersonic carbon cluster research at Rice University was funded by the National Science Foundation and the Robert A. Welch Foundation. Our bare metal cluster research is funded by the Department of Energy, Division of Chemical Sciences, while that on semiconductor clusters was funded by the Office of Naval Research and (for gallium arsenide) the US Army Research Office.

REFERENCES

- (1) Rohlfsing, E. A., Cox, D. A., and Kaldor, A. J. Chem. Phys., 1984, 81, 3322.
- (2) Kroto, H. W., Heath, J. R., O'Brien, S. C., Curl, R. F., and Smalley, R. E., Nature, 1985, 318, 162.
- (3) Curl, R. F., and Smalley, R. E., Science, 1988, 242, 1017.
- (4) Kroto, H. W., Science, 1988, 242, 1139.
- (5) Zhang, Q. L., O'Brien, S. C., Heath, J. R., Liu, Y., Curl, R. F., Kroto, H. W., and Smalley, R. E., J. Phys. Chem., 1986, 90, 525.
- (6) Iijima, S., J. Phys. Chem., 1987, 91, 3466.
- (7) Gerhardt, Ph., Loffler, S., and Homann, K. H., Chem. Phys. Lett., 1987, 137, 306.

THE ROLE OF IONS IN SOOT AND DIAMOND FORMATION

H. F. Calcote
AeroChem Research Laboratories, Inc.
P.O. Box 12, Princeton, NJ 08542

INTRODUCTION

Soot and diamonds are different forms of carbon. It is thus natural to examine mechanisms which have been proposed for the formation of soot with respect to the mechanism of diamond film deposition. Frenklach and Spear have done this with respect to the free radical mechanism of soot formation (1). Diamond deposition is frequently a plasma process and ions have been proposed in several mechanisms to explain the process. There is considerable evidence (2) of an ionic mechanism of soot formation. The demonstration that diamonds can be deposited from combustion flames (3, 4) also makes it timely to consider soot forming processes in flames as they might relate to diamond deposition. Thus we briefly review the ionic mechanism of soot formation and the evidence for an ionic role in diamond deposition; we then make a few observations relevant to the role of ions in the mechanism of diamond deposition.

IONS IN SOOT FORMATION

The ionic mechanism of soot formation, Figure 1, postulates that chemiions, HCO^+ and C_3H_3^+ , which are present in excess of equilibrium in hydrocarbon flames, rapidly grow by ion-molecule reactions in which several neutral species continue to add to an increasingly larger ion. As an ion becomes larger, it is neutralized by the electrons produced in the chemiionization reactions. This process gives both charged and neutral incipient soot particles which continue to grow by the addition of acetylene and other small neutral species. There are two important considerations in the ionic mechanism: (1) the large rate coefficients for ion-molecule reactions, and (2) the rapid isomerization of ions to produce a cyclic structure. Formation of the first ring is the main problem with the neutral mechanism and has absorbed much of the research attention relevant to the neutral mechanism.

The soot concentration, in many flames, is in excess of equilibrium so must be driven by a species whose concentration exceeds equilibrium. Chemiionization is a nonequilibrium process producing ionic concentrations orders of magnitude in excess of equilibrium.

In Figure 1, the direct path to C_3H_3^+ appears unimportant in flames (5) but may be important in pyrolysis systems producing soot, where ions are also observed (6). Therefore C_3H_3^+ is probably generated by a series of ion-molecule reactions from HCO^+ . The ion C_3H_3^+ grows by adding small neutral species in a series of ion-molecule reactions, in which any one of the growth species, see, e.g., Figure 1, may add to a given ion to produce a larger ion. At each stage the ion may also be neutralized by reaction with an electron produced in the initial chemiionization step. The product of this reaction, usually a dissociative recombination, is identified in Figure 1 as "neutral reactant" (e.g., a polycyclic aromatic hydrocarbon) and this neutral species may continue to grow by a neutral free radical mechanism, also leading to an incipient soot particle.

All of the ions proposed in the ionic mechanism have been observed in flames up to mass 557 amu; the concentration of ions has been demonstrated experimentally to be sufficient to account for the concentration of soot measured; and the rates of ion formation in both premixed (7) and diffusion (2) flames are about the same order of magnitude as the rate of soot formation.

IONS IN DIAMOND FORMATION

Diamond films have been deposited by many different techniques including electrical discharge systems, e.g., microwave, rf, and dc glows; dc and rf arcs; and arc jets. They have also been made with ion beams, combustion flames, and hot filaments. The electrical discharge systems are based upon electrically driven plasmas. From the above discussion, it is clear that the combustion system is also a plasma. This leaves only the hot filament technique as not obviously involving a plasma.

It has been demonstrated, however, that in the hot filament technique, the application of an electric field to the substrate can influence the rate of diamond film deposition. Yarbrough (8), e.g., found that a positive voltage on the substrate increased the rate of diamond deposition and a negative voltage prevented deposition. This indicates the importance of charged species in the deposition process and puts this system as well in the plasma category. The source of the ionization is most likely electron emission from the hot filaments which were tantalum tubes heated to 2370 to 2470 K (9). Thus all diamond preparation systems have a unifying feature--the presence of ions.

In a magneto-microwave plasma, Susuki et al. (10) also observed the rate of film deposition to be accelerated by application of a positive electric field to the substrate. In these two systems, observations indicate either diamond deposition enhancement by negative ions or electrons, or an inhibiting effect by positive ions.

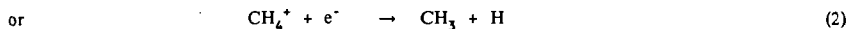
On the other hand, others have found that accelerating positive ions toward the substrate surface enhances the rate of diamond deposition (11), or more generally the application of a negative bias to the substrate increases the rate of film deposition or alters the properties of diamond (12) or diamond-like (13) films.

MECHANISTIC IMPLICATIONS

Since a plasma generated by an electric field is a common component of many diamond film deposition processes, we examine the process of creation of active species in an electrical discharge device. Most deposition processes use a mixture of hydrogen containing a few percent methane, so we examine the chemistry expected in this system. In Figure 2 the electron energy distribution for three different electron temperatures is presented along with the collision cross section for the initial reactions by which electric power is coupled to the gas. There are several points to be made from this figure. First, the electron temperature must be very high compared to deposition temperatures, typically 800-1300 K, for a significant percentage of the electrons to dissociate or ionize the reactants. Even in a low temperature discharge, measured by the gas temperature, the electron energy must be high enough to produce ions to maintain the discharge. For hydrogen and methane, dissociation occurs at electron energies, 3 to 6 eV below where ionization sets in; higher cross sections are reached at the energies at which ionization sets in. Yet, to maintain the discharge, ionization must occur, so that some of the electrons have energies in the neighborhood of 14 to 18 eV.

Thus the initial reactive species concentrations are present at equivalent temperatures far above the gas temperature and certainly far above the substrate temperature. The initial system is far from equilibrium and any modeling of the process must start with this condition. The nonequilibrium condition is, of course, consistent with the fact that diamond is thermodynamically metastable with respect to graphite. The chemistry occurring between the super-equilibrium formation of active species and their striking the substrate surface is of interest. Thus models must start with the formation of active species and these may be different for the many techniques which have been used to produce diamond and diamond-like films.

The question of whether ions or free radicals play the dominant role in electrical discharge chemistry has not been resolved and must depend upon the specific system (see e.g., Avni and coworkers (17) or Marcus and Platzner (18)). Ion-molecule reaction rate coefficients are orders of magnitude greater than free radical rate coefficients but the ions are generated in smaller initial concentrations. Further, as ions recombine with electrons, also a very rapid process, they dissociate to produce hydrogen atoms or free radicals, e.g.,



Thus the nonequilibrium formation of ions plays a role in the production of super-equilibrium concentrations of hydrogen atoms and free radicals. H atoms are considered important in suppressing graphite buildup in competition with the deposition of diamonds (19), as well as in abstracting hydrogen atoms from the growing surface.

The observations that electric fields affect the rate of diamond deposition and the fact that plasmas contain ions, have led to proposals that ions are important in diamond deposition (11, 13, 20). All of these proposals incorporate positive ions, e.g., CH_3^+ in the mechanism. Tsuda et al. (20) describe a mechanism for diamond growth in which the diamond surface first becomes covered by methyl groups and then a methyl cation strikes the surface, simultaneously binding three methyl carbons to form the diamond structure. This concerted process does not allow the surface to graphitize. A very detailed mechanism is developed for which an activation energy of 27.4 kcal/mol is deduced. This is less than measured activation energies for diamond deposition which lie between 55 kcal/mol (19, 21) and 80 kcal/mol (19).

In the Frenklach-Spear mechanism (1) a hydrogen atom abstracts a hydrogen atom from a surface site where an acetylene molecule then adds. They develop a kinetic scheme from which an energy barrier of only 17.4 kcal/mol is obtained, even lower than for the Tsuda et al. mechanism and even further below the measured activation energy!

The implication of the importance of ions, because of the effect of electric fields, on the deposition of diamonds, coupled with the probably small concentration of ions relative to free radicals and other neutral species, suggests a mechanism in which an ion plays the role of a catalyst or the seed in a nucleation step, neutrals providing much of the ultimate mass.

The effectiveness of both positive and negative voltages clouds the picture. The source of positive ions is clear, but if negative ions, rather than electrons, are important, their source is not clear. Electron attachment may form a route for the formation of negative ions in hot wire or electrical discharge systems used to prepare diamond films. However, a calculation of the equilibrium constants from the free energies of formation as a function of temperature, shows that among the simple neutral species expected in the H_2/CH_4 system, the attachment of an electron to a hydrogen atom or CH radical is a candidate; equilibrium favors H^- below about 1800 K and CH^- below about 2200 K. The hydrogen reaction would require a third body. In the case of the hot filament, the negative ions could be formed on the filament. Catalytic decomposition or thermal decomposition could account for other species, including possibly, ions of both signs.

Negative ions have been observed (22, 23) in sooting flames but they have not been identified mass spectrometrically; they are assumed to be large molecular ions produced by electron attachment. In somewhat leaner, nonsooting flames, negative ions have also been identified, Figure 3, but their mechanism of formation is vague; they do not seem to be formed by simple attachment (24). They are present at about 1% of the positive ion concentration at an equivalence ratio of 1, stoichiometric flames, and their maximum concentration occurs at a higher equivalence ratio, fuel rich, than for positive ions. Their concentrations decrease with increasing total pressure. To my knowledge no measurements of the effect of voltage on diamond deposition in combustion systems have been made. Interestingly, diamonds are deposited from the flame in the region where soot is formed and where ions are present (25).

The growth species which adds to the ionic nuclei may be a stable molecule e.g., acetylene as suggested by Frenklach and Spear (1) or the methyl radical which has frequently been suggested (20). Angus (21) measured the rate of deposition of diamond in a hot filament environment to be first order in the methane pressure and one-half order with respect to ethylene pressure, from which he deduced that the growth mechanism must involve the addition of a species containing only one carbon atom. Similarly, Sato, Kamo, and Setaka (26) examined the effect of hydrocarbons, including alkanes, alkenes and acetylene on growth and Raman spectra of diamond films prepared in a microwave system and concluded that growth features and morphology are dependent approximately on the number of carbon atoms in the molecule. On the other hand, Fedoseev and associates (19) observed that the highest activation energy and the lowest rates were associated with growth from methane, and the lowest activation energy and the highest rates were associated with acetylene and that other hydrocarbons fell between these. This is reminiscent of the effect of molecular structure on both ion formation and soot formation in flames (2). Is there a connection?

CONCLUSIONS

The plasma condition seems to be a prerequisite for diamond film deposition, even by the hot filament technique and from a combustion flame. The ions in the plasma are at a concentration

considerably in excess of their equilibrium concentration at the substrate temperature, as are free radical and hydrogen atoms. Thus any model of the process must start with these conditions in the plasma. Both positive and negative ions (or electrons) seem to be involved. The source of positive ions is fairly clear, but the source and nature of negative ions are not. Because of the low concentration of ions compared to other species it is most likely that their role in diamond coating technology is analogous to that in flames, i.e., they act as nucleation agents, not as growth species.

ACKNOWLEDGEMENTS

Drs. David Keil and Robert Gill's helpful discussions are gratefully acknowledged, as is Dr. Gill's calculation of the heats of formation of the negative hydrocarbon ions as a function of temperature.

REFERENCES

- (1) Frenklach, M. and Spear, K.E. *J. Mater. Res.*, 1988, **3**, 133.
- (2) Calcote, H.F., Olson, D.B., and Keil, D.G. *Energy & Fuels*, 1988, **2**, 494.
- (3) Carrington, W.A., Hanssen, L.M., Snail, K.A., Oakes, D. and Butler, J.E., "Diamond Growth in $O_2+C_2H_4$ and $O_2+C_2H_2$ Flames" submitted to *Metallurgical Transactions*, 1988.
- (4) Hirose, Y. and Konda, N., Japan Applied Physics, 1988 Spring Meeting, p. 434.
- (5) Eraslan, A.N. and Brown, R.C., *Combust. and Flame*, 1988, **74**, 19.
- (6) Kern, R.D., Singh, H.J., and Xie, K. "A Systematic Search for the Presence of Chemi-ions in Pyrolytic and Oxidation Systems" 22nd Symp. (Int.) on Combustion, Seattle, Washington, August 14-19, 1988, Poster 100.
- (7) Keil, D.G. and Calcote, H.F. unpublished work.
- (8) Yarbrough, W. A., The Pennsylvania State University, personal communication, 10 November 1987.
- (9) Yarbrough, W.A. and Roy, R., "Nanocomposite Diamond Films by Hot Filament Assisted CVD," MRS Extended Abstracts, Diamond and Diamond-Like Materials Synthesis, G.H. Johnson, A. R. Badzian, and M. W. Geis, Eds., April 5-9, 1988, 33.
- (10) Susuki, J.I., Kawarada, H., Mar, K.S. Yokota, Y., and Hiraki, A. "Large Area CVD of High Quality Diamond Films Using High-Density Magneto-Microwave Plasma at Low Pressure," Paper No. T3, Diamond Technology Initiative Symposium, Arlington, VA 12-14 July 1988.
- (11) Namba, Y., Japan Applied Physics, 1987 Fall Meeting, Abstract 17P-A-1.
- (12) Hirata, T. and Nage, M., MRS Extended Abstracts Diamond and Diamond-Like Materials Synthesis, G.H. Johnson, A. R. Badzian, and M. W. Geis, Eds., April 5-9, 1988, 49.
- (13) Koidl, P. and Wild, CH., MRS Extended Abstracts Diamond and Diamond-Like Materials Synthesis, G.H. Johnson, A. R. Badzian, and M. W. Geis, Eds., April 5-9, 1988, 41.
- (14) Rapp, D. and Englander-Golden, P. *Journal of Chemical Physics*, 1965, **43**, 1464.
- (15) Winters, H.F. *Journal of Chemical Physics*, 1975, **63**, 3462.
- (16) Corrigan, S.J.B. *Journal of Chemical Physics*, 1965, **43**, 4381.
- (17) Avni, R., Carmi, U., Inspector, A., and Rosenthal, I. *Journal of Vacuum Science and Technology*, 1985, **A3**, 1813.

- (18) Marcus, P. and Platzner, I. *International Journal of Mass Spectrometry and Ion Physics*, 1979, 32, 77.
- (19) Fedoseev, D.V., Varnin, V.P., and Deryagin, B.V. *Russian Chemical Reviews*, 1984, 53, 435.
- (20) Tsuda, M., Nakajima, M., and Oikawa, S. *J. Amer. Chem. Soc.*, 1986, 108, 5780.
- (21) Angus, J.C. "Growth Studies of Diamond and Diamond Like Phases," Paper No. W1, Diamond Technology Initiative Symposium, Arlington, VA 12-14 July 1988.
- (22) Homann, K.H. and Strofer, E. *Soot in Combustion Systems and Its Toxic Properties*. J. Lahaye and G. Prado, Eds., Plenum, 1983, 217.
- (23) Keil, D.G., Gill, R.J., Olson, D.B., and Calcote, H.F. *20th Symp. (Int.) on Combustion*, The Combustion Institute, 1984, 1129.
- (24) Calcote, H.F., Kurzius, S.C. and Miller, W.J. *10th Symp. (Int.) on Combustion*, The Combustion Institute, 1965, 605.
- (25) Hanssen, L.M., Carrington, W.A., Butler, J.E., and Snail, K.A., "Diamond Synthesis Using an Oxygen-Acetylene Torch" submitted to *Materials Letters*, 1988.
- (26) Sato, Y., Kamo, M. and Setaka, N. *Proceedings 8th International Symposium of Plasma Chemistry*, Vol. 1, 1987, p. 2446.

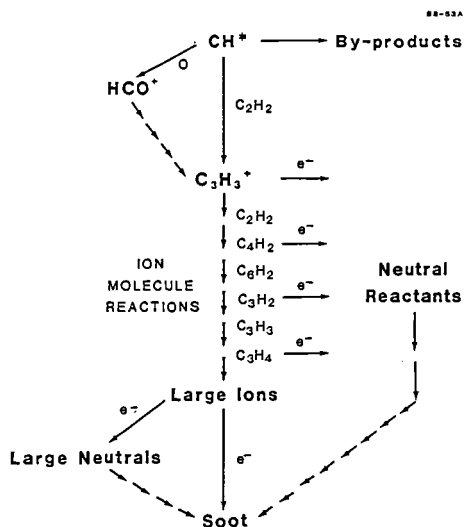


Figure 1. Ionic Mechanism for the Formation of Incipient Soot

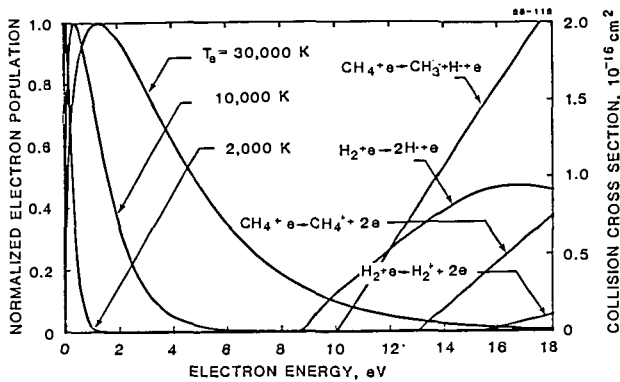


Figure 2. Electron Collision Dissociation of Methane and Hydrogen
 Ionization of Methane from Ref. 14.
 Dissociation of Methane from Ref. 15.
 Dissociation and Ionization of Hydrogen from Ref. 16.

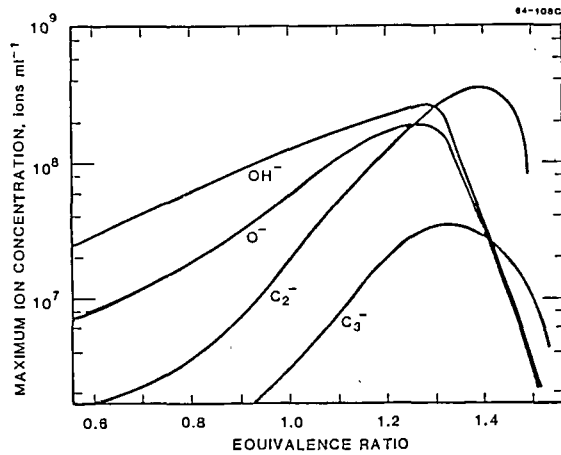


Figure 3. C_2H_2/O_2 Flame at 0.27 kPa.
 Total Fflow = $70 \text{ cm}^3/\text{s}$ (STP).

GAS PHASE KINETICS DURING DIAMOND GROWTH: CH₄ AS GROWTH SPECIES

Stephen J. Harris
Physical Chemistry Department
General Motors Research Labs
Warren, MI 48090

Introduction

There has been considerable interest in the growth of diamond thin films in recent years^{1,2}. This interest derives from the superlative properties of diamonds: they are very hard, have a high thermal conductivity, are chemically inert, and have an extremely wide optical transmission window. In addition, single crystal diamonds have the potential for being uniquely good semiconductors².

Unfortunately, at present we have little understanding of the chemical processes which are involved in and which control diamond nucleation and growth. This is because there have been no experiments which have simultaneously characterized both the chemical environment and the kinetics of diamond growth. Recently C₂H₂ (acetylene)^{3,4}, C₂H₄ (ethylene)³, CH₃ (methyl radical)³, and H (atomic hydrogen)³ have been detected during filament-assisted diamond growth experiments. Harris et al.⁴ used a simple zero-dimensional chemical kinetics model to show that only CH₄ (methane), C₂H₄, C₂H₂, and/or CH₃ could be contributing significantly to surface growth in those experiments. This result is consistent with semi-empirical quantum mechanical studies of the diamond growth mechanism which suggest that the growth species is either C₂H₂⁵ or CH₃⁶.

Earlier detailed measurements of the kinetics of diamond growth on diamond seed crystals from CH₄-H₂ mixtures were made by Chauhan, Angus, and Gardner⁷. Although the chemical species present were not determined in their work, we recognized that the gas phase chemistry could be approximately modeled based on the information that was provided. In this work we analyze the data of Chauhan et al.⁷ to determine which species accounted for the diamond growth that was observed.

Analysis

The experiments of Chauhan et al.⁷ were carried out on a microbalance which allowed the rate of diamond growth to be measured. For the particular experiment that we modeled, labeled 44-C, a 0.5 torr mixture of 70% CH₄ and 30% H₂ passed through a cylindrical 2.54 cm diameter flow tube into the top of a spherical 10.16 cm diameter pyrex reaction chamber, at the center of which was suspended a crucible holding 98.934 mg of diamond seed crystals. The gases were pumped away at the bottom of the reaction chamber through a 3.81 cm diameter flow tube. The seed crystals, which had a BET surface area of 7 m²/g, were heated to 1438 K by radiation from a lamp; there were no other heaters in the system. The wall temperature of the reaction chamber was maintained below 500 K, eliminating heterogeneous pyrolysis chemistry there. The gas velocity was not specified, but Chauhan et al.⁷ stated that the gases flowed at a rate "such that the methane available was more than 50 times that required to obtain the observed deposition rates." This implies an input flow velocity of at least 94 cm/s, readily achieved in flow tubes of this size. Chauhan et al.⁷

determined that all of the initial weight gain as monitored by the microbalance was due to diamond, although as time progressed more and more of the weight gain came from non-diamond (pyrolytic) carbon. In this work we model only the initial growth period, before any formation of pyrolytic carbon.

The measurements of Chauhan et al.⁷ showed an initial fractional growth rate of

$$\frac{1}{m} \frac{dm}{dt} = 1.31 \times 10^{-3} \text{ min}^{-1}, \quad (1)$$

where m is the mass of the diamond crystals. This rate corresponds to a specific surface growth rate of 3.1×10^{-10} g/cm²·s. For a growth species depositing n_c carbon atoms with each reaction, Eqn. (1) implies that $1.6 \times 10^{13}/n_c$ molecules reacted/cm²·s. This reaction rate is equal to the collision rate of growth species with the diamond surface (calculated from the kinetic theory of gases⁸) times the reaction probability R that a given collision leads to reaction,

$$\frac{1.6 \times 10^{13}}{n_c} = 3.52 \times 10^{22} \frac{P}{\sqrt{MT}} R, \quad (2)$$

where P is the growth species pressure in torr, M is the molecular weight of the growth species, and T is the temperature in degrees Kelvin. For $M = 15n_c$ and $T = 1438$ K, the growth species mole fraction is $X = 1.3 \times 10^{-7}/R\sqrt{n_c}$. Since $R \leq 1$ the mole fraction for the growth species must be at least $X_{\min} = 1 \times 10^{-7}$ (0.1 parts per million) for reasonable (i.e., small) values of n_c . This is our first constraint on the growth species.

Diamond growth acts as a sink for growth species, so in order to maintain a *steady state* concentration greater than X_{\min} the growth species must not be depleted faster than they are created and transported to the diamond seed crystals for reaction. From Eqn. (1), the diamond growth rate was 2.2×10^{-6} g/s, all of which mass must ultimately have come from CH_4 . This implies that at least 8.1×10^{16} CH_4 molecules reacted per second, and that at least $8.1 \times 10^{16}/n_c$ growth species were formed per second (unless CH_4 was itself the growth species). This is our second constraint on the growth species.

We have modeled the gas phase pyrolysis chemistry in this system in order to determine which hydrocarbons satisfied these two constraints in the system of Chauhan et al.⁷ Several approximations and assumptions were used; these are discussed in a separate section below.

The experiment is modeled as follows. We assume 1-dimensional flow so that the gas temperature and species concentrations depend only on the distance Z along the tube or reaction chamber. The gas is assumed to enter the 2.54 cm diameter flow tube at $Z = 0$, $T = 300$ K, and $v_0 = 94$ cm/s. The gas flows into the reaction chamber at $Z = 35.1$ cm and $T = 500$. Beyond that point the gas temperature is assumed to rise linearly with Z until it reaches a maximum of 1438 K at the crucible, taken to be at $Z = 40$. The temperature then falls slowly (heat loss to the relatively distant reaction chamber walls assumed small) to 1250 K as it exits the reaction chamber at $Z = 44.7$. For $Z > 44.7$, where the gas is again in a flow tube, the temperature drops to 500 K by $Z = 85$ cm. The gas velocity in the system is calculated assuming that the flux is given by $\rho v A = \text{constant}$, where ρ is the gas density and A is the cross sectional area of the tube or reaction chamber. We estimate that $v = 28$ cm/s at the crucible and that the gas has a residence time in the reaction chamber of 250 ms. The gas phase chemistry is modeled using the Sandia burner code⁹ together with

the reaction mechanism shown in Table I. A similar mechanism was successful in predicting the species concentration profiles in a number of premixed flat flames^{10,11}. Although the mechanism considers species as large as C_4H_6 , only the C_1 and C_2 part of the mechanism is shown since the concentrations of larger species are always extremely small and since the C_3 and C_4 chemistry is less well known. The pressure-dependent reactions shown in the Table are in the low pressure limit. Rate constants $k = AT^n e^{-E_a/RT}$ are given for the forward direction; rate constants for the reverse direction are calculated using thermodynamic data from the Chemkin data base¹², supplemented where necessary by other standard sources¹³.

Results

The predictions of the model are shown in Figure 1, which displays steady state profiles of all species that reach mole fractions of at least 10^{-14} . The reaction chamber is located between $Z = 35.1$ and 44.7 cm, and the crucible is located at $Z = 40$.

Chemical reaction is initiated in this system by the reverse of Reaction 2 of Table I (denoted A_{-2}) which produces H and CH_3 and which occurs only at the highest temperature positions near $Z = 40$. The H is rapidly consumed by A_3 , forming additional CH_3 . Within the reaction chamber the CH_3 mole fraction (and the mole fractions of many other species) is nearly independent of Z because the gas velocity there is low, and mixing by diffusion is rapid. As the CH_3 formed by A_{-2} and A_3 diffuses upstream toward the flow tube, it is consumed by A_{-3} , creating H atoms. CH_3 decay for $Z < 35.1$ is due mainly to A_{-14} , which is nearly irreversible at the low temperatures in the flow tube. C_2H_6 , formed mainly between $Z = 33$ and $Z = 35$ by A_{-14} , is for the most part carried downstream into the reaction chamber. However, some C_2H_6 diffuses upstream against a high gas velocity, giving the falloff in concentration for $Z < 34$. C_2H_5 (ethyl radical) is formed in the reaction chamber by both A_{12} and A_{13} , but near $Z = 40$ it decomposes rapidly via A_{15} to make C_2H_4 , accounting for the drop in the C_2H_5 mole fraction there. A_{17} produces small amounts of C_2H_2 at $Z = 40$. Some C_2H_4 and C_2H_2 formed there diffuse upstream into the flow tube.

Because of the low pressure (0.5 torr) and short residence time (250 ms) in the reaction chamber, the chemical reactions are far too slow for the CH_4/H_2 mixture to attain equilibrium. For example, at equilibrium the mole fraction of C_2H_2 at the crucible would be 0.19, thirteen orders of magnitude higher than shown in Figure 1. The equilibrium mole fractions of some other relevant species are $X_{CH_4}^{eq} = 3.2 \times 10^{-4}$, $X_H^{eq} = 2.8 \times 10^{-4}$, $X_{C_2H_4}^{eq} = 4.8 \times 10^{-5}$, $X_{C_2H_6}^{eq} = 3.6 \times 10^{-6}$, and $X_{CH_3}^{eq} = 2.7 \times 10^{-6}$. Comparing these values to those shown in Figure 1, it is clear that the assumption of equilibrium is totally unjustified in this system. We showed previously⁴ that the assumption of equilibrium is equally untenable during filament-assisted diamond growth. Instead, the compositions in these systems are kinetically controlled.

Discussion

The first conclusion we draw from Figure 1 is that aside from CH_4 ($X = 0.7$), only C_2H_6 and CH_3 have mole fractions above $X_{min} = 1 \times 10^{-7}$. Using Eqn. (2), we can calculate the reaction probability R required if we assume that one of these species is responsible for the observed diamond growth. The result is $R_{CH_4} \sim 10^{-7}$, while $R_{C_2H_6}$ and $R_{CH_3} \sim 10^{-1}$. To put these numbers into perspective, the reaction probability for CH_4 decomposing on pyrolytic carbon¹⁴ is 1.5×10^{-8} at 1438 K, with a roughly similar reaction probability for

C_2H_6 ¹⁵. Based on these data, the value required here for R_{CH_4} appears quite reasonable while that for $R_{C_2H_6}$ does not. On the other hand, a high value for R_{CH_3} is plausible, as CH_3 is a radical. $X_{C_2H_4}$ and especially $X_{C_2H_2}$ are so small that these species can be excluded from further consideration.

Although X_{CH_3} and $X_{C_2H_6}$ both exceed X_{min} , we must also consider our second constraint and estimate the rate that CH_3 and C_2H_6 could have been generated from CH_4 decomposition. For purposes of this analysis we will make two extreme assumptions: (1) Every molecule of CH_4 which reacted at all was converted permanently into CH_3 or C_2H_6 . That is, we ignore all reactions such as A_{-3} which destroyed either species. (2) No matter where in the system these species were formed, they were transported to the crucible for addition to the diamond seed crystals. With these two assumptions we can calculate an upper limit to the rate of diamond growth from CH_3 and C_2H_6 .

Our analysis shows that at steady state approximately 95% of the CH_4 that reacted did so via A_3 , with nearly all the rest reacting via A_{-2} . Thus, we can calculate the total number of CH_4 molecules reacting/s by evaluating for each Z the rates of these 2 reactions, shown in Figure 2, multiplying them by the volume element $dV = AdZ$, and then integrating with respect to Z . The result is that the calculated steady state reaction rate integrated over the entire apparatus is 1.8×10^{14} CH_4 molecules/s. Since this rate is nearly 500 times lower than that required by our second constraint, we conclude that neither CH_3 nor C_2H_6 (nor any other species) was produced in this system at a rate fast enough to contribute significantly to diamond growth. We infer that diamond growth occurred in this system by direct decomposition of CH_4 on the diamond surface.

It is interesting to compare growth of diamond from CH_4 with growth of pyrolytic carbon from C_2H_2 . The kinetics of the latter reaction can be described using a single Arrhenius expression between 600 and 1700 K with an activation energy of only 25 kcal/mole^{16,17}. Since it is unlikely that a reaction involving radicals made from C_2H_2 would have such a low activation energy at 600 K, we expect that the acetylene reaction forming pyrolytic carbon is also a direct molecular decomposition on the carbon surface. It is, however, substantially faster than the decomposition of CH_4 to make pyrolytic carbon or diamond.

As pointed out above, the value we obtained here for R_{CH_4} is similar to that for CH_4 decomposition on pyrolytic carbon^{14,16}. Furthermore, the 55 kcal/mole activation energy measured by Chauhan et al.⁷ (or the 58 kcal/mole activation energy measured by Tesner et al.¹⁸ for the same reaction) is similar to the 65 kcal/mole for addition of CH_4 to pyrolytic carbon¹⁷. Finally, we note that H_2 acts as an inhibitor to growth of both diamond⁷ and pyrolytic carbon¹⁴ in CH_4 systems. It is tempting to imagine that diamond and pyrolytic carbon growth are similar processes. If so, we would speculate that diamond—like pyrolytic carbon—can grow from a direct reaction of a variety of hydrocarbons¹⁶, although the reaction probabilities for different species could vary considerably. Continuing with this line of speculation, the propensity of different growth species to form pyrolytic carbon (rather than diamond) could be different. For example, a molecule such as C_2H_2 , with its multiple bonds, could be more likely to form pyrolytic carbon than CH_4 , which is already sp^3 bonded. (However, even CH_4 does produce pyrolytic carbon.) In that case, since the C_2H_2 concentration increases approximately as the square of the CH_4 concentration when CH_4 is the starting material, we would expect a deterioration in the quality of the diamond films grown with increasing CH_4 concentration. Such a deterioration is in fact observed².

Although one of the main conclusions of this work is that the diamond growth results of Chauhan et al.⁷ cannot be accounted for by C_2H_2 or CH_3 , we emphasize that our results do not contradict the calculations of Frenklach and Spear⁵ or Tsuda et al.⁶, who claimed that C_2H_2 or CH_3 is the principal growth species in filament- or plasma-assisted diamond film growth. Our results show, instead, that diamond films *can and do* grow from CH_4 , and that neither C_2H_2 nor CH_3 is required. However, given the roughly similar concentrations of CH_4 , CH_3 , C_2H_4 , and C_2H_2 under filament-assisted diamond growth conditions^{3,4}, C_2H_4 , C_2H_2 and/or CH_3 could well contribute more than CH_4 to diamond growth there.

Because some of the experimental parameters used in this modeling effort were not measured, we had to make a number of approximations and assumptions. In this section we consider how they affect our conclusions.

The most important approximation is that the temperature and species mole fraction fields were 1-dimensional. In fact, the wall temperatures were stated to be below 473 K, even at the location we have called $Z = 40$, where we have assumed a temperature of 1438 K. And we have not accounted for radical destruction which can take place on the walls. Thus, for both temperature and chemical reasons the walls are sinks for radicals. Because of the importance of diffusion in this system, processes which occur at the walls can be expected to have an impact at the crucible, 5 cm away. In our model we can simulate the presence of such a sink 5 cm from the crucible by changing the assumed temperature profile so that it drops to 500 K (instead of 1250 K) by $Z = 45$. This results in reductions by factors of 2-3 in X_{CH_3} and X_H and factors of 4-6 in $X_{C_2H_2}$ and $X_{C_2H_4}$. By no means does this simple exercise accurately take into account the effect of the walls. What it does show, however, is that the presence of the cool walls lowers the mole fractions of the pyrolysis products (species other than CH_4 and H_2). We conclude that the mole fractions shown in Figure 1 are upper limits to their true values, reinforcing our conclusion that no species besides CH_4 could have contributed significantly to diamond growth.

Beyond considering the walls as radical sinks, we have not attempted to model any possible heterogeneous chemistry taking place in this system. We do not expect that extraneous heterogeneous chemistry affected the diamond growth kinetics for three reasons. (1) The rate for pyrolytic carbon growth measured by Chauhan et al.⁷ is within a factor of 2 of the rate of pyrolytic carbon growth calculated from the formula of Fedoseev et al.¹⁴ for the same CH_4 and H_2 pressures but in the absence of any diamond. Since this difference is smaller than the experimental uncertainty, we conclude that the presence of diamond has no effect on the growth rate of pyrolytic carbon. Similarly, the analysis of Chauhan et al.⁷ shows that the presence of pyrolytic carbon does not affect the growth rate of diamond (except to the extent that it reduces the available diamond surface area). These results make plausible the assumption that extraneous heterogeneous chemistry on the diamond also did not affect the kinetics of diamond growth. (2) The kinetics of diamond growth was the same in flow tubes with hot (~ 1200 K)^{18,19} and cool (< 500 K)⁷ walls. We conclude that heterogeneous chemistry on walls of the system did not affect the kinetics of diamond growth. (3) The kinetics of diamond growth was unaffected when platinum, graphite, or quartz were used as crucibles^{7,19}. That even a highly active catalytic material such as platinum did not affect the kinetics of diamond growth is perhaps not surprising if the growth species was CH_4 .

References

1. R.C. DeVries, *Ann. Rev. Mater. Sci.* **17**, 161 (1987).
2. J.C. Angus and C.C. Hayman, *Science* **241**, 913 (1988).
3. (a) F.G. Celli, P.E. Pehrsson, H.-t. Wang, and J.E. Butler, *Appl. Phys. Lett.* **52**, 2043 (1988). (b) F.G. Celli, P.E. Pehrsson, H.-t. Wang, H.H. Nelson, and J.E. Butler, Second Diamond Technology Initiative Symposium, paper W-2, July 13, 1988.
4. S.J. Harris, A.M. Weiner, and T.A. Perry, *Appl. Phys. Lett.*, **53**, 1605 (1988).
5. (a) M. Frenklach and K.E. Spear, *J. Mater. Res.* **3**, 133 (1988). (b) M. Frenklach and K.E. Spear, Second Diamond Technology Initiative Symposium, paper W-8, July 13, 1988.
6. (a) M. Tsuda, M. Nakajima, and S. Oikawa, *J. Am. Chem. Soc.* **108**, 5780 (1986). (b) M. Tsuda, M. Nakajima, and S. Oikawa, *Japanese J. Appl. Phys.* **26**, L527 (1987).
7. a. S.P. Chauhan, J.C. Angus, and N.C. Gardner, *J. Appl. Phys.* **47**, 4746 (1976).
b. S. P. Chauhan, "Diamond Growth from Vapor at Low Pressurs," Thesis, Chemical Engineering Division, Case Institute of Technology, 1972.
8. G.A. Somorjai, "Principles of Surface Chemistry," Prentice-Hall, New Jersey.
9. (a) M.D. Smooke, *J. Comp. Phys.* **48**, 72 (1982). (b) R.J. Kee, J.F. Grcar, M.D. Smooke, and J.A. Miller, Sandia Report SAND85-8240, 1985.
10. S.J. Harris, A.M. Weiner, R.J. Blint, and J.E.M. Goldsmith, *Twenty-first Symposium (International) on Combustion*, The Combustion Institute, 1033 (1986).
11. S.J. Harris, A.M. Weiner, and R.J. Blint, *Combust. Flame* **72**, 91 (1988).
12. R.J. Kee, F.M. Rupley, and J.A. Miller, Sandia Report SAND87-8215, 1987.
13. (a) D.R. Stull, E.F. Westrum, and G.C. Sinke, *Chemical Thermodynamics of Organic Compounds*, Wiley, New York, 1969; (b) A. Burcat in *Combustion Chemistry* (W.C. Gardiner, Ed.), Springer-Verlag, New York, 1984, p. 455.
14. D.V. Fedoseev, S.P. Vnukov, and V.P. Varnin *Dokl. Akad. Nauk* **218**, 399 (1974).
15. D.V. Denisevich and P.A. Tesner, *Dokl. Akad. Nauk* **212**, 660 (1973).
16. S.J. Harris and A.M. Weiner, *Ann. Rev. Phys. Chem.* **36**, 31 (1985).
17. E.F. Aref'eva, I.S. Rafal'kes, and P.A. Tesner, *Khimiya Tverdogo Topliva (Solid Fuel Chemistry)* **11**, 113 (1977).
18. P.A. Tesner, A.E. Gorodetskii, E.V. Denisevich, A.P. Zakhorov, and T.V. Tehunova, *Dokl. Akad. Nauk* **222**, 1384 (1975).
19. B.V. Derjaguin and D.V. Fedoseev, *Carbon* **11**, 299 (1973).
20. J. Warnatz in *Combustion Chemistry* (W.C. Gardiner, Ed.), Springer-Verlag, New York, 1984, p. 197.
21. D.B. Olson and W.C. Gardiner, *Combust. Flame* **32**, 151 (1978).
22. (a) J.E. Butler, J.W. Fleming, L.P. Goss, and M.C. Lin, in "Laser Probes for Combustion Chemistry," ACS Symposium Series **134**, 397 (1980). (b) P. Glarborg, J.A. Miller, and R.J. Kee, *Combust. Flame* **65**, 177 (1986).
23. W.J. Pitz and C.K. Westbrook, *Combust. Flame* **63**, 113 (1986).

Table I

Methane/Hydrogen mechanism

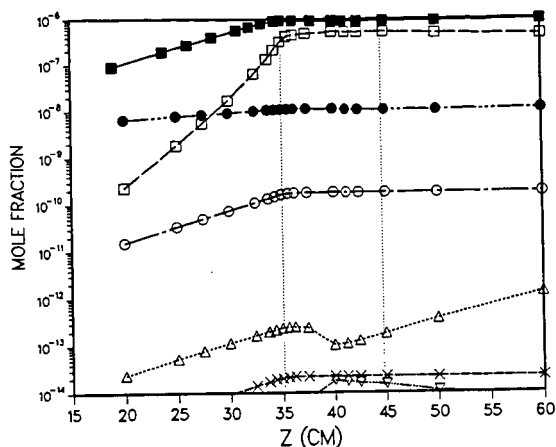
REACTIONS	A	n	E _a	Ref
A1) $H + H + M = H_2 + M$	9.7E+16	-0.6	0.0	20
A2) $CH_3 + H + M = CH_4 + M$	8.0E+26	-3.0	0.0	20 ^a
A3) $CH_4 + H = CH_3 + H_2$	2.2E+04	3.0	8.8	20
A4) $CH_4 + CH_2 = CH_3 + CH_3$	1.0E+13	0.0	0.0	21
A5) $CH_3 + CH_3 = C_2H_5 + H$	8.0E+14	0.0	26.5	20
A6) $CH_3 + H = CH_2 + H_2$	7.2E+14	0.0	15.1	21
A7) $CH_3 + CH_2 = C_2H_4 + H$	2.0E+13	0.0	0.0	21
A8) $CH_3 + M = CH_2 + H + M$	1.0E+16	0.0	90.6	20
A9) $CH_2 + H = CH + H_2$	4.0E+13	0.0	0.0	20
A10) $CH + CH_4 = C_2H_4 + H$	6.0E+13	0.0	0.0	22
A11) $CH + CH_3 = C_2H_3 + H$	3.0E+13	0.0	0.0	22
A12) $C_2H_6 + H = C_2H_5 + H_2$	5.4E+02	3.5	5.2	20 ^b
A13) $C_2H_6 + CH_3 = C_2H_5 + CH_4$	5.5E-01	4.0	8.3	20 ^b
A14) $C_2H_6 + M = CH_3 + CH_3 + M$	1.0E+19	0.0	68.0	20 ^b
A15) $C_2H_5 + M = C_2H_4 + H + M$	1.0E+17	0.0	31.0	20 ^b
A16) $C_2H_5 + CH_3 = C_2H_4 + CH_4$	7.9E+11	0.0	0.0	23
A17) $C_2H_4 + M = C_2H_2 + H_2 + M$	2.6E+17	0.0	79.4	20 ^b
A18) $C_2H_4 + M = C_2H_3 + H + M$	2.6E+17	0.0	96.6	20
A19) $C_2H_4 + H = C_2H_3 + H_2$	1.5E+14	0.0	10.2	20
A20) $C_2H_4 + CH_3 = CH_4 + C_2H_3$	4.2E+11	0.0	11.2	20
A21) $C_2H_3 + H = C_2H_2 + H_2$	2.0E+13	0.0	0.0	20
A22) $C_2H_3 + M = C_2H_2 + H + M$	3.0E+15	0.0	32.0	20
A23) $C_2H_3 + CH_3 = C_2H_2 + CH_4$	7.9E+11	0.0	0.0	23
A24) $C_2H_2 + M = C_2H + H + M$	4.0E+16	0.0	107.0	20
A25) $C_2H_2 + H = C_2H + H_2$	6.0E+13	0.0	23.7	20

$k = AT^n e^{-E_a/RT}$, $R = 1.99 \times 10^{-3}$ kcal/mole-deg

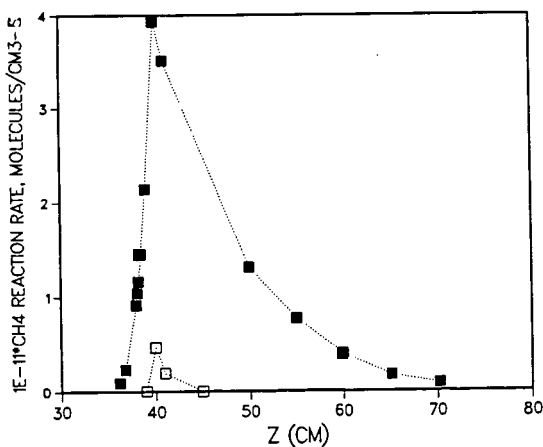
Units are cm³, moles, seconds, kilocalories

^a Results at $Z = 40$ are more sensitive to the value of this rate constant than to any other rate constant.

^b Results at $Z = 40$ show significant sensitivity to the value of this rate constant.



1. \log_{10} of mole fractions of all species calculated to have mole fractions of at least 10^{-14} . The vertical dotted lines indicate the location of the reaction chamber; the crucible holding the diamond seed crystals is at $Z = 40$ cm. Solid squares, C_2H_6 ; open squares, CH_3 ; solid circles, H ; open circles, C_2H_4 ; triangles, C_2H_5 ; crosses, C_2H_2 ; inverted triangles, CH_4 and H_2 , with mole fractions of 0.7 and 0.3, respectively, are not shown.



2. Molecules of CH_4 which reacted/cm³-s as a function of Z . Solid squares, Reaction A_1 : $CH_4 + H \rightarrow CH_3 + H_2$. Open squares, Reaction A_{-2} : $CH_4 + M \rightarrow CH_3 + H + M$. For this analysis these reactions are considered only in the direction indicated by the arrows.

DIAGNOSTICS OF FILAMENT-ASSISTED DIAMOND GROWTH CHEMISTRY

F.G. Celii,* P.E. Pehrsson and J.E. Butler
Chemistry Division, Naval Research Laboratory, Washington, D.C. 20375-5000

ABSTRACT

The use of in-situ optical diagnostics for probing the gas phase in the chemical vapor deposition (CVD) of diamond is described. Radical species (H and CH_3) as well as stable molecules (CH_4 , C_2H_2 , C_2H_4) have been detected with these techniques. We summarize here the results of resonance-enhanced multiphoton ionization (REMPI) studies and infrared diode laser absorption measurements made under filament-assisted diamond CVD conditions. The concentrations of two potential carbon-transport species, CH_3 and C_2H_2 , both increased as a function of the initial CH_4/H_2 fraction (F_0), whereas the H atom concentration decreased with increasing F_0 . In conjunction with known diamond film growth results, we interpret these observations as evidence for the *surface* role of atomic hydrogen in the diamond growth mechanism.

INTRODUCTION

Diamond has outstanding material properties, such as extreme hardness and high thermal conductivity.[1] The same properties make diamond exceedingly difficult to modify (*e.g.*, by machining or doping). Modification could in principle be more easily accomplished during vapor phase deposition, so the prospect of CVD-synthesized diamond is of great practical importance. Various diamond CVD techniques have already been demonstrated,[2] but development of improved deposition methods will be hindered without an understanding of the diamond formation mechanism. The fact that CVD diamond growth proceeds under temperature and pressure conditions at which graphite is the stable carbon form indicates that a delicate balance is needed for growth. Diamond deposition might be further manipulated once the mechanisms leading to this balance are understood.

Much insightful work has led to an empirical understanding of the diamond growth environment. Supersaturation of atomic hydrogen is crucial[3] for diamond deposition, although its exact role in the growth process is not clear. The postulated carbon-transport species have generally been hydrocarbon pyrolysis products, notably CH_3 , [3,4] CH and atomic carbon.[5] Other proposed mechanisms[6-8] find low calculated activation barriers based on C_2H_2 [6], or $\text{CH}_3^+/\text{CH}_3$ [7] as the active growth species. Only recently have in-situ gas phase measurements[9-11] been performed enabling testing of these hypotheses. We report here on determinations of the filament-assisted diamond growth chemistry made through the use of spectroscopic probes.

EXPERIMENTAL

The chamber used for both the deposition of diamond films and the infrared absorption measurements was described previously.[9] Briefly, a tungsten filament was suspended 1.5 cm above a substrate (*e.g.*, Si wafers or Ni foil) and mounted in the center of a stainless steel 6-way cross. Typical growth conditions included a slow flow (100 sccm) of <1.0% CH_4 in H_2 at 25 Torr total pressure, and a tungsten filament temperature (T_{fil}) of ~ 2000 C (measured with a 2-color pyrometer). The substrate, heated by radiation and convection, was maintained

in a temperature range necessary for diamond growth (~ 900 C).

Mirrors were mounted inside the chamber to provide a multi-pass geometry for the infrared absorption measurements. The diode laser beam passed ~ 20 times through the chamber, including a region located few mm above the substrate, before being focussed onto an infrared detector. Molecular species within the pathlength resonantly absorb the tunable IR light and are detected by the concomitant power loss at the detector. For the REMPI experiments, a focussed dye laser beam ($1-15$ mJ/pulse, $\Delta\nu \sim 0.2$ cm^{-1}), made 1 or 2 passes through the chamber. The substrate holder was biased ($\sim 150\text{V}$) to provide efficient collection of photoelectrons (generated by the MPI process) at a Pt probe wire inserted 2-4 mm above the substrate and 1-2 mm from the focal volume of the laser.[11]

RESULTS AND DISCUSSION

The films deposited in this chamber were analyzed with a variety of techniques which definitively established diamond deposition: SEM micrographs showed faceted crystallites, whether isolated or in polycrystalline films; Raman spectra exhibited an intense, sharp 1332 cm^{-1} band, with little evidence for graphitic or amorphous carbon; small-spot Auger electron spectroscopy detected only carbon, with a lineshape similar to that of natural diamond; x-ray diffraction spectra yielded a diamond lattice constant.[9] All spectroscopic investigations were conducted under similar diamond growth conditions, although deposits were not always analyzed.

With $F_0 = 0.5\%$ and $T_{fil} = 2000$ C, the following gas phase species concentrations present during diamond CVD were determined from infrared absorption measurements: CH_4 , $8 \pm 3 \times 10^{14} \text{cm}^{-3}$ (~ 50 mTorr @ 300 C); CH_3 , $2 \bullet 1.5 \times 10^{12}$; C_2H_4 , $6 \pm 2 \times 10^{12}$; and C_2H_2 , $2 \pm 1 \times 10^{14}$. No absorption lines due to C_2H_6 or stable C_3H_y species were found. Experiments to follow the concentration of these species as a function of various growth parameters are currently in progress.

The IR observations can be qualitatively understood by consideration of the initial gas mixture at elevated temperatures ($1300 < T < 2500$ C), where C_2H_2 is the thermodynamically-favored carbon-containing molecule. Various hydrocarbon fuels would be predicted to generate similar species by this technique. Detection of transient species (i.e., C_2 , CH and C_3), which are predicted by the thermodynamic model to be present in detectable concentrations, was attempted using laser-excited fluorescence (LEF), but only C_3 was tentatively identified. The absence of ground state C_2 and CH in detectable concentration indicates that while these species may be produced at the hot filament, they are consumed by reactions occurring at lower temperature during transport to the surface. Both CH and C_2 have been detected from their excited-state optical emission spectrum during plasma-assisted diamond growth, but were not present in sufficient quantity to account for the observed rate of filament-assisted diamond growth. The observed concentrations of CH_4 , CH_3 , C_2H_2 or C_2H_4 could account for the diamond deposition rate.

Using in-situ mass spectrometric analysis, Harris, *et al.*[10] also observed significant conversion of CH_4 to C_2H_2 in a filament-assisted diamond CVD chamber. The radical species concentrations predicted by their kinetic modeling study are in agreement with our observations. It was concluded that the probable carbon-transport species in this system are CH_3 , C_2H_2 , CH_4 and C_2H_4 , with preference given to CH_3 and C_2H_2 based on reactivity.[10]

The 2+1 REMPI band at 333.5 nm[12] was employed for in-situ detection of CH_3 . The spatial resolution of the REMPI detection provides relative concentration measurements in a

volume directly above the growth surface. In Fig. 1, the C_2H_2 concentration derived from the IR absorption measurements is compared with the CH_3 REMPI signal. Note that for $F_0 = 0.5\%$ the average CH_3 concentration through the diode beam path is about 2 orders of magnitude lower than that of C_2H_2 . Both species concentrations increased for increased F_0 , with C_2H_2 growing at perhaps a faster rate.

To monitor the concentration of atomic hydrogen, the REMPI technique was employed, with specific detection provided by the 3+1 resonant transition at 364.7 nm.[13] An interference effect was observed in the single pass (travelling wave-TW) geometry due to the generation of third harmonic light, manifested by the absence of the resonant REMPI feature at 364.68 nm. The resonant REMPI peak was obtained using standing-wave (SW) excitation (a spherical mirror re-focussed the UV beam back along the optical axis). The observations are consistent with theoretical predictions[14] and experimental verifications (in rare gases)[15] of an interference effect between odd harmonics of the laser field (in this case, the first and third harmonics, at 364.7 nm and 121.6 nm, respectively).

The hydrogen atom concentration can be monitored using the intensity of the resonant REMPI signal from the SW excitation geometry. The T_{fil} dependence of the 365.68 nm feature for pure H_2 (Fig. 2(a)) agrees with the thermodynamics for H_2 dissociation. The signal attenuation at $F_0 = 0.5\%$ and 1.0% reflects a loss in H atom flux in a probed volume located 8 mm from the filament, probably due to gas-phase reactions. The $F_0 = 3\%$ curve (Fig. 2(d)) suggests a poisoning of the filament surface resulting in severely reduced H atom concentration for T_{fil} less than 2200 C. The poisoning, perhaps related to a tungsten carbide phase, might be avoided with the use of alternate filament materials, such as rhenium.

For CH_4 in H_2 , it has been shown that $F_0 < 1\%$ is necessary for growth of reasonable purity diamond. The diminished H atom flux for $F_0 > 1\%$ correlates with observations[16,17] of increased deposition of graphitic and amorphous carbon under these conditions; however, the measured concentration of CH_3 and C_2H_2 both increase with F_0 , even for $F_0 > 1\%$ (Fig. 1). We interpret these results as suggesting that the dominant role played by atomic hydrogen in diamond CVD is surface-related (e.g., dangling surface bond termination, preparation of active surface sites, and/or preferential etching of non-diamond forms of carbon), rather than generation of gas-phase intermediates.

SUMMARY

Our present model of the filament-assisted gas phase environment, in concert with that of Harris, *et al.*, [10] is one in which thermodynamically-favored species (e.g., C_2H_2 , CH_3) are formed at high temperature near the filament, followed by depletion of the more reactive species during transport to the diamond growth surface. The carbon-transport, or growth, species for this system may be CH_4 , C_2H_4 , CH_3 or C_2H_2 , but CH and C₂ do not appear to play a significant role in carbon deposition. Some aspects of polycrystalline diamond film growth correlate with hydrogen atom concentration, and we conclude that the interaction of hydrogen atom with the growing diamond surface is important, while the role of H atoms in gas phase chemistry appear to be less important.

ACKNOWLEDGEMENTS

We thank Drs. John Reintjes, Steve Harris, H. Doug Ladouceur and Ms. Tina Shih for helpful and insightful discussions. This work was supported in part by the Office of Naval Research.

REFERENCES

- * National Research Council Postdoctoral Fellow.
1. Field, J. E. "*The Properties of Diamond*," Academic Press, New York, 1979.
 2. See, for example: Angus, J. C., Will, H. A. and Stanko, W. S. *J. Appl. Phys.*, 1968, 39, 2915; Spitsn, B. V., Bouilov, L. L. and Derjaguin, B. V. *J. Cryst. Growth*, 1981, 52, 219; Kamo, M., Sato, Y., Matsumoto, S. and Setaka, N. *J. Cryst. Growth*, 1983, 62, 642; Sawabe A. and Inzuka, T. *Appl. Phys. Lett.*, 1985, 46, 146; Kasi, S., Kang, H. and Rabalais, J. W. *Phys. Rev. Lett.*, 1987, 59, 75.
 3. For excellent reviews, see: DeVries, R. C. *Ann. Rev. Mater. Sci.*, 1987, 17, 161; Angus, J. C. and Hayman, C. C. *Science*, 1988, 241, 913; Badzian, A. R. and DeVries, R. C. *Mat. Res. Bull.*, 1988, 23, 385; Derjaguin, B. V. and Fedoseev, D. B. *Sci. Amer.*, 1968, 233 (5) 102.
 4. Hirose, Y. and Terasawa, Y. *Jap. J. Appl. Phys.*, 1986, 25, L519.
 5. Matsumoto, S., Sato, Y., Tsutsumi, M. and Setaka, N. *J. Mater. Sci.*, 1982, 17, 3106.
 6. Frenklach, M. and Spear, K. E. *J. Mater. Res.*, 1988, 3, 133; Huang, D., Frenklach M. and Maroncelli, M. *J. Phys. Chem.*, 1988, 92, 6379.
 7. Tsuda, M., Nadajima, M. and Oikawa, S. *J. Amer. Chem. Soc.*, 1986, 108, 5780.
 8. Sommer, M., Mui, K. and Smith, F. W. *Appl. Phys. Lett.*, in press.
 9. Celii, F. G., Pehrsson, P. E., Wang, H. -t. and Butler, J. E. *Appl. Phys. Lett.*, 1988, 52, 2043.
 10. Harris, S. J., Weiner, A. M. and Perry, T. A. *Appl. Phys. Lett.*, 1988, 53, 1605.
 11. Celii, F. G. and Butler, J. E. *Appl. Phys. Lett.*, submitted for publication.
 12. Hudgens, J. W., DiGuseppe, T. G. and Lin, M. C. *J. Chem. Phys.*, 1983, 79, 571.
 13. Tjossem, P. J. H. and Cool, T. A. *Chem. Phys. Lett.*, 1983, 100, 479.
 14. Jackson, D. J. and Wynne, J. J. *Phys. Rev. Lett.*, 1982, 49, 543; Payne, M. G., Garrett, W. R. and Ferrell, W. R. *Phys. Rev. A*, 1986, 34, 1143.
 15. Glownia, J. H. and Sander, R. K. *Phys. Rev. Lett.*, 1982, 49, 21.
 16. Singh, B., Aric, Y., Levine, A. W. and Mesker, O. R. *Appl. Phys. Lett.*, 1988, 52, 451.
 17. Zhu, W., Randall, C., Badzian, A. R. and Messier, R., to be published.

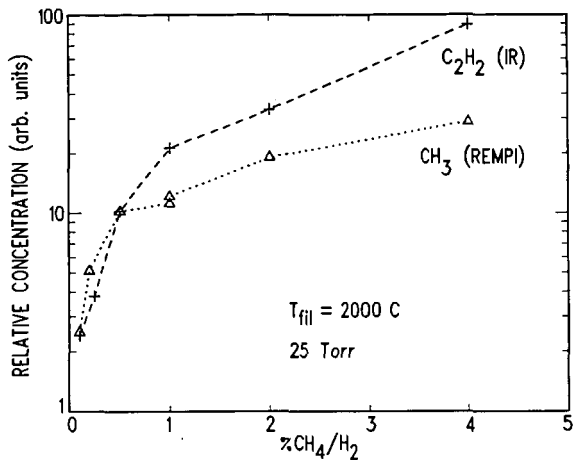


Figure 1: Relative concentrations of C₂H₂ (crosses, from infrared absorption), and CH₃ (triangles, REMPI data) vs. F₀. The IR measurements were not spatially resolved.

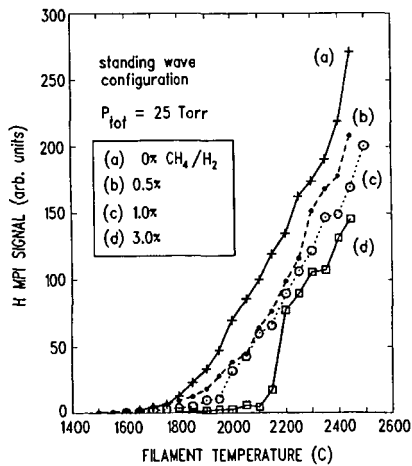


Figure 2: Relative H atom concentrations vs. filament temperature. The lines are merely to connect data points for each initial F₀ value, given in the figure. All data are for a filament-probe separation of 8 mm.

Ultrasensitive Absorption Spectroscopy
by Intracavity Laser Techniques

George H. Atkinson and James J. O'Brien
Department of Chemistry and Optical Sciences Center
University of Arizona, Tucson, Arizona 85721

INTRODUCTION

Diagnostic techniques which can be used to monitor spectroscopically the gas phase during the chemical vapor deposition (CVD) of material on a substrate are of significant value both in the analysis of reaction mechanisms and in the real time control of deposition conditions. The *in situ* detection of gas phase intermediates during CVD is of special importance in obtaining a realistic understanding of the mechanism(s) underlying the preparation of a specific deposited material. These *in situ* diagnostic measurements also can be utilized to optimized processing conditions.

Laser induced fluorescence (LIF) has often been used to monitor reaction intermediates because of its high sensitivity for detecting gas phase molecules. Many chemical conditions which facilitate CVD, however, are not well suited for LIF spectroscopy due to highly reactive environments and pressure conditions which quench emission yields or because of the large amounts of background emission created by the dissociative processes, e.g., during plasma discharge. By contrast, absorption spectroscopy has long been recognized as a widely applicable technique which can be readily utilized in chemical, pressure, and radiation conditions not conducive to LIF detection. The major limitation is sensitivity which in conventional absorption spectroscopy has prevented its application to monitoring low concentrations of molecules and radical concentrations.

Recently, the limited detection sensitivity of absorption spectroscopy has been addressed through the development of intracavity laser spectroscopy (ILS) [1,2]. ILS techniques have been used in a variety of instrumental configurations to demonstrate enhanced detection sensitivities for absorption measurements of many orders of magnitude relative to conventional absorption spectroscopy [1,2]. The enhanced sensitivity derives from the competition between the gain in the laser medium and the wavelength-dependent losses within the laser resonator. By placing the species of interest inside the optical resonator cavity of a longitudinally multimode laser, the absorption spectrum of the intracavity atomic or molecular species is superimposed on the wavelength-dispersed spectrum of the laser output.

EXPERIMENTAL

The ILS laser system is shown schematically in Figure 1. A modified dye laser (Coherent 590) is pumped by an argon ion laser (Coherent I-53-8 or Coherent I-53-18). The pumping radiation is attenuated as a function of time (33 Hz) by passing it through an acousto-optic modulator (AOM1). AOM1 diverts enough pump power to prevent the dye laser from reaching threshold conditions. When AOM1 is switched off, the pump laser brings the dye laser rapidly above threshold (~0.15 μ s). The dye laser output passes through a second acousto-

optic modulator (AOM2) which deflects part of the dye laser output to the spectrometer. The wavelength-dispersed radiation exiting the spectrometer is focused onto the face of an intensified vidicon camera. Such multichannel detection makes it feasible to monitor substantial portions of the rovibronic absorption spectrum of the intracavity species in real time.

The period of time during which the dye laser operates above threshold and AOM2 remains open determines the generation time, t_g , of the ILS laser system [3]. It has been shown that the intracavity absorption obeys a Beer-Lambert relationship with the equivalent pathlength of absorption, L_{eq} , given by $L_{eq} = R \cdot t_g \cdot c$ where R is the ratio of the pathlength of the laser through the intracavity absorber to the length of the laser resonator cavity and c is the velocity of light. For the results presented here, L_{eq} was in the range of 3 - 50 km.

The wavelength of the ILS dye laser is controlled by angle tuning an intracavity pellicle. The spectral bandwidth of the dye laser is 0.8 nm (22 cm^{-1}) and the overall spectral resolution of the detection system is about 95000 (0.18 cm^{-1}). The spectra presented here are a composite of a number of individual spectra obtained from overlapping wavelength regions.

Contained within the 1 m long cavity of the dye laser is the sample cell. It is equipped with 0.5 inch thick, fused-silica windows positioned at Brewster's angle. During the CVD process, these windows are continuously flushed with hydrogen or argon to prevent contamination by any particulate products of the decomposition which would render the cell windows opaque to the transmission of the laser radiation. The sample cell is modular in design consisting of sections of quartz tubing joined together using stainless steel fittings (Cajon Ultra-Torr). Decomposition of the source material in the intracavity cell is accomplished by (1) a microwave discharge in an Everson-Broida cavity operated at ~100 W and in a geometry concentric with the laser axis or (2) pyrolysis in an 1500 W tube furnace surrounding the central 6" section of the cell. The various gases used are introduced into the cell by stainless steel handling systems which include flowmeters and mass flow controllers.

In order to examine resulting deposited films, 1/4" x 1/2" sections of oxidized (~1 μm thick) silicon wafer are placed inside the decomposition zone of the intracavity CVD cell. The surface composition of the films prepared by the CVD processes are examined by XPS analysis.

RESULTS AND DISCUSSION

We have previously reported the ILS detection of silylene (SiH_2) in the microwave discharge decomposition of silane in argon [4,5]. Electronically excited argon and H_2 species are observed also under some of these conditions. Different concentrations of SiH_2 are observed by ILS in the microwave discharge decomposition of phenylsilane, ethylsilane and ethyltrichlorosilane under similar experimental conditions. Since several studies [6] have indicated that SiH_2 is a dominant precursor to Si and $\alpha\text{-Si-H}$ deposition, its detection is of special importance in examining source materials for the preparation of silicon.

Figure 2 shows a section of the ILS spectrum observed during the pyrolysis of silane at 750 °C and with a total pressure of 6.2 Torr in a 1:1 mix with H₂. The wavelength region is within the (0,3,0)-(0,0,0) vibronic band in the A-X transition of SiH₂. Almost all the absorption features in this spectrum are due to known transitions of SiH₂. Spectra in this wavelength region also have been obtained during the pyrolysis of a number of organosilanes. Different relative intensities of SiH₂ absorption transitions are observed under similar pyrolysis conditions. For example, more intense SiH₂ absorptions can be observed in the pyrolysis of ethylsilane than in the pyrolysis of silane.

A primary obstacle to the use of organosilanes for the CVD of silicon is the seemingly inevitable incorporation of carbon in the resulting silicon films. It is thought that carbon deposition under these conditions occurs via a polymeric process [7]. As a consequence, the radical C₂ is a possible gas phase precursor to carbon incorporation in the films. Figure 3 shows a section of the ILS spectrum obtained of the microwave discharge decomposition of 0.1 Torr of acetylene in 0.8 Torr of argon in the region of the 0-1 band head of the C₂ Swan system [8].

Both the SiH₂ and C₂ ILS absorption spectra are recorded under real time, *in situ* CVD conditions which produce deposited films. In the case of pyrolysis of silane (Figure 2), XPS analysis of the deposited material show that it is essentially pure crystalline silicon. The XPS analysis of the films produced during the plasma discharge of acetylene demonstrate a pure carbon composition. The short (1-5 sec) accumulation times for these ILS data facilitate the control and optimization of CVD conditions through diagnostic measurements of gas phase species.

Stable molecules also can be monitored directly by ILS through either allowed (e.g., visible electronic transitions of NO₂ [9,10]) or forbidden absorptions (e.g., vibrational overtone transitions in the ground electronic state of CH₄ [11,12]). Although the latter overtone transitions are of particular interest in astronomical spectroscopy [13], they also may be used in absorption diagnostics via ILS. Figure 4 presents the overtone absorption spectrum of CH₄ recorded by ILS near 682 nm for a room temperature sample (610 Torr). The absorption strength of this line has been measured by ILS [11,12] as have collisional broadening parameters [12].

The diagnostic capabilities of ILS in CVD have one additional experimental characteristic which can be of significant practical advantage. Since the spectral information is contained on the laser beam which exits the dye laser cavity, the ILS data can be transmitted over optical fibers. It has recently been demonstrated that absorption data recorded by ILS can transverse an optical fiber without significant distortion [14].

REFERENCES

1. G.H. Atkinson, in Advances in Chemical Reaction Dynamics (P.M. Rentzepis and C.Capellos, eds.) (1986) 207.
2. J.J. O'Brien, N. Goldstein, and G.H. Atkinson in Laser Applications in Chemical Dynamics (M.A. El-Sayed, ed.) (1987) 87-95.
3. F. Stoeckel and G.H. Atkinson, Appl. Optics, 24 (1985) 3591.
4. J.J. O'Brien and G.H. Atkinson, Chem. Phys. Lett., 130 (1986) 321.

5. J.J. O'Brien and G.H. Atkinson, *J. Phys. Chem.* **92** (1988) 5782.
6. For example, B.A. Scott, R.M. Plecenik and E.E. Simonyi, *Appl. Phys. Letters* **39** (1981) 73.
7. J.S. Francisco, S.A. Joyce, J.I. Steinfeld and F. Walsh, *J. Phys. Chem.* **88** (1984) 3098.
8. J. G. Phillips, *Ap. J.* **108** (1948) 434.
9. G.H. Atkinson, T. Heimlich and M.W. Schuyler, *J. Chem. Phys.* **66** (1977) 5002.
10. N. Goldstein, T.L. Brack and G.H. Atkinson, *Chem. Phys. Lett.* **116** (1985) 223.
11. E.N. Atonov, E.B. Berik and V.G. Koloshnikov, *J. Quant. Spectrosc. Radiat. Transfer* **22** (1979) 45.
12. J.J. O'Brien, P. Cvijin Vujkovic, K. Wells, D. Hunten, J. Lunine, and G.H. Atkinson (unpublished results).
13. L.P. Giver, *J. Quant. Spectrosc. Radiat. Transfer* **19** (1978) 311.
14. J.J. O'Brien, W. Torruellas and G.H. Atkinson, *Appl. Optics.* **26** (1987) 4563.

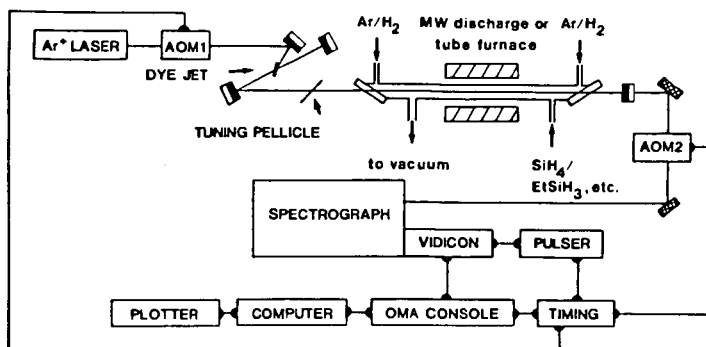


Figure 1. Instrumentation used for intracavity laser spectroscopy of gaseous species produced in the pyrolytic and/or microwave discharge decomposition of source compounds for SiH₂.

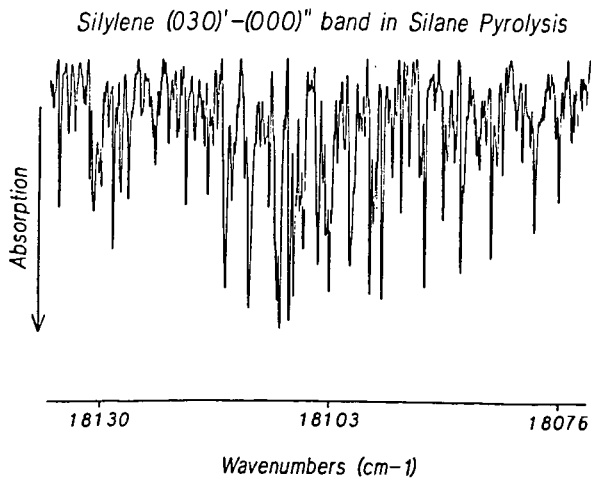


Figure 2. ILS spectrum for the pyrolysis of 52% silane in H₂ at 8.5 Torr of total pressure and with T₀ = 800 °C (t₀ = 125 μs). This spectrum is in the region of the strongest transitions of the (030)⁺ - (000)⁺ band of SiH₂. The base line corresponds to zero laser intensity, i.e., 100% absorption.

(0-1) band head of C-C Swan system

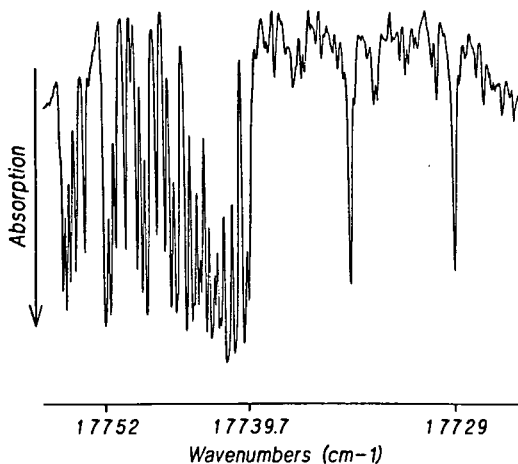


Figure 3. ILS spectrum of a microwave discharge of C_2 acetylene in argon at 0.7 Torr total pressure. The spectrum is centered at the (0-1) bandhead of the C, Swan system.

ILS spectrum of Methane at 610 torr & 295 K

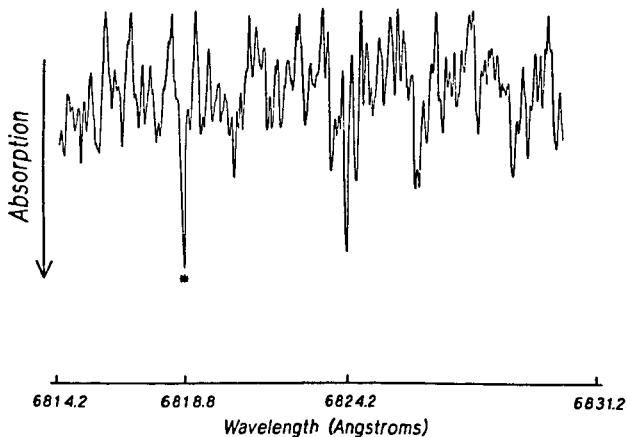


Figure 4. The ILS spectrum of a part of the 682 nm band of methane (assigned as $2v_2 + 3v_3$). This spectrum is a composite of individual spectral profiles and is obtained by joining together spectral profiles recorded for overlapping spectral regions. The most prominent feature is labeled by an asterisk (*).

DIAGNOSTICS AND MODELING OF PLASMA PROCESSES

Richard A. Gottscho
AT&T Bell Laboratories, Murray Hill, NJ 07974

INTRODUCTION

The full exploitation of rf and dc glow discharges for microelectronic and photonic device fabrication, coherent and incoherent light sources, and high voltage switching will only be realized when we have reliable numerical models with which processes can be simulated. It is perhaps ironic that we can simulate device operation¹ in great detail but must resort to trial and error development for device fabrication. This dichotomy is more remarkable when one realizes that the physics of semiconductor devices and plasma reactors are identical. Chemistry complicates the modeling of plasma reactors.

This talk will focus on recent fluid models of discharge physics and *in situ*, non-intrusive diagnostic experiments designed to test these models.²⁻⁸ Specific examples related to diamond film growth and hydrogen-containing plasmas will be highlighted as appropriate. Emphasis will be placed on experimental and theoretical results for electric fields, ion densities, reactive atomic concentrations, and degrees of dissociation.

ELECTRIC FIELDS

Consider sheath electric fields. Understanding the magnitudes and shapes of sheath fields constitutes the most basic understanding of a discharge. The local sheath field depends on not only the applied field but also the space charge distribution. In one dimension, Poisson's equation is solved to obtain the local field:

$$\frac{\partial E}{\partial x} = \frac{e}{\epsilon_0} (n_p - n_e - n_n) \quad (1)$$

where n_p , n_e , and n_n are the positive ion, electron, and negative ion densities, respectively, and E is the electric field. Electric fields can be measured non-intrusively and with high spatial and temporal resolution by exploiting molecular and/or atomic Stark effects.^{6,9-12} Positive ion densities in Eq. 1 can be measured by laser-induced fluorescence spectroscopy.¹³⁻¹⁵ Negative ions can be probed using photodetachment spectroscopy.^{7,8,16} Combined, this set of measurements provides stringent tests for theory.

LOCAL FIELD AND BEAM ELECTRON MODELS

The simplest fluid theories entail the solution of Poisson's equation above coupled with equations of continuity for ion and electron densities:

$$\frac{\partial n_i}{\partial t} + \frac{\partial (n_i u_i)}{\partial x} = F - L \quad (2)$$

where i denotes p , e , or n , u is the average (fluid) velocity, F is the rate of formation, L is the rate of loss. When the local field approximation is valid, *i.e.* the collisional mean free paths are much smaller than the distances over which electric fields and densities change significantly, the source and loss terms in Eq. (2) can be expressed as functions of just E/N . Following this approach, Boeuf² recently calculated sheath fields and charge densities in rf discharges through He and obtained good *qualitative* agreement with measurements of sheath electric fields in both low and high frequency discharges containing BCl_3 .⁶

Although the local field approximation works reasonably well for electric fields and current-voltage characteristics, it fails miserably for the calculation of ionization and excitation rates. In the sheaths, the electric field varies so rapidly in both space (and time for rf discharges) that the electron energy distribution and electron-impact collision rates are not unique functions of the local value of E/N . To deal with this problem, Graves *et al.* and Sawin *et al.* have expressed the ionization rate coefficient as a function of the average electron energy, which is determined by solving the electron energy conservation equation simultaneously with the continuity and Poisson equations.³⁻⁵ In this fashion, excellent agreement was obtained between calculated and measured space-time dependent optical emission intensities in high frequency discharge.^{5,17}

An alternative approach to using an electron energy balance equation is to use electron beam models.¹⁸⁻²⁰ Electrons created by secondary emission processes at the cathode are considered as a separate group from bulk electrons. Continuity and energy balance equations for these ballistic or beam electrons are solved along with Poisson's equation and continuity equations for bulk electrons and ions. Results from such beam models show good agreement with experiment.²⁰

MULTI-DIMENSIONAL EFFECTS

Up until now, the modeling of dc and rf discharges has been mostly limited to one-dimensional systems. Although most parallel-plate reactors can be operated in quasi-one-dimensional regimes and careful experimental design can ensure one-dimensional measurements, most plasma processes do not utilize well-confined discharges. Thus, multi-dimensional effects are important. Recent work at low frequency shows that the electron-beam model is a useful framework within which the ion transport and electric field profiles of asymmetrical parallel-plate discharges can be understood.²¹ For example, radial ion density profiles are non-uniform in asymmetrical discharges because the electron beam responsible for ionization has smaller cross sectional area when the small electrode is the momentary cathode than when the large electrode is the momentary cathode. Because the electron beam is created mostly by ion-impact collisions with the electrodes, the non-uniformity is reinforced on every half-cycle. These effects lead directly to non-uniform thin film etching and deposition rates. Although beam models qualitatively explain a variety of ion density and electric field measurements in these asymmetrical discharges, it remains to model these data self-consistently and quantitatively.

REACTIVE SPECIES

Another area for model improvement involves the prediction of reactive species densities.

Although there are numerous models for predicting these quantities, they generally lack self-consistency. The models have either been semi-empirical or have made assumptions about the electric field profile. The simplest chemical discharges to model are those through diatomic gases such as N_2 or H_2 . Using 2 photon laser-induced fluorescence, the concentrations of reactive atoms such as N and H can be measured and compared to the results of fluid simulations.^{15,22-24} Using spontaneous Raman spectroscopy, it should be possible to calibrate these measurements and also determine the degree of dissociation.²⁵

SUMMARY

The use of reliable discharge models for predicting sheath electric field profiles, ion and electron currents, reactive species concentrations, and degrees of dissociation will alleviate the tortuous nature of trial-and-error process development. The optimal process parameter space can be derived more rapidly, key parameters for improved process control can be more readily identified, and data from process monitors can be more easily interpreted and exploited in a feedback control system.

REFERENCES

- [1] For example see C.M. Snowden, Rep. Prog. Phys. **48**, 223 (1985).
- [2] J.P. Boeuf, Phys. Rev. Lett. **36**, 2782 (1987).
- [3] D.B. Graves and K.F. Jensen, IEEE Trans. Plasma Sci. **14**, 78 (1986).
- [4] A.D. Richards, B.E. Thompson, and H.H. Sawin, Appl. Phys. Lett. **50**, 492 (1987).
- [5] D.B. Graves, J. Appl. Phys. **62**, 88 (1987).
- [6] R.A. Gottscho, Phys. Rev. A. **36**, 2233 (1987).
- [7] R. A. Gottscho and C. E. Gaebe, IEEE Trans. Plasma Science **14**, 92 (1986); J. Vac. Sci. Technol. A **4**, 1795 (1986).
- [8] C.E. Gaebe and R.A. Gottscho, "Laser (and other) diagnostics of rf discharges," in *Radiative Processes in Discharge Plasmas*, edited by J.M. Proud and L.H. Luessen, Plenum (1986), p. 495.
- [9] D. K. Doughty and J. E. Lawler, Appl. Phys. Lett. **45**, 611 (1984).
- [10] B.N. Ganguly and A. Garscadden, Appl. Phys. Lett. **46**, 540 (1985); B.N. Ganguly and A. Garscadden, Phys. Rev. A **32**, 2544 (1985).
- [11] B.N. Ganguly, J. Appl. Phys. **60**, 571 (1986).
- [12] J. Derouard and N. Sadeghi, Opt. Comm. **57**, 239 (1986).
- [13] R. A. Gottscho, R. H. Burton, D. L. Flamm, V. M. Donnelly, and G. P. Davis, J. Appl. Phys. **55**, 2707 (1984).
- [14] V. M. Donnelly, D. L. Flamm, and G. Collins, J. Vac. Sci. Technol. **21**, 817 (1982).

- [15] R. A. Gottscho and T. A. Miller, *Pure and Appl. Chem.* **56**, 189 (1984).
- [16] J. Taillet, *C. R. Acad. Sc. Paris* **269**, 52 (1969); M. Bacal, G. W. Hamilton, A. M. Bruneteau, H. J. Doucet, and J. Taillet, *J. de Physique* **40**, C7-791 (1979); K. E. Greenberg, G. A. Hebner, and J. T. Verdeyen, *Appl. Phys. Lett.* **44**, 299 (1984).
- [17] E. Gogolides and H.H. Sawin, American Vacuum Society National Symposium, Atlanta, GA, October 1988, abstract # PS-WeA3.
- [18] A.V. Phelps, B.M. Jelenkovic, and L.C. Pitchford, *Phys. Rev. A* **36**, 5327 (1987).
- [19] J.P. Boeuf and P. Segur, in "Interactions Plasma Froids Materiaux," ed. by C. Lejeune, Les Editions de Physique (1988), p. 113.
- [20] R.A. Gottscho, A. Mitchell, G.R. Scheller, N.L. Schryer, D.B. Graves, and J.P. Boeuf, *Proc. 7th Symp. Plasma Proc., Electrochem. Soc.* (1988), edited by G.S. Mathad, G.C. Schwartz, and D.W. Hess, page 1.
- [21] R.A. Gottscho, G.R. Scheller, D. Stoneback, and T. Intrator, *J. Appl. Phys.* (to be submitted).
- [22] J. Bokor, R.R. Freeman, J. C. White, and R. H. Storz, *Phys. Rev. A* **24**, 612 (1981); W. K. Bischel, B.E. Perry, and D.R. Crosley, *Chem. Phys. Lett.* **82**, 85 (1981) and *Appl. Opt.* **21**, 1419 (1982); M. Alden, H. Edner, P. Grafstrom, and S. Svanberg, *Opt. Comm.* **42**, 244 (1982); P. Brewer, N. Van Veen, and R. Bersohn, *Chem. Phys. Lett.* **91**, 126 (1982); M. Heaven, T.A. Miller, R.R. Freeman, J. White, and J. Bokor, *Chem. Phys. Lett.* **86**, 458 (1982).
- [23] L. F. DiMauro, R. A. Gottscho, and T. A. Miller, *J. Appl. Phys.* **56**, 2007 (1984).
- [24] R. Walkup, K. Saenger, and G.S. Selwyn, *Mat. Res. Soc. Symp. Proc. Vol.* **38**, 69 (1985).
- [25] B.L. Preppernau, D.A. Dolson, R.A. Gottscho, and T.A. Miller, *Plasma Chem. Plasma Proc.* (in press).
- [26] P.J. Hargis and K.E. Greenberg, 41st Annual Gaseous Electronics Conference, Minneapolis, MN (October 1988), Abstract # LA-3.

CARS DIAGNOSTICS IN REACTING MIXTURES

James J. Valentini

Department of Chemistry
University of California
Irvine, CA 92717

INTRODUCTION

Coherent anti-Stokes Raman scattering (CARS) is a coherent optical variant of the inelastic light scattering process known as the Raman effect. CARS spectroscopy possesses the universality of Raman spectroscopy but with greatly enhanced sensitivity. It is insensitive to background luminescence, can be configured to allow remote measurements, has excellent temporal and spatial resolution, and can provide detailed information on both the chemical composition and physical state of gas, liquid, and solid samples. Because of these desirable attributes CARS has become an important optical diagnostic method, in particular for characterizing combustion media, plasmas, and chemically reacting mixtures. This article provides a brief introduction and overview of such applications of CARS, with a particular emphasis on the last of these.

PHENOMENOLOGY

CARS is non-linear optical process, a four-wave mixing process, in which optical radiation at three incident frequencies, $\omega_1, \omega_2, \omega_3$, interacts with a sample to generate optical radiation at a fourth frequency, ω_0 :

$$\omega_0 = \omega_1 - \omega_2 + \omega_3. \quad (1)$$

It is not necessary to have three distinct incident frequencies, and in fact CARS is most generally carried out with $\omega_1 = \omega_3$. It is conventional then to describe ω_1 as the "pump" or "laser" frequency, and designate it ω_L , and to call ω_2 the Stokes frequency, and write it as ω_S , so that Eq. 1 becomes

$$\omega_{AS} = \omega_L - \omega_S + \omega_L = 2\omega_L - \omega_S, \quad (2)$$

with ω_0 replaced by ω_{AS} , the so-called anti-Stokes frequency. Both ω_L and ω_S are provided by high intensity laser beams, and the signal at ω_{AS} is laser-like also, in that it too is coherent. The four-wave mixing process of CARS generates a signal at ω_{AS} under all conditions for all media. However, the magnitude of the signal is greatly enhanced when the frequency difference $\omega_L - \omega_S$ is resonant with the frequency, ω_R , of a Raman-allowed transition in the sample in which the four-wave mixing is taking place,

$$\omega_S = \omega_L - \omega_R \quad (3)$$

for which

$$\omega_{AS} = \omega_L + \omega_R \quad (4)$$

Although the Raman transition may be between different electronic states of a molecule or atom, it is most commonly a transition between different vibrational or rotational states of a molecule.

An energy level schematic for CARS illustrating the relation between ω_L , ω_S , and ω_{AS} is shown in Fig. 1. The molecular rovibrational states connected by the Raman transition are labeled r and g. The states labeled o and p are the lowest excited electronic states of the molecule, and those labeled v are virtual electronic states. Since only the frequency difference $\omega_L - \omega_S$ matters, the frequencies can be chosen arbitrarily, and only one of these frequencies need be tunable. To take advantage of efficient fixed-frequency and tunable pulsed lasers these frequencies are usually chosen to be in the visible region of the spectrum. A very common choice is a Nd:YAG/dye laser system, in which the second harmonic of the Nd:YAG laser at 532 nm serves both as ω_L and as the pump source for the dye laser, which generates ω_S .

Figure 2 shows a block diagram of the essential elements of a CARS spectroscopy apparatus. Note that the ω_L and ω_S beams are crossed at some angle θ , and that the angle between the ω_L and ω_{AS} beams is ϕ . The angle θ is chosen to satisfy the phase-matching requirement,

$$\underline{k}_L + \underline{k}_L = \underline{k}_S + \underline{k}_{AS} \quad (5)$$

where k_α is the wave-vector for the optical beam at frequency α . The magnitude of the wave-vector is given by

$$k_\alpha = \omega_\alpha n_\alpha / c, \quad (6)$$

with n_α the index of refraction at frequency α . For gases at pressures less than about 1 atmosphere, the medium is essentially dispersionless, that is $n_\alpha = 1$ for all α . For such dispersionless media $\theta = \phi = 0$ and all the beams are collinear.

APPLICATIONS

As a light scattering technique CARS has very high intrinsic temporal resolution, determined solely by the temporal widths of the laser pulses used to generate the signal. This makes CARS a very attractive technique for the investigation of rapidly time-varying phenomena, such as chemical reactions and photochemistry. This has been the principal application of CARS in our laboratory. The high temporal resolution is complemented by the universality of Raman scattering, making CARS suitable for monitoring chemical species not easily detected by other spectroscopic

techniques. Figure 3 shows an example of such an application. This is the vibrational Q-branch spectrum of $O_2(^3\Sigma_g^-)$ formed in the photolysis of ozone. The spectrum is recorded 2 nanoseconds after photolysis, and characterizes the nascent rotational and vibrational distribution of this O_2 photofragment, without any collisional relaxation. The peaks at $1550 - 1560\text{ cm}^{-1}$ are due to the 300K thermal distribution of O_2 impurity in the O_3 sample. Note that the photofragments are produced in high rotational and vibrational states that are not appreciably populated under 300K thermal equilibrium conditions. Figure 4 shows portions of a Q-branch CARS spectrum of H_2 formed in the $H + HI$ reaction. The H atoms were generated by pulsed-laser photolysis of HI, and the H_2 detected only 3.5 ns later, a time delay which allowed at most one H atom collision. Very high rotational and vibrational states are observed, with internal energies as great as $17,750\text{ cm}^{-1}$, equivalent to kT at 25,000 K. The spectrum indicates a population inversion between $v = 1$ and $v = 0$.

Transient species can also be detected under the non-thermal-equilibrium conditions of an electric discharge. Figure 5 shows a CARS spectrum taken in a pure oxygen microwave discharge. Q-branch and O-branch transitions of the ground and first excited vibrational states of $O_2(^3\Sigma_g^-)$, which is the ground electronic state, are evident. Also in the spectrum are transitions due to $O_2(^1\Delta_g)$, the first excited electronic state of molecular oxygen. Under the conditions of the discharge only a few percent of the 5-Torr sample is in the $^1\Delta_g$ state.

Figures 6 and 7 exemplify further the generality of CARS, showing detection of two important radical species, OH and CH_3 . The former was produced by laser photolysis of hydrogen peroxide, the latter by laser photolysis of methyl iodide. In each case the sample pressure was a few hundred millitorr, at which a spectrum with very good signal-to-noise ratio could be obtained in a scan of a few minutes duration.

ACKNOWLEDGMENTS

Financial support for this work was provided by the National Science Foundation and the Division of Chemical Sciences, Office of Basic Energy Sciences, Office of Energy Research, U. S. Department of Energy.

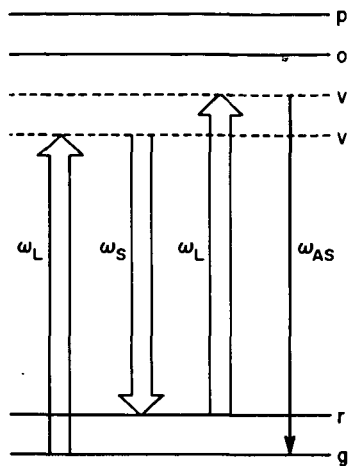


Figure 1. Energy level schematic for CARS.

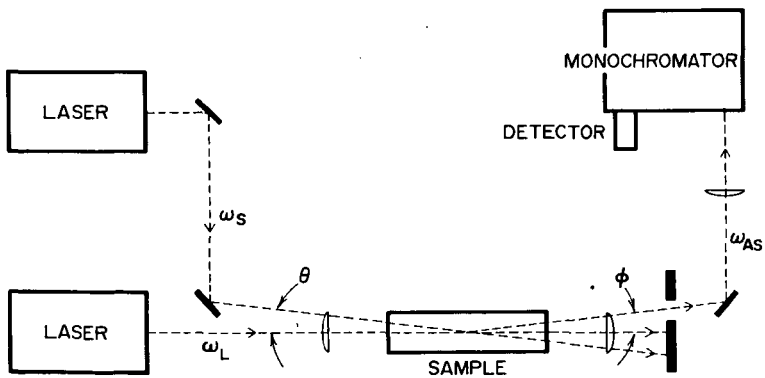


Figure 2. Block diagram of a CARS apparatus.

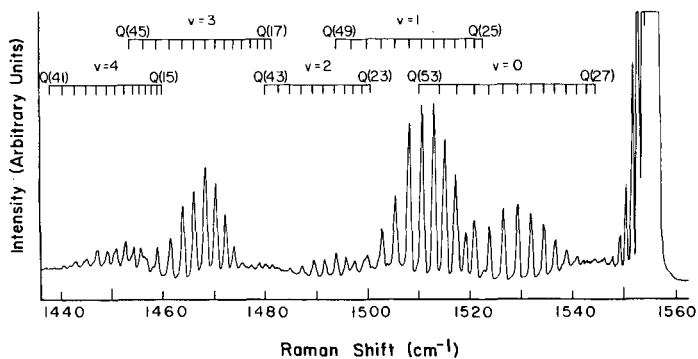


Figure 3. Vibrational Q-branch CARS spectrum of $O_2(3\Sigma_g)$ photofragment from the photolysis of O_3 .

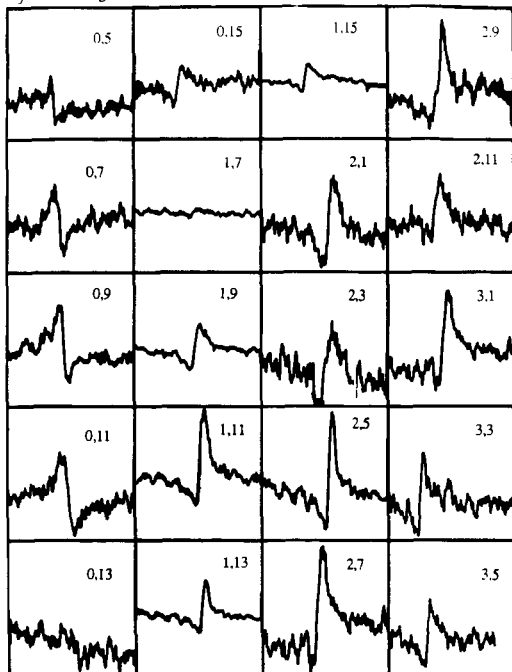


Figure 4. Vibrational Q-branch CARS spectrum of H_2 from the $H + HI \rightarrow H_2 + I$ reaction at 1.6 eV collision energy. The peaks are labeled as v, J .

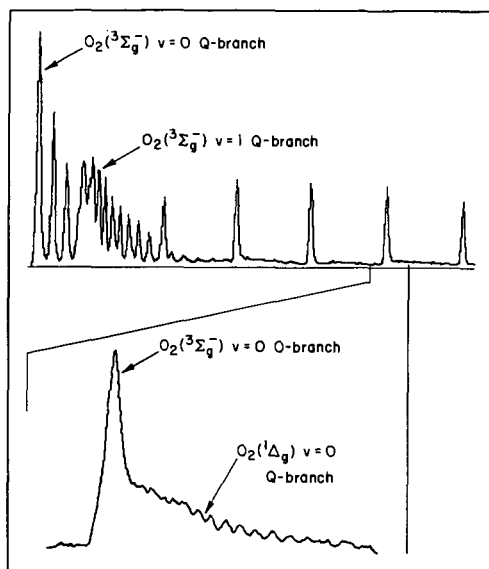


Figure 5. CARS spectrum of an O_2 microwave discharge.

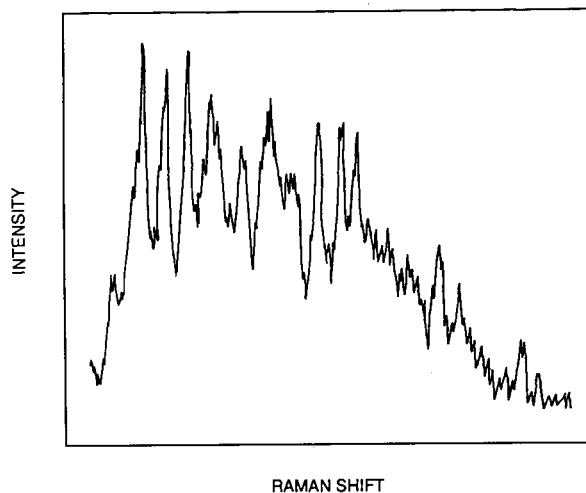


Figure 6. Vibrational Q-branch CARS spectrum of the CH_3 ν_1 vibration at 3000 cm^{-1} . The methyl radicals were formed by photolysis of methyl iodide.

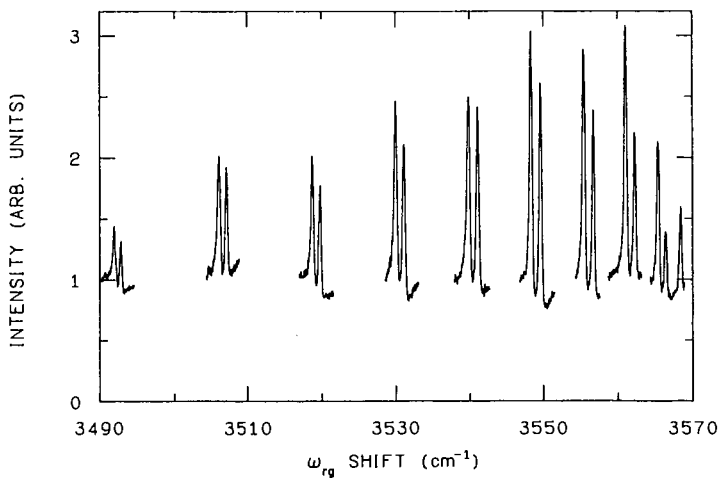


Figure 7. Vibrational Q-branch CARS spectrum of OH radicals from the photolysis of hydrogen peroxide.

LOW PRESSURE PLASMA DIAGNOSTICS BY CARS AND OTHER TECHNIQUES

Nobuhiro Hata

Materials Science Division
Electrotechnical Laboratory
1-1-4 Umezono, Tsukuba-shi, Ibaraki 305, JAPAN

ABSTRACT

Within the past several years, intensive research activities relating amorphous-silicon technology have stimulated plasma-chemical-vapor-deposition (plasma-CVD) diagnostics by laser-spectroscopic techniques. Among them, coherent anti-Stokes Raman spectroscopy (CARS) has attracted much attention because of its great success in combustion diagnostics, and has been employed for low-pressure-plasma studies. Gas-phase species such as SiH_4 , H_2 , Si_2H_6 , SiH_2 , and GeH_4 have been detected, time dependences of their concentration and spatial profiles of their concentration and rotational temperature have been determined, and the gas-phase mechanisms have been discussed. This talk will employ those results as examples, and discuss (1) the potential of CARS for gas-phase analysis in CVD (including (i) what species are monitored, (ii) what information is obtained, and (iii) what are the advantages and limitations), and (2) some other diagnostic techniques that provide additional information for better understandings of CVD mechanisms.

INTRODUCTION

Diamond synthesis from the gas phase has attracted much attention in science and applications (1-7). There are a lot of techniques to produce carbon thin films, and they are divided into chemical vapor deposition (CVD), and physical vapor deposition (PVD). In CVD methods, source gas molecules containing carbon atoms are activated thermally, optically, or by electron collision, and molecular fragments are created. They then diffuse in the gas phase to the substrate surface to feed the surface processes that grow carbon thin films. In PVD methods, particles that contain carbon atoms are fed to the surface. Sputtering and ion-beam deposition are classified in this category.

There are a lot of applications of carbon thin films. Among them, one of the most attractive ones is the micro-electronic applications. Diamond has a high resistivity, thermal conductivity, transparency, and wide band-gap width. It shows semiconducting characteristics when some impurities are doped. These features suggest that thin film diamond will possibly be used as an important material for insulator of field-effect devices, photoconductors, high-temperature devices, short-wavelength light-emitting devices, and radiation resistive devices. In order to realize those electronic applications, development of low-temperature fabrication technology with less damage to the substrate and high controllability of structure and characteristics is required very much.

Thin film carbon has a lot of structural types such as diamond, diamond-like carbon, i-carbon, amorphous carbon, and graphite. Relationships between the film structure and the fabrication methods as well as the operating conditions are partly

known empirically. Understanding of the gas-phase and surface mechanisms that govern those relationships will lead to superior fabrication technology with high controllability. And the first step to such understanding is the observation of the gas phase and surface.

Within the past several years, amorphous silicon related materials have been investigated intensively because of their potential for applications. At present, they are mostly fabricated by plasma-chemical-vapor deposition (plasma-CVD), and their properties are sensitive to the plasma operating conditions. Therefore, the research activities relating the amorphous-silicon technology have stimulated plasma-CVD diagnostics, especially those by laser spectroscopic techniques. Gas-phase process diagnostics by laser spectroscopy have several advantages and enable non-intrusive in-situ observation.

Among them, coherent anti-Stokes Raman spectroscopy (CARS) has attracted much attention because of its great success in combustion diagnostics (8), and has been employed for low-pressure-plasma studies (9). Gas-phase species such as SiH_4 , H_2 , Si_2H_6 , SiH_2 , and GeH_4 have been detected, time dependences of their concentration and spatial profiles of their concentration and rotational temperature have been determined, and the gas-phase mechanisms have been discussed (9-14).

In addition to CARS, laser induced fluorescence (LIF) was employed, and gas-phase species such as Si and Ge were measured. Optical emission spectroscopy, which is, in fact, not a laser spectroscopy, was also employed, and Si, SiH , H_2 , H, and Ge in their electronically ground states were measured. It has been demonstrated that all those techniques provide information about different sets of species to one another, and therefore, more information is obtained by combining several techniques (13,14).

Low-temperature CVD processes such as plasma-CVD for amorphous-silicon-related materials are preferred for micro-electronic applications to PVD and thermal-CVD processes because of their film growth at lower temperature with less damages to the substrate. Although the crystalline size is different from that of thin film diamond, microcrystalline silicon ($\mu\text{c-Si}$) film is more like to it than amorphous silicon (a-Si) film. The deposition conditions for $\mu\text{c-Si}$ is higher in excitation power and hydrogen dilution than those for a-Si. This tendency is almost the same to the deposition conditions for thin film diamond compared with those for carbon films of other structures. Another similarities are their low growth rates, which sometimes are serious problems for applications.

Once the gas-phase profiles of specie concentration and temperature were measured and understood, the efforts of the process-diagnostic research have come to be directed to some key issues in the deposition processes. They are: (1) the effects of ion bombardment to the surface (15), (2) the roles of hydrogen in the gas-phase and at the surface, (3) the dominant species that contribute to the deposition, and (4) the role of O and N atoms to the growth rate (5). Recently, methyl radical CH_3 , which was long considered as the dominant specie, was experimentally detected by infrared diode laser spectroscopy (16). And atomic hydrogen was detected by laser ionization technique (17). Those are the typical examples of the recent trend in process diagnostic research.

This talk includes (1) our experimental setup for gas-phase process diagnostics, (2) a review of the important results in the diagnostics of plasma-CVD for amorphous-silicon-related materials, (3) potential of the techniques for gas-phase analysis in diamond CVD, and (4) another technique to reveal the key mechanisms.

EXPERIMENTAL

Light Sources

Gas pressure in plasma CVD is much lower than the atmospheric pressure, and therefore, high power is required for the CARS light sources. Furthermore, tunable ultraviolet light is necessary for LIF of Si and Ge, and it has to be generated by frequency mixing laser lights. Those are the requirements for a high power laser as the light source. In the experiment, Q-switched Nd:YAG laser (Quanta-Ray, Model DCR-2A) system with an amplifier and an second harmonics generator was used to produce 532 nm second harmonics with 2 ns pulse width and 350 mJ pulse energy, as well as the fundamental 1064 nm laser light. Some part of the 532 nm laser light was used to pump the pulsed dye laser (Quanta-Ray, Model PDL-1) with an amplifier and a wavelength control interface (Quanta-Ray, Model MCI-1). To obtain tunable ultraviolet light for LIF measurements, the dye laser light was frequency doubled and mixed with the fundamental 1064 nm light from the Nd:YAG laser by using the wavelength extender (Quanta-Ray, Model WEX-1). Another dye laser (Quanta-Ray, Model PDL-2) was used to obtain tunable visible light.

All those laser systems were set on a long optical bench, and mirrors and beam splitters were arranged so as to generate laser lights necessary to CARS, LIF and another technique. For CARS, 545-690 nm dye laser light and 532 nm Nd:YAG laser second harmonics were collinearly collimated using a dichroic mirror and then introduced into the plasma-CVD chamber through a focusing lens. And for LIF, 245-280 nm tunable ultraviolet light was generated and introduced into the chamber through quartz optics.

Plasma-CVD Chamber

A specially designed capacitively-coupled diode-type radio-frequency (13.56 MHz) plasma-CVD chamber equipped with three optical window ports was used. The diameters of cathode and anode were 90 and 110 mm, respectively, and their separation was 30-40 mm (variable). The chamber wall was 250 mm apart from the center, and the optical ports were 100 mm long and had quartz windows of 100 mm in diameter at the ends. The chamber was pre-evacuated to 10^{-5} Pa by a 6-inch oil-diffusion pump, and then the valve was closed, the reactant gas was introduced, and was pumped out with a root pump to keep the pressure typically at 10-100 Pa.

Detection Optics

Detection optics for CARS were designed to separate CARS signal light from laser lights, plasma emission, and ambient lights. Mixed beams of lasers and CARS signal were collimated using a lens, and laser lights were separated away using two

dichroic filters, and 1-m double monochromator (Jobin Yvon, Model U1000). Non-resonant CARS signal was rejected using an analyzer, while polarizers were placed in the light source optics to constitute the polarization CARS configuration (18). The CARS signal was detected by an intensified photo-diode array detector (Princeton Applied Research, Model 1420).

Detection optics for LIF and OES were designed to collect the emitted light from gas-phase species. Two quartz lenses of 350 mm focal length and 60 mm diameter were used to collect the light and introduce it into the entrance slit of 32 cm grating monochromator (Jobin Yvon, Model HR320). The signal light was detected by a photomultiplier (HAMAMATSU, Model R292).

Control and Data Acquisition

The Nd:YAG laser was operated at 10 shots per second, and the CARS signal was accumulated at each dye laser wavelength for 10-100 laser shots, and then the dye laser wavelength was changed. Plasma conditions were set manually, and the measuring point was changed by moving the plasma-CVD chamber. The LIF signal from the photomultiplier was accumulated in a boxcar integrator (Princeton Applied Research, Model 4420) with the laser shots as the trigger pulses, and the noises that did not coincide with the laser shots were removed.

PLASMA-CVD FOR AMORPHOUS SILICON RELATED MATERIALS

Temperature Profile

Silane (SiH_4) molecule is abundant in the gas phase of most of the plasma-CVD for amorphous-silicon-related materials. Therefore, temperature determination from SiH_4 CARS signal was performed. A simple equation for SiH_4 CARS spectrum:

$$(\sum_j \exp[-hcBJ(J+1)/kT] \exp\{-[\delta\nu - \nu_0 - \Delta BcJ(J+1)]^2 / (\Delta\nu)^2\})^2 \quad (1)$$

was assumed and the spectral shapes for different values of rotational temperature T were calculated (12). Then the measured CARS spectra were compared with those calculated curves to find the best fitted one, from which the values of rotational temperature were obtained. From the result, the effects of the substrate heating and radio-frequency discharge to the gas-phase temperature were discussed.

Hydrogen (H_2) molecule is abundant in the gas phase not only of the plasma-CVD for amorphous-silicon-related materials but also many other CVD processes. It is known in diamond CVD that heavily diluting the source gas molecule with hydrogen is very important for obtaining diamond structure. Both the ro-vibrational and pure rotational CARS spectra of H_2 show a series of peaks that corresponds to a series of the rotational quantum states (19-21). That is due to the large values of the rotational constants of H_2 molecule consisting of light H atoms. From the ratio of the CARS signal peak intensities, distribution within those rotational states, and therefore, the rotational temperature is obtained. The pure rotational CARS signal is about 100 X stronger in intensity than the ro-vibrational signal, and suited for low-pressure plasma-CVD

diagnostics. The relative peak intensities are given by the square of the non-linear electric susceptibility $\chi^{(3)}(J,J+2)$, which is written as (20),

$$\chi^{(3)}(J,J+2) = N(J+1)(J+2)[X(J,T)-X(J+2,T)] / Q(T)(2J+3) \quad (2)$$

$$X(J,T) = g_J \exp[-E(J)/kT] \quad (3)$$

$$Q(T) = \sum g_J(2J+1) \exp[-E(J,v)/kT] \quad (4)$$

$$E(J,v) = E_v^0 + B_v J(J+1) + D_v J^2(J+1)^2 + H_v J^3(J+1)^3 \quad (5)$$

By measuring the hydrogen CARS spectra from one point to another, the temperature profile in the gas phase was determined (20). From the results, it was concluded that the gas-phase temperature is mostly determined by the substrate and chamber-wall temperatures and is little affected by the other plasma operating conditions within the range used for amorphous-silicon deposition. That is consistent with the fact that the gas-phase temperature relaxation time determined by the ratio of the heat capacity to thermal conductivity is much shorter than the gas residence time in the chamber. And the gas-phase temperature in the vicinity of the film-growing surface agreed with the surface temperature measured with a thermocouple.

Concentration Profile

The concentration of molecule is determined from the CARS signal intensity by using the quadratic dependence of the CARS signal intensity I_{CARS} to the concentration $[M]$ of the resonant molecule M:

$$I_{\text{CARS}} \propto |\chi^{(3)}|^2 \propto [M]^2 \quad (6)$$

By measuring the CARS signal from one point to another, the concentration profile is obtained. The absolute value of the molecular concentration is determined by using the gas of known concentration for calibration. OES signal also represents the relative concentration of the species that emit the photons when the emission efficiency is constant and the absorption of the emitted photons by other species is neglected. In addition to the necessary conditions for OES signal to be a measure of specie concentration, if the excitation light is not attenuated much along its path, the LIF signal is a measure of the specie concentration.

The concentration profiles of SiH_4 , Si, and Si^+ were measured between the cathode and anode along the central axis, and much different profiles were obtained among those species. Si concentration had a two distinct peaks at about 10 mm from the cathode and anode, while SiH_4 concentration changed more gradually and was almost constant in the discharge volume except the sheath regions (14). The result was interpreted that a lot of Si atoms are created by electron collision in the regions where electron energy is high. The highly energetic electrons are created by the acceleration of secondary emitted electrons from the electrodes by the sheath electric fields. SiH_4

molecule, on the other hand, is dissociated or excited even by electrons with lower kinetic energy, thus more gradual change in the discharge region is realized.

The concentration profiles of SiH_4 and GeH_4 in a plane parallel to the electrode surface were also measured, and gradual concentration changes of the both molecules toward the radial direction were observed (13). The result was interpreted in terms of dissociation and excitation of the source gas molecules supplied from outside of the discharge by molecular diffusion.

Transient Behavior

Concentrations of SiH_4 and Si_2H_6 were measured as functions of time after the discharges were switched on in a closed discharge chamber (11). The concentrations of source gas molecules decreased exponentially with time, and the decay time constants were obtained from the slope of the concentration plotted semi-logarithmically against time. From the time constants, the average loss rates were calculated and their dependences on the gas pressure and discharge power were studied. In Si_2H_6 discharges, SiH_4 molecule was observed, and the time dependence of its concentration was studied. The result was interpreted in terms of the average creation rate, and compared with the average loss rate to discuss the formation mechanism of SiH_4 in Si_2H_6 discharges.

Effect of Hydrogen Dilution

Effect of Hydrogen dilution on the OES and LIF signals of Si^* , Ge^* , Si, and Ge was studied (13). Emission signal from Ge^* from GeH_4 discharge decreased very much with dilution of the source gas GeH_4 with H_2 , while emission signal from Si^* did not change very much with H_2 dilution. Si and Ge atoms in their electronically ground states measured by LIF changed like their emissive species with H_2 dilution. The results were interpreted in terms of the gas-phase mechanisms with H_2 dilution.

DIAMOND CVD

As the first step for process diagnostics, measurements of temperature and specie concentration profiles will provide much information. The laser spectroscopic process-diagnostic techniques demonstrated in plasma CVD for amorphous-silicon-related materials are applicable to other CVD systems if some suitable optical windows are equipped. The arguments are what species are detected, what the detection limit is, and what information is obtained. The situation seems better for CARS measurements in diamond CVD processes, since the gas pressure is usually higher than that in plasma-CVD for amorphous-silicon-related materials. Hydrogen (H_2), methane (CH_4), and some other carbon-containing molecules will be detected by CARS, and their concentration profiles will be measured. Temperature measurement by pure-rotational CARS signal of H_2 will also be practical, and temperature profile will be obtained. As in the case of plasma CVD for amorphous-silicon-related materials, species detected by LIF will be limited to some molecular fragments, but LIF will still add information to

CARS data. Thus the first step of the diamond-CVD diagnostics will be fulfilled with the techniques used in the plasma-CVD diagnostics.

ANOTHER TECHNIQUE

What should be carried out at the next stage is to focus on the key issues: (1) the role of hydrogen, (2) the dominant species contributing to the film growth, (3) the effects of ion bombardment, and (4) the effects of O and N. For that purpose the detection of hydrogen atom by resonance-enhanced multiphoton laser-induced-fluorescence experiment was planned and is now in progress. That method is similar to the resonance-enhanced multiphoton ionization technique (17) but promises the detection of H even in the plasma CVD environment.

SUMMARY

Laser-spectroscopic gas-phase process diagnostic techniques such as CARS and LIF have been demonstrated in the plasma CVD for amorphous-silicon-related materials. Gas-phase profiles of specie concentration as well as temperature were measured in-situ non-intrusively, and the results were interpreted in terms of gas-phase kinetics. Those techniques will be applicable to other CVD processes, especially those for diamond thin films.

Process diagnostics have come to the stage where the direct observations of the key issues in the processes are strongly emphasized. Understanding of the key mechanisms that determine the growth rate, structure, and properties of thin films is very important. The processes occurring at the film growing surface were mentioned little in this talk, but it plays the other important part in the mechanisms, and should be studied extensively.

ACKNOWLEDGEMENTS

Financial support for this work was provided by the Solar Energy Research Program of the Sunshine Project, AIST, MITI. Encouragements and discussion during this work were by Drs. K. Tanaka and A. Matsuda of the Electrotechnical Laboratory.

REFERENCES

- (1) Angus, W.G., Will, H.A., and Stanko, W.S.: *J. Appl. Phys.*, 39 (1968) 2915.
- (2) Spitsyn, B.V., Boulov, L.L., and Derjaguin, B.V.: *J. Cryst. Growth*, 52 (1968) 219.
- (3) Matsumoto, S., Sato, Y., Kamp, M., and Setaka, N.: *Jpn. J. Appl. Phys.*, 21 (1982) L183.
- (4) Sawabe, A. and Inuzuka, T.: *Appl. Phys. Lett.*, 46 (1985) 146.
- (5) Hirose, Y. and Terasawa, Y.: *Jpn. J. Appl. Phys.*, 25 (1986) L519.
- (6) Suzuki, K., Sawabe, Y., Yasuda, H., and Inuzuka, T.: *Appl. Phys. Lett.*, 50 (1987) 728.
- (7) Matsumoto, S., Hono, M., and Kobayashi, T.: *Appl. Phys. Lett.*, 51 (1987) 737.
- (8) Eckbreth, A.C.: *J. Propulsion and Power*, 3 (1987) 210, and references therein.
- (9) Hata, N., Matsuda, A., Tanaka, K., Kajiyama, K., Moro, N., and Sajiki, K.: *Jpn. J. Appl. Phys.*, 22 (1983) L1.
- (10) Hata, N., Matsuda, A., and Tanaka, K.: *J. Non-Cryst. Solids*, 59-60 (1983) 667.
- (11) Hata, N., Matsuda, A., and Tanaka, K.: *Jpn. J. Appl. Phys.*, 25 (1986) 108.
- (12) Hata, N., Matsuda, A., and Tanaka, K.: *J. Appl. Phys.*, 59 (1986) 1872.
- (13) Hata, N., Matsuda, A., and Tanaka, K.: *J. Appl. Phys.*, 61 (1987) 3055.
- (14) Hata, N. and Tanaka, K.: *J. Non-Cryst. Solids*, 77-78 (1985) 777.
- (15) Angus, J.C., Doidl, P., and Domitz, S.: in "Plasma Deposited Thin Films" ed. by Mort, J. and Jansen, F. (CRC Press, Florida, 1986) pp. 89-127.
- (16) Celii, F.G., Pehrsson, P.E., Wang, H.-t., and Butler, J.E.: *Appl. Phys. Lett.*, 52 (1988) 2043.
- (17) Celii, F.G., Pehrsson, F., Wang, T.-t., Nelson, H.H., and Butler, J.E.: in "Extended Abstract of the International Symposium on the Characterization of Diamond" (Tsukuba, Japan, Oct. 27-28, 1988).
- (18) Brakel, R. and Schneider, F.W.: in "Advances in Non-Linear Spectroscopy" ed. by Clark, R.J.H. and Hester, R.E. (John Wiley & Sons, Chichester, 1988) pp. 149-192.
- (19) Pealat, M., Taran, J.P.E., Taillet, J., Bacal, M., and Bruneteau, J. *Appl. Phys.*, 52 (1981) 2687.
- (20) Marowsky, G., Gierulski, A., Dick, B., Sowada, U., and Vehrenkamp, R.: *Appl. Phys.*, B39 (1986) 47.
- (21) Hata, N., Matsuda, A., and Tanaka, K.: in "Symposium Proceedings, 8th International Symposium on Plasma Chemistry" ed. by Akashi, K. and Kinbara, A., (IUPAC, Tokyo, 1987) pp. 500-505.

CARS DETECTION OF GASEOUS SPECIES FOR DIAMOND DEPOSITION PROCESS

Ward C. Roman and Alan C. Eckbreth

United Technologies Research Center
Propulsion Science Laboratory
East Hartford, CT 06108

ABSTRACT

In order to understand the complicated chemical and physical processes that occur during the deposition of hard face coatings such as diamond, diagnostics that are remote, nonintrusive and sensitive to potential chemical species are necessary. One particularly promising approach is coherent anti-Stokes Raman spectroscopy (CARS) useful for measurements of temperature and species concentrations. Results to be described will include CARS measurements on a PACVD reactor used for depositing high quality diamond films. A mixture of acetylene (C_2H_2) and Argon, tested over a range of total pressures down to 0.1 Torr, was used to calibrate the CARS system. With the existing CARS system, detectivity of C_2H_2 to 5 mtorr was demonstrated. This paper describes details of the scanned narrowband colinear CARS system and examples of CARS spectra obtained for CH_4 and C_2H_2 species under rf PACVD diamond deposition conditions and also using an alternate filament-assisted technique.

INTRODUCTION

Nonequilibrium reactive plasmas are recognized as a novel approach for a wide variety of material coating applications (1). This type of plasma provides a unique environment wherein deposition of thin, hard face, conformal coatings can occur at much lower temperatures (critical for inhibiting stresses) and within more complex chemical environments than are possible by conventional vapor deposition techniques. A need exists for in-situ nonintrusive techniques for diagnosing and controlling PACVD systems used for thin coating deposition (2). If improvements can be made in durable hard face coatings, increased utilization of lightweight materials under advanced development may follow. A complete understanding of the process requires information on a large number of physical and chemical processes involving gas phase and gas-surface interactions and the associated synergistic effects. Knowledge of plasma species concentrations and "temperature" is required for correlation with the corresponding physical and chemical properties of the coatings.

Emission spectroscopy is often used for the measurement of atomic and molecular species, but the emission from excited atomic levels is often much larger than for excited molecular levels, thus the atomic species dominate the spectra and molecular signatures are difficult to extract. Species concentration is difficult to infer from plasma emission spectra because they involve excited electronic levels that are not generally in thermodynamic equilibrium with the ground state. An alternative diagnostic technique, sensitive to the molecular ground state, is Coherent Anti-Stokes Raman Spectroscopy (CARS), a nonlinear optical technique useful for measuring the concentration and "temperature" of molecular constituents since all molecules have at least one Raman active vibrational mode.

The outstanding combination of unique material properties of diamond offers the potential for applying diamond coatings in many commercial applications ranging from protective and tribological coatings to films/heat sinks for semiconductors to optical lenses to electronic devices for space environments. Before diamond coatings can be applied to commercial type applications, many questions need to be answered.

Ti-6Al-4V was selected as the reference substrate material. It represents a critical alloy of paramount interest in many commercial/aerospace applications. Its strength to weight and low temperature oxidation/corrosion resistance are excellent. However, erosion and wear occur rapidly, thus the need for durable hard face coatings.

APPARATUS

Figure 1 is a schematic of the nonequilibrium PACVD reactor under current investigation at UTRC. The longitudinal, tube type radio frequency (rf) geometry was selected as a design viable for later scale up to continuous production operation. In addition it permits high reactant gas flows and plasma power levels; increasing these parameters nominally results in enhanced deposition rates. The 3.6-cm-ID test section is constructed of high purity fused silica and high vacuum flanges for rapid disassembly. Up to 5 different reactant gases can be simultaneously injected at the inlet region. A 5 kW rf power supply operating at 13.56 MHz is used to inductively couple the rf power into the plasma through a multiple-turn water-cooled copper work coil. Exploratory test results revealed the importance of minimizing contamination in the PACVD system as required for providing high quality coatings onto the 1.3-cm-dia x 2-mm-thick Ti-6Al-4V substrates. As a result, a completely oil-free, venturi, vacsorb, cryopump and vacion pump system are used, including a MKS flow metering system with special traps (e.g., GaInAl) and getters to remove water vapor and oxygen. To augment pumpdown time and provide operating range flexibility, a 380 l/s turbomolecular pumping system, modified for corrosion resistant operation, is used; a residual gas analyzer to monitor trace impurities is also used. This system is capable of initial operating pressures down to 10^{-7} torr. The cleanliness of the substrate prior to coating deposition is believed to be a key requirement for achieving good coating adherence to the substrate. Therefore, a test sample holder and isolated load-lock and transport system are interfaced with the PACVD system (3). This technique allows direct Secondary Ion Mass Spectrometry/Ion Scattering Spectrometry (SIMS/ISS) analysis of the substrates immediately following in-situ plasma cleaning and provides a unique capability not reported in the literature. Additional advantages of this type system include the provision for conformal coverage for complex shapes, graded composition control, and provision for independent biasing and temperature monitoring of the substrate.

As hardness and adhesion are critical parameters for characterizing thin, hard face coatings, a state-of-the-art ultramicrohardness tester and UTRC custom built adhesion test apparatus have been installed and preliminary calibration testing initiated. The ultramicrohardness tester (Nanoindenter) can resolve forces as small as 2.5 μ N and displacements of 0.4 nm. The adhesion measurements are made on a computer-controlled pin-on-disc apparatus that has a 3-axis force transducer and a device to measure the advance of the pin into the coating. A modification to this device using an ultrasonic sensor allows for coating delamination detection. Reference 3 describes details of this equipment and initial test results.

DIAGNOSTICS

The theory of CARS is explained in several recent reviews (4,5). Figure 2 is a simplified schematic of the colinear phase-matched CARS system used in these experiments. As illustrated in Figure 2, incident laser beams at frequencies ω_1 and ω_2 , termed the pump and Stokes respectively, where $\omega_1 > \omega_2$, interact through the third-order, nonlinear susceptibility of the medium to generate the coherent CARS radiation at frequency $\omega_3 = 2\omega_1 - \omega_2$. The frequency difference $\omega_1 - \omega_2$ is adjusted to access the Raman-active vibrational-rotational resonances in a given constituent. Since the characteristic vibrational frequencies of most molecules are well separated, individual species are easily addressed. The CARS process must be phase matched so that the developing signal grows constructively. The scanned, narrowband CARS approach, rather than a broadband approach, was selected due to its very high spectral resolution and maximum species detectivity. It is best used to study temporally-steady processes such as PACVD, but it has the disadvantage of being quite time consuming. Species measurements can be made from the absolute signal strength. In addition to the resonant signal from the Raman modes of interest, there is also a nonresonant electronic background contribution from all the molecules or atoms present in the control volume. This leads, due to destructive interference effects in the coherent wave mixing, to spectral signatures which are also concentration sensitive. Thus fractional concentrations can be obtained from spectral shapes without regard to signal level fluctuations caused by beam steering or particle attenuation.

As shown in Figure 2, the dye laser is scanned to generate the CARS spectrum. In this way all of the available laser pump energy excites a single transition of the resonant molecule and increases the sensitivity

by several orders of magnitude. For equivalent laser powers, decreasing the Stokes bandwidth from the typical broadband value of 150 cm^{-1} increases the CARS signal by over 10^3 due to the increased spectral intensity. Spectral scanning from $60\text{--}100\text{ cm}^{-1}$ requires about 30 minutes.

The basic equipment includes an injection-seeded, single-mode, Nd:YAG primary beam pump laser which is frequency doubled to produce narrow bandwidth ($\sim 50\text{ MHz}$), 10^{-8} sec pulses at 532 nm at a 10 Hz repetition rate and a narrow bandwidth (0.4 cm^{-1}) scanned Stokes dye laser. A major portion of the primary beam is split off to drive the dye laser. The remaining 532 nm beam serves as the pump and is combined colinearly with the Stokes beam at a dichroic prior to focussing in the plasma test region. The frequency-shifted CARS signal is formed in the laser focus and all three beams exit the reactor where a dichroic separates the CARS from the incident wave mixing beams. Digital acquisition of the CARS and reference signals are obtained from fast, gated PMT detectors. The digital acquisition system also records the wavelength shift of the scanned dye laser for calibration of the CARS spectrum. All signals from the PMT are digitized on every pulse and processed in a computer. As the dye laser is scanned, successive transitions of the molecular resonances are excited and modulate the intensity of the CARS signal. The result is a spectrum of the ro-vibrational manifold of the medium from which identification of species, their concentration and temperature (vibrational and rotational) can be obtained. Typically, ten CARS pulses are averaged per spectral step which corresponds to 0.1 cm^{-1} . With appropriate referencing, the molecular concentration can be measured to within $\pm 1\%$ of the total gas density and the population in the vibrational and rotational states determined for assignment of temperatures.

RESULTS TO DATE AND DISCUSSION

In the exploratory experiments directed at diamond coatings, a mixture of 1% CH_4 in H_2 was used at a total pressure of 5 torr . The rf coils were located at the optical port location. Figure 3 is an example of the CARS methane signal obtained for the ν_1 mode. It illustrates the effect of increasing rf power from zero up to 400 Watts on depleting the methane concentration. Measurements were also made of the weaker $2\nu_2$ and ν_3 modes as shown in Figure 4.

Very little is known about the chemical mechanisms of diamond film growth. Several global kinetic theories have been proposed based on nucleation theory and equilibrium. Other proposed mechanisms rely on the presence of C_2H_2 or CH_3^+ . Spear and Frenklach at Pennsylvania State University (6) have proposed an alternative mechanism for diamond growth. It basically consists of two alternating steps. First, the surface is activated by H-atom removal of a surface-bonded hydrogen. The surface activated carbon radical then acts as a site for adding more carbons to the structure by reacting with acetylene (C_2H_2) in the plasma. To provide more quantitative experimental information to verify these proposed theories and improve the basic understanding of the diamond growth process, a series of CARS experiments was conducted focused on measurement of the C_2H_2 molecular species. C_2H_2 is a linear molecule with five fundamental vibrations. Three of the five modes are Raman active. Figure 5 displays a scan generated CARS spectrum of 5% C_2H_2 in an Ar background (ν_1 band) measured using the CARS system shown in Figure 2. This measurement was made at room temperature and 10 torr reactor total pressure while flowing the mixture of 5% C_2H_2 in Argon. High purity C_2H_2 , as checked via a gas chromatograph, in concentrations of both 5% and 0.5% in Argon were used in these measurements. The measurements obtained using both concentrations indicate a C_2H_2 detectability of 5 mtorr was achieved with the present system. Continued improvements in spectral filtering should significantly improve this sensitivity level.

To determine the effect of rf plasma location on the ability to detect the C_2H_2 , a series of tests was conducted for the different configurations shown in Figure 6. In each case the total pressure was 3 torr . The 5% C_2H_2 in Argon was only detected when the rf plasma was located downstream of the laser optical ports. In the other locations, the concentration of C_2H_2 was less than 5 mtorr . The next step was to investigate the configuration and test parameters under which high quality diamond coatings have been deposited. The results for the CARS spectrum of C_2H_2 , ν_1 mode observed at 3 torr , is shown in Figure 7. The rf power input

to the plasma was 300 watts and the H_2 and CH_4 flow rates were 99 and 1 sccm respectively. The rf coils were located at the optical port axis and the Ti-6Al-4V substrate was located within the plasma plume and 1-cm downstream of the optical centerline. Additional experiments have also included measurements with the substrate located approximately 1 mm from the laser beam. No significant C_2H_2 CARS signal was observed in any of these tests. This would indicate, if C_2H_2 were present, that it was at concentration levels less than the 5 mtorr current detection limit of the CARS system.

To apply this CARS technique to other diamond deposition systems, a hot filament reactor configuration, similar to that reported by Celii, et al. (7) was fabricated and measurements were made of the C_2H_2 CARS spectrum. Figure 8 is a schematic of the test geometry. The gas flow was 1% CH_4 in H_2 at a pressure of 150 Torr and maintained at 200 sccm. A 2-mm-dia. x 2-cm-long tungsten filament heated to approximately 2630K was located 2 cm from the Ti-6Al-4V substrate. Figure 9 shows the scan generated CARS spectrum of the C_2H_2 ν_1 band, thus verifying the presence of C_2H_2 close to the surface of the substrate as reported by Celii, et al.

Figure 10 is an example of the test results obtained using Raman scattering on a Ti-6Al-4V substrate that was coated with the polycrystalline diamond film using the rf PACVD process. In these measurements, a tunable cw dye laser operated in a single frequency configuration with a line width of < 5 MHz, tuned to 16956.18 cm^{-1} , was used as the excitation source. Raman spectra reported by Matsumoto (8) for thin diamond films indicate only one sharp peak at about 1333 cm^{-1} . This is very close to the value 1332.5 cm^{-1} reported for natural diamond by Solin and Ramdas (9). A feature of the UTRC diamond coating obtained via rf PACVD is that no graphite peak was detected in any of the Raman measurements. X-ray diffraction measurements indicated the observed interplanar spacings are in close agreement with reported values (2.065 and 1.262 \AA) of natural diamond (ASTM 6-675) and UTRC reference natural diamond material.

Based on the above experiments, the following are the preliminary results: 1) a CH_4 CARS spectrum was observed in the rf plasma, 2) increasing the rf plasma power reduced the CH_4 CARS signal, 3) the rf plasma significantly reduces the C_2H_2 CARS signal in C_2H_2/Ar flow, 4) the C_2H_2 CARS spectrum was not observed in rf plasma CH_4/H_2 diamond deposition tests to date. The present C_2H_2 detectability limit is 5mtorr, and 5) the C_2H_2 CARS spectrum was observed in the hot filament reactor configuration.

SUMMARY

Laser/optical diagnostic techniques, such as the CARS system described in this paper, are candidates for application as plasma gas phase materials processing diagnostic tools, each with its own inherent advantages and associated limitations. Recognizing that no one diagnostic technique will suffice, it will only be through the complementary use of several of these techniques that a fundamental understanding of the relationship between plasma process variables and properties of the processed material coating will evolve. This may ultimately lead to simple process control strategies, including in-situ laser diagnostics and sensors, to ensure high quality, economic, reproducible plasma deposition of advanced coatings such as diamond in a production scale environment. Research addressing these aspects is continuing.

REFERENCES

- (1) National Research Council, National Materials Advisory Board Report NMAB-415, *Plasma Processing of Materials*, National Academy Press, March 1985.
- (2) Roman, W., *Laser/Optical Diagnostic Techniques for Plasma Materials Processing*. Invited Paper at Spring 1987 Materials Research Society Meeting; Anaheim, CA, Published in Proceedings of Symposium K - *Plasma Processing and Synthesis of Materials*, April 20-24, 1987.
- (3) Roman, W., Stufflebeam, J., and Eckbreth, A., *Diagnostic Techniques for PACVD Systems for Depositing Protective Coatings*, Paper C2.2 - Proceedings of Materials Research Society Spring Meeting, Vol. 117, Process Diagnostics: Materials, Combustion, Fusion. Reno, NV, April 1988.

- (4) Eckbreth, A. and Stufflebeam, J., *CARS Diagnostics for Combustion and Plasma Processes*, Paper C4.2, Proceedings of Materials Research Society Spring Meeting, Vol. 117, Process Diagnostics: Materials, Combustion, Fusion. Reno, NV, April 5-9, 1988.
- (5) Eckbreth, A. and Roman, W., *Laser Diagnostics for Plasma Processing of Materials*, Keynote Invited Paper, Proceedings of ASM National Thermal Spray Conference, Cincinnati, Ohio, October 23-27, 1988.
- (6) Spear, K., and Frenklach, M., *Mechanistic Hypotheses on Diamond Growth from the Vapor*. Presented at 3rd SDIO/IST - ONR Diamond Technology Initiative Symposium, Arlington, VA. July 1988.
- (7) Celii, F. G., Pehrsson, P. E., Wang, H. T. and Butler, J. E., *Infrared Detection of Gaseous Species During the Filament - Assisted Growth of Diamond*, Appl. Phys. Lett., Vol. 52, No. 24, June 13, 1988.
- (8) Matsumoto, S., Y., Kamo, M., Tenaka, J., and Setaka, N., *Chemical Vapor Deposition of Diamond from Methane-Hydrogen Gas*, Proc. 7th International Conference on Vac. Metallurgy, pp. 386-391, Tokyo, Japan, 1982.
- (9) Solin, S., and Ramdas, A., *Raman Spectrum of Diamond*, Phys. Rev. B1, pp. 1687-1698, 1970.

- (6) Spear, K., and Frenklach, M., *Mechanistic Hypotheses on Diamond Growth from the Vapor*. Presented at 3rd SDIO/IST - ONR Diamond Technology Initiative Symposium, Arlington, VA. July 1988.
- (7) Celii, F. G., Pehrsson, P. E., Wang, H. T. and J. E. Butler, *Infrared Detection of Gaseous Species During the Filament - Assisted Growth of Diamond*, Appl. Phys. Lett., Vol. 52, No. 24, June 13, 1988.
- (8) Matsumoto, S., Y., Kamo, M., Tenaka, J., and Setaka, N., *Chemical Vapor Deposition of Diamond from Methone-Hydrogen Gas*, Proc. 7th International Conference on Vac. Metallurgy, pp. 386-391, Tokyo, Japan, 1982.
- (9) Solin, S., and Ramdas, A., *Raman Spectrum of Diamond*, Phys. Rev. B1, pp. 1687-1698, 1970.

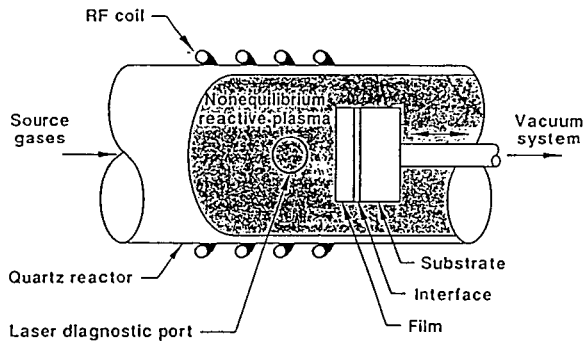


FIGURE 1. SCHEMATIC OF PACVD REACTOR USED FOR DIAMOND DEPOSITION EXPERIMENTS .

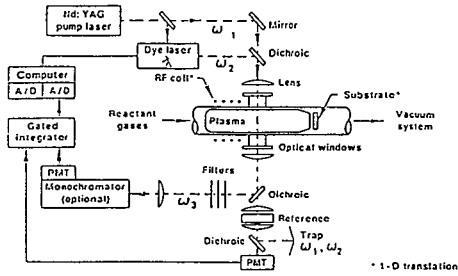


FIGURE 2. SCHEMATIC OF NARROWBAND, COLINEAR SCANNED CARS SYSTEM USED IN PACVD DIAMOND FILM DEPOSITION

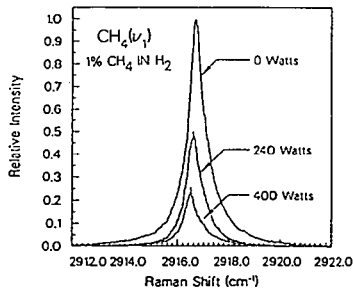


FIGURE 3. EFFECT OF RF PLASMA POWER ON CARS METHANE SPECTRUM

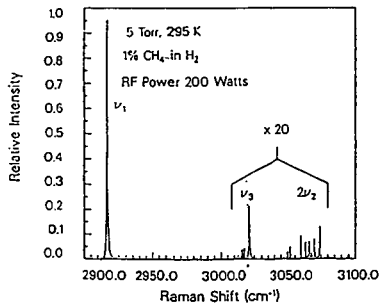


FIGURE 4. CARS METHANE SPECTRUM OF DIFFERENT MODES

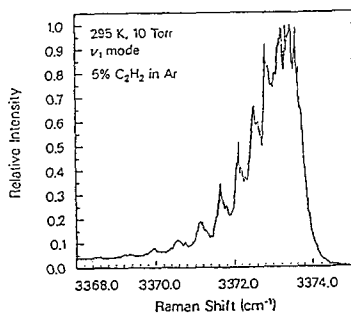


FIGURE 5. CARS SPECTRUM OF ACETYLENE

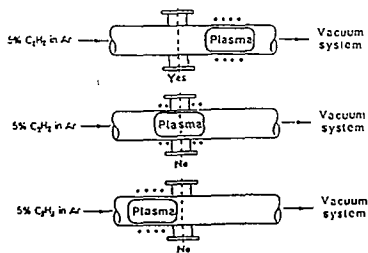


FIGURE 6. C_2H_2 DETECTION LOCATIONS

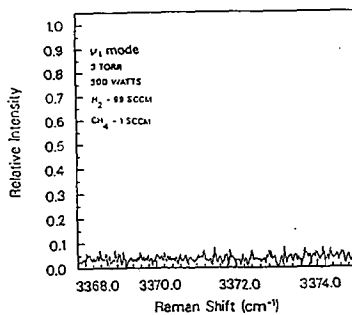


FIGURE 7. CARS SPECTRUM OF ACETYLENE IN PACVD DIAMOND COATING DEPOSITION

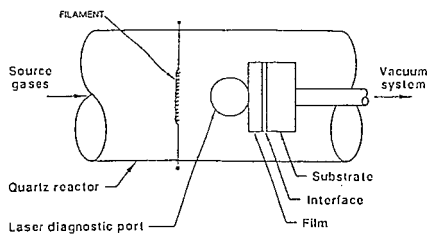


FIGURE 8. SCHEMATIC OF HOT FILAMENT REACTOR CONFIGURATION

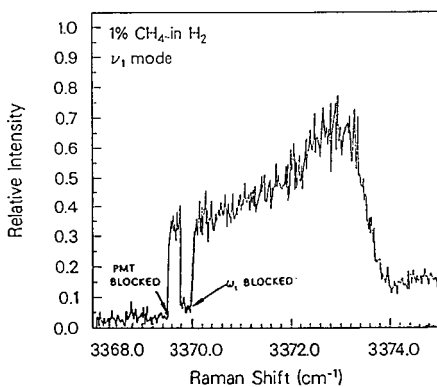


FIGURE 9. CARS SPECTRUM OF ACETYLENE IN HOT FILAMENT CONFIGURATION

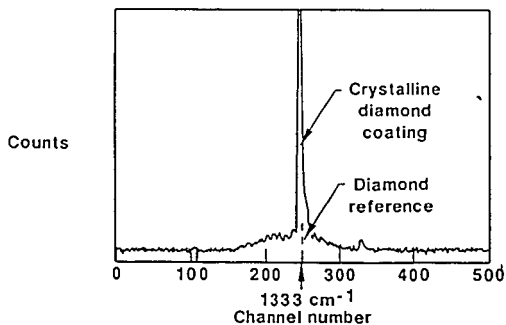


FIGURE 10. RAMAN SPECTRA OF DIAMOND COATING DEPOSITED VIA PACVD ON Ti-6Al-4V SUBSTRATE.

IN SITU CHARACTERIZATION OF DIAMOND NUCLEATION AND GROWTH BY XPS

David N. Belton, Stephen J. Harris,
Steven J. Schmieg, and Anita M. Weiner
Department of Physical Chemistry
General Motors Research Laboratories
Warren, MI 48090

Abstract

Filament assisted chemical vapor deposition (CVD) diamond film growth on Si(100) was studied using X-ray Photoelectron Spectroscopy (XPS) to examine the sample at selected intervals during the nucleation and growth processes. The sample was transferred under vacuum from the growth chamber to the attached XPS analysis chamber without exposure to air. Before growth XPS showed that the Si sample is covered by a layer of SiO₂ and carbonaceous residue; however, after 15 minutes of growth both of these substances are removed and replaced by a distinct SiC layer [Si(2p)=100.3 eV and C(1s)=282.7 eV]. Between 15 minutes and 4.5 hours the SiC layer grows and diamond nucleation begins. The XPS signal from diamond [C(1s)=284.3 eV] saturated after 17 hours. The identification of diamond was confirmed with Raman spectroscopy. This work identifies SiC as the substrate for diamond nucleation and growth during filament assisted CVD diamond growth on Si.

Introduction

Diamond films grow at relatively low pressures (≤ 1 atm) and temperatures (≤ 1300 K) when the proper mixture of CH₄ and H₂ flows over a substrate that is near a hot filament [1-3] or electric discharge [4-6]. This method of diamond production offers the possibility for inexpensive diamond coatings on tools, wear surfaces, and optical components. Single crystal diamonds ultimately could be prepared for use as high performance electronic devices. New technologies involving chemical vapor deposition (CVD) diamond films have not yet been implemented in part because there is no understanding of the chemical and physical processes which control the properties of the diamond films. In particular, there have been no adequate characterizations of the surfaces on which the films grow.

In order to examine the surface chemistry of diamond film growth we coupled a diamond growth chamber to an ultrahigh vacuum (UHV) system equipped with X-ray photoelectron spectroscopy (XPS). By stopping the growth at selected intervals we are able to obtain a time dependent characterization of the surface during the nucleation and growth processes without exposure to air. This experiment, which is the first to offer such a time dependent monitoring of the surface during diamond growth, allows us to characterize the surface on which diamonds are actually grown as opposed to the substrate we place in the growth chamber. These data may assist in developing better models for diamond growth [7]. In this experiment we examined growth on Si because such a large amount of work has been done on this material. We identified three distinct phases of diamond film growth: removal of initial substrate contaminants, formation of a SiC layer, and nucleation and growth of diamonds. From these results we can conclude that diamonds form on SiC as opposed to clean Si, Si oxides, or a carbonaceous layer.

Experimental Aspects

The experiments were performed in a system that coupled a UHV analytical chamber to a diamond growth chamber. The UHV chamber is a custom built system that contains a Leybold-Heraeus EA11, 150 mm hemispherical analyzer with multichannel detection and is isolated from the growth chamber with a gate valve. The sample was transferred between the two chambers on a bellows motion. The growth chamber is a 6-way 2 3/4 inch cross pumped with a 50 l/sec turbo pump. The gas supply was a premixed 0.2% CH₄ in H₂ cylinder that was connected to the growth chamber with a 100 sccm flow controller. The outlet of the growth chamber was connected through a stainless steel leak valve to a rotary vane pump that controlled the total pressure at 50 Torr as measured by a capacitance manometer. A 0.020 inch diameter W filament was mounted 2 mm from the Si(100) substrate at a temperature of 2350 K as measured by an optical pyrometer. The Si sample was cut from a Si(100) wafer, polished using 1 micron diamond paste, and washed with acetone followed by methanol prior to mounting on the transfer device. After growing for a prescribed time the pressure was reduced to 10⁻⁷ Torr before opening the gate valve and introducing the sample into the analytical chamber. XPS data were obtained about 30 minutes after stopping the growth.

Results and Discussion

Prior to growth ($t=0$) the Si(100) substrate was introduced into the analytical chamber and characterized with XPS by obtaining a survey scan and high resolution scans of the C(1s), Si(2p), and O(1s) regions. The survey scan shows that only C, O, and Si are present on the surface. The C(1s) region (fig. 1a) contains one relatively broad transition at 285.1 eV due to adventitious carbon whose probable source is hydrocarbons deposited on the sample prior to introduction. The Si(2p) region (fig. 2a) indicates the presence of both reduced Si (at 99.0 eV - used for calibration) and SiO₂ (at 102.7 eV) [8]. Similar data were obtained from three different Si samples suggesting that a carbon covered SiO₂ surface is typical for Si substrates treated in the manner reported above.

Following the initial Si(100) characterization the sample was returned to the growth chamber for a 15 minute growth. XPS data obtained at that point (fig. 2b) show no Si(2p) peak from SiO₂ (102.7 eV), but instead a new peak at 100.3 eV which we assign to SiC [8]. The elemental Si peak at 99.0 eV is reduced by 50% (fig. 2b) compared to the sample prior to growth (fig. 2a) indicating that the SiC is on top of the Si. Identification of the Si(2p) peak at 100.3 eV as SiC, is confirmed by the observation of a new C(1s) peak at 282.7 eV (fig. 1b) of the proper intensity and energy for carbide-type carbon [8,9]. In addition, the adventitious carbon seen in fig. 1a is removed during the first 15 minutes of growth. These four spectra (figs. 1a,b and 2a,b) show that after only 15 minutes of diamond growth the SiO₂ and carbon contamination are replaced by a SiC layer.

After 45 minutes XPS (figs. 1c and 2c) shows an increased SiC intensity in both the Si(2p) and C(1s) regions. Between 45 minutes and 4.5 hours the SiC Si(2p) peak increases in intensity while the elemental Si peak decreases to less than 5% of its original intensity (fig. 2e). By assuming a SiC layer of uniform thickness and a Si(2p) escape length of 25 Å, we estimate from fig. 2e that the SiC layer is greater than 90 Å thick. Another observation after 4.5 hours is the detection of a new type of carbon with a C(1s) peak at 284.3 eV (fig. 1e).

For longer growth periods (figs. 1f,g and 2f,g) two phenomena occur: the C(1s) peak at 284.3 eV increases in intensity concurrent with a decline in the SiC feature (282.7 eV) and the

Si intensity drops very low with no change in peak position. Figures 1f,g and 2f,g show that the surface is being covered with the new form of carbon that exhibits a C(1s) peak at 284.3 eV. The XPS survey scan after 17 hours of growth shows only a single form of carbon and a very small amount of Si. No further changes were observed by XPS after 17 hours of growth. To confirm that the C(1s) peak at 284.3 eV was due to diamond, the sample was removed from the apparatus and a Raman spectrum was obtained which exhibited the characteristic diamond line at 1332 cm^{-1} .

Conclusions

The application of XPS has for the first time elucidated some of the surface chemistry which occurs during the nucleation and growth of diamond films. We characterize the nature of the substrate prior to growth showing that the Si(100) is covered with a layer of SiO₂ and carbonaceous contamination. After a short period the SiO₂ layer and the carbonaceous contamination are removed and replaced by a layer of SiC which increases in thickness with time. Finally, diamonds nucleate and grow on the SiC layer. No other forms of carbon are observed. This experiment represents a significant improvement in the level of understanding of diamond film growth.

References

1. J.C. Angus and C.C. Hayman, *Science* **241**, 913 (1988).
2. S. Matsumoto, Y. Sato, M. Kamo, N. Setaka, *Jpn. J. Appl. Phys.* **21**, 183 (1982).
3. V.P. Varnin *et. al.*, *Kristallografiya* **22**, 893 (1977).
4. C.I.H. Ashby, *Appl. Phys. Lett.* **43**, 609 (1983).
5. K. Kurihara, K. Sasaki, M. Kawaradi, N. Koshino, *Appl. Phys. Lett.* **52**, 437 (1988).
6. S. Matsumoto, M. Hino, T. Kobayashi, *Appl. Phys. Lett.* **51**, 737 (1987).
7. S.J. Harris, A.M. Weiner T.A. Perry, *Appl. Phys. Lett.* **53**, 1605 (1988).
8. C.D. Wagner, W.M. Riggs, L.E. Davis, J.F. Moulder, and G.E. Muilenberg, Handbook of X-ray Photoelectron Spectroscopy (Perkin-Elmer, Eden Prairie, MN, 1979).
9. Y. Mizokawa, T. Miyasato, S. Nakamura, K.M. Geib, and C.W. Wilmsen, *Surface Sci.* **182**, 431 (1987).

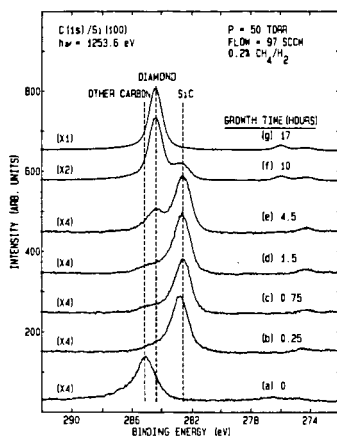


Fig. 1: XPS spectra of the C(1s) region for different growth times. Data for the substrate prior to growth, $t=0$, show carbon contamination typical for Si cleaned with methanol prior to introduction. The other spectra, b-g, show the formation of a carbide layer (282.7 eV) followed at later times by diamond growth (284.3 eV).

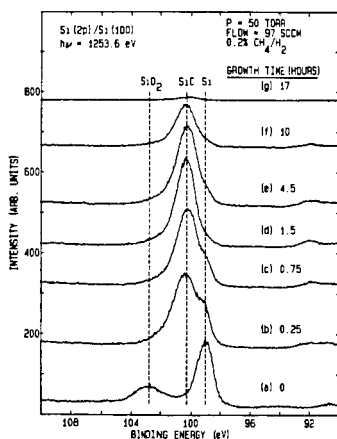


Fig. 2: XPS spectra of the Si(2p) region for different growth times. Data for the substrate at $t=0$, prior to growth, show that the Si(100) is covered with a thin layer of SiO_2 . Data at later times show that the oxide is replaced by a carbide layer (100.3 eV) which then declines in intensity as the surface is covered with diamond.

SOME THERMODYNAMIC ASPECTS OF CVD FILAMENT PROCESS FOR DIAMOND GROWTH

Himanshu B. Vakil
GE Corporate Research and Development
P.O. Box 8, CEB 479
Schenectady, New York 12301

INTRODUCTION

Low pressure synthesis of diamonds from hydrocarbons has seen an enormous resurgence in the last decade. After the pioneering work by Eversole in 1958 and decades of patient - but often non-reproducible - work by Deryagin and co-workers, the recent work in Japan by Matsumoto and co-workers has led to the universal acceptance of the viability of low pressure, metastable growth of crystalline diamond (ref. 1). As a result of recent work, not only has the chemical vapor decomposition (CVD) of diamonds by a simple thermal decomposition process been confirmed, but a plethora of low pressure processes have been developed - among them, plasma assisted CVD (RF, microwave, and DC), electron beam and laser assisted CVD, and deposition from ion beams, to name a few.

Despite the wide diversity of processes and operating conditions there are a few observations that have gained a near universal acceptance:

1. An abundant supply of atomic hydrogen is required at the growing diamond surface.
2. The exact chemical nature of the starting carbon source is not crucial. Almost any form of carbon source has been found satisfactory for growing diamonds. Alkanes, alkenes, alkynes, aldehydes, alcohols, and ketones have been used successfully to date.
3. Carbon concentration in the gas phase should be very low. An excessive amount leads to graphitic deposits.
4. For the thermal, filament process carbide-forming refractory metal filaments are successful in growing diamonds; carbon filaments apparently do not work. Other filaments such as platinum also do not work.

Finally, while it is generally believed that the reaction is kinetically limited, the exact rate limiting step and the growth mechanism are still topics of controversy. There have been many proposals as to which carbon specie is critical for the diamond growth with the list being made up of free radicals like $\text{CH}_3\cdot$ and $\text{C}_2\text{H}\cdot$, gaseous carbon atoms and clusters, molecules like CH_4 or C_2H_2 , and ionic species e.g., CH_3^+ .

The objective of this paper is to apply thermodynamic analyses to the diamond CVD process, on the one hand to give insights as to what some of the "universal" observations tell us about the process, and on the other to provide a framework for evaluating alternate hypotheses for growth mechanisms. Following a long-standing tradition at GE, our group is involved in research on a wide variety of processes for diamond synthesis, including those mentioned above. However, for the purpose of this paper, we have selected only one process - the hot filament, thermal process - primarily because it is the simplest CVD process and likely to be more amenable to thermodynamic analyses than others. In the following sections we will present results of thermodynamic equilibrium calculations aimed specifically at answering such questions as why carbon filaments do not work, or which carbon species are unlikely to be critical in diamond growth.

Thermodynamic Calculations

Thermodynamics of thermal decomposition of hydrocarbons has long been a topic of interest in the context of deposition of coke or pyrolytic carbon (ref. 2). However, most of this work has dealt with atmospheric and higher pressures, and is of little direct use to the diamond CVD process. More recently, there have been a few studies aimed especially at diamond CVD (e.g., ref. 3); we hope that this paper will serve to augment such studies and provide a slightly different perspective.

Equilibrium calculations presented here were carried out using the JANAF database, with 14 gaseous species containing C and H, and one condensed specie - graphite. Diamond phase was not included since the free energy difference between graphite and diamond is quite small compared to that between gaseous species and graphite; in our opinion, the resultant simplification well justifies incurring relatively minor errors in carbon activities and gas phase specie concentrations.

Why do carbon filaments not work?

A logical place to begin an investigation of why carbon filaments apparently do not work is to examine the condensed phase activity using conditions typical of filament growth. We have selected a feed composition of 1.5 mole% methane in hydrogen at a pressure of 0.01 atmosphere (7.6 torr or 10.13 mbar) with substrate temperatures from 700C to 1100C and filament temperatures from 2000C to 2600C. Figure 1 shows the carbon activity as a function of temperature. Over the entire range of filament temperatures the condensed phase activity is below unity, thereby indicating that the gas phase is below saturation with respect to solid carbon. Conversely, substrate temperature range shows carbon activity to be significantly greater than unity, reaching a peak supersaturation of 100 in the vicinity of 1000C. This strongly suggests that it is necessary for the filament to operate with a carbon activity in the range of 0.25 to 0.9; carbide forming refractory metals meet this criterion, but carbon filaments require that the gas phase be saturated with respect to carbon.

Another way to illustrate the same point is to calculate the carbon atom fraction in the gas phase in equilibrium with solid carbon at filament temperatures. This is shown in Figure 2. In order to be in equilibrium with a carbon filament, the reactor feed needs to be as high as 28% methane at the upper end of the range, decreasing to just below 2% at a filament temperature of 2000C which may be too low to produce an adequate amount of atomic hydrogen. This would explain why the use of a carbon filament produces graphitic deposits, similar to those obtained with an excessive amount of carbon in the feed. Lower melting filaments, such as platinum, are also unsuccessful because they are unable to generate an adequate supply of atomic hydrogen.

Equilibrium distribution of hydrocarbon species

Next, let us examine the equilibrium distribution of hydrocarbon species as a function of temperature. Figure 3 is a plot of the partial pressure (in atmospheres on a logarithmic scale) over the entire temperature range for the selected case of 1.5% methane in hydrogen as a feed. Several features can be noted from the figure.

Filament region:

1. Atomic hydrogen concentration increases rapidly from less than 10% at 2000C to over 50% at 2600C.

2. Almost all of the carbon is present as either C_2H_2 or C_2H , with all the other minor species accounting for roughly 0.5% of the total carbon. Only when the temperature exceeds 2500C do the species C and C_3 account for more than 1% of the carbon. The concentration of methyl radical is well below 0.1% over the entire temperature range.

Substrate region:

1. The predominant species are molecular hydrogen and methane.
2. At temperatures above 900C acetylene concentration increases gradually, overtaking methane between 1000C & 1100C - reportedly the preferred range for growing good diamond crystals. Ethylene is a distant third accounting for at best 1% of the carbon at its peak.

From these observations one is led to conclude that the role of the filament is to convert molecular hydrogen to atomic hydrogen, and to convert methane - or, for that matter, any other hydrocarbon source - to primarily acetylene and C_2H . The insensitivity of the process to the exact source of hydrocarbon suggests that this rearrangement proceeds fairly rapidly producing an equilibrium distribution of species, thereby obliterating any history of the feed composition. At the substrate, reverse reactions producing molecular hydrogen and methane take place, in addition, of course, to a rather slow carbon deposition reaction to form diamonds. In view of the extremely low mass transfer Peclet number in a typical filament reactor, which makes it behave more like a continuous stirred-tank reactor (CSTR), the steady-state concentrations of hydrocarbon species is determined by a balance between the source and sink rates at the filament and the substrate.

Calculated impingement rates of the various carbonaceous species using equilibrium concentrations at the filament, which provide an absolute upper bound for all species except methane and ethylene, can be compared with the observed growth rates of diamond films to obtain an estimate of the incorporation ratio (fraction of collisions resulting in film growth) required for a specific specie to be the critical one for diamond growth. Based on typical growth rates of 1 to 10 microns/hour, an average incorporation rate is approximately 4×10^{-8} g-atoms/cm²/sec. At this growth rate, the required incorporation ratio for acetylene and C_2H is roughly 1 in 1000, while that for C & C_3 is roughly 1 in 10. Since these ratios have been calculated assuming the maximum possible concentrations (equilibrium at the filament and no re-combinations thereafter), and since the substrate surface is supposedly almost totally covered with hydrogen, acetylene and C_2H appear to be the most likely candidates for the critical species, with C_3 and C being less likely (but possible) ones, particularly at high filament temperatures. Other free radicals such as CH , CH_2 , and particularly CH_3 are at too low a concentration to account for the growth rates. Methane is always a possible candidate since it can be abundant near the substrate, and ethylene can not be ruled out if one assumes complete equilibrium at the substrate. A substantial back-conversion of acetylene to methane has been experimentally observed by us based on reactor gas sample analyses, confirming the importance of the back-conversion reaction.

Simultaneous deposition of diamond and etching of graphite

It is often mentioned that one of the key elements of low pressure growth of diamonds is the ability of atomic hydrogen to etch away any graphite that may get deposited leaving behind only the diamond phase. In a process that operates in a cyclic manner (whether in time or space) there would be no inconsistencies in alternating between graphite deposition and etching conditions. In a steady-state process, however, to

maintain that bulk graphite can be deposited and then etched away would constitute a serious thermodynamic violation, since it would imply a carbon activity that was simultaneously greater than unity for deposition and less than unity for etching. If one were to invoke non-uniform temperatures on the substrate, as seen from Figure 1 parts of the substrate would have to be above 2000C for the activity to drop below unity. Experimentally, we have observed many instances where graphite is nucleated on a growing diamond film and then grows alongside the diamonds for the remainder of the experiment. This proves that once graphite is deposited during the course of diamond growth, it is there to stay unless the reactor conditions are altered.

A more difficult question to address is what happens when one uses a graphite substrate in a filament reactor: During the early stage of diamond nucleation is the graphite substrate etched? In the absence of the filament (e.g., in a furnace at 1000C) the answer would, of course, be no. Even with the filament, if the homogeneous phase were in local thermodynamic equilibrium there could be no etching. However, in the close proximity of the filament the presence of non-equilibrium concentration of atomic hydrogen makes thermodynamic arguments inapplicable. An experimental resolution of this question, while beyond the scope of this paper, is also made difficult by the fact that in the early stage of the experiment the filament is gradually coming to equilibrium with the gas by incorporating carbon, thereby significantly affecting the gas phase composition. Only a series of careful experiments can hope to resolve this very interesting question.

CONCLUSIONS

Thermodynamic equilibrium calculations were carried out for the hot filament CVD process for diamond deposition under typical conditions. It was shown that the carbon activity is considerably below unity at the filament and very high at the substrate. The failure of carbon filaments to grow diamonds was shown to be due to the gas phase in equilibrium with the filament to be excessively rich in carbon, thereby exceeding the supersaturation limits for diamond growth. Details of the gas phase concentrations were used to evaluate the likelihood of the various gas species to be critical for diamond growth.

ACKNOWLEDGEMENTS

The author would like to thank the management of GE Research and Development and GE Superabrazives for their permission to publish this paper. The author would also like to thank Dr. Steve Spacil for his valuable assistance on the program for thermodynamic calculations, Mr. R.J. Kehl for his help with the experiments, and Drs. Tom Anthony and Bill Banholzer for many valuable discussions.

REFERENCES

- [1] R.C. DeVries, Annual Rev. Mat. Sciences, 17:161 (1987).
- [2] B. Lersmacher, et. al., Carbon, vol. 5, p. 205 (1967).
- [3] M. Sommer, et. al., presented at the Diamond Technology Initiative Symposium, Crystal City, VA (July, 1988).

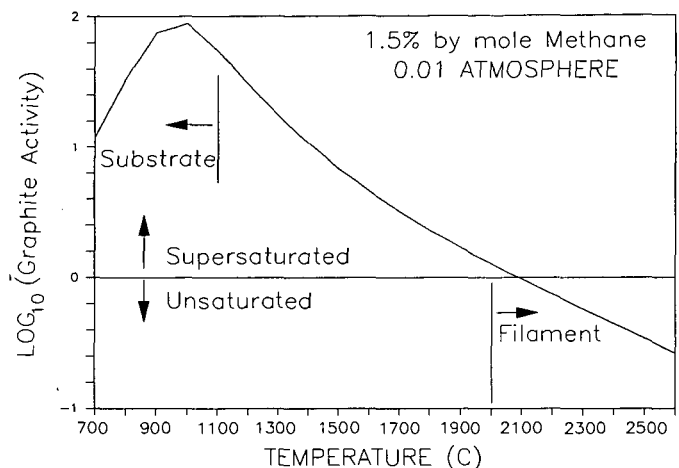


Figure 1: Graphite Activity as a function

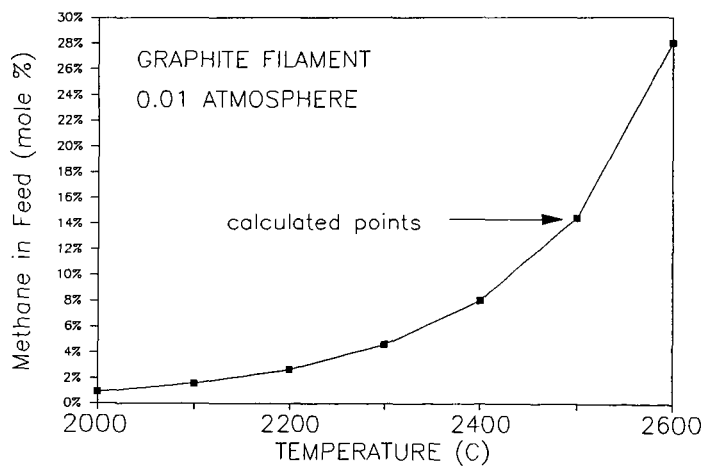


Figure 2: Feed Methane Concentration in Equilibrium with Carbon Filament

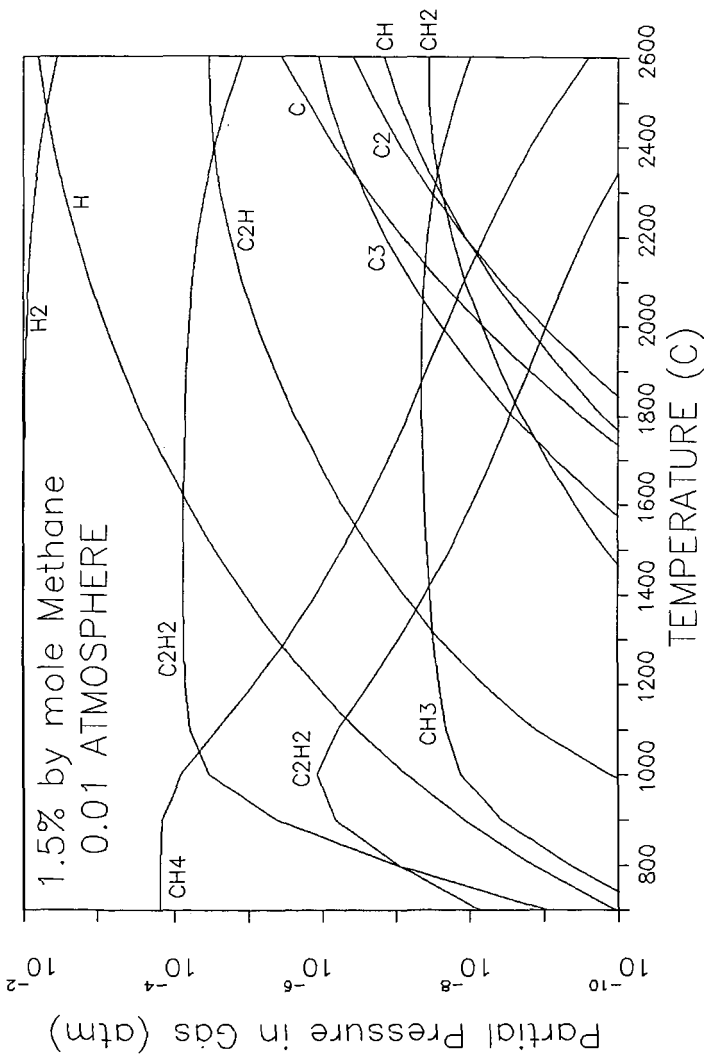


Figure 3: Equilibrium Partial Pressures in Gas

DIAMONDS IN THE CHEMICAL PRODUCTS OF DETONATION

N. Roy Greiner
Los Alamos National Laboratory
Los Alamos, New Mexico 87545

ABSTRACT

Diamonds have been found among the solid carbonaceous chemical products of high-explosive detonations. Explosives are fuel-oxidizer systems premixed on a molecular scale. This talk discusses some aspects of the chemical and hydrodynamic environment in which these diamonds form and some characteristics of the diamonds recovered. Diamonds have been recovered from detonations of composite explosives composed of trinitrotoluene (TNT) mixed with other powdered solid explosives, such as cyclo-trimethylenetrinitramine (RDX), triaminotrinitrobenzene (TATB), ammonium nitrate (AN), and nitroguanidine (NQ). The detonations were carried out in a 1.5-m³ tank, usually filled with 1 atm of Ar gas. Other explosive composites and one-component explosives have also been investigated. The diamonds have been characterized by transmission electron microscopy, x-ray diffraction, and various chemical means.

INTRODUCTION

Detailed knowledge of the chemical kinetics and equilibria of detonation has long been a desired, but elusive goal. One focus of this chemistry is the coagulation of carbonaceous solid (soot) from carbon initially present as the skeletal atoms of small organic molecules (typically consisting of 20 to 50 atoms). The "fuel" portion of the explosive molecule is the atoms of carbon and hydrogen, and the "oxidizer" is a number of nitro (-NO₂) groups. During detonation the fuel and oxidizer react to form water and oxides of carbon, the nitrogen forms N₂, and the carbon left over forms the soot. At least that is what is visualized. Most of what is "known" of the chemistry of detonation is an intricately convoluted mixture of supposition, computer modeling, and calibration of the models against hydrodynamic measurements of detonating material.

A brief description of the detonation process is appropriate here. The literature affords a wealth of further detail (see, for example, Refs. 1-3). The hydrodynamic aspects of the detonation process are quite well known; that is, the density (d), pressure (P), and velocity (D) of the detonation wave for particular explosives are well established. Temperature and chemical composition are obtained as secondary information derived from a hypothetical equation of state of the detonation products calibrated against d - P - D data for a set of explosives. The equation of state must account for extreme nonideality (compressibility factors of 15-25) and must contain a mixing rule for the different molecular species in the products. Knowledge of the kinetics of the detonation process is almost entirely empirical.

Our explosive charges were cylinders 50 mm dia x 100 mm long. They were initiated by a detonator-booster system on one end of the cylinder axis. The detonation wave propagates from the booster at the detonation velocity, about 8 mm/ μ s, as a somewhat spherical wavefront to the other end of the charge. The density of the unexploded charge is about 1.7 g/cm³, the density in the detonation front is about 2.3 g/cm³, and the detonation pressure is about 245 000 atm. The detonation wave traverses the length of the charge in about 12 μ s. As the material detonates, the outer surface of the charge begins to expand into the external environment, in our case a large tank evacuated or filled with 1 atmosphere of Ar gas. The inner core of the detonated charge remains at a pressure near 100 000 atm for about 3 μ s after passage of the detonation wave, providing a considerable time for carbon coagulation within or very near the bulk diamond stability field (Figs. 1 and 2). The most common form of the equation of state (1,4) gives a temperature of 2600 K in the steady portion of the wave and a chemical composition of H₂O, CO₂, N₂, and solid C. Chemical products recovered from quenched detonations contain many other components (3,5). There is much discussion about processes that may occur during quenching and about how to recover true detonation products (3,5).

EXPERIMENTAL

The experimental details of the detonations have been described (4). In these detonation reactions, O and N are present as well as C and H. The atomic fractions can be seen from the formulas TNT: C₇H₅N₃O₆, RDX: C₃H₆N₆O₆, TATB: C₆H₆N₆O₆, NQ: CH₄N₄O₂, and AN: NH₄NO₃. Atomic ratios are much different than those of typical chemical vapor deposition (CVD) processes. The charge compositions were made by adding solid powders to molten TNT in the following weight percentages: #27: 40 TNT/60 RDX, #36: 50 TNT/50 AN, #60: 50 TNT/50 TATB, #63: 50 TNT/50 NQ, and #10/41: 50 TNT/50 NQ. The charges were fired in a cylindrical vessel 1.5 m³ in volume, either evacuated or filled with 1 atm of Ar gas (2,4). The soot was recovered from the vessel after the detonation of each charge. The soots were then oven dried at 105°C to constant weight.

The micromorphologies of the soots were recorded by transmission electron microscopy (TEM); the diamonds were recovered by oxidizing the soot with HNO₃/HClO₄ (4); the diamonds in the residue were identified by their x-ray diffraction (XRD) powder patterns, and the diameters of the recovered diamonds were determined with an x-ray diffractometer. Thermally labile components of the soot were measured with thermogravimetric analysis (TGA), and some of the components were identified with direct insertion probe mass spectrometry (DIP/MS) or gas chromatography with mass spectrometric (GC/MS) detection.

RESULTS AND DISCUSSION

TEM has shown that the soots are composed of graphite ribbons having a smallest dimension of 3-10 nm and sometimes of diamonds having diameters of 3-7 nm (4).

The interplanar spacings measured in these samples agree well with the spacings of bulk diamond.

The crude residue containing the diamonds was sometimes found by XRD to contain minor amounts of other materials such as Al_2O_3 , MgO , and SiO_2 knocked loose from the vessel walls. When diamonds were present, this residue amounted to 15-22 wt% of the dried soot. Diamonds were found by TEM and in the oxidation residues of samples #27, #60, and #63, but not in samples #36 and #10/41. The diameters of the diamonds in the oxidation residues were determined by the widths of their diffraction lines measured on an x-ray diffractometer, and in all three cases, they were equal to the diameter of the diamonds observed in the TEM images. The diameters determined in this manner were 7 nm in #27, 3 nm in #60 and 3 nm in #63.

No measurable residue was obtained from #10/41 (TNT/NQ), which was fired in a vacuum. This result can be compared with that of #63 (also TNT/NQ, but fired in 1 atm of Ar) where diamonds were found. Sample #10/41 underwent a process called reshock, whereby the detonation products expanding in the vacuum are shocked to a high temperature when they collide abruptly with the vessel wall. Typically this results in the reaction



advancing far to the right because it is favored by high temperature at low density (3). Perhaps the diamonds in sample #10/41 were consumed preferentially by reaction 1. When the vessel is filled with Ar gas, much of the kinetic energy of the expanding products is absorbed by the Ar, mitigating the effects of reshock.

The residue from #36 (TNT/AN) contained only a small amount of Al_2O_3 but no diamonds. We have no explanation for this at this time.

Neither the graphite nor the diamond morphologies observed in the detonation soots seem to fit the picture of growth by aggregation. The detonation graphite appears as ribbons a few nanometers thick, not as aggregated smaller particles or crystals (4). This observation can be contrasted with the reported structures of graphitic soots from hydrocarbon flames, which are typically spheres 10-500 nm in diameter, composed of many small graphitic crystallites a few nanometers thick (6). The detonation diamonds appear to be perfect single crystals 3-7 nm in diameter and not aggregates of smaller crystals. Furthermore, the sizes of the diamond and graphite particles observed in these detonations appear to be too small for unrestricted growth by aggregation.

A model for growth of carbon solid by diffusive aggregation in the detonation product environment has been developed by Shaw and Johnson (SJ) (7). We can apply the SJ model to these detonations with the aid of a hydrodynamic model for the expansion of the detonation products. The model for the expansion also has been described (8).

Figures 1 and 2 show computed hydrodynamic histories of some representative volume elements in the charges used here. A large portion of the charge is maintained at a density near the detonation density for a time of about 3×10^{-6} s, whereas the characteristic time for aggregation in the SJ model is 2×10^{-12} s. The ratio of these two times gives the number of atoms in the most probable particle size, which is 1.5×10^6 atoms. If the most probable particle were a crystalline diamond sphere it would be 26 nm in diameter, whereas the largest particle we see is only 7 nm. By the SJ model, the volume of the most probable particle size is proportional to aggregation time, so the difference between the model and observation is large. Conversely, the size observed could be attained in only 5×10^{-9} s, if unrestricted aggregation were the limiting mechanism. The differences suggest that particle growth has additional restrictions and that aggregation progresses in increments closer in size to atoms than to small crystals.

The small size of the diamonds and the graphite ribbons raise the possibility that surface chemistry may play a role in their relative stabilities. In a spherical diamond 3 nm in diameter 37% of the carbon atoms are on the surface. If this surface were particularly stable, diamond might be more stable than graphite even without a high-pressure environment. Unfortunately, we have no direct information about the diamond or graphite surfaces in the unaltered soot. Moreover, the information we do have suggests a broad range of possibilities for the chemistry of the diamond and graphite surfaces.

Gouy-balance measurements on the raw soot show evidence of unpaired electrons, a common feature of finely divided solid carbons. Elemental analysis of the dry soots shows the presence of H, N, and O in addition to C atoms. About 1/10 to 1/20 of the atoms are N and 1/10 to 1/50 are H. TGA analysis indicates that about 30% of the soot is heat-labile (Fig. 3). Initial results from DIP and GC/MS analyses of the gases driven off of soots with moderate heat (350-400°C) show mass spectra attributable to H_2O , NH_3 , CO_2 , CO , HCN , $HOCN$, urea, alkanes, alkenes, and polycyclic aromatics often substituted with $-CN$ and $-NH_2$ groups. DIP analysis indicates CO_2 and CO , in about a 2/1 molecular ratio, driven off a diamond residue recovered by the $HClO_4$ oxidation process. Auger/ESCA analysis of the recovered diamond residue shows the presence of N and O atoms that are removed by Ar-ion sputtering of the surface. This technique also shows that the interior of the recovered diamonds is made up of nearly pure C. These results show that the soot has a rich chemistry involving heteroatoms. The surfaces of the 3-nm diamonds contain only about 1% of the atoms in the original explosive. Given that a number of exotic chemical species have been found in the soot in quantities comparable to the number of surface atoms on the diamonds, it seems that surface chemistry of the diamonds is practically an open question.

Determining when in the hydrodynamic history (Figs. 1 and 2) the diamond growth takes place would also be of great interest.

CONCLUSIONS

Diamonds are now a well-established chemical product of the detonation process. The conditions under which they grow can be described. They appear as single crystals, not aggregates of smaller crystals, and their growth rate seems to be limited by something more than the diffusion of carbon precursors in the dense gaseous detonation products. Determination of the surface chemistry of the detonation diamonds and when in the hydrodynamic history their growth takes place remains to be done.

ACKNOWLEDGEMENTS

It is a pleasure to acknowledge the assistance of John O'Rourke and Brad Roof with the x-ray diffraction measurements, Yvonne Rogers and Dorothy Hoard with the oxidations, Doug Farr with the Auger/ESCA analyses, Al Sattleberger with the Gouy-balance measurements, Liz Foltyn with the TGA, and Dale Spall and Rob Hermes with the analysis of the soot volatiles. Chuck Mader and J. D. Johnson offered much support and shared many insights.

REFERENCES

- (1) Mader, C. L., *Numerical Modeling of Detonations* (University of California Press, Berkeley, 1979).
- (2) Volk, F., Bathelt, H., Schedlbauer, F., Wagner, J., *Proceedings of the Eighth Symposium (International) on Detonation*, 1985, p. 577.
- (3) Ornellas, D. L., "Calorimetric Determinations of Heat and Products of Detonations for Explosives: October 1961 to April 1982," Lawrence Livermore National Laboratory report UCRL-52821, 1982.
- (4) Greiner, N. R., Phillips, D. S., Johnson, J. D., and Volk, F., *Nature*, 1988, **333**, 440.
- (5) Blais, N. C. and Greiner, N. R., *J. Energetic Materials* (in press).
- (6) Lahaye, J. and Prado, G., in *Particulate Carbon Formation During Combustion*, D. C. Siegla and G. W. Smith, Eds. (Plenum Press, New York, 1981), p. 33.
- (7) Shaw, M. S. and Johnson, J. D., *J. Appl. Phys.*, 1987, **62**, 2080.
- (8) Greiner, N. R., *Proceedings of the 19th International Conference of ICT*, 1988, p. 36-1.

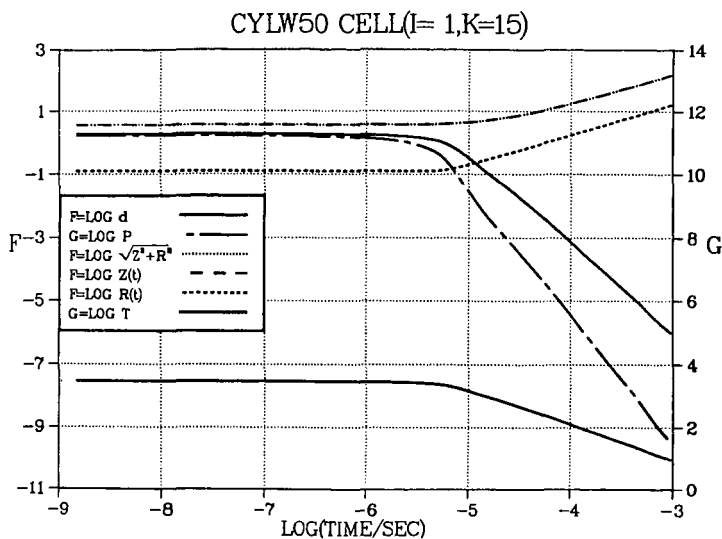


Figure 1. Hydrodynamic history of a volume element on the axis of the explosive charge 12.5 mm from the end opposite the booster charge. This volume element is representative of the detonation wave properties. The scales are logarithmic, and the units are CGS units, that is, density (d) is in g/cm^3 , pressure (P) is in dyne/cm^2 , coordinate of the volume element along the charge axis (Z) is in cm, coordinate along the charge radius (R) is in cm, and temperature derived from the equation of state (T) is in K. $\log P$ is given on the G scale, where the value 11 represents 100 000 atm. $\log P$ begins to depart from this value at about 3×10^{-6} s.

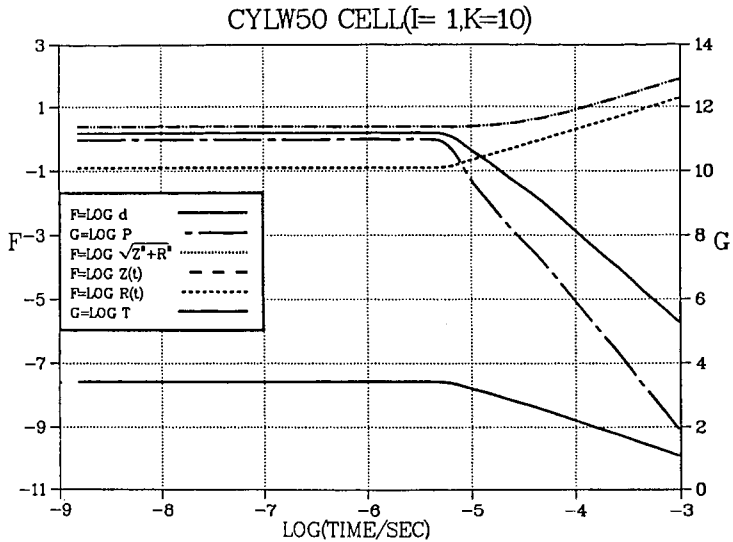


Figure 2. Hydrodynamic history of a volume element along the charge axis midway between the detonation wavefront and the booster (same scales and units as in Fig. 1). Log P is somewhat below 11 in this element, and it begins to drop below 11 after 5×10^{-6} s.

TGA73, #60 in He

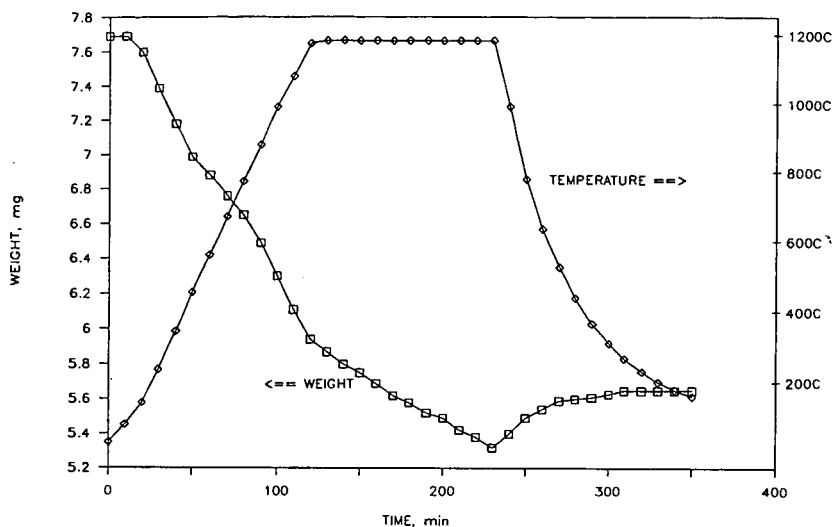


Figure 3. Thermogravimetric analysis of #60 in 1 atm of He gas. There is about 10% weight loss up to 400°C, the upper limit of the evolved gas analyses, and about 25% at the termination of the run at 1200°C.

SOME EXPERIMENTS ON THE MECHANISM OF
DIAMOND FILM GROWTH

L. R. Martin and A. R. Calloway
Aerophysics Laboratory
The Aerospace Corporation, P.O. Box 92957
Los Angeles, CA 90009

INTRODUCTION

Since direct crystallization of diamond from carbon atoms is thermodynamically unfavorable at low pressures, it has been suggested by Fedoseev, et al.(1) that an "organic synthesis" picture of diamond formation is more accurate. In this picture, a diamond structure is built up by chemical reaction with carbon-containing free radicals or ions, and structure formation is controlled by kinetics rather than thermodynamics. A key problem in low pressure diamond film synthesis is the lack of a generally accepted chemical mechanism for this process. (For an example of a proposed mechanism, see Tsuda, et al.(2).) Resolution of the mechanistic question will require identification of the various chemical species present in diamond synthesis systems, and correlation of the growth rate with the concentrations of the species. A complete understanding of the mechanism can provide a rational basis for the design of improved methods for diamond synthesis.

EXPERIMENT

We have constructed a simple diamond film synthesis system with the objective of gaining mechanistic information. Our laboratory is not yet able to measure the concentrations of free radicals and ions directly, so we have designed experiments to give differing initial mixtures of free radicals. The interpretation of such experiments is complicated by the fact that rapid gas-phase chemistry takes place to change the mix of radicals, but it is possible to estimate the progress of such chemistry with kinetic modeling.

The apparatus consists of a quartz bell jar on a vacuum manifold with provision for vacuum ultraviolet (VUV) irradiation of the substrate region as well as hot tungsten filament dissociation of the gas atmosphere. The VUV source is a hydrogen microwave discharge. The substrate material, usually single crystal silicon, was mounted on a silicon nitride heating element. The atmosphere was typically 1% organic vapor and 99% hydrogen gas at 10 torr, flowing at 100 sccm. The filament, when in use, was at 2000 Celsius and 5mm from the substrate, and the

substrate was at 850 Celsius. Experiments were done with methane, carbon monoxide, acetone, acetylene, and methyl bromide. Our assessment of the most probable initial species produced is based on thermochemistry for the tungsten filament (3) and known photochemistry for the VUV source (4).

Table 1 summarizes the experiments carried out. If we consider only neutral chemistry, our interpretation of these experiments is as follows: CH_3 and C_2H_2 are more likely to be reactants than are C, C_2H , or CH_2 . This conclusion must be taken with caution because of the important influence of the gas phase chemistry. For example, a crude analysis of the reaction manifold will show that methyl radicals, CH_3 , will recombine very rapidly under the conditions of the experiment, and are probably regenerated by the reaction of H-atoms with undissociated methane. This interpretation explains the apparent paradox in the table: methyl bromide is a good source of methyl radicals, yet it produces no observable diamond film. The explanation is that methyl bromide reacts rapidly with hydrogen atoms to produce a large initial concentration of methyl radicals, but these quickly recombine and leave no new source of radicals. Our experiments give no direct information about the importance of ions. In our view, ions might be generated by electron bombardment of the substrate, and therefore their possible importance cannot be ruled out in these experiments.

ACKNOWLEDGEMENT

This work was supported by the Aerospace Sponsored Research program.

REFERENCES

- 1) D. V. Fedoseev, V. P. Varnin, and B. V. Deryagin, Russian Chemical Reviews, 53 435-444 (1984).
- 2) M. Tsuda, M. Nakajima, and S. Oikawa, J. Am. Chem. Soc. 108, 5780-5783 (1986).
- 3) J. L. Franklin, et al., Ionization Potentials, Appearance Potentials, and Heats of Formation of Gaseous Positive Ions NSRDS-NBS 26, U. S. Dept of Commerce (1969).
- 4) J. G. Calvert and J. N. Pitté, Jr, Photochemistry, Wiley, New York, (1966).

TABLE I

SUMMARY OF EXPERIMENTS

CARBON SOURCE	VUV	HOT WIRE	SPECIE.	RESULTS
CH ₄		X	CH ₃	SMALL AMOUNT OF DIAMOND
	X		CH ₂	(no data)
CO		X	CO*	DEPOSIT OF TUNGSTEN CARBIDE
	X	X	C	LONSDALEITE
(CH ₃) ₂ CO		X	CH ₃	ABUNDANT DIAMOND
	X	X	CH ₃	ABUNDANT DIAMOND, MORE NUCLEATION
C ₂ H ₂		X	C ₂ H ₂ *	SOME DIAMOND
	X		C ₂ H	SLIGHT DIAMOND, LESS THAN THERMAL
CH ₃ Br		X	CH ₃	GRAPHITE
	X		CH ₃	NO DIAMOND DEPOSIT

OXIDATION OF SELECTED ORGANOSULFUR COMPOUNDS IN DODECANE
OVER A HEATED METAL SURFACE

Robert E. Morris and George W. Mushrush

Chemistry Division, Code 6180
U.S. Naval Research Laboratory
Washington, D.C. 20375-5000

INTRODUCTION

The use of jet fuel as a heat exchange medium imposes significant levels of thermal stress. Hydrocarbon fuels subjected to such temperatures have been shown to undergo considerable degradation. This observed degradation can be manifested by the formation of deposits on heat exchanger surfaces, on filters, in nozzles and on combustor surfaces (1,2). Heteroatoms, i.e., oxygen, nitrogen and sulfur and ash have been found to comprise as much as 40 percent of such deposits (3).

Sulfur can constitute the most abundant heteroatom present in military jet fuel (JP-4 and JP-5), since up to 0.4% total sulfur by weight is allowed per MIL-T-5624M. In commercial jet fuels, the ASTM Standard Specification for Aviation Turbine Fuels (4) permits up to 0.3% total sulfur by weight. Trace levels of sulfur, particularly as thiols, have been found to greatly increase the deposit forming tendencies of fuels during thermal stress. For this reason, much more stringent controls over thiol content are generally exercised. Deposits formed in jet fuel over the temperature range of 150 to 650°C in the presence of oxygen have been found to contain a much greater percentage of sulfur, up to a 100-fold increase, than that present in the fuel itself (1,5). The sulfur content of these deposits has been found to vary from 1 to 9% (6). The formation of such deposits has been attributed to the participation of mercaptans, sulfides and disulfides (7). Trace levels of thiols, sulfides and polysulfides were found to increase deposit formation even in deoxygenated jet fuels (7,8,9). In contrast, accelerated storage testing of fuels at 120-135°C indicated that while thiols promoted deposit formation, sulfides and disulfides exhibited inhibitory effects on deposition by decomposing peroxides (10).

Previous work in our laboratory has shown that aldehydes, thiols, sulfides and disulfides could be readily oxidized by hydroperoxides (11,12,13). During accelerated storage testing of a jet fuel at 65°C for four weeks, we have found (14) peroxide levels of 0.1 meq/kg. In the presence of 0.03% (w/w) sulfur from thiophenol, the accumulation of peroxides increased to 1.4 meq/kg. If the oxygen availability is limited but the temperature is sufficiently high, the hydroperoxide level will then be limited by free radical decomposition. In studies of the same jet fuel in our laboratory using a modified JFTOT apparatus, the maximum

hydroperoxide concentration reached after sparging with air for 15 min before stressing was 0.7 meq/kg; sparging with pure oxygen for a similar time before stressing raised the maximum hydroperoxide concentration to 2.8 meq/kg at 280°C.

It is difficult to identify specific reaction pathways from studies of fuels, which are complex mixtures. Model studies have been utilized to determine trace reaction products. These model studies were conducted in sealed borosilicate glass tubes at 120°C for up to 60 min. From the t-butylhydroperoxide (tBHP) initiated oxidation of dodecane thiol and hexyl sulfide (13) the major oxidation products were the dodecyl disulfide and hexyl sulfoxide, respectively. Similar studies revealed the major product of the oxidation of thiophenol by tBHP or oxygen to be phenyl disulfide.

We have utilized our modified JFTOT apparatus as a first step in determining the applicability of the findings from the model studies with changes occurring in aircraft fuel systems. This paper describes studies of the oxidation of thiophenol and hexyl disulfide in dodecane during stress in the JFTOT.

EXPERIMENTAL

Reagents. n-Hexyl disulfide and Thiophenol were obtained from Aldrich Chemical Co. They were distilled in vacuo to 99.9% purity before use. n-Dodecane (99% min.) was obtained from Phillips Petroleum Co. and was used without further purification.

Methods. Samples were thermally stressed in the modified JFTOT apparatus which has been described previously (15). The sulfur compound was blended into the dodecane in a glass vessel and aerated samples with dry air for 15 minutes, where applicable. To increase the heated surface area available and to reduce the steepness of the tube temperature profile, 304 stainless steel JFTOT heater tubes with five-inch heated sections were employed. The modified JFTOT apparatus permits sampling of stressed samples after passing over the heater tube and before returning to the reservoir (15). Procedures for determining the oxygen and hydroperoxide concentrations in the stressed dodecane have been described earlier (16). Product identification was obtained by combined GC/MS (EI mode). The GC/MS unit consisted of a Hewlett-Packard Model 5980 GC coupled to a Finnigan MAT ion trap detector. An all glass GC inlet system was used in combination with a 0.2mm x 50m OV-101 fused silica capillary column. A carrier gas flow of 1mL/min was used with an inlet split ratio of 60:1. A temperature program with an initial hold at 70°C for 2 min, increasing at 6°C/min, with a final temperature of 240°C.

RESULTS AND DISCUSSION

The influence exerted by sulfur compounds in controlled testing is affected not only by the structure of the organosulfur compound but also by the stress regimen employed. In the JFTOT, the liquid

flows at a rate of approximately 3 ml/min. With the non-standard length JFTOT heater tubes employed in this study, the sample passes over the tube in approximately 28 sec. While the JFTOT does not simulate turbulent flow conditions such as those in the heat exchangers, it does however provide a relatively short reaction time under conditions of limiting oxygen availability.

As the dodecane comes in contact with the hot metal surface of the heater tube, reaction with oxygen leads to autoxidation and the formation of peroxy radicals. The ensuing propagation mechanism continues as long as the temperature is sufficient to produce more free radicals. In the JFTOT where the reaction time is relatively short, the available dissolved oxygen is not fully depleted until the tube temperature approaches 300°C. This is evident in the temperature profiles of oxygen (Fig. 1) and hydroperoxide concentrations (Fig. 2) measured in neat dodecane. The profiles indicate a correspondence between oxygen consumption and hydroperoxide concentrations. While some peroxidation occurs below 220°C, rapid oxidation ensues above that temperature. At temperatures exceeding approximately 280°C, the dodecyl hydroperoxide undergoes decomposition (15), which accounts for the decrease in concentration above that temperature.

The addition of 0.4% (w/w) sulfur from n-hexyl disulfide (HDS) suppressed peroxidation (Table I) by about 46% of the level attained in the neat fuel. Additions of 0.2% (w/w) sulfur from HDS resulted in suppression to approximately 68% that of the neat dodecane.

Table I. Hydroperoxide Concentrations Measured in Dodecane Containing Organosulfur Compounds as a Function of JFTOT Maximum Heater Tube Temperature

Maximum Tube Temp., °C		Hydroperoxides, meq/kg			
		Hexyl Disulfide		Thiophenol	
	neat	0.2% S	0.4% S	0.005% S	0.03% S
21-120	nd ^a	nd	nd	nd	nd
200	0.11	0.01	nd	nd	nd
240	2.15	1.09	1.50	0.13	nd
280	2.25	1.03	1.52	1.02	nd
320	1.60	0.36	nd	0.69	nd

^anot detected, less than 0.01 meq/kg.

While a proportional response between HDS concentration and suppression of peroxidation was observed, it was far from quantitative, given the great excess of sulfur over the quantity of hydroperoxide formed in the neat dodecane. This is probably a consequence of the limitations imposed by the relatively short reaction time. The oxidation of disulfides in non-aqueous media has been reported (17) to proceed via successive coordination of oxygen

to the sulfur centers to produce the α -disulfone which cleaves to yield the sulfonic acid. Comparison of oxygen consumption profiles shown as a function of temperature in Fig. 1 reveal that direct oxidation by dissolved oxygen did not play a role in peroxide reduction. Therefore, the disulfide was reacting with dodecane autoxidation products to block the formation of hydroperoxides. Attempts to identify the oxidation products of hexyl disulfide in the JFTOT effluent were complicated by the low concentration of products and the difficulties experienced in detection. Future studies directed towards model studies of hexyl disulfide oxidation by t-butyl hydroperoxide are expected to provide information concerning product distributions and allow for optimization of detection procedures.

Thiophenol was much more reactive and completely suppressed peroxidation when added at 0.03% (w/w) Sulfur (Table I). By reducing the amount of sulfur from thiophenol to 0.005% (w/w), a detectable amount of hydroperoxides accumulated at temperatures between 240 and 280°C. Previous model studies in our laboratory (13), have shown that the oxidation of thiophenol by t-BHP results in the formation of the corresponding disulfide, phenyl disulfide. The oxidation of thiols classically occurs through the formation of the thiyl radical, which in the case of thiophenol, would be favored by resonance stabilization through the phenyl group. Thus, it is not surprising that thiophenol would be such an effective radical trap, terminating the chain reactions early in the propagation step. Examination of the oxygen consumption profiles generated from dodecane containing 0.03% and 0.005% (w/w) sulfur from thiophenol confirm that the free radical chain reactions were being terminated very quickly before significant autoxidation could ensue. In the presence of thiophenol, the oxygen consumption was reduced with respect to that of the neat dodecane.

Examination of the reaction products of thiophenol oxidation in the JFTOT by combined GC/MS confirmed the presence of phenyl disulfide. Examination of JFTOT effluent taken over a range of temperatures by GC/MS (Fig. 2) revealed that the formation of the disulfide corresponded to the temperature at which dodecane autoxidation proceeded and the hydroperoxide concentration in the neat dodecane reached a maximum. Thus thiophenol was being oxidized to the phenyl disulfide by dodecane autoxidation products, most likely by dodecoxy radicals, which suppressed the formation of hydroperoxides. The conversion to phenyl disulfide reached a maximum at temperatures above 300°C, which corresponds to the temperature at which all the available oxygen has been consumed and where dodecyl hydroperoxide disproportionates. To determine the contribution of the anaerobic thermal decomposition of the thiophenol to thiyl radicals and dimerization to phenyl disulfide, deoxygenated dodecane containing 0.03% (w/w) sulfur from thiophenol was examined. The corresponding curve (Fig. 2) for disulfide/thiol ratios indicated that thermal decomposition was significant only at temperatures above 320°C and would not account for the magnitude of phenyl disulfide conversion observed.

CONCLUSIONS

The principal products arising from the liquid phase oxidation of thiophenol by peroxides formed in situ by reaction of the dodecane with dissolved oxygen at elevated temperatures were identical to those identified in the model studies. Thus, these data indicate that the findings of the model studies can be applicable to aircraft fuel systems. The major route of oxidation of thiophenol most likely involved the donation of a hydrogen radical to the dodecoxy radical. While the resultant alcohol was not detected, interaction with dodecylperoxy radical would result in the formation of dodecyl hydroperoxide. However this is ruled out since hydroperoxides were not detected. While in the model studies, the disproportionation of tBHP was responsible for providing the alkoxy radicals, in the JFTOT, dodecane autoxidation provided the source of free radicals. Due to the ease of formation of the thiylphenyl radical, free radical chains were effectively terminated thus suppressing formation of dodecyl hydroperoxide. Although oxidation of thiophenol by dissolved oxygen in the JFTOT was not significant, thermal decomposition of thiophenol was observed to occur above 280°C to form the disulfide.

The behavior of hexyl disulfide in the JFTOT was consistent with an oxidation mechanism which involves coordination of oxygen to the sulfur centers. Since disulfides cannot act as peroxide reducers, by donating hydrogen radicals, minimal effects were realized on peroxidation during short reaction times in the JFTOT. There was no evidence of direct oxidation of the disulfide by dissolved oxygen.

LITERATURE CITED

1. Hazlett, R. N. and Hall, J. M., 1985. "Jet Aircraft Fuel System Deposits in Chemistry of Engine Combustion Deposits". L. B. Ebert, ed., Plenum Press: New York, 245-261.
2. Scott, G., 1965. "Atmospheric Oxidation and Antioxidants". Elsevier: Amsterdam, Chapter 3.
3. Nixon, A. C., 1962. "Autoxidation and Antioxidants of Petroleum, in Autoxidation and Antioxidants". Lundberg, W. O. ed., Wiley Interscience: New York, 695-856.
4. ASTM "Standard Specification for Aviation Turbine Fuels". In Annual Book of ASTM Standards; ASTM: Philadelphia, 1987; Part 23, ASTM D1655-82.
5. Taylor, W. F., 1976. "Deposit Formation From Deoxygenated Hydrocarbons II. Effects of Trace Sulfur Compounds". Ind. Eng. Chem. Prod. Res. Dev., 15, 64-68.
6. Coordinating Research Council, 1979. "CRC Literature Survey on the Thermal Oxidation Stability of Jet Fuel". CRC Report No. 509; CRC, Inc: Atlanta, GA.

7. Taylor, W. F., and Wallace, T. J., 1968. "Kinetics of Deposit Formation from Hydrocarbons". *Ind. Eng. Chem. Prod. Res. Dev.*, 7, 198-202.
8. Taylor, W. F., and Frankenfeld, J. W., December 1975. "Development of High Stability Fuel". Final Report for Phase II, Contract Nol N00140-74-C-0618, Exxon/GRU.15GAF.75.
9. Wallace, T. J., 1964. "Chemistry of Fuel Instability". In *Advances in Petroleum Chemistry and Refining*, Wiley-Interscience: New York, 353-407.
10. Daniel, S. R. and Heneman, F. C., 1983. "Deposit Formation in Liquid Fuels: Effects of Selected Organo-Sulphur Compounds on the Stability of Jet A Fuel". *Fuel*, 62, 1265-1268.
11. Mushrush, G. W. and Hazlett, R. N., 1985a. "Liquid Phase Radical Reactions of Octanal and tert-Butyl Hydroperoxide." *J. Org. Chem.*, 50, 2387-2390.
12. Mushrush, G. W., Hazlett, R. N. and Eaton, H. G., 1985b. "Liquid Phase Oxidation of Undecanal by t-Butylhydroperoxide in Dodecane." *Ind. Eng. Chem. Prod. Res. Dev.*, 24, 290-293.
13. Mushrush, G. W., Watkins, J. M., Hazlett, R. N. and Hardy, D. R., 1987. "Liquid Phase Oxidation of Hexyl Sulfide and Dodecanethiol by t-Butyl Hydroperoxide in Benzene and Tetradecane". *Ind. Eng. Chem. Prod. Res. Dev.*, 26, 662-667.
14. Watkins, J. M., Mushrush, G. W., Hazlett, R. N. and Beal, E. J., 1988. "Hydroperoxide Formation and Reactivity in Jet Fuels". *Energy & Fuels*, accepted for publication.
15. Hazlett, R. N., Hall, J. M. and Matson, M., "Reactions of Aerated n-Dodecane Liquid Flowing over Heated Metal Tubes", *Ind. Eng. Chem., Prod. Res. Dev.*, (16), No.2, p.171, 1977.
16. Morris, R. E., Hazlett, R. N. and McIlvaine, C. L., 1988. "The Effects of Stabilizer Additives on the Thermal Stability of Jet Fuel". *Ind. Eng. Chem. Res.*, 27, 1524-1528.
17. Oae, S. (Ed.), "Organic Chemistry of Sulfur". Plenum Press, New York, 1977.

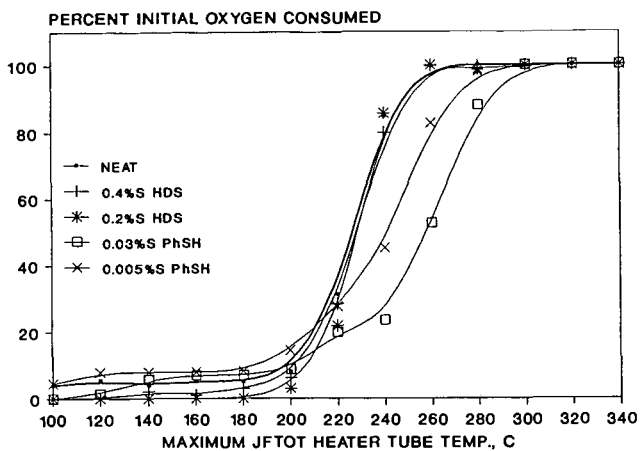


Figure 1. Temperature Dependence of Oxygen Consumption by neat and Doped Dodecane During Stress in the JFTOT.

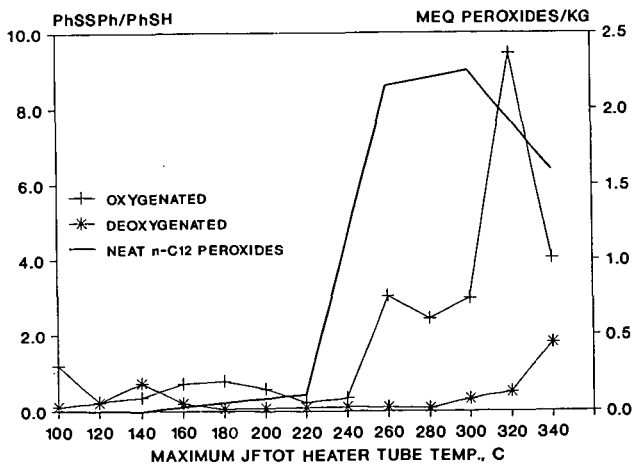


Figure 2. Phenyl Disulfide/Thiophenol Conversion Ratios by GC/MS (left ordinate scale) and Peroxidation of Neat Dodecane (right ordinate scale).

ESCA AND FTIR STUDIES OF BITUMINOUS COAL

Cara L. Weitzsacker, James J. Schmidt
Joseph A. Gardella, Jr.

Department of Chemistry and Surface Science Center
University of Buffalo, SUNY, Buffalo, NY 14214

ABSTRACT

Bituminous coal from the Illinois #6, Upper Freeport, Pittsburgh and Kentucky #9 seams were examined by Electron Spectroscopy for Chemical Analysis (ESCA) and Fourier Transform Infrared Spectroscopy (FTIR). These coals were stored under various conditions (air, N₂, mine water) and received in forms progressing from raw to ash - removed coal, (raw, milled, processed). ESCA was utilized to determine surface elemental composition and functional groups with particular attention given to C, O, N and S. Sulfur and oxidized coal models have been examined to determine the sulfur and carbon species present at the surface. FTIR has been used to correlate functional group assignments with the ESCA results.

INTRODUCTION

The surface composition characteristics of coal are important to the behavior of coal in various processing techniques. This study focuses on the surface of coal in powder form, with emphasis on the elemental composition of the surface of coal, and the functionality of C, O, N and S. One interesting application of this information would be to study the wettability of coal, of concern in agglomeration in various cleaning processes. Agglomerated coal could be separated from mineral matter.(1,2)

Both ESCA and FTIR were used in the study of four bituminous coals. These coals were taken from the Illinois #6, Kentucky #9, Pittsburgh and Upper Freeport seams. The ROM coals were stored under three conditions - in ambient air, mine site tap water and dry nitrogen. Portions of these samples were also milled and processed (mineral matter removed), and these were then analyzed. These samples will serve as reference samples for an ongoing aging experiment to be described in later papers.

EXPERIMENTAL

Raw, milled and processed coals were received under N₂ in sealed bottles from Otisca Industries, Ltd. Raw coals were analyzed as received. Milled and processed coals had to be vacuum dried to remove water and water/pentane respectively. All samples were stored under dry N₂ when received.

Vacuum drying was done on a glass vacuum line. Samples were manipulated under dry N_2 when loaded in vacuum tubes and when the dried coal was removed from the vacuum tube. A liquid nitrogen trap was used to prevent pump oil from backstreaming onto the samples. Samples were evacuated at room temperature for five hours. After vacuum drying all three types of samples were treated the same for sample preparations. Air exposure has been minimized to less than two minutes for the transfer of samples into instruments.

ESCA spectra were recorded on Physical Electronics Model 5100 with a Mg $K_{\alpha 1,2}$ X-ray source (1253.6 eV). Experimental conditions of the X-ray were 300 W, 15 kV and 20 mA. Base pressure of the instrument was 2×10^{-9} torr and operating pressure ranged from 1×10^{-7} to 2×10^{-8} torr depending on the sample. The pass energy was 35 eV for high resolution narrow scans. All spectra were taken using a 45° take-off angle. The sampling depth at this take-off angle was approximately 60 Å.

For ESCA analysis sample preparation was accomplished by pressing coal powder onto double-sided sticky tape on a sample stage. The coal was transferred immediately to the introduction chamber of the instrument and pumped down for one hour before being moved into the main chamber for analysis. Wide scan spectra were taken for 15 - 20 minutes, followed by high resolution narrow region scans for a total of 50 minutes. There was no evidence of sample damage after 65 - 70 minutes under the X-ray.

Infrared spectra were acquired on two different FTIR systems. The first system was a Nicolet 7199A FTIR Spectrometer with an MCT detector. The bench was purged with dry air. Spectra were taken with 1000 scans. The second instrument was a Mattson Alpha Centauri with a DTGS detector. The bench was purged with dry N_2 . Spectra acquired were the result of 32 scans.

Samples for FTIR were prepared by KBr mull. Approximately .42g KBr was mixed with .006 - .01g of coal. The mull was pressed into a KBr pellet using a 13mm die under 8000 psi for 45 - 60 seconds.

RESULTS AND DISCUSSION

For this study, seven samples from each of the four seams were analyzed. In each sample set, three samples were raw coal (stored under air, N_2 or water), two were milled (air stored) and two were processed (stored under air and N_2). Tables 1 - 3 show surface atomic concentration results from ESCA analysis. Common to every one of these samples was the detection of C, O, and N. Sulfur was not detectable on the surface of three of the raw samples. Other elements found were Al, Si, Na, Fe and K. Na was found in both the Illinois #6 and Upper Freeport coals. Fe and K were only found in one of the Illinois raw samples.

Inorganic elements were detected in the greatest quantities in the raw samples. The percent surface atomic

concentrations decreased slightly after milling and decreased significantly after the coal was processed. In the processed samples, the inorganics were reduced to less than 1 % or, in many cases, were no longer detectable.

The storage conditions of the raw coals only showed a significant difference in the Illinois #6 and Upper Freeport coals. In the Kentucky #9 and Pittsburgh coals, the resultant % surface atomic concentrations were consistent through all three storage conditions. See Table 1. The two milled samples of Illinois #6 also showed inconsistency in the % surface atomic concentrations. For the other three coals, % surface atomic concentrations of the two milled samples were approximately equal. See Table 2. In the processed coals, the % surface atomic concentration of carbon was 85 - 88 % through all four coals. The % surface atomic concentration of oxygen was 10 - 12 %. Nitrogen remained consistent through all storage and processing steps, with a % surface atomic concentration of approximately 1 - 2 %. The % S remaining in the processed coals varied from .50 - 1.1 %. See Table 3.

In ESCA analysis, differential charging of the inorganic and organic species in the coals was noted. Standards consisting of mineral matter from each mine were run to determine the charge correcting for the inorganics. Si, Al, Na, K, Fe and inorganic S were corrected using Si (SiO_2), binding energy 103.4 eV. The organic species (C, O, N and organic S) were charge corrected using C 1s (hydrocarbon), binding energy 285.0 eV.

The C 1s region was curve fitted to five bands (3,4). See Table 4 and Figure 1. The initial band was set after standards of graphite were analyzed. This peak was at a binding energy of 284.6 eV. Oxidized coal was also analyzed to solidify the assignments of the carbon / oxygen species. Quantitation was done based on the curve fits. See Table 5. From raw to processed coal, a decrease is seen in the elemental / graphitic C and an increase in the aliphatic / aromatic C. C - O remained consistent, while C = O varied widely.

Sulfur has also been found to be present in inorganic and organic species. The inorganic sulfur is postulated to be sulfate compounds. In many samples, nitrogen appears as a broad peak at approximately 400 eV. Pyridine and pyrrole (5) appear at approximately 398.8 and 400.2 eV. It is postulated that both of these could be present.

Transmission FTIR spectra of all samples were collected. Correlations between FTIR and ESCA results support the observations of changing surface composition as raw coals went through processing. Peaks assigned to inorganics such as silicates vary in intensity proportional to the quantities found by ESCA. Similar correlations are found with the

organics.

CONCLUSIONS

ESCA and FTIR are useful methods in the analysis of coal surfaces. Composition and surface functionality can be elucidated. FTIR can be used to correlate these results deeper into the sample by transmission experiments.

ACKNOWLEDGEMENTS

Support for this work has been provided by the Department of Energy under Contract # DE - AC22 - 87PC79880 DOE Pittsburgh Energy Technology Center with a subcontract to Otisca Industries Ltd.

REFERENCES

1. Schobert, H. H., 'Coal The Energy Source of the Past and Future'; American Chemical Society: Washington DC 1987
2. Frederick Simmons; private communications
3. Perry, D. L. and Grint, A., FUEL 1983, 62, 1024 - 1033
4. Wandass, J. H.; Gardella, Jr., J. A.; Weinberg, N. L.; Bolster, M. E.; Salvati, Jr., L. J. Electrochem. Soc. 1987, 134 (11), 2734 - 2739
5. Bartle, K. D.; Perry, D. L.; Wallace, Fuel Process. Technol. 1987, 15, 351 - 361

TABLE 1

	Illinois Raw			Kentucky Raw		
	Air	N	Water	Air	N	Water
C	43	23	33	71	69	71
O	40	51	48	21	22	22
N	1.1	.60	1.1	2.0	1.8	1.0
S	.30	---	---	1.1	1.2	1.2
Al	5.0	7.9	6.5	2.4	2.6	1.2
Si	9.2	15	11	3.2	3.5	2.8
Na	1.4	1.9	1.4	---	---	---
Fe	---	3.1	---	---	---	---
K	---	.89	---	---	---	---

TABLE 2

	Illinois		Pittsburgh	
	Milled			
C	54	66	72	72
O	35	27	22	22
N	1.5	1.5	1.5	1.5
S	.67	.45	.54	.62
Al	3.4	2.2	2.0	2.1
Si	5.9	4.4	3.3	3.5
Na	.50	.86	---	---

TABLE 3

	Illinois		Upper Freeport	
	Air	Processed	Air	N
C	85	85	86	88
O	12	12	9.7	9.4
N	1.2	1.5	1.8	1.4
S	.72	1.1	.86	.52
Al	---	---	.74	---
Si	.92	.55	1.0	.44
Na	---	---	---	---

TABLE 4

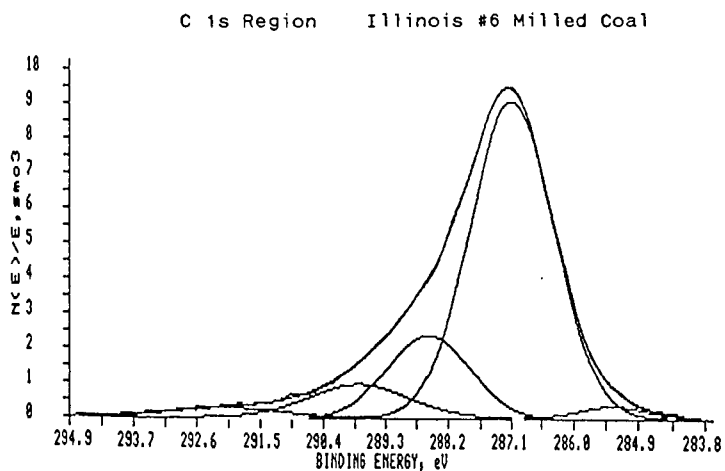
I	284.2 eV	graphitic / elemental C
II	~ 285.0 eV	hydrocarbon (aliphatic or aromatic)
III	~ 286.6 eV	C - O
IV	~ 288.0 eV	C = O
V	~ 290.5 eV	COOH, carbonate or π to π^* shakeup

TABLE 5
% C Species by Curve Fitting

Illinois #6

	Raw	Milled	Processed
I	13.85	2.61	2.43
II	58.22	67.27	70.70
III	19.24	17.25	18.26
IV	7.02	9.46	3.88
V	1.67	3.41	4.73

Figure 1



THE FORM-OF-OCCURRENCE OF CHLORINE IN U.S. COALS: AN XAFS INVESTIGATION

Frank E. Huggins¹, Gerald P. Huffman¹, Farrel W. Lytle², and Robert B. Gregor²

¹University of Kentucky, Lexington, KY 40506

²The Boeing Company, Seattle, WA 98124

ABSTRACT

X-ray absorption fine structure (XAFS) spectroscopy determinations have been made at the chlorine K absorption edge on a number of U.S. coals in order to investigate the form-of-occurrence of chlorine in the coals. The coals vary in chlorine content from 0.04 to 0.84 wt% and in rank from lignite to hvA bituminous. For the most part, the chlorine K-edge XAFS spectra of the coals are very similar and no significant variation is noted among spectra of leached samples of the same coal. The coal XANES spectra differ significantly from spectra of all organo-chlorine compounds and inorganic chlorides examined. However, spectra of hydrated chloride species, including NaCl solutions and $\text{CaCl}_2 \cdot 6\text{H}_2\text{O}$, and of organic hydrochlorides, are quite similar to the coal spectra. Analysis of the EXAFS region for the coals suggests the presence of a relatively long bond ($\sim 3.0 - 3.1\text{\AA}$) to water molecules in the nearest neighbor shell around the chlorine. These data and results are compatible with hydrated chloride anions in the moisture associated with coals as the major form-of-occurrence of chlorine in U.S. coals.

INTRODUCTION

Coals with appreciable chlorine contents (>0.3 wt%) can be troublesome during utilization due to the corrosive effect of chlorine on both metallic and ceramic materials. In the U.S., such problems related to chlorine content are relatively uncommon except for certain deep-mined coals from the Illinois basin in which the chlorine contents can be as high as 1 wt% (1). Although much of the chlorine in Illinois coals can be removed by aqueous leaching treatments (2,3), the form-of-occurrence in these and other U.S. coals is still not known with any certainty. Float-sink tests for "organic affinity" as developed by Zubovic (4) do not appear to have been applied to chlorine in U.S. coals. Compositional correlations have been used to suggest that chlorine has both inorganic (NaCl) and organic forms in Illinois coals (1,5). Conversely, the lack of the association of chlorine with other elements in a microprobe study of Upper Freeport coal has been interpreted as indicating organic chlorine forms (6). However, other investigators, based largely on microscopic examinations, list only inorganic chlorides, such as NaCl, KCl, $\text{MgCl}_2 \cdot 6\text{H}_2\text{O}$, etc., as the primary occurrences of chlorine in coal (7,8). Chakrabarti (9), working principally with Gondwana coals, has described detailed analytical procedures for determining both organic and inorganic forms of chlorine in coal. British researchers working with their native high chlorine coals for the most part have proposed that most, if not all, of the chlorine in coal is inorganic and derived from NaCl-rich ground waters penetrating the coal seam (10,11). Recent pyrolysis/mass spectroscopic work (12) on British coals has rather convincingly confirmed this occurrence.

X-ray absorption fine-structure (XAFS) spectroscopy is perhaps the best method currently available for elucidating the local structure and bonding of a specific element in a complex, heterogeneous, noncrystalline matrix such as coal. Not only can the element be investigated directly in coal at quite dilute levels (~ 100 ppm), but, in principle, information about the immediate coordinating ligands can also be derived from an analysis of the XAFS spectrum. In this work, XAFS spectroscopy

was used to examine the occurrence of chlorine in a number of U.S. coals. From these measurements it can be concluded that much, if not all, of the chlorine in these coals is present as chloride anions in the moisture associated with the pores and microcracks of the coal matrix.

EXPERIMENTAL

Samples: Pulverized samples of as-collected Illinois basin coals and the same coals subjected to an aqueous leaching treatment were provided by Professor H. L. Chen, Southern Illinois University. These samples were originally collected by the Illinois State Geological Survey. Other coal samples used in this study were selected from the Pennsylvania State University coal bank on the basis of their high chlorine contents. Chlorine contents and apparent rank data for the coals are listed in Table I. A large number of standard organochlorine compounds and inorganic chlorides were also assembled for XAFS spectral measurements, including:

Aryl chlorides: 1,2,4,5-tetrachlorobenzene, 9,10-dichloroanthracene, 2,6-dichlorophenol;

Acyl chlorides: diphenylacetyl chloride, 2-naphthoyl chloride;

Alkyl chlorides: polyvinylchloride, 1,2-bis(chloromethyl)benzene, 1,4-bis(chloromethyl)benzene;

Org. hydrochlorides: semicarbazide hydrochloride, tetracycline hydrochloride;

Gases and vapors: Cl_2 , CCl_4 , $\text{C}_2\text{H}_4\text{Cl}_2$;

Alkali chlorides: NaCl , KCl , RbCl , CsCl , saturated NaCl solution;

Alk. earth chlorides: CaCl_2 , SrCl_2 , $\text{CaCl}_2 \cdot 2\text{H}_2\text{O}$, $\text{CaCl}_2 \cdot 6\text{H}_2\text{O}$;

Misc. Cl compounds: KClO_3 , $\text{H}_2\text{PtCl}_6 \cdot 6\text{H}_2\text{O}$, Hg_2Cl_2 , HgCl_2 , CuCl_2 , CuOCl .

XAFS Experiments: XAFS experiments were performed at the Stanford Synchrotron Radiation Laboratory (SSRL) under dedicated running conditions. Electron energies were held at 3.0 GeV while the beam current decayed from 80 to 40 mA between beam fills, which were typically eight hours or more apart. A pure helium path to the sample was employed to minimize attenuation of the X-ray intensity at the low energies in the vicinity of the chlorine K absorption edge (2820-2835 eV). XAFS spectra were recorded in fluorescent geometry in a Stern-Heald type detector (13) for all coals and standards from approximately 100 eV below the edge to about 400 eV above the edge using a rotating double crystal Si(111) monochromator. At the high-energy end of the scan, the K absorption edge for argon (from air contamination in the beam path) was encountered at 3205 eV. This edge served effectively as an internal energy calibration point. The X-ray near-edge structure (XANES) data and spectra shown in the paper are given relative to the zero point defined as the maximum in the differential of the XAFS spectrum of sodium chloride, which occurs at 2826 eV. It was found that the variation in position of the argon edge relative to the NaCl zero point was less than 0.1 eV for the different spectra measured. Spectra were obtained from the coal samples and from solid standards as pressed pellets in pressed boric acid (HBO_3) supports; liquid samples were contained in mylar bags or on filter papers; gaseous and vaporous species were introduced to the sample chamber at dilute (<1%) levels in helium (14). Analysis of the spectral data was performed on a MicroVAX II computer using conventional methods (15,16) for the XANES and extended fine-structure (EXAFS) regions of the spectra.

TABLE I: COALS EXAMINED BY CHLORINE XAFS

Coal Seam & State	Rank	Wt% Chlorine	Source
#6 seam, Illinois*	hvAb	0.82	C-20154 (ISGS)
#6 Seam, Illinois*	hvAb	0.42	C-8601 (ISGS)
-- after 1st. leaching		0.24	
-- after 2nd. leaching		0.12	
#6 Seam, Illinois*	hvAb	0.42	C-22175 (ISGS)
-- after 1st. leaching		0.18	
-- after 2nd. leaching		0.13	
Pittsburgh, PA	hvAb	0.22	USS Mining
Elkhorn #3, KY	hvAb	0.33	PSOC - 1475
Mineral seam, KS	hvAb	0.27	PSOC - 251
Mineral seam, OK	hvAb	0.24	PSOC - 768
Wildcat sbb, TX	sbbC	0.06	PSOC - 639
Beulah lignite, ND	lig	0.04	PSOC - 1483

*supplied by Prof. H. L. Chen, Southern Illinois University

RESULTS

XANES Spectra: Figure 1 shows the XANES spectra of an Illinois #6 coal that contains 0.42 wt% chlorine and two samples obtained from the coal after aqueous leaching treatments (2,3) that first reduced the chlorine content to 0.24 wt% and then to 0.12 wt%. It is obvious from this sequence that the chlorine K-edge absorption spectrum is not significantly changed by the leaching treatments and therefore it can be concluded that chlorine has only one significant form-of-occurrence in this coal. Furthermore, the reason that chlorine becomes progressively more difficult to remove from the coal is not because of the response of different forms of chlorine to the leaching treatment but because the one form-of-occurrence of chlorine becomes less accessible or more strongly bound to the coal as its abundance decreases.

Very similar XANES spectra to those in Figure 1 are exhibited by all the coals listed in Table I with two exceptions: the Illinois coal with the highest chlorine content (0.84 wt%) and the Beulah lignite with the lowest chlorine content (0.04 wt%). Figure 2 documents the similarity of the chlorine K edge XANES spectra of three coals from different coal basins. Figure 3 shows the XANES spectrum of chlorine in the two Illinois coal with highest chlorine contents. The differences between these spectra can be explained readily by the presence of a minor component (<25%) of crystalline NaCl in the Illinois #6 coal with 0.84 wt% chlorine. The extra peaks in the spectra of this coal match exactly with prominent peaks in the spectrum of NaCl, which is also shown in Figure 3. The XANES spectrum of the Beulah lignite, although very weak, differs significantly from those of the other coals and the position of its main peaks are well outside the ranges for the two peaks present in the spectra of the coals of higher rank. Based on XANES peak position

TABLE II: CHLORINE XANES DATA SYSTEMATICS*

Compound	Zero Point (ev)	1st. Peak (ev)	2nd. Peak (ev)
Mercury chlorides	-3.62 - -3.60	-3.0 - -2.6	13.4 - 13.6
Alky ¹ chlorides	-3.35 - -2.80	-2.5 - -1.2	11.0 - 20.8
Acy ¹ chlorides	-2.60 - -2.50	-1.3 - -1.0	15.3 - 20.9
Ary ¹ chlorides	-2.40 - -2.00	-0.8 - -0.4	16.1 - 19.2
Beulah lignite	-1.80	-0.7	18.5
All other coals	-1.75 - -1.20	0.9 - 1.3	19.0 - 21.2
Sat. NaCl solution	-1.55	0.2, 3.1	20.9
Organohydrochlorides	-1.10 - -1.00	1.1 - 2.1	19.2 - 20.7
Alkali chlorides	-0.90 - 0.00	0.4 - 2.2	16.9 - 20.6
Hydrated Ca chlorides	-0.75 - -0.60	2.3 - 2.5	21.6
Alk. earth chlorides	-0.60 - -0.45	1.7 - 2.1	19.0 - 19.6
Copper chlorides	-0.60 - -0.30	1.4 - 3.0	19.8 - 27.3
Chloroplatinic acid	-0.20	4.2	18.7
Potassium chlorate	4.20	5.8	18.5

Energies of zero point and peaks relative to zero point for NaCl.

*For most standard chlorine compounds, data are given only for the two peaks that most closely match the peaks in the coal spectra.

systematics (Table II), the XANES spectrum from chlorine in the lignite is most similar to that from chlorine bound to aromatic rings. However, given the low abundance of chlorine in this coal and the poor quality spectrum, it is perhaps premature to conclude that this coal has a significantly different form-of-occurrence for chlorine.

With the possible exception of the lignite, the data in Table II and the general appearance of the XANES spectra from chlorine in the coals, compared to those of the numerous standard chlorine compounds examined, indicate that the form-of-occurrence of chlorine is clearly neither an organochlorine compound nor one of the traditional crystalline inorganic chlorides. The substances that most closely resemble the XANES spectral data from chlorine in coal are (i) $\text{CaCl}_2 \cdot 6\text{H}_2\text{O}$, (ii) saturated NaCl solution, and (iii) organohydrochlorides. A comparison of the XANES spectra of these substances to that of the Illinois #6 coal is shown in Figure 4. The XANES spectra of all three substances exhibit an overall general similarity to the coal spectra, but minor differences are apparent upon close inspection so that it can not be concluded that one or other of these substances is the preferred match. However, all three substances do have some structural and bonding features in common that are, no doubt, reflected in similar XANES spectra: (i) chlorine is present in these substances as chloride anions, (ii) the bonding is relatively weak and largely ionic in character, and (iii) the chlorine-oxygen or chlorine-nitrogen distances are quite long: between 3.0 and 3.2Å (17,18). The chlorine in coals can be expected to be similar.

EXAFS Spectra: As is usually done (15,16), the EXAFS regions of the spectra were treated mathematically first to isolate the EXAFS periodic structure from the absorption step. Then, by converting this oscillatory structure to a wave vector representation and performing a Fourier transform, a radial structure function (RSF)

is obtained that represents the distribution of shells of atoms or ions around the chlorine atom or ion. Satisfactory radial structure functions were obtained for most of the standard compounds and for some of the coals with the higher chlorine contents. RSFs for the aryl compounds were noticeably more complex than those for the acyl and alkyl organochlorine compounds. This observation reflects the rigid structural relationship of the chlorine to the six carbons of the benzene ring present in the aryl compounds but which is lacking when chlorine is in a peripheral $-COCl$ or $-CH_2Cl$ group that has some rotational freedom. The RSFs for compounds with these latter groups resemble those obtained from the simple molecules, CCl_4 , $C_2H_4Cl_2$, etc.

Radial structure functions for chlorine in the inorganic compounds were generally complex and lacking in any strong correlative trends. Given the variety of structures and the range in degree of covalency exhibited by these compounds, this should not be surprising. $CaCl_2 \cdot 6H_2O$ has a structure (17) in which the Ca and Cl ions are not nearest neighbors but are separated by water molecules. Hence, this compound can act as a model compound for chloride anions surrounded by water molecules. The RSF for this compound is shown in Figure 5a; it is dominated by one major peak representing the coordination shell of six water molecules at a distance of 3.1 - 3.2 Å from the central chloride anion. Bond-lengths were extracted from the better RSFs of chlorine in coals (e.g. Figure 5b) using the phase-shift data obtained empirically from $CaCl_2 \cdot 6H_2O$ for the water molecule shell at ~ 3.15 Å. An excellent correlation of the phase shifts was found at a Cl-H₂O distance of 3.03 Å for the coals. The phase-shift data correlated considerably better than that between $CaCl_2 \cdot 6H_2O$ and the saturated NaCl solution, which implies, perhaps, that the chlorine anions in the saturated NaCl solution have significant contribution from sodium ions in the nearest neighbor shell. The RSFs for the organic hydrochloride compounds consist of one major peak at similar distances (3.1 - 3.3 Å) arising from nitrogen atoms in basic amine groups to which the chloride anions are bound (18). However, correlation of the Cl-N phase-shift data with the coal data was not as good as that found between $CaCl_2 \cdot 6H_2O$ and chlorine in coal. Although such distinctions are not necessarily definitive, the analysis of the EXAFS region does appear to favor water molecules as the most likely environment around chlorine in the coals examined.

CONCLUSIONS

Analysis of chlorine K-edge XAFS data for a number of U.S. coals has shown that in the majority of the coals chlorine is present in a single form as chloride anions in the moisture associated with the microcracks and pores of the coal. In the coal with the highest chlorine content, a second form-of-occurrence was also identified, namely crystalline NaCl, which presumably had precipitated from the chloride-rich solution as the coal dried. The only other exception was a low-chlorine lignite, in which chlorine appeared to be present in organic form. However, given the very low chlorine concentration (0.04 wt%) and the related poor spectral quality, it is premature to attach much significance to this observation at this time.

With chloride anions in moisture as the predominant form-of-occurrence of chlorine in U.S. coals, it is relatively easy to rationalize some of the apparently contradictory conclusions made in previous investigations regarding whether chlorine is inorganically or organically bound in coal. As a result of the association of chlorine with coal moisture, chlorine will have properties similar to a dispersed organically bound element. For example, in microprobe or SEM X-ray mapping techniques, chlorine will be found to be distributed widely in low concentrations in macerals and not strongly correlated with other elements, and in float-sink tests of "organic" affinity, chlorine will favor the maceral-rich float fractions.

Conversely, observations of specific inorganic chlorides in coals can be explained as precipitates that crystallize as the coal moisture evaporates.

With the form-of-occurrence of chlorine now established for U.S. coals, it would appear that it should be possible to remove virtually all of the chlorine from troublesome coals by the combination of fine grinding and aqueous leaching treatments. It is interesting to note that a similar treatment was used by British researchers to remove the supposed "organic" chlorine fraction from an Illinois #6 coal that was left after earlier leaching treatments (12). Alternatively, the fact that the chlorine is now known to be associated with the moisture in coal may lead to new methods for chlorine removal.

ACKNOWLEDGEMENTS

We are grateful to Professor Han Lin Chen of Southern Illinois University for providing us with samples of raw and leached Illinois #6 coals. This work was supported by the U.S. DOE under Contract No. DE-FG22-86 PC90520. We also acknowledge the U.S. DOE for its support of the Stanford Synchrotron Radiation Laboratory, where the XAFS experiments were performed.

LITERATURE CITED

1. H. J. Gluskoter, and R. R. Ruch, *Fuel*, **50**, 65, (1971)
2. H. L. Chen, N. M. Rao, and D. S. Viswanath, *Fuel Proc. Technol.*, **13**, 261, (1986)
3. H. L. Chen, and M. Pagano, *Fuel Proc. Technol.*, **13**, 271, (1986)
4. P. Zubovic in: *Coal Science*, (ed. R. F. Gould), *Advances in Chemistry Series*, Volume **55**, 221, American Chemical Society, Washington, D. C., (1966)
5. H. J. Gluskoter, R. R. Ruch, W. G. Miller, R. A. Cahill, G. B. Dreher, and J. K. Kuhn, Illinois State Geological Survey, Circular **499**, (1977)
6. J. A. Minkin, E. C. T. Chao, and C. L. Thompson, *ACS Division of Fuel Chemistry, Preprints*, **24**(1), 242, (1979)
7. M. T. Mackowsky, Chapter 2.23 in: *Stach's Handbook of Coal Petrology*, (eds. E. Stach et al.), 121, Gebrüder Borntraeger, Berlin, W. Germany, (1975)
8. R. B. Finkelman, and R. W. Stanton, *Fuel*, **57**, 763, (1978)
9. J. N. Chakrabarti, Chapter 10 in: *Analytical Methods for Coal and Coal Products*, (ed. C. Karr, Jr.), Vol. 1, 323, Academic Press, New York, (1978)
10. S. A. Caswell, *Fuel*, **60**, 1164, (1981)
11. N. J. Hodges, W. R. Ladner, and T. G. Martin, *J. Inst. Energy*, **56**, 158, (1983)
12. G. Fynes, A. A. Herod, N. J. Hodges, B. J. Stokes, and W. R. Ladner, *Fuel*, **67**, 822, (1988)
13. E. A. Stern, and S. Heald, *Rev. Sci. Instrum.*, **50**, 1579, (1979)
14. F. W. Lytle, R. B. Gregor, E. C. Marques, D. R. Sandstrom, G. P. Huffman, and F. E. Huggins, *Stanford Synchrotron Radiation Laboratory Activity Report for 1986*, **87/01**, 115, (1987)
15. P. A. Lee, P. H. Citrin, P. Eisenberger, and B. M. Kincaid, *Rev. Mod. Phys.*, **53**, 769, (1981)
16. G. S. Brown, and S. Doniach in: *Synchrotron Radiation Research*, (eds. H. Winick and S. Doniach), 353, Plenum Press, New York, (1980)
17. R. W. G. Wyckoff, *Crystal Structures*, Vol. 3, J. Wiley & Sons, New York, (1963)
18. R. W. G. Wyckoff, *Crystal Structures*, Vol. 6, J. Wiley & Sons, New York, (1969)

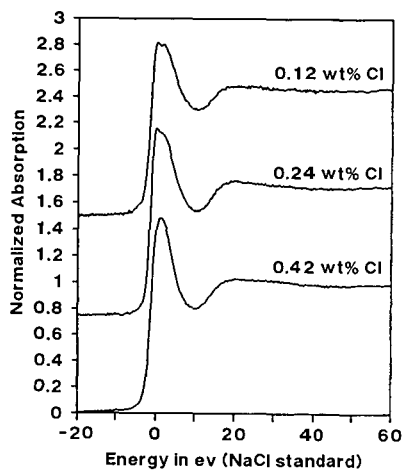


Figure 1. Chlorine K-edge XANES spectra of Illinois #6 coal and two samples of same coal after leaching treatments. Note the similarity of the spectra.

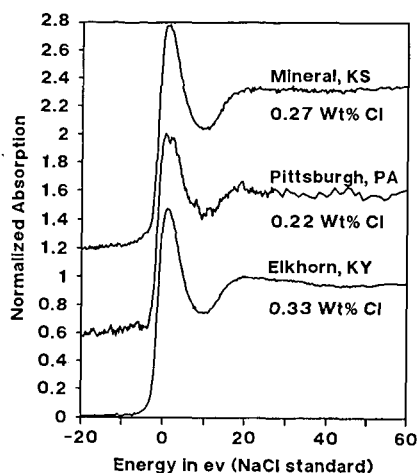


Figure 2. Chlorine K-edge XANES spectra of three coals from different states and geological provenances. Note the similarity of the spectra.

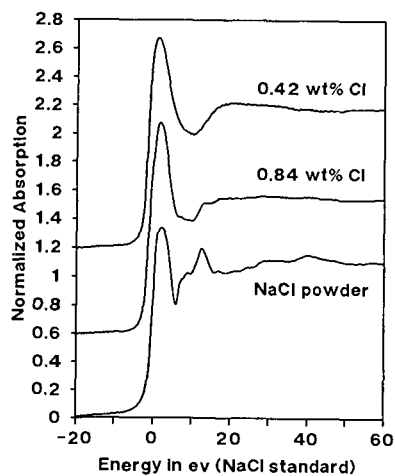


Figure 3. Chlorine K-edge XANES spectra of two high-chlorine Illinois #6 coals and of NaCl.

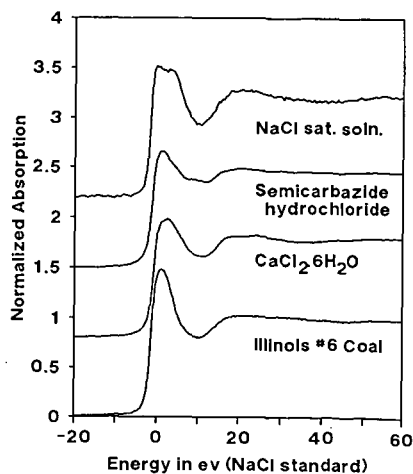


Figure 4. Chlorine K-edge XANES spectra of Illinois #6 coal and various standard Cl compounds with similar spectra.

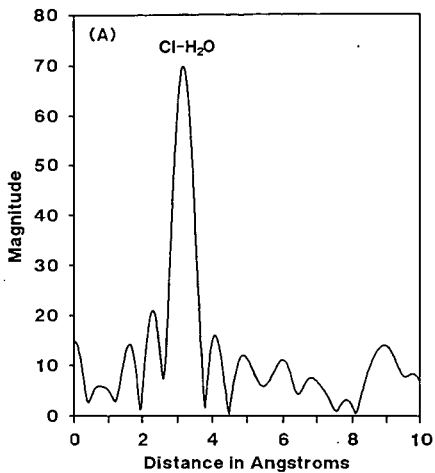


Figure 5(a). Phase-shift corrected radial structure function for the compound, $\text{CaCl}_2 \cdot 6\text{H}_2\text{O}$.

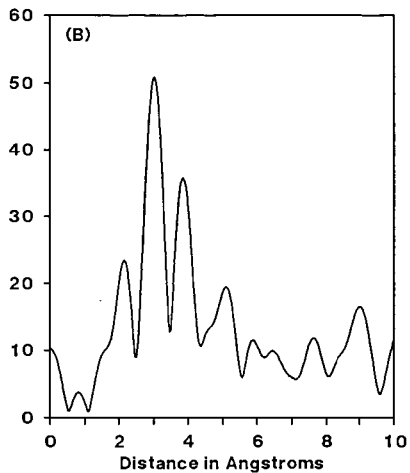


Figure 5(b). Phase-shift corrected radial structure function for chlorine in an Illinois #6 coal.

HYDROGEN BONDING AND COAL SOLUBILITY AND SWELLING

Paul Painter, Yung Park and Michael Coleman

Materials Science and Engineering Department
Steidle Building
The Pennsylvania State University
University Park, PA 16802

Most descriptions of the thermodynamic properties of coal solutions and the swelling of coal are based on models that in their original form only dealt with simple van der Waals or London dispersion forces. It is now well-known that such descriptions are inadequate when applied to systems where there are strong specific interactions such as hydrogen bonds. In part, this is because for weak forces random contacts between unlike segments can be assumed, allowing interactions to be formulated in a mean field form, $\Delta E_{int} \phi_A \phi_B$, where ΔE_{int} is an exchange interaction term; $\phi_A \phi_B$ are the volume fractions of the components A and B and their product is proportional to the number of unlike contacts in a solution where there is random mixing. Hydrogen bonds are different and cannot be dealt with by means of a simple approximation. Polymer segments and solvent molecules that interact in this manner are truly associated and above the T_g there is a dynamic equilibrium distribution of hydrogen bonded species. There is a non-random arrangement of the hydrogen bonding functional groups (relative to one another) and this leads to modifications in the entropy of mixing. Theories that deal only with the enthalpy of hydrogen bonding interactions are thus inadequate.

In recent work (1-4) we have developed an association model that essentially consist of a Flory-Huggins type of equation with an additional term (ΔG_H) describing the free energy changes associated with the changing pattern of hydrogen bonding that occurs as a function of composition:

$$\frac{\Delta G_M}{RT} = \frac{\phi_A}{N_A} \ln \phi_A + \frac{\phi_B}{N_B} \ln \phi_B + \phi_A \phi_B \chi + \frac{\Delta G_H}{RT}$$

Although it may appear that we have arbitrarily added a term accounting for non-random contacts to a random mixing theory, association models are more subtle than that and it can be shown that the above equation can be derived directly from a lattice model (2). The ΔG_H term has a complex appearance (but once you get used to it has an easily understandable structure), but it is important to note that all terms in this equation are determined from experimental FTIR measurements and the equations describing the stoichiometry of hydrogen bond formation. (Space does not permit a reproduction of these equations here, and the interested reader should consult the literature.) Accordingly, given a knowledge of χ , or a reasonable way of estimating this parameter, we could predict the free energy of mixing coal with hydrogen bonding solvents. It is relatively easy to show that the ΔG_H term is either zero or negative, the χ term is positive for purely van der Waals or London dispersion interactions, while the combinatorial entropy term of course favours mixing. The χ and ΔG_H terms have very different temperature dependencies and the balance between these forces leads to the prediction of a rich variety of phase behaviors (2, 4, 5-7). In initial work on coal solutions we have determined general trends, through a calculation of the free energy of mixing pyridine with model coal structures (4).

These initial results provide some fundamental insight, but there now remains the more difficult task of calculating the behavior of specific systems and determine expressions for the chemical potentials, so that the model can be extended to swelling and molecular weight

measurements. Here we consider the first part of this task and we will commence by first defining an average coal structure per OH group. This sounds as if we are arbitrarily classifying a coal molecule as a set of "average" repeat units. In a certain sense we are, but this is not a fallacious approach, as we will show. In the classic work of Scott (8), performed more than thirty years ago, it was demonstrated that the "physical" (ie. non-hydrogen bonded) interactions of a copolymer of any degree of heterogeneity could be described by a solubility parameter that is a volume fraction average of the contributions of its constituents. We can therefore use the method of van Krevelen (9) to determine the parameter δ_{coal} . This requires first of all a knowledge of the coal composition and the relative proportions of aromatic and aliphatic carbon, which have been determined directly for many coals by ^{13}C nmr, or can be estimated from FTIR measurements of the relative proportions of aromatic and aliphatic CH groups. In addition, we also need to define a reference volume for the coal that can correspond to any arbitrarily defined segment (because we will simply calculate the free energy change per segment upon mixing). Van Krevelen (9) calculated his solubility parameter in terms of the molar volume of a coal "molecule" per carbon atom, V_M/C , using:

$$\frac{V_M}{C} = \frac{1200}{C'd}$$

where C' is the weight percent carbon in the sample and d is the density. In the same fashion we define a molar volume per OH group as:

$$\frac{V_M}{O_{\text{OH}}^1} = \frac{1600}{O_{\text{OH}}^1 d}$$

where O_{OH}^1 is the weight percent oxygen in the sample that is present as OH groups (O_{OH}^1 and d are known or measurable quantities). This allows us to calculate the free energy contribution from hydrogen bonding interactions per molar volume of the average coal segment containing one OH group.

The χ parameter is then calculated from solubility parameters in the usual fashion, while ΔG_H , the free energy of hydrogen bonding interactions, can be calculated in a straightforward manner by methods we will describe below. The definition of a "segment" of a coal molecular per OH group, therefore merely serves to place the calculations of χ and ΔG_H on a common scale of unit volume. As long as the OH groups in coal are more or less randomly distributed our definition of an arbitrary segment is conceptually sound.

The quantity ΔG_H is calculated from a knowledge of the number of OH groups present in a sample (more precisely, the molar volume per OH group) and equilibrium constants describing the free energy change per hydrogen bond (the equation describing ΔG_H is then a simple counting of the change in the number of hydrogen bonds of various types upon mixing). These are determined by FTIR. Fortunately, we do not have to measure these directly on coal. It is a consequence of the lattice model (2) that equilibrium constants for a particular functional group determined in one molecule can be transferred to a different molecule with the same functional group by simply adjusting according to the molar volume

$$\text{ie. } K_B^1 V_B^1 = K_B^2 V_B^2$$

Using values determined for phenol and cresols ($K_B^1 V_B^1$) we can thus calculate appropriate values for a coal segment defined by V_B^2 . (This result has worked extremely well in predicting the phase behavior of blends of polyvinyl phenol with various polyethers and polyesters (6). The values of the equilibrium constants describing the self-association of phenol have been determined by Whetsel and Lady (10). (This splendid paper, published in Spectrometry of Fuels a number of years ago, anticipates our use of association models for coal and has the almost forgotten virtue of tabulating all data obtained, in this case in both the near and mid IR. We were thus able to check all calculations and determine the appropriate values of the equilibrium constants.) We have expanded our treatment of self association to

also account for the hydrogen bonds that can form intramolecularly between coal OH and ether oxygens. This is conceptually straightforward and comes at the expense of a minor increase in the algebraic complexity of the equations. The equilibrium constants describing interactions between phenolic OH groups and ethers, and indeed between OH and most of the functional groups found in solvents commonly used to swell coals, are tabulated in the literature (eg see the review by Murthy and Rao (11)). We are fortunate that interactions involving both alkyl and phenolic OH groups have been so widely studied. The parameters used in the calculations are listed in table 1 and our computational procedures are described elsewhere (2-4, 6).

Typical results are shown in figure 1. The data points represent spinodals and were calculated for various coal-pyridine mixtures. This naturally requires that the structural parameters of the coals have been determined and we used a data set compiled for a set of vitrinite concentrates (12). In the accessible range of temperature (up to about the boiling point of pyridine) we determine a classic inverted U shape coexistence curve characterized by an upper critical solution temperature near 0°C, for a coal of 78.3% carbon content. As the carbon content of coal increases the calculated solubility parameter decreases to a minimum near a carbon content of 88% C (9).

For the three coals from which we have performed detailed calculations, with carbon contents of 78.3%, 84.7% and 90.1%, the value of χ thus decreases with increasing carbon content, favoring mixing. At the same time, however, the number of OH groups systematically decreases, thus decreasing the favorable contribution of hydrogen bonding. This latter effect dominates, so as the carbon content of the coal increases we predict that the upper critical solution temperature shifts to higher temperature and for a coal of 90.1% carbon content we calculate spinodals characteristic of a phase separated system throughout the accessible temperature range.

At first sight these results might seem inconsistent with some of the known characteristics of coal (13-18), where swelling reaches a maximum in about the middle range of carbon contents we have considered. It should be kept in mind, however, that in our calculations we have assumed that the chains are not cross-linked (The phase diagrams in figure 1 were determined for a coal molecule of "degree of polymerization" 100, relative to the molar volume of a pyridine molecule). Such molecules are predicted to be soluble at room temperature for a low carbon content coal, and to phase separate into a dilute coal solution and a solvent swollen coal gel at higher carbon contents. The degree of swelling depends not only on the phase behavior of these systems as defined by their chemical potentials, but also upon the degree of cross-linking. We have obtained appropriate expressions for the contribution of hydrogen bonding interactions to the chemical potentials and plan to incorporate these into theories of swelling. Of more interest to us here, however, is the overall effect of hydrogen bonding interactions on phase behavior. Pyridine forms relatively strong bonds with phenolic OH groups, so we would like predict that for solvents that hydrogen bond less strongly, such as THF, the contribution of ΔG_H would be smaller. It must be kept in mind that hydrogen bonding alone does not determine phase behavior, the contribution of the "physical" (usually repulsive) forces measured by χ , together with the combinatorial entropy of mixing, all contribute to the balance. As it happens, the χ value for the coal-THF mixtures considered here are larger than their coalpyridine counterparts and this combined with the smaller contributions to ΔG_H from hydrogen bonding results in the spinodals shown in figure 2, which indicate that the coals are less soluble and would swell less in this solvent.

Obviously solubility is molecular weight dependent and the phase behavior of the 84.7% coal as a function of molecular weight (defined in terms of a degree of polymerization N_B relative to the molar volume of the solvent molecule) is shown in figure 3. This model predicts that for this coal fairly large molecules. ($N_B > 30$) would be soluble in boiling pyridine, although some of the high molecular weight material would

precipitate out at room temperature, depending upon the concentration of the solvent. Only relatively low molecular weight material would be completely soluble in THF.

Finally, we must re-emphasize that for any specific coal the overall phase behavior is determined by the balance between hydrogen bonding and physical forces. The former is measured by the equilibrium constant for association, which we define by the symbol K_A . Values listed in the literature (11) are reproduced in Table 2, together with values of the solubility parameter. For the coals considered here we would therefore qualitatively expect that NMP and pyridine would be the best solvents (large K_A , δ_s in the range 10.7 to 11.5); dimethyl formamide hydrogen bonds strongly but has a somewhat larger χ than these solvents; DMSO hydrogen bonds very strongly but would have an even larger value of χ ; while the remaining solvents would not give comparable swelling or solubility characteristics. Obviously detailed calculations are required for quantitative predictions and these are presently being performed.

Acknowledgment. We gratefully acknowledge the support of the Office of Basic Energy Sciences, Division of Chemical Sciences, Department of Energy, under Grant No. DE-FG02-86ER13537.

References

1. Painter, P.C., Park, Y., Coleman, M.M., *Macromolecules*, 1988, 21, 66.
2. Painter, P.C., Park, Y., and Coleman, M.M., *Macromolecules* (accepted for publication).
3. Painter, P.C., Park, Y., and Coleman, M.M., *Macromolecules* (accepted for publication).
4. Painter, P.C., Park, Y., and Coleman, M.M., *Energy and Fuels*, 1988, 2, 693.
5. Coleman, M.M., Skrovanek, D.J., Hu, J. and Painter, P.C., *Macromolecules*, 1988, 21, 59.
6. Coleman, M.M., Lichkus, A.M., and Painter, P.C., *Macromolecules* (accepted for publication).
7. Coleman, M.M., Hu, J., Park, Y. and Painter, P.C., *Polymer*, 1988, 29, 1659.
8. Scott, R.L., *J. Polym. Sci.*, 1952, 9, 423.
9. van Krevelen, D.W., *Fuel*, 1965, 45, 229.
10. Whetsel, K.B. and Lady, J.H. in *Spectrometry of Fuels*, Friedel, H., ed., Plenum, London, 1970, p. 259.
11. Murthy, A.S.N. and Rao, C.N.R., *Applied Spect. Revs.*, 1968, 2, 69.
12. Painter, P.C. Starsinic, M. and Coleman, M.M. in "Fourier Transform Infrared Spectroscopy", (J.R. Ferraro and L.J. Basile editors) Academic Press (1985), Chapter 5.
13. Green, T., Kovac, J., Brenner, D., Larsen, J.W. in "Coal Structure", Meyers, R.A., ed., Academic Press, New York, 1982.
14. Larsen, J.W. in "Chemistry and Physics of Coal Utilization", AIP Conference Proceedings, No. 70, Cooper, B.R., Petrakis, L., eds., AIP, New York, 1981.
15. Larsen, J.W., Green, T.K. and Kovac, J.J. *Org. Chem.*, 1985, 50, 4729.
16. Lucht, L.M. and Peppas, N.A. in "Chemistry and Physics of Coal Utilization", AIP Conference Proceedings, 18, Cooper, B.R., Petrakis, L., eds., AIP, New York, 1981.
17. Lucht, L.M. and Peppas, N.A., *Fuel*, 1987, 66, 803.
18. Lucht, J. and Peppas, N.A., *J. Appl. Polym. Sci.*, 1987, 33, 2777.

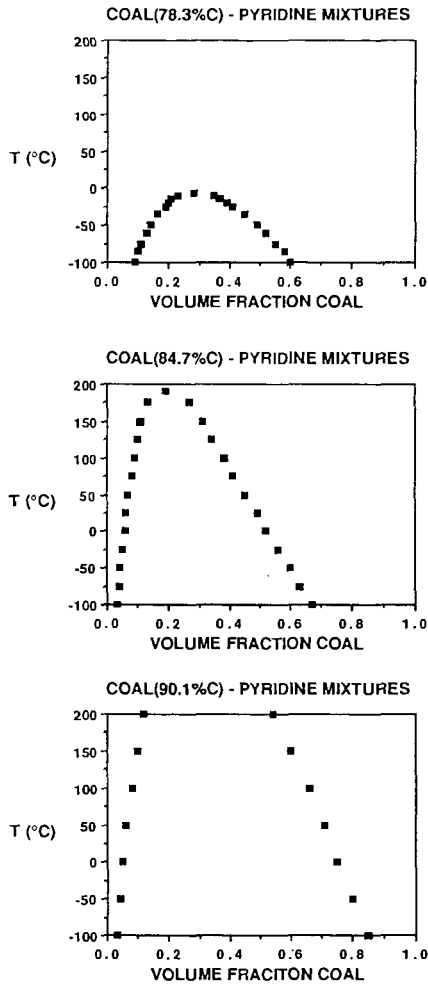


FIGURE 1. Phase diagrams (spinodals) for various coals with pyridine.

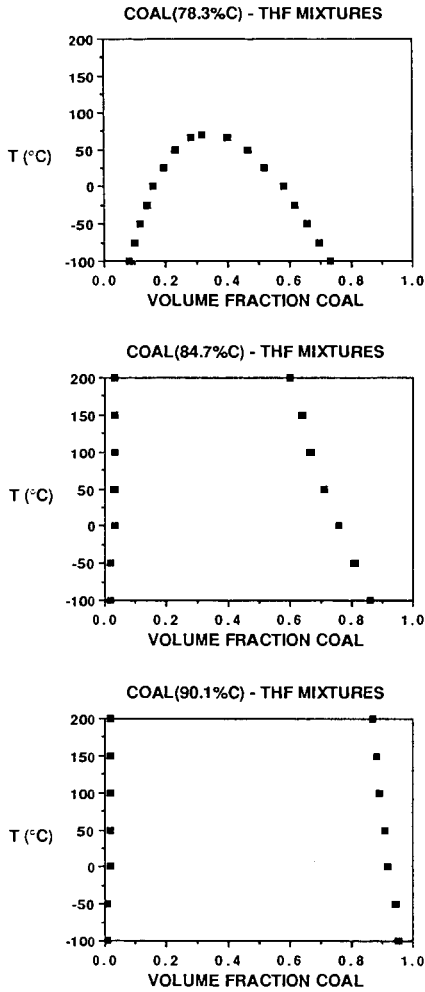
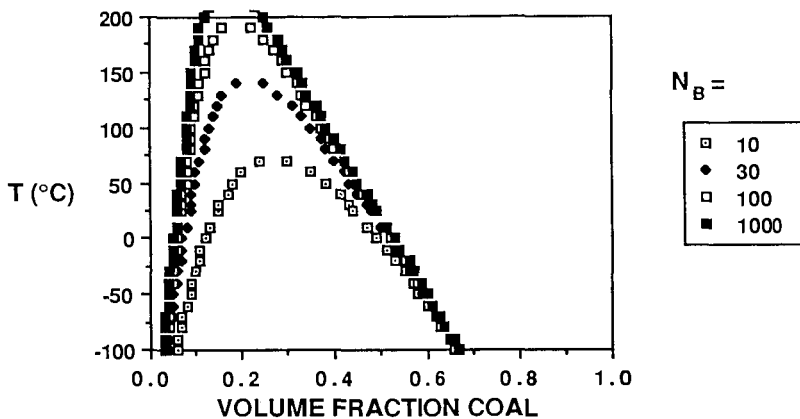


FIGURE 2. Phase diagrams (spinodals) for various coals with THF.

COAL(84.7%C) - PYRIDINE MIXTURES



COAL(84.7%C) - THF MIXTURES

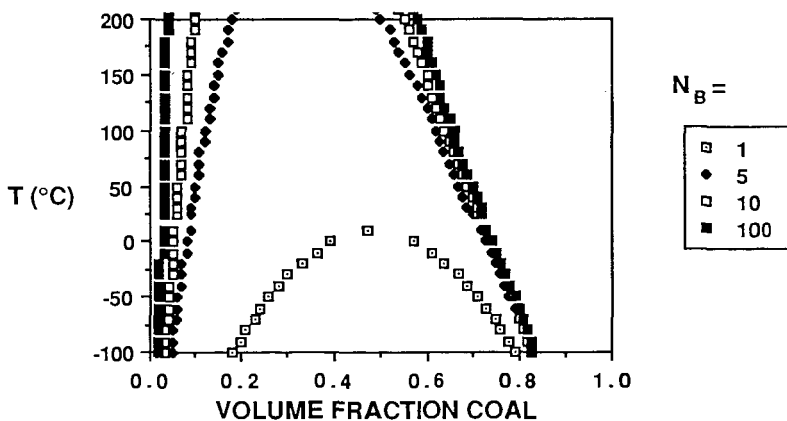


FIGURE 3. Phase diagrams (spinodals) as a function of molecular weight.

Table 1. Parameters for Coal at 25°C

	78.3%C	84.7%C	90.1%C
molar vol, (V_B) $\text{cm}^3 \text{mol}^{-1}$	227.92	286.23	4102
molar vol, (V_E) $\text{cm}^3 \text{mol}^{-1}$	151.95	384.62	440
δ_C , $(\text{cal cm}^{-3})^{1/2}$	11.5	11.27	10.78
K_2	8.33	6.64	0.46
h_2 , kcal mol^{-1}	5.6	5.6	5.6
K_E	19.44	15.48	1.08
h_E , kcal mol^{-1}	5	5	5
K_B	26.67	21.23	1.48
h_B , kcal mol^{-1}	5.2	5.2	5.2

Parameters for Solvents at 25°C

	pyridine	THF
molar vol, (V_S) $\text{cm}^3 \text{mol}^{-1}$	81	74.3
δ_S , $(\text{cal cm}^{-3})^{1/2}$	10.6	9.9

Table 2

SOLVENT	K_A (l mol^{-1}) (20°C)	δ_S (cal cm^{-3})
PYRIDINE	60	10.6
NMP	163	11.2
DIMETHYL FORMAMIDE	64	12.1
DMSO	60	10.6
THF	18.8	9.9
ACETON	12.3	9.9
DIETHYL ETHER	9.6	7.5
ACETONITRILE	5.0	11.8
BENZENE	0.3*	9.1

- * Weak H-bonds between OH groups and Π electrons have been proposed.

REGIOSELECTIVE THERMOLYSIS OF 1,4-DIPHENYLBUTANE
ENHANCED BY RESTRICTED RADICAL MOBILITY

P. F. Britt, A. C. Buchanan, III, and C. A. Biggs
Chemistry Division
Oak Ridge National Laboratory
P. O. Box 2008
Oak Ridge, TN 37831-6197

INTRODUCTION

Thermal decomposition of coal has been postulated to involve the formation of free radicals by processes such as the homolysis of aliphatic or ether-containing bridges which connect polycyclic aromatic units into a macromolecular structure.¹ Understanding the thermal reactivity of coal is important in the study of pyrolysis, liquefaction, and coking.² Mechanistic insights into the chemical reactivity of coal at the molecular level can be gained from the study of model compounds which represent structural features in coal. However, radicals generated in a cross-linked macromolecular material such as coal may experience restricted mobility when the radical center remains bound to the residual molecular structure. To model the effects of restricted radical mobility on thermally induced decomposition reactions, thermolyses of model compounds covalently attached to an inert support have been studied. Thermolysis of surface-immobilized 1,2-diphenylethane showed a substantially altered free radical reaction pathway compared with the corresponding liquid phase behavior,³ while thermolysis of surface-immobilized 1,3-diphenylpropane (---DPP) showed unexpected regioselectivity resulting from conformational restrictions on hydrogen transfer reactions as the surface coverage of ---DPP decreased.⁴ In order to further explore the regioselectivity of hydrogen transfer induced by restricted diffusion, the thermolysis of surface-immobilized 1,4-diphenylbutane (---DPB) is being examined.

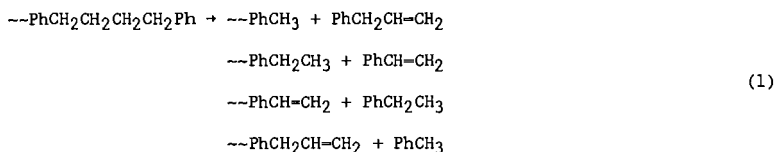
EXPERIMENTAL

p-(4-phenylbutyl)phenol (HODPB) was prepared in a four-step synthesis from the Wittig reaction of cinnamyltriphenylphosphonium chloride with *p*-anisaldehyde to afford 1-(4-methoxyphenyl)-4-phenyl-1,3-butadiene which was catalytically reduced (10% Pd/C) and demethylated (HBr/HOAc). Repeated crystallizations from hexanes afforded HODPB in >99.9% purity (GC). Surface-immobilized 1,4-diphenylbutane was prepared at saturation coverage by condensation of excess HODPB with the surface hydroxyls of a high purity fumed silica (Cab-O-Sil, M-5, Cabot Corp., 200 m²/g) at 225°C for 1 h, as previously described.³ Excess phenol was sublimed from the Cab-O-Sil by heating at 270°C for 45 min under vacuum (5 x 10⁻³ Torr). Following base hydrolysis of the Cab-O-Sil (to liberate surface-bound phenol) and silylation, GC analysis gave coverages for three different batches as 0.504, 0.548, and 0.541 mmol of ---DPB per gram of final product with a purity >99.7%.

Thermolysis of ---DPB was performed at 400 ± 1°C in T-shaped pyrex tubes sealed under high vacuum (≈10⁻⁶ Torr). The volatile products were collected in a cold trap while the surface-bound products were removed from the silica as the corresponding phenols by basic digestion and then silylated to form trimethylsilyl ethers. The samples were analyzed by capillary GC with flame ionization detection or by GC-MS. Quantitative measurements were made with the use of internal standards and measured GC detector response factors.

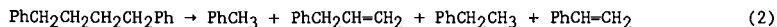
RESULTS AND DISCUSSION

Thermolysis of --DPB at 400°C has been studied at 2-12% conversion with two high coverage batches, 0.541 mmol/g (Batch A) and 0.504 mmol/g (Batch B). At the lowest conversion (ca. 2% in 10 min), the major gas phase products of the cracking reaction detected in the cold trap were toluene (PhMe), ethylbenzene (PhEt), styrene (PhVi), and allylbenzene (PhAll). The surface-attached products obtained as phenols from basic digestion of the sample were *p*-cresol (corresponding to --PhMe), *p*-ethylphenol (--PhEt), *p*-hydroxystyrene (--PhVi), and *p*-hydroxyallylbenzene (--PhAll). These eight products (shown in eq. 1) account for >97% of the products formed at 2% conversion and 93% at 12% conversion. The product distribution for the four gas phase hydrocarbon products, which will be examined in more detail below, is shown as a function of conversion in Figure 1. The two high coverage batches gave similar product distributions with reaction rates slightly faster for Batch B (ca. 15%).



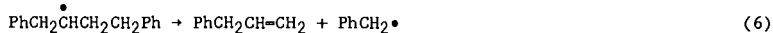
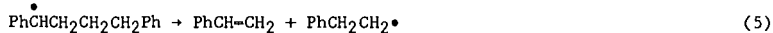
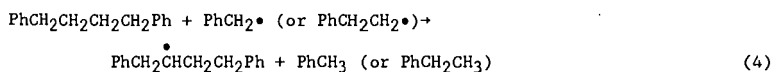
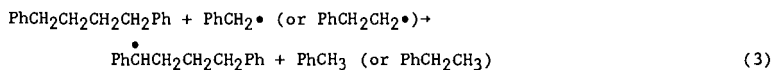
As conversion of --DPB increased, secondary products formed at the expense of the surface-bound olefinic products. At the highest conversion studied (12%), 7.0 mol% of the products results from secondary reactions. The major secondary reactions appear to be rearrangement of --PhCH₂CH=CH₂ to --PhCH=CHCH₃ (2.6 mol %), and radical addition to --PhVi and --PhAll to produce, following hydrogen abstraction, --PhCH₂CH₂CH₂Ph (0.6 mol %), --PhCH₂CH₂CH₂Ph-- (0.7 mol %; identified as the corresponding diphenol), --PhCH₂CH₂CH₂CH₂Ph-- (0.5 mol %), and isomers of --C₂₄H₂₄-- (1.0 mol %; diphenols of triphenylhexane). Comparable secondary radical addition reactions have been reported to occur during thermolysis of liquid DPB.⁵

Thermolysis of liquid 1,4-diphenylbutane (DPB) has been shown to proceed by a radical chain decomposition reaction in which DPB is cracked to give four major products, as shown in equation 2.⁵

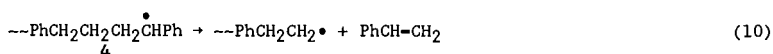
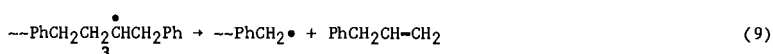
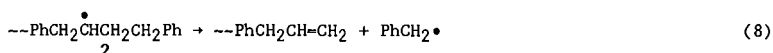
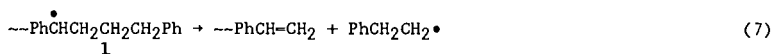


By comparison, surface-immobilized DPB reacted to form the same set of gas phase products as well as a corresponding set of surface-attached products (eq. 1). This results from the nonequivalence of the two ends of the surface-attached DPB molecule. Therefore, at low conversion, liquid DPB and --DPB react in an analogous manner to produce the same slate of products. The initial rate of --DPB thermolysis at high coverage ($15 \pm 2\% \text{ h}^{-1}$ at 400°C based on 2-12% conversion) is somewhat faster than that of liquid DPB. Comparison of the rate of reaction of liquid DPB and --DPB at 400°C for 10 min shows that the surface-immobilized DPB reacts 10-fold faster. It is also interesting that while the rate of decomposition of liquid DPB exhibited a mildly autocatalytic behavior, the rate of --DPB decomposition calculated at each time point was independent of conversion. Additional studies will probe these observations further and examine the dependence of the thermolysis rate on surface coverage.

In the radical chain propagation steps for the decomposition of DPB, a benzyl radical (or a 2-phenylethyl radical) abstracts a hydrogen atom from DPB in a competitive process to form a benzylic and a nonbenzylic diphenylbutyl radical (eqs. 3 and 4). The β -scission of the benzylic radical leads to PhVi and ultimately PhEt, while the nonbenzylic radical leads to PhAll and ultimately PhMe (eqs. 5 and 6).

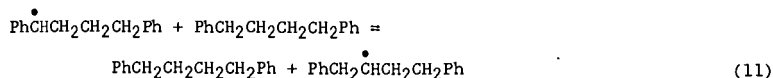


In the case of $\sim\sim$ DPB, there are four different methylene units which can form two distinct benzylic (1 and 4) and two distinct nonbenzylic (2 and 3) radicals. Following initiation by the homolysis of a small amount of $\sim\sim$ DPB, the β -scission steps of the four possible radicals formed by hydrogen abstraction are shown in equations 7-10.



The free and surface-bound radicals can propagate the chain by reacting with $\sim\sim$ DPB to form free and surface-bound PhMe and PhEt while regenerating the surface-bound DPB radicals.

The regioselectivity for thermolysis of fluid phase DPB was found to be concentration dependent.⁵ This was explained by a substrate-dependent hydrogen abstraction reaction which interconverts the benzylic and the nonbenzylic radicals, equation 11.



In the neat liquid at 400°C, conditions under which the reaction in eq. 11 occurs efficiently, the regioselectivity of thermolysis as determined from the PhEt/PhMe ratio extrapolated to zero conversion, was a minimum of 1.22. Interestingly for $\sim\sim$ DPB at 400°C, the analogous regioselectivity for formation of 1 relative to 2, determined from the PhEt/PhMe ratio, at 2% conversion is 1.23, while the benzylic/nonbenzylic selectivity for the pair farthest from the surface (4 relative

to 3), determined from the PhVi/PhAlI ratio, is a somewhat smaller value of 1.08. These observations suggest that hydrogen exchange reactions on the surface analogous to eq. 11 may also be important for surface-immobilized --DPB at high coverage.

The selectivity for formation of benzylic radicals 4 and 1 can be probed by the PhVi to PhEt yield ratio since these products are not consumed by secondary reactions. At low conversions (2%), the ratio has a value of 1.0 indicating no selectivity, but as the conversion increases, the ratio increases to 1.2 at 12% conversion. A similar type of conversion dependent selectivity for the benzylic radical farthest from the surface has been reported in the thermolysis of --DPP at saturation coverages in which the selectivity varied from 1.0 at <4% conversion to 1.3 at 23% conversion. The explanation for this conversion dependent regioselectivity for --DPB lies in the hydrogen transfer propagation step. As the conversion increases, --DPB molecules are increasingly separated from the surface-bound hydrogen abstracting benzylic and 2-phenylethyl radicals, and hydrogen abstraction at the benzylic carbon farthest from the surface to form radical 4 becomes favored. Additional insight into this regioselectivity should be obtained from the current studies being performed at lower surface coverages.

CONCLUSIONS

Covalent attachment of organics to an inert support has proven useful in modeling the effects of the restricted radical mobility in the thermal reactions of coal related model compounds. Thermolysis of surface-immobilized 1,4-diphenylbutane at 400°C was found to proceed through a facile free radical chain decay pathway giving products analogous to those found in the thermolysis of liquid DPB, but with a somewhat faster rate. For --DPB at low conversions, there is little regioselectivity between the four radical chain decay pathways which cycle through radicals at benzylic and nonbenzylic methylene sites suggesting that a hydrogen exchange reaction may be important at high surface coverages. At the highest conversion studied (12%), the cracking favors hydrogen abstraction from the benzylic carbon farthest from the surface. Additional studies are in progress to examine the effects of lower surface coverages on the regioselectivity and rate of the thermal cracking of --DPB. The results from thermolysis of --DPP and --DPB support the idea that a free radical chain induced decomposition reaction can be an effective mechanism for the mild thermal degradation of polymethylene chains connecting aromatic moieties in coal even under conditions of restricted diffusion.

ACKNOWLEDGMENTS

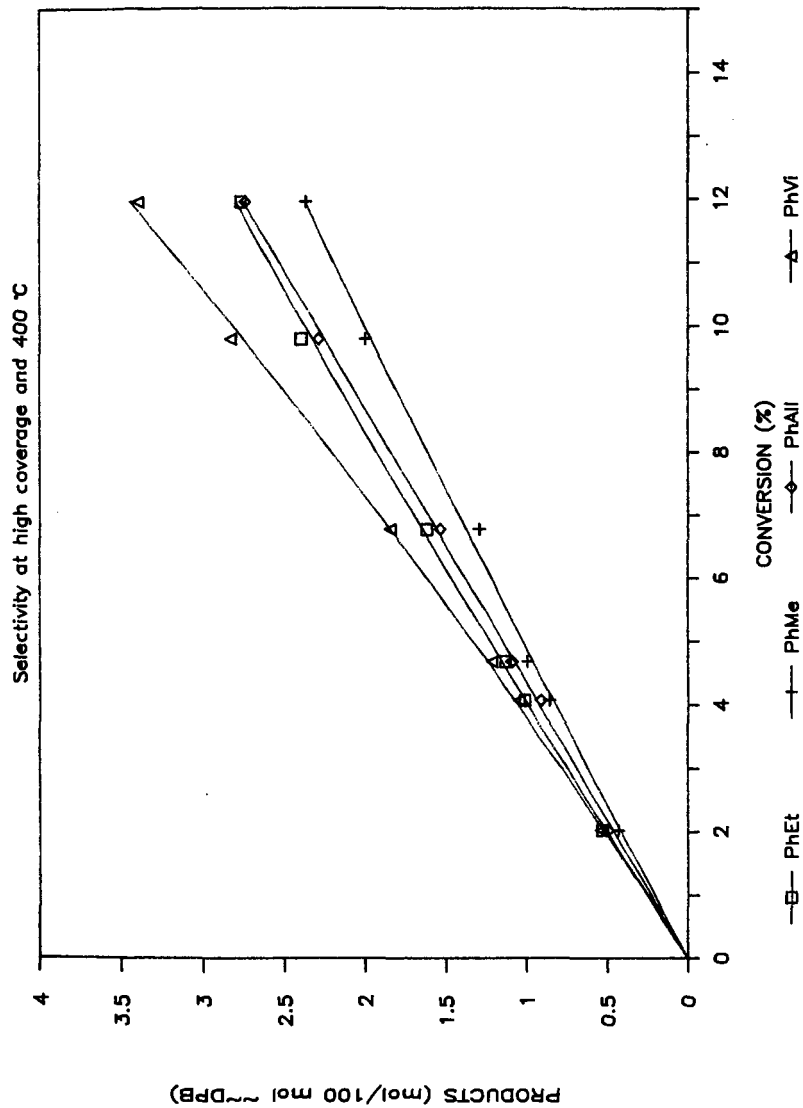
This research was sponsored by the Division of Chemical Sciences, Office of Basic Energy Sciences, U.S. Department of Energy, under contract DE-AC05-84OR21400 with Martin Marietta Energy Systems, Inc.

REFERENCES

1. (a) Whitehurst, D. D. *ACS Symp. Ser.* 1978, 1. (b) Schlosberg, R. H., Ed. *Chemistry in Coal Conversion*, Plenum: New York, 1985.
2. Elliott, M. A., Ed. *Chemistry of Coal Utilization*, Wiley-Interscience: New York, 1981; Suppl. Vol. 2: (a) Howard, J. B., Chapter 12. (b) Gorin, E., Chapter 27.

3. Buchanan, III, A. C.; Dunstan, T. D. J.; Douglas, E. C.; Poutsma, M. L. *J. Am. Chem. Soc.* **1986**, *108*, 7703.
4. (a) Buchanan, III, A. C.; Biggs, C. A. *Prepr., Am. Chem. Soc., Div. Fuel Chem.* **1987**, *32 (3)*, 175. (b) Buchanan, III, A. C., Biggs, C. A. *J. Org. Chem.*, in press.
5. Poutsma, M. L.; Dyer, C. W. *J. Org. Chem.* **1982**, *47*, 4093.

Figure 1. Thermolysis of $\sim\text{Ph}(\text{CH}_2)_4\text{Ph}$



THE LUBRICITY PROPERTIES OF JET FUEL
AS A FUNCTION OF COMPOSITION
PART 1: METHOD DEVELOPMENT

Bruce H. Black^a, and Dennis R. Hardy

CODE 6180, Naval Research Laboratory, Washington, DC 20375-5000
^aGEO-Centers, Inc., Fort Washington, MD 20744

ABSTRACT

In recent years, the quality of petroleum feedstocks used by refineries has decreased. This has necessitated the use of severe refinery processes in order to produce jet fuels of high thermal stability and cleanliness. Unfortunately, these processes remove naturally occurring polar material which impart a fuel's inherent lubricity. As a result, the lubricity properties of jet fuel products have decreased. This critical fuel property is essential for sustained high performance of fuel lubricated engine components. This paper describes a method that correlates naturally occurring and added carboxylic acids with fuel lubricity as measured by the Ball-on-Cylinder Lubricity Evaluator (BOCLE).

INTRODUCTION

In recent years, the quality of petroleum feedstocks has decreased. Thus, it has become necessary to employ severe refining processes in order to produce jet fuels of high thermal stability and cleanliness. Processes such as hydrotreating, hydrocracking, and clay filtering effectively remove the compounds which decrease thermal stability and hinder water removal by coalescence.¹⁻⁴ Unfortunately, some of these compounds are believed to impart a fuel's natural lubricity. Removal of these compounds, therefore, leads to a decrease in the operational lifetime of fuel lubricated engine components in some military and commercial aircraft. This in turn causes increased maintenance costs and down-time of aircraft. For the commercial airlines, this can cause a loss of revenue while an aircraft is grounded. For the military, this can lead to a decreased state of readiness.

Lubricity is a qualitative description of the relative abilities of two fluids, with the same viscosity, to limit wear and friction between moving metal surfaces.^{2,4} It may be the most critical fuel property degraded by refinery processes.^{5,6} There have been instances where the use of low lubricity fuel has caused loss of aircraft and human life.⁷

Considerable effort has been made in the development of a mechanical method which can be performed in the laboratory which will measure fuel lubricity. The current and most widely accepted method is the Ball-on-Cylinder Lubricity Evaluator (BOCLE). The lubricity of a fuel is determined by the measurement of a wear scar on a ball which has been in contact with a rotating cylinder partially immersed in a fuel sample. The reported value is the average of the major and the minor axes of the oval wear scar in millimeters. Typical values for jet fuels are between 0.45

and 0.95 mm.

This paper describes a method for estimating the lubricity properties of jet fuel by compositional analysis. The information developed by this technique is compared to measurements of the same fuels on the BOCLE. The method is based on a previously developed method for determining the concentration of corrosion inhibitor as a lubricity enhancer additive in fuel.⁸⁻¹⁰ The analysis procedure involves a base extraction of a fuel sample with subsequent analysis by high resolution size exclusion chromatography. The amount of naturally occurring organic acids extracted from the fuels correlate well with their respective BOCLE measurements.

EXPERIMENTAL

Reagents- HPLC grade uninhibited tetrahydrofuran (THF) and HPLC grade methylene chloride were obtained from Fisher Scientific. Six test fuels and a hydrocarbon standard used for BOCLE repeatability and reproducibility studies were obtained from the Naval Air Propulsion Center, Trenton, NJ. These samples included: two JP-4 fuels, one of which had been clay filtered; two Jet A fuels, one of which had been clay filtered; a JP-5 fuel; a JP-7 fuel; and ISOPAR M, an isoparaffinic fluid used as a low lubricity standard. A model JP-5 fuel was prepared using technical grade (99.7% purity) n-dodecane obtained from Phillips 66 Co. HPLC grade toluene was obtained from Burdick and Jackson Laboratories Inc. Other constituents of the model fuel were obtained from Fisher Scientific. These compounds included indan, decalin, t-butylbenzene, and cyclohexylbenzene. To investigate the effect of organic acid type on lubricity enhancement, the following acids were used: octanoic, decanoic, lauric, palmitic, stearic, cyclohexane carboxylic acid, and dodecylbenzene sulfonic acid.

Equipment and Materials- Samples were analyzed using a Beckman-Altex Microspherogel high resolution, size exclusion column, Model 255-80 (50A pore size, 30cm x 8.0mm I.D.). Uninhibited THF was used as the mobile phase. The THF was periodically sparged with dry nitrogen to inhibit formation of hazardous peroxides. The injector was a Rheodyne Model 7125. A Beckman Model 100-A HPLC pump was used for solvent delivery with a Waters Model 401 differential refractometer for detection. Peaks were identified using a Varian Model 9176 strip chart recorder. A Fisher Accumet pH Meter Model 610A and a Fisher Standard Combination Electrode Catalog Number 13-639-90 were used for pH adjustments. BOCLE measurements were performed at twenty different laboratories worldwide. The BOCLE used was an InterAV Model BOC 100. The cylinders used were Timken Rings Part Number F25061 obtained from the Falex Corp., Aurora, IL. The test balls used were 12.7mm diameter, SKF Swedish Steel, Part Number 310995A obtained from SKF Industries, Allentown, PA.

Method- Fuel samples were analyzed for organic acid concentration by a previously developed method.⁸ For each sample, 100 ml were extracted with 100 ml of 0.2M aqueous sodium hydroxide. The aqueous phase was drained into a clean beaker and acidified dropwise with concentrated hydrochloric acid. The pH of the aqueous solution was lowered to 2.0 ± 0.03 . The acidified aqueous phase was back-extracted with 100 ml HPLC

grade methylene chloride. The methylene chloride was drained into a clean beaker and allowed to evaporate. After evaporation, the residue was dissolved in 2.0 ml HPLC grade THF and transferred to a glass vial with a teflon-lined cap.

BOCLE measurements on the seven fuel samples were performed in duplicate at twenty laboratories in the United States and Europe. The BOCLE method used was according to appendix Y of the Aviation Fuel Lubricity Evaluation published by the Coordinating Research Council, Inc.¹¹ The lubricity of each sample was measured using both a 500 and a 1000 gram load for the ball on cylinder. The compositional analysis data is correlated with the 500 gram load BOCLE data.

To determine the effect of sulfonic acid on lubricity enhancement, six model fuel samples were prepared for BOCLE analysis. These samples are listed with their relative wear scar diameter measurements in Table 1.

RESULTS

Figures 1 and 2 are size exclusion chromatograms for the seven fuel samples. Figure 1 represents those fuels which were determined to have high lubricity. Figure 2 represents those fuels which were found to have low lubricity. The region of interest on the chromatogram is the area where retention volume is between 5.25 ml and 7.5 ml. The peaks which elute after 7.5 ml are artifacts and were not extracted from the fuel. In Figures 1a and 1b, the peaks with retention volumes less than 6.25 ml correspond to the presence of the lubricity enhancer additive. The peak which elutes at approximately 5.85 ml represents the major active ingredient in most commercial additives, dilinoleic acid (DLA). It has a molecular weight of 562 daltons. This material is prepared by a 1,4-cycloaddition (Diels-Alder) reaction of two linoleic acid molecules. The product is a monocyclic compound with a molecular weight twice that of linoleic acid. It possesses two carboxylic acid groups which are believed to be the points of adsorption to active surface sites.

The small peak which elutes at approximately 5.4 ml corresponds to the presence of trilinoleic acid (TLA). TLA, which is also a product of the Diels-Alder reaction, may possess either a partially unsaturated fused dicyclic ring structure or two isolated partially saturated cyclohexyl rings. It has a molecular weight approximately three times that of linoleic acid (840 daltons).

The fuels whose chromatograms are depicted in Figures 1c and, Figures 2a through 2d, do not possess the lubricity enhancer additive. Their lubricity properties are, for the most part, solely related to the presence of naturally occurring carboxylic acids. The correlation of acidic materials present which elute at 7.25 ml is made with the BOCLE measurements. This retention volume was arbitrarily chosen because it was representative of naturally occurring organic acids present in each of the samples.

Table 2 lists the BOCLE results of the seven fuel samples. Statistically, it can be seen that there are two distinct groups. Three

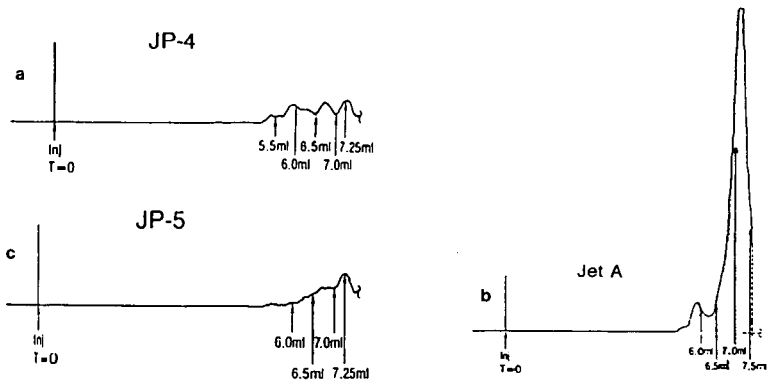


FIGURE 1: HPLC Chromatograms of High Lubricity Fuels as Determined by the Ball-on-Cylinder Lubricity Evaluator.

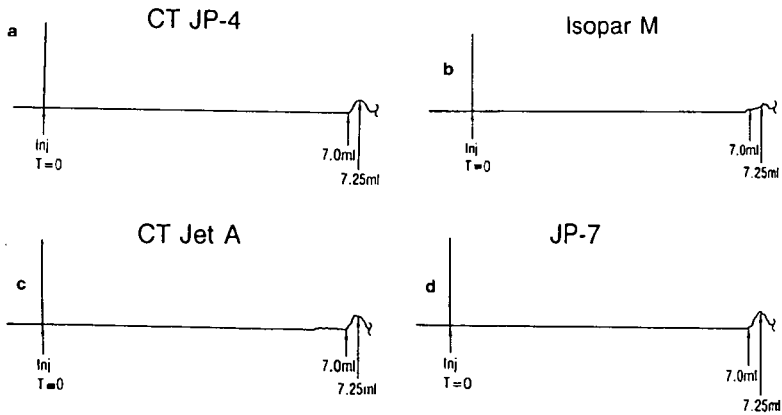


FIGURE 2: HPLC Chromatograms of Low Lubricity Fuels as Determined by the Ball-on-Cylinder Lubricity Evaluator.

fuels, JP-4, Jet A, and JP-5, were found to have high lubricity, and the four others, clay filtered JP-4, ISOPAR M, clay filtered Jet A, and JP-7, were found to have low lubricity. The results within each set are statistically the same. The average relative wear scar diameter for the high lubricity fuels is $0.64 \text{ mm} \pm 0.05 \text{ mm}$ (7.8%). The average relative wear scar diameter for the low lubricity fuels is $0.94 \pm 0.10 \text{ mm}$ (10.6%). This implies that the precision of the BOCLE is better for high lubricity rather than low lubricity fuels.

Table 3 compares the the peak height at 7.25 ml with the BOCLE measurements for each of the fuels. Both JP-4 and Jet A possess the lubricity enhancer additive. It is, therefore, not surprising that these were high lubricity fuels. It can be seen in Figure 1b and Table 3 that the Jet A sample had a significantly higher concentration of the naturally occurring carboxylic acids and lubricity enhancer additive than either the JP-4 or JP-5. The lubricity of the Jet A, however, was not significantly higher than the other high lubricity fuels. Previous work has shown that there is a minimum possible wear scar diameter. The addition of more lubricity enhancer additive or the presence of a greater amount of naturally occurring lubricity enhancing species will not decrease the wear scar diameter.¹¹ In each of the high lubricity fuels, the maximum lubricity has been achieved. Thus, the lubricity measurements for these fuels are the same.

There may be some question as to why the JP-5 sample had significantly higher lubricity than the four low lubricity fuels. In Table 3, it can be seen that the JP-5 sample has only twice the concentration of acidic species eluting at 7.25 ml than the low lubricity fuels, yet the lubricity properties are significantly better. By comparison of Figure 1c with Figures 2a through 2d, it can be seen that each of the fuels in Figure 2 possess a single peak which elutes at 7.25 ml. The JP-5 sample depicted in Figure 1c has, not only this peak, but higher molecular weight acidic species which elute between 6.25 and 7.0 ml. We propose that the presence of these naturally occurring components in addition to two to three times the concentration of material eluting at 7.25 ml, yields the higher lubricity characteristics.

Dodecylbenzene sulfonic acid (DBSA) was found to have no effect on lubricity at concentrations that are normally found in jet fuel. Table 1 shows that at DBSA concentrations up to 1.0 ppm, DBSA did not decrease wear scar diameter measurements for the model fuel. This is in agreement with work performed by Lazarenko, et al. They found that corrosion inhibitors based on sulfonic acids did not increase jet fuel lubricity.¹⁴ Model fuel doped with 96.0 ppm of a carboxylic acid mixture had, however, significantly lower wear scar diameter measurements, i.e., lubricity had increased as expected.

DISCUSSION AND CONCLUSIONS

The effect of long chain carboxylic acids on boundary lubrication is well established. The presence of naturally occurring long chain carboxylic acids in jet fuel is believed to play a major role in lubricity enhancement. Any refinery procedure which removes these acids will have a

detrimental effect on the lubricity of jet fuel products. Thus, processes such as hydrotreatment, hydrocracking, and clay filtration will decrease jet fuel lubricity.

It is well known that clay filtration adversely affects jet fuel lubricity. It has long been believed that this is a result of the removal of naturally occurring polar materials in fuel which impart lubricity.^{2,3,7,12,13} The results of the BOCLE measurements confirm that lubricity does indeed decrease after clay filtration. The compositional changes can be seen by comparison of Figures 1b and 2c which represent Jet A fuel before and after clay filtration. The concentration of lubricity imparting organic acids has been drastically reduced. The lubricity enhancer additive has also been completely removed. The corresponding result is an extreme reduction in fuel lubricity. Comparison between clay filtered and non-clay filtered JP-4 cannot be made since these were two different fuels. It can be seen, however, that the mandatory corrosion inhibitor/lubricity enhancer additive is not present in the clay filtered sample.

This work has shown that a direct relationship between the presence of naturally occurring carboxylic acids and BOCLE measurements exists. Previous work by has also shown this relationship.⁸ They analyzed a series of additive-free JP-5 and Jet A samples for naturally organic acids and correlated their presence with the fuels' respective BOCLE measurements. Additional work, which will be published in a subsequent paper, has shown the relationship in Naval JP-5 field samples as well as Air Force JP-4 field samples.

Sulfonic acids, however, were not found to influence BOCLE measurements and, therefore, do not enhance lubricity. Other polar material in jet fuel may contribute to lubricity enhancement. The carboxylic acids, which are well known surface active and lubricity enhancing species, are likely to be the major contributor.

In the future, it appears as though the BOCLE will be accepted as the standard method for measuring lubricity in the laboratory. The compositional analysis method can be used as a supplementary method to the BOCLE for verification of lubricity measurements. There are, however, a few advantages to the compositional analysis method over the BOCLE. First, the BOCLE is operator sensitive. Second, the instrument is sensitive to contamination of the fuels and test materials. Third, the presence of dissolved oxygen and water in a sample will influence the wear scar generated. Fourth, the BOCLE is very sensitive to relative humidity.

The compositional analysis method is not sensitive to relative humidity or dissolved oxygen and water in a fuel sample. Trace contamination between samples does not occur as readily with the compositional analysis method and its influence is significantly less. The compositional analysis method is also able to distinguish between three types of high lubricity fuel which the BOCLE cannot. These include; a high lubricity fuel without corrosion inhibitor, a high lubricity fuel with corrosion inhibitor, and a low lubricity fuel with corrosion inhibitor.

Although the lubricity enhancer additive is mandatory in U.S. military

jet fuel, a number of Naval JP-5 fuel samples were indentified where the lubricity additive may not have been necessary. Addition of the lubricity enhancer additive to these fuels may have been an unnecessary expense. In addition, the lubricity enhancer additive has been shown to adversely effect the removal of water from fuel by coalescence. The use of the additive, therefore, may actually be detrimental rather than beneficial in some fuels.

Finally, for those fuels which have had the lubricity enhancer additive blended in at the refinery, the compositional analysis method can be used as a quality assurance and quality control procedure. Both the refiner and user can analyze a fuel for levels of both naturally occurring and added lubricity imparting organic acids.

TABLE 1

<u>SAMPLE</u>	<u>Conc. DBSA (ppm)</u>	<u>Conc. R-COOH (ppm)</u>	<u>Normalized WSD</u>
1	0.0	0.0	0.99
2	0.5	0.0	0.98
3	1.0	0.0	1.00
4	0.0	96.0	0.49
5	0.5	96.0	0.51
6	1.0	96.0	0.53

The Effect of Dodecylbenzene Sulfonic Acid on Lubricity as Measured by the BOCLE in the Presence and Absence of Carboxylic Acids.

TABLE 2

<u>SAMPLE</u>	<u>Normalized WSD</u>	<u>± 2σ</u>
JP-4	0.63	0.05
JET A	0.64	0.05
JP-5	0.65	0.05
CT JP-4	0.92	0.11
ISOPAR M	0.93	0.09
CT JET A	0.93	0.09
JP-7	1.00	0.11

The Lubricity of Fuel Samples as Measured by the Ball-on-Cylinder Lubricity Evaluator.

TABLE 3

<u>SAMPLE</u>	<u>Normalized WSD</u>	<u>Pk Hgt @ 7.25 mL</u>
JP-4*	0.63	10.0 mm
JET A*	0.64	>165.0 mm
JP-5	0.65	** 15.5 mm
CT JP-4	0.92	6.5 mm
ISOPAR M	0.93	4.5 mm
CT JET A	0.93	6.0 mm
JP-7	1.00	7.5 mm

* Contained a lubricity enhancer additive

** Higher molecular weight acidic species were also present

The Comparison of Organic Acid Composition at 7.25 mL Retention Volume with Lubricity as Measured by the Ball-on-Cylinder Lubricity Evaluator.

REFERENCES

1. Vere, R. A. Soc. Automot. Eng., SAE Reprint Number 690667, National Aeronautic and Space Engineering and Manufacturing Meeting, Los Angeles, CA, October, 1969; pp 2237-2244.
2. Moses, C. A.; Callahan, T. J.; Cuellar, Jr., J. P.; Dodge, L. G.; Likos, W. E.; Naegeli, D. W.; Valtierra, M. L. "An Alternative Test Procedure to Qualify Fuels for Navy Aircraft"; Final Report, Naval Air Propulsion Center Contract Number N00140-80-C-2269, Report Number NAPC-PE-145C; Southwest Research Institute, San Antonio, TX, 1984.
3. Petrarca, Jr., J. "Lubricity of Jet A-1 and JP-4 Fuels"; NTIS Number AD-784772; Report Number AFAPL-TR-74-15, Air Force Aero Propulsion Laboratory, Wright-Patterson AFB, OH, 1974.
4. Goodger, E.; Vere, R. Aviation Fuels Technology; MacMillan Publishers Ltd.: Houndmills, Basingstoke, Hampshire, England, 1985; pp 80-82.
5. Biddle, T. B.; Meehan, R. J.; Warner, P. A. "Standardization of Lubricity Test"; Report Number AFWAL-TR-87-2041, Air Force Wright Aeronautical Laboratories, Aero Propulsion Laboratory (AFWAL/POSF), Wright-Patterson AFB, OH, 1987.
6. Master, A. I.; Weston, J. L.; Biddle, T. B.; Clark, J. A.; Gratton, M.; Graves, C. B.; Rone, G. M.; Stoner, C. D. "Additional Development of the Alternative Test Procedure for Navy Aircraft Fuels"; Naval Air Propulsion Center Contract Number N00140-84-C-5533, Report Number NAPC-PE-160C; United Technologies Corporation, Pratt and Whitney, West Palm Beach, FL, 1987.
7. Fishman, E.; Mach, M. H.; Fraser, L. M.; Moore, D. P. "Navy Mobility Fuels Evaluation"; Final Report, Naval Research Laboratory Contract Number N00014-82-C-2370; TRW Energy Technology Division, Redondo Beach, CA, 20 July 1984.
8. Black, B. H.; Wechter, M. A.; Hardy, D. R. J. Chromatogr. 1988, 437, 203-210.
9. Hardy, D. R.; Black, B. H.; Wechter, M. A. J. Chromatogr. 1986, 366, 351-361.
10. Wechter, M. A. "Quantitative Determination of Corrosion Inhibitor Levels in Jet Fuels by HPLC"; Final Report, Naval Research Laboratory Contract Number N00014-85-M-0248; Southeastern Massachusetts University, North Dartmouth, MA 1986.
11. Coordinating Research Council "Aviation Fuel Lubricity Evaluation"; CRC Report Number 560, CRC Inc., Atlanta, GA, 1988.
12. Grabel, L. "Lubricity Properties of High Temperature Jet Fuel"; NTIS Number AD-A045467; Report Number NAPC-PE-112, Naval Air Propulsion Test Center, Trenton, NJ, 1977.
13. Grabel, L. "Effect of Corrosion Inhibitors on the Lubricity and WSM of JP-5 Fuels"; Interim Report Number NAPC-LR-80-7, Naval Air Propulsion Center, Trenton, NJ, 1980.
14. Lazarenko, V. P.; Skorvorodin, G. B.; Rozhkov, I. V.; Sablina, Z. A.; Churshukov, E. S. Chemistry and Technology of Fuels and Oils 1975, 11, No. 5 & 6, 356-359.

**THE LUBRICITY PROPERTIES OF JET FUEL
AS A FUNCTION OF COMPOSITION
PART 2: APPLICATION OF ANALYSIS METHOD**

Bruce H. Black^a, and Dennis R. Hardy

CODE 6180, Naval Research Laboratory, Washington, DC 20375-5000

^aGEO-Centers, Inc., Fort Washington, MD 20744

ABSTRACT

In recent years, the quality of petroleum feedstocks used by refineries has decreased. This has necessitated the use of severe refinery processes in order to produce jet fuels of high thermal stability and cleanliness. These processes, however, tend to decrease the lubricity properties of jet fuel products. As a result, fuel lubricated engine components have been experiencing greater wear and mechanical failure. To alleviate this problem, a highly effective lubricity enhancer additive, based on mixtures of carboxylic acids, is mandatory in all U.S. military jet fuel. The additive, however, has been shown to interfere with the removal of water from jet fuel by coalescence. In addition, some fuels possess high levels of naturally occurring, lubricity enhancing carboxylic acids and, therefore, do not need the additive. This paper describes the application of an analysis method that distinguishes between fuels with and without the additive, and fuels that possess naturally occurring, lubricity enhancing carboxylic acids.

INTRODUCTION

In part 1 of this work, it was shown that a direct correlation exists between the presence of naturally occurring carboxylic acids and Ball-on-Cylinder Lubricity Evaluator (BOCLE) measurements.¹ This correlation was applied to a series of fuel samples that were used to determine the repeatability and reproducibility of the BOCLE instrument. Extensive BOCLE data had been generated to which the compositional analysis results could be compared. The compositional analysis method was found to be able to distinguish between naturally occurring and added lubricity enhancing carboxylic acids.

This paper applies the compositional analysis method to a series of Navy JP-5 jet fuel samples obtained from a worldwide survey of storage depots. BOCLE measurements were performed at the Naval Air Propulsion Center (NAPC), Trenton, NJ. As in the previous work, the presence of carboxylic acids in a fuel sample increased its inherent lubricity. The compositional analysis method also identified fuels which were deficient in the mandatory lubricity enhancer additive.

EXPERIMENTAL

Reagents- HPLC grade uninhibited tetrahydrofuran (THF) and HPLC grade methylene chloride were obtained from Fisher Scientific. Seven JP-5 fuel

samples, from the Navy's Second Worldwide Fuel Survey, were obtained from the Naval Air Propulsion Center.

Equipment and Materials- Samples were analyzed using a Beckman-Altex Microspherogel high resolution, size exclusion column, Model 255-80 (50A pore size, 30cm x 8.0mm I.D.). Uninhibited THF was used as the mobile phase. The THF was periodically sparged with dry nitrogen to inhibit formation of hazardous peroxides. The injector was a Rheodyne Model 7125. A Beckman Model 100-A HPLC pump was used for solvent delivery with a Waters Model 401 differential refractometer for detection. Peaks were identified using a Varian Model 9176 strip chart recorder. A Fisher Accumet pH meter Model 610A and a Fisher standard combination electrode Catalog Number 13-639-90 were used for pH adjustments. An Interav Model BOC 100 Ball-on-Cylinder Lubricity Evaluator was used for lubricity measurements. The cylinders were 100% spheroidized annealed bar stock, consumable vacuum melted AMS 6444 steel obtained from Jayna Enterprises, Inc., Vandalia, OH. The balls used were 12.7mm diameter, SKF Swedish Steel, Part Number 310995A obtained from SKF Industries, Allentown, PA.

Method- Fuel samples were analyzed for carboxylic acid concentration by a previously developed method.² For each sample, 100 ml were extracted with 100 ml of 0.2M aqueous sodium hydroxide. The aqueous phase was drained into a clean beaker and acidified dropwise with concentrated hydrochloric acid. The pH of the aqueous phase was lowered to $\text{pH } 2.0 \pm 0.03$. The acidified aqueous phase was back-extracted with 100 ml HPLC grade methylene chloride. The methylene chloride was drained into a clean beaker and allowed to evaporate. After evaporation, the residue remaining was dissolved in 2.0 ml HPLC grade THF and transferred to a glass vial with a teflon-lined cap.

BOCLE measurements were performed in triplicate on each of the fuel samples. The method used was according to appendix Q of the Aviation Fuel Lubricity Evaluation published by the Coordinating Research Council, Inc.³ The sum of the values obtained for each sample was averaged and the relative wear scar diameter measurements are reported in Table 1.

RESULTS AND DISCUSSION

As in previous work, the presence of carboxylic acids, both naturally occurring and added, correlates well with BOCLE measurements. The relative average wear scar diameter for each sample is listed in Table 1. The cylinders used for this work were somewhat softer than the Timken rings previously used in Part 1 of this work. As a result, the actual wear scar diameter measurements were somewhat lower with a narrower range.

It can be seen in Table 1 that five of the seven fuels analyzed possessed the lubricity enhancer additive. Four of these fuels had both the major constituent, dillinoic acid (DLA), and a minor component present in some lubricity enhancer additives, trillinoic acid (TLA). Two of the fuels analyzed, however, did not possess any appreciable amount of the mandatory lubricity enhancer additive.

In Figures 1 through 5, the major lubricity enhancer additive

component, DLA, elutes at approximately 5.85 ml. The DLA component has a molecular weight of about 560 daltons. This material is prepared by a 1,4-cycloaddition (Diels-Alder) reaction of two linoleic acid molecules. The product is a monocyclic compound with a molecular weight twice that of linoleic acid. It possesses two carboxylic acid moieties which are believed to be the points of attachment to active surface sites.

In Figures 1 through 4, the peak corresponding to the TLA component is also present. This component elutes at approximately 5.4 ml. The TLA component, which is also a product of the Diels-Alder reaction, has a molecular weight of approximately 840 daltons. It may possess either a partially unsaturated fused dicyclic ring structure or two isolated partially saturated cyclohexyl rings.

As expected, the fuels that possess the lubricity enhancer additive were found to have the highest lubricity. Those fuels that did not possess the lubricity enhancer additive, and were also deficient in naturally occurring carboxylic acids, were found to have the lowest lubricity. From what is known about carboxylic acids with respect to lubricity enhancement, continued use of these fuels could lead to lubricity related problems.

Table 2 lists the peak heights for the added and naturally occurring carboxylic acids extracted from the fuel samples. Fuel samples 1 through 3 each possessed similar amounts of the lubricity enhancer additive. Fuel sample 4 had slightly less than the first three fuel samples, while fuel 5 was devoid of the TLA component and had significantly less of the DLA component. Two sets of data for the naturally occurring carboxylic acids are listed. In previous work, it was found that some fuels possess two distinct molecular weight ranges of naturally occurring carboxylic acids.^{1,2} These two ranges are designated regions 3 and 4. These components have retention volumes of approximately 6.5 and 7.0ml respectively and can be clearly seen in Figure 3.

High resolution, size exclusion chromatography separates components on the basis of molecular shape and size and, therefore, to an extent, molecular weight. In general, one would expect a normal distribution of straight chain alkanic acids which parallels the distribution of normal alkanes present in a fuel. The presence of two separate peaks for the naturally occurring carboxylic acids indicates the presence of two distinct classes of constituents. Region 3 corresponds to the straight chain alkanic acids, while region 4 corresponds to mono- and polycyclic carboxylic acids. The maxima for regions 3 and 4 correspond to the molecular weight of tetradecanoic acid (C₁₄), and octanoic acid (C₈) respectively. The condensed size of a cyclic compound, as opposed to a straight chain compound, yields a calculated molecular weight lower than its actual molecular weight. For this reason, region 4 is most likely comprised of not only monocyclic carboxylic acids, but polycyclic acids as well.

Maxima for regions 3 and 4 are not as well defined in other fuels examined. For these fuels, the height was measured at a retention volume that corresponds to the maxima in Figure 3. In Figures 1, 2, and 5, the concentration of carboxylic acids present in region 3 increased gradually as the molecular weight decreased. In each case, there is a very rapid

increase in carboxylic acid concentration in the region 4 molecular weight range. Similar results were found in earlier work.^{1,2}

In each fuel previously examined, there was some minimum amount of carboxylic acids present in region 4. Not all fuels, however, possessed the carboxylic acids which correspond to region 3. Some had very low concentrations, some had approximately equal concentrations. These differences may be a result of crude source, refinery operations, or storage conditions.

CONCLUSIONS

The compositional analysis method has been applied to a series of field samples to determine the presence of naturally occurring and added carboxylic acids are known to enhance jet fuel lubricity. The concentration present in a given fuel sample correlates well with its inherent lubricity as measured by the BOCLE.

A number of molecular weight ranges of carboxylic acids are present in most jet fuels. Two of these regions correspond to the presence of an added lubricity enhancer, and two or more correspond to naturally occurring lubricity enhancing carboxylic acids. The relative effectiveness of each region has not yet been determined. It is believed, however, that the dimer of linoleic acid is more effective than the trimer. This is a result of steric hindrance between trimer molecules when attached to surfaces.⁴⁻⁶

The relative effectiveness of the naturally occurring carboxylic acids is believed to increase as chain length increases. Daniel found that, in general, the ease of adsorption increases with increasing chain length.⁷ Boundary lubrication also increases as chain length increases.^{8,9} The lubricity properties of jet fuel, therefore, may increase as the presence of longer chain carboxylic acids increases. At some point, however, there is probably a limit to lubricity enhancement by increasing chain length. The relative effectiveness of region 3 over region 4, therefore, may be substantially different due to the differences in structure.

There may be some question as to why the mandatory lubricity enhancer additive is absent from two of the fuels examined. There are possible explanations for this. First, the lubricity enhancer additive was originally added to the fuel to inhibit corrosion to fuel handling and storage systems which resulted from dissolved oxygen and free-water present in fuel. The carboxylic acid based corrosion inhibitors were serendipitously found to enhance the lubricity properties of low lubricity fuels.¹⁰⁻¹³ As lubricity related problems became more prevalent, the primary purpose for the corrosion inhibitor was lubricity enhancement. Unfortunately, the military specification for jet fuel was not modified to include lubricity properties. Second, the additives are accepted and used, not for their ability to enhance lubricity, but to inhibit corrosion. Some of these additive are based on acylated glycols and acylated alkanolamines. the compositional analysis method described in this paper is not suitable for analysis of these materials. It should be noted that

these materials have been shown to be relatively ineffective lubricity enhancers. Third, the additive was not added at the refinery as it should have been. Additive loss due to adsorption in fuel handling has been found to be insignificant. Previous work has shown that as little as 3% is lost due to adsorption on the surfaces of a 100 mile pipeline.¹⁴

The compositional analysis method can be used as a supplement to the BOCLE. The BOCLE can determine if a fuel has sufficient lubricity characteristics. The compositional analysis method can determine if the lubricity is a result of naturally occurring or added carboxylic acids or both.

REFERENCES

- (1) Black, B. H.; Hardy, D. R. "The Lubricity Properties of Jet Fuel as a Function of Composition: Part 1- Correlation of Fuel Composition with Ball-on-Cylinder Lubricity Evaluator (BOCLE) Measurements"; Submitted for Publication in Energy and Fuels, 1988.
- (2) Black, B. H.; Wechter, M. A.; Hardy, D. R. J Chromatogr. 1988, 437, 203-210.
- (3) Coordinating Research Council "Aviation Fuel Lubricity Evaluation"; CRC Report Number 560, CRC Inc., Atlanta, GA, 1988.
- (4) Dacre, B.; Savory, B.; Wheeler, P. A. "Adsorption of Lubricity Additive Components, Part 1"; Technical Report AC/R/13 1977, Royal Military College of Science, Shrivenham, Swindon, Wiltshire, England; Contract Number AT/2160/025/ENG D, Procurement Executive, Ministry of Defense, London.
- (5) Dacre, B.; Wheeler, P. A.; Savory B. "Adsorption of Lubricity Additive Components, Part 2"; Technical Report AC/R/30 1979, Royal Military College of Science, Shrivenham, Swindon, Wiltshire, England; Contract Number AT/2160/025/ENG D, Procurement Executive, Ministry of Defense, London.
- (6) Dacre, B.; Wheeler, P. A.; "Adsorption of Lubricity Additive Components, Part 3- Kinetics of Adsorption"; Technical Report AC/R/33 1980, Royal Military College of Science, Shrivenham, Swindon, Wiltshire, England; Contract Number AT/2160/025, Procurement Executive, Ministry of Defense, London.
- (7) Daniel, S. G. Trans. Faraday Soc. 1944, 47, 1345-1359.
- (8) Allen, C. M.; Drauglis, E. Wear 1969, 14, 363-384.
- (9) Levine, O.; Zisman, W. A. J. Phys. Chem. 1957, 61, 1188-1200.
- (10) Vere, R. A. Soc. Automot. Eng., SAE Reprint Number 690667, National Aeronautic and Space Engineering and Manufacturing Meeting, Los Angeles, CA, October, 1969; pp 2237-2244.

(11) Petrarca, Jr., J. "Lubricity of Jet A-1 and JP-4 Fuels"; NTIS Number AD-784772; Report Number AFAPL-TR-74-15, Air Force Aero Propulsion Laboratory, Wright-Patterson AFB, OH, 1974.

(12) Martel, C. R.; Bradley, R. P.; McCoy, J. R.; Petrarca, Jr., J. "Aircraft Engine Turbine Corrosion Inhibitors and Their Effects on Fuel Properties"; NTIS Number AD-787191; Report Number AFAPL-TR-74-20, Air Force Aero Propulsion Laboratory, Wright-Patterson AFB, OH, 1974.

(13) Grabel, L. "Lubricity Properties of High Temperature Jet Fuel"; NTIS Number AD-A045467; Report Number NAPTC-PE-112, Naval Air Propulsion Test Center, Trenton, NJ, 1977.

(14) Black, B.H.; Hardy, D.R.; Wechter, M.A. "The Determination and Use of Isothermal Adsorption Constants of Jet Fuel Lubricity Enhancer Additives"; Ind. Eng. Chem. Res., In Review, 1988.

TABLE 1

<u>SAMPLE</u>	<u>Relative WSD</u>	<u>TIA Present</u>	<u>DLA Present</u>
1. Roosevelt Roads, P.R.	0.67	YES	YES
2. Guantanamo, Cuba	0.70	YES	YES
3. Diego Garcia	0.71	YES	YES
4. Iorizaki, Japan	0.77	YES	YES
5. Gatun, Panama	0.79	NO	YES
6. Cartagena, Spain	0.86	NO	NO
7. Azores	1.00	NO	NO

The Relative Lubricity of Fuel Samples as Measured by the Ball-on-Cylinder Lubricity Evaluator.

TABLE 2

<u>SAMPLE</u>	<u>TIA Pk Hgt</u>	<u>DLA Pk Hgt</u>	<u>Reg. 3 Pk Hgt</u>	<u>Reg. 4 Pk Hgt</u>
1	4.0	15.5	14.5	126.0
2	4.0	15.0	11.0	25.0
3	4.0	16.0	20.0	22.0
4	1.5	11.0	4.0	3.5
5	0.0	7.5	12.0	74.0
6	0.0	0.0	5.0	8.5
7	0.0	0.0	7.5	6.5

The Results of the Compositional Analysis of Fuel Samples for Natural and Added Carboxylic Acids.

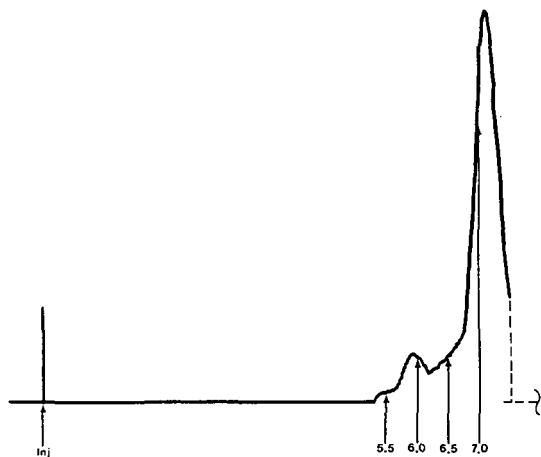


FIGURE 1: HPLC Chromatogram of Base Extracted JP-5 Jet Fuel from Roosevelt Roads, Puerto Rico.



FIGURE 2: HPLC Chromatogram of Base Extracted JP-5 Jet Fuel from Guantanamo, Cuba.

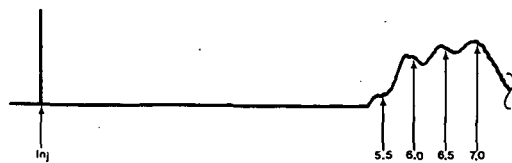


FIGURE 3: HPLC Chromatogram of Base Extracted JP-5 Jet Fuel from Diego Garcia.



FIGURE 4: HPLC Chromatogram of Base Extracted JP-5 Jet Fuel from Iorizaki, Japan.

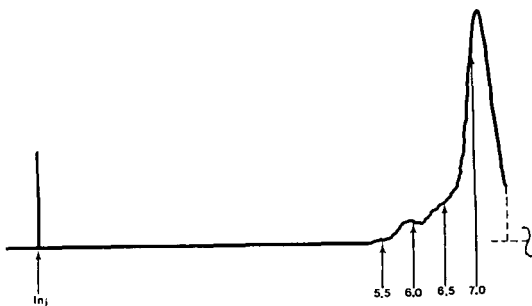


FIGURE 5: HPLC Chromatogram of Base Extracted JP-5 Jet Fuel from Gatun, Panama.



FIGURE 6: HPLC Chromatogram of Base Extracted JP-5 Jet Fuel From Cartagena, Spain.



FIGURE 7: HPLC Chromatogram of Base Extracted JP-5 Jet Fuel from the Azores.

ALKALI AND ALKALINE EARTH PROMOTED CATALYSTS FOR COAL LIQUEFACTION APPLICATIONS

Anastasios Papaioannou and Henry W. Haynes, Jr.
Department of Chemical Engineering
University of Wyoming
P. O. Box 3295, University Station
Laramie, WY 82071

INTRODUCTION

The promotion of Co (or Ni) Mo/Alumina hydrotreating catalysts with percentage quantities of alkali and alkaline earth metals has been proposed as a means of reducing carbon formation when the catalyst is subjected to a high coking environment (1, 2, 3). We recently reported the results of a study in which a sodium promoted NiMo catalyst was compared with the untreated catalyst while hydrotreating a coal-derived liquid (4). In terms of hydrogenation activity, the treated and untreated catalysts were essentially equivalent. Both possessed excellent activity and this activity was well maintained over the 400 hour run duration. Carbon deposition on the used catalyst was substantially reduced by the sodium treatment. The incorporation of sodium into the catalyst did, however, reduce the hydrodenitrogenation activity. The present study was undertaken to ascertain whether similar effects could be realized by promotion with the alkaline earth metals.

EXPERIMENTAL

Catalyst deactivation runs were conducted in the bench scale trickle bed hydro-treater described previously (4). The reactor is charged with only three grams of catalyst, and at this scale of operation it is difficult to obtain reliable kinetics information due principally to the low liquid mass velocities characteristic of such systems (5). One should therefore not attach too much significance to the absolute values of the reported rate constants. Rather it is the relative values of the rate constants that is significant. The system has proven to be a reliable catalyst screening tool as the data are reproducible and conditions are chosen such that differences in activity level are readily observed.

The catalyst selected for this investigation is a CoMo/Alumina catalyst (Amocat 1A-nominal 16 wt% MoO₃, 3 wt% CoO) provided by the Amoco Oil Company. This catalyst was designed specifically for coal liquefaction applications as described in (6, 7). A calcium promoted catalyst was prepared from the Amocat 1A by the incipient wetness impregnation with aqueous calcium nitrate followed by calcining for four hours at 450°C. The finished catalyst contained 5.3 wt% CaO. A magnesium promoted catalyst (3.8 wt% MgO) was prepared similarly. Both weight percentages correspond to a loading of 0.9 mole alkaline earth per mole molybdenum. Properties of all three catalysts are summarized in Table I. The catalysts were sulfided in 10% H₂S/H₂ prior to characterization.

The feedstock employed in this investigation is a mildly hydrogenated creosote oil (560-835°F) spiked with 20 wt% ash free coal liquid vacuum bottoms (1000°F) obtained from the Advanced Coal Liquefaction Research Facility at Wilsonville, Alabama, Run 247. Properties of the feedstock HCO1-R are compiled in Table II.

Crude kinetics models were developed for the HC01-R/Amocat 1A feedstock/catalyst system in a manner similar to the procedure described by Baker, et al. (4). Details are provided in a final DOE report (8). The hydrogen uptake kinetics are first order reversible; whereas, the hydrodenitrogenation kinetics are taken to be first order and irreversible. Deactivation run conditions are summarized in Table III. These conditions, while severe by hydrotreating standards, are not out of line when compared to coal liquefaction conditions.

BET surface areas were calculated from the nitrogen adsorption isotherm at liquid nitrogen temperatures. Pore size distributions were obtained by mercury porosimetry. Prior to characterization, all used catalysts were extracted in tetrahydrofuran (THF) for 24 hours and dried under vacuum at 100°C for 48 hours. The used THF extracted catalysts were analyzed for carbon-hydrogen content in a combustion tube apparatus. All catalysts were subjected to acid sites characterization by the Temperature Programmed Desorption (TPD) of t-butylamine (9, 10). We calculate a Relative Acid Density (RAD) by dividing the high temperature "β-peak" area by the BET surface area. This quantity is an indication of the acid sites density when compared with other catalysts in the program. Attempts to interpret the maximum peak temperature as a measure of acid site strength are complicated by the decomposition of the adsorbed base prior to its desorption from the sample (11).

RESULTS AND DISCUSSION

Hydrogen uptake deactivation curves for the three catalysts are plotted in Figure 1. While there may have been some loss in day one activity due to the addition of promotor metals, it seems clear that the hydrogenation activities are essentially equivalent after the first few hours on stream. Similar results were observed in an earlier study of sodium promoted catalysts (4). In contrast the hydrodenitrogenation activities are significantly lowered by the incorporation of alkaline earth metals into the catalyst, Figure 2. (An upset was experienced prior to the last balance period during the run with unpromoted catalyst, hence the dashed line.) Furthermore, the reduction in activity appears to be related to catalyst acidity as can be ascertained from the RAD values in Table I. The most acidic catalyst, i.e. the unpromoted catalyst, possesses the highest hydrodenitrogenation activity; whereas, the least acidic Ca-promoted catalyst exhibits the lowest activity. The Mg-promoted catalyst lies in between these extremes with regard to both acid site density and hydrodenitrogenation activity. It appears that acid sites are essential for good hydrodenitrogenation activity presumably because they provide preferential adsorption sites for basic nitrogen species. Acid sites are evidently not essential for good hydrogenation activity, however.

Properties of the used THF extracted catalysts are compiled in Table IV. By comparison with the fresh catalyst values of Table I, it is apparent that a modest reduction in surface area has occurred with the greatest reduction being for the untreated catalyst. The loss in pore volume is more substantial with the pore volume reduction ranging from 33% for the Ca-promoted catalyst to 49% for the unpromoted catalyst. This is also evident from a comparison of cumulative pore size distributions plotted in Figures 3 and 4.

The most interesting information in Table IV is the carbon deposition data. Indeed promotion with alkaline earth metals does serve to reduce coke deposition. Calcium promotion is more effective than magnesium promotion, and again the results suggest that coke deposition may be related to catalyst acidity.

Higher coke levels are observed on the more acidic catalysts.

The results of this study are broadly consistent with recent results reported by Shimada and coworkers (12). These investigators also observed that doping with Ca and Mg served to reduce both coke level and hydrodenitrogenation activity. Consistent with previous results for sodium promoted catalysts (13) they find that activity losses are reduced by adding the alkaline earth metal as a last step in the preparation, i.e. after the active metals have been added. Somewhat contrary to our findings is their observation that hydrogenation activity is also reduced by the alkaline earth treatment. However, it may be important to note that this conclusion is based on the hydrogenation of a model compound in a batch reactor. Their results thus reflect initial activity levels. As noted above our initial hydrogenation activity appears to be higher for the unpromoted catalyst, but after a few hours on stream this advantage disappears. Similar results were obtained with sodium promoted catalysts (4).

Our results for both alkali (4) and alkaline earth promoted hydrotreating catalysts have been explained in a rather straightforward manner in terms of catalyst acidity. However, in a study of hydrotreating catalysts prepared on different support materials (14), we report findings that appear somewhat contradictory of the present results. In particular we observe a trend of decreasing coke formation with increasing RAD. This may be due to the fact that characterization of catalyst acidity by TPD of t-butylamine is far from complete. In particular, our analysis provides little or no information regarding the strength (11) or type (Bronsted or Lewis) of acidity. These factors may be expected to effect both coking tendency and activity levels.

CONCLUSIONS

The promotion of an otherwise finished CoMo/Alumina hydrotreating catalyst with percentage quantities of alkaline earth metals offers an effective means of reducing coking tendency while maintaining a high hydrogenation activity. The treatment does have an adverse affect on hydrodenitrogenation activity. Alkali and alkaline earth promotion may therefore be beneficial in applications such as coal liquefaction where the primary function of the catalyst is to hydrogenate and the reaction environment is conducive to coking.

ACKNOWLEDGEMENTS

This work was jointly sponsored by the U.S. Department of Energy (Grant DE-FG22-88PC88942) and the Amoco Oil Company. We are grateful for both the financial support and the helpful consultations provided by these organizations.

REFERENCES

1. Kelly, J.F. and M. Ternan, Can. J. Chem. Eng. **57**, 726 (1979).
2. Kelly, J.F.; Kriz, J.F. and M. Ternan, Canadian Pat. No. 1,121,293, April 6, 1982.
3. Kageyama, Y. and T. Masuyama, "Hydrogenation Catalysis of Coal Liquid Bottoms", Proc. 1985 Int. Conf. Coal Sci., Sidney, Oct. 28-31, 1985.
4. Baker, J.R.; McCormick, R.L. and H.W. Haynes, Jr., I & EC Res. **26**, 1895 (1987).

5. Satterfield, C.N., AICHE Jour. 21, 209 (1975).
6. Bertolacini, R.J.; Gutberlet, L.C.; Kim, D.K. and K.K. Robinson, "Catalyst Development for Coal Liquefaction", Final Rept. AF-1084, EPRI, June 1979.
7. Kim, D.K.; Bertolacini, R.J.; Forgac, J.M.; Pellet, R.J.; Robinson, K.K. and C.V. McDaniel, "Catalyst Development for Coal Liquefaction", Final Rept. AF-1233, EPRI, Nov. 1979.
8. Haynes, H.W. Jr., "Improved Catalysts for Coal Liquefaction", Final Rept. DOE/PC/70812-13, USDOE, April, 1988.
9. Mieville, R.L. and B.L. Meyers, J. Catal. 74, 196 (1982).
10. Nelson, H.C.; Lussier, R.J. and M.E. Still, Appl. Catal. 7, 113 (1983).
11. McCormick, R.L.; Baker, J.R.; Haynes, H.W. Jr. and R. Malhotra, Energy & Fuels 2, 740 (1988).
12. Shimada, H.; Sato, T; Yoshimura, Y.; Nishijima, A.; Matsuda, M.; Konakahara, T. and K. Sato, Sekiyu Gakkaishi 31, 227 (1988).
13. Boorman, P.M.; Kriz, J.F.; Brown, J.R. and M. Ternan, Proc. 4th Climax Int. Conf. Chem. and Uses of Molybdenum, 192 (1982).
14. McCormick, R.L.; King, J.A.; King, T.R. and H.W. Haynes, Jr., "The Influence of Support on the Performance of Coal-Liquids Hydrotreating Catalysts", sub. to I & EC Res., 1988.

Table I
Fresh Catalyst Properties

	<u>Amocat 1A</u>	<u>Mg-Promoted</u>	<u>Ca-Promoted</u>
BET Surface Area, m ² /g	167	144	135
Pore Volume (> 60 Å dia.), cc/g	0.71	0.69	0.69
Avg. Micropore Diameter, Å	130	125	125
Avg. Macropore Diameter, Å	4500	4500	4500
Relative Acid Density, m ⁻²	0.049	0.036	0

Table II
Feedstock Properties (HC01-R)

wt% C	91.43
wt% H	6.84
wt% S	0.20
wt% N	0.68
wt% O (BD)	0.85
wt% Asphaltene	12
wt% Preasphaltene	4
Sp. Gr. (60/60 F)	1.1232

Table III
Nominal Deactivation Run Conditions

Pressure =	2000 psig
Temperature =	440°C (825°F)
WHSV =	3.0
H ₂ Treat Rate =	5500 SCF/BBL

Table IV
Used Catalyst Properties

	<u>Amocat 1A</u>	<u>Mg-Promoted</u>	<u>Ca-Promoted</u>
BET Surface Area, m ² /g	137	137	118
Pore Volume (> 60 Å dia.), cc/g	0.36	0.41	0.46
Avg. Micropore Diameter, Å	100	100	100
Avg. Macropore Diameter, Å	4000	4100	4100
Relative Acid Density, m ⁻²	0.020	0.014	0
Wt% Carbon	17.2	13.2	9.80
Wt% Hydrogen	1.34	1.01	1.03

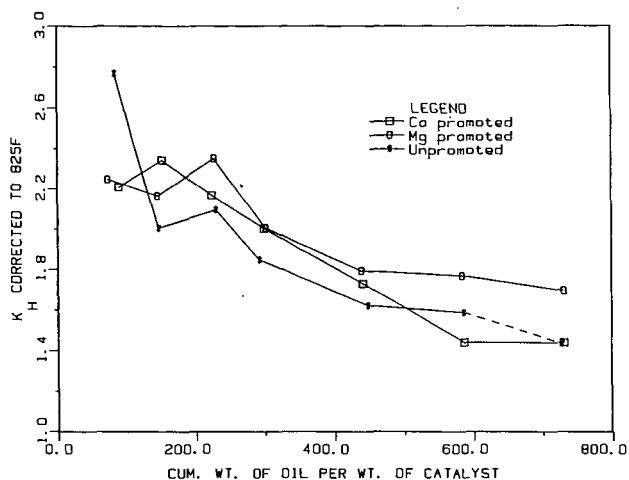


Figure 1. Deactivation curves for hydrogen uptake.

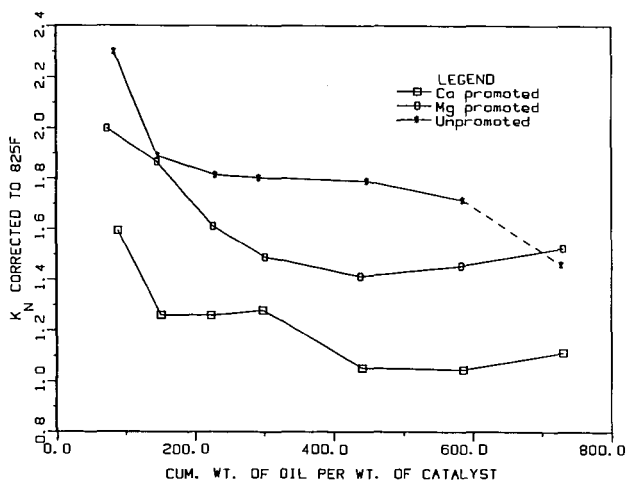


Figure 2. Deactivation curves for hydrodenitrogenation.

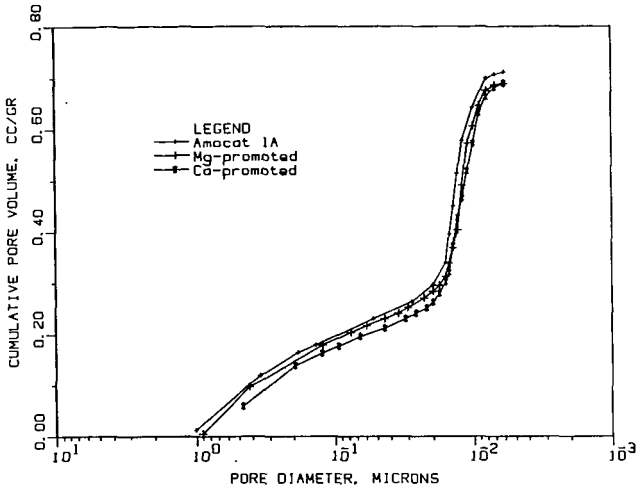


Figure 3. Cumulative pore size distributions for fresh catalysts.

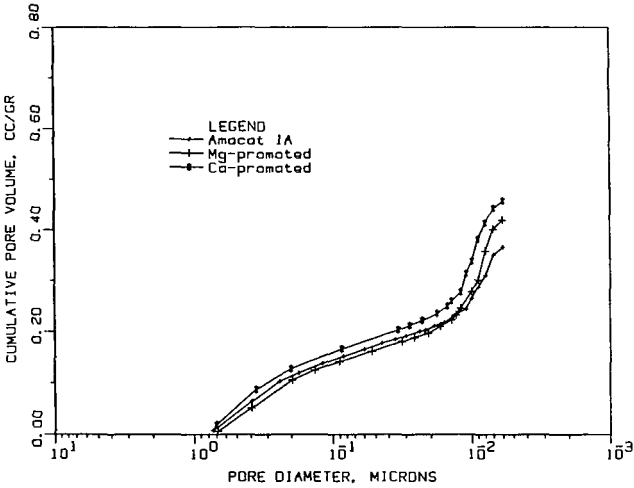


Figure 4. Cumulative pore size distributions for used catalysts.

REACTIONS OF LOW-RANK COALS WITH PHENOL

Edwin S. Olson, Ramesh K. Sharma, and John W. Diehl
University of North Dakota Energy and Mineral Research Center
Box 8213 University Station, Grand Forks, ND 58202

Although the acid-catalyzed reaction of coals with phenol has been investigated for some time, the nature of the products, especially with respect to molecular weights, remains unclear. Heredy investigated the reaction of coals with phenol and boron trifluoride at 100°C, with the objective of selectively degrading the coal macromolecules so that monomeric units could be isolated (1,2). The resulting product from a high volatile bituminous coal was claimed to be soluble to a large extent (61% in phenol). The definition of solubility, however, was simply that the phenol extract was filtered through Celite. The particle size was not measured nor was the absence of a Tyndall effect noted. Molecular weight measurements were carried out on various fractions by ebullioscopic measurements in benzene, benzene-methanol or pyridine. The molecular weight of the phenol soluble material was reported to be 1150 daltons using pyridine ebullioscopy. The chemistry of the reaction is believed to be a transalkylation of the methylene bridging group between two aromatic systems onto a molecule of the phenol. A substantial amount of phenol was chemically incorporated into the products resulting from the treatment.

Stating the same objective as Heredy, Ouchi (3) reacted coals with phenol and p-toluenesulfonic acid as the catalyst at 185°C. Pyridine Soxhlet extraction of the product from a Yubari coal (84.6% C, 6.1% H) resulted in high yields of material. Molecular weights as measured by pyridine boiling point elevation were less than 500.

These acid-catalyzed transalkylation reactions with phenol appear to fragment the macromolecular network of the coals to give extracts which the phenol solvent alone cannot give. The question of the colloidal nature of the extract has been addressed by Larsen (4,5) and Sharma (6). Since the pyridine extracts were found to plug 0.5 micron filters, a significant amount of the material in the extract was colloidal. Centrifugation at 120,000 x g for three hours precipitated the colloidal material. The actual amount of colloidal material present varied with the coal, but was as high as 80%. Gel permeation chromatography of the "truly soluble" material with VPO measurement of collected fractions gave a molecular weight (M_n) distribution which indicated that most of the material had a molecular weight greater than 6000. The early-eluting material appeared to be highly polydisperse, hence the VPO measurements were likely to be inaccurate and overly influenced by the smaller molecular weight material present (7). The conclusion of Larsen was that the soluble products were very large molecules and only limited depolymerization had occurred.

Although Givens's and Larsen's observations and arguments are persuasive, reports of alleged depolymerization continue to appear in the literature. Ouchi (8) has recently claimed to have depolymerized an Australian (Yallourn) brown coal, while advancing the argument that a low-rank coal should behave differently toward the phenolation reaction than the higher rank coals investigated by Larsen. Unfortunately Ouchi did not address the colloidal nature of the products and inappropriately used VPO and size exclusion chromatography for the determination of molecular weights. Thus, his number average molecular weight value of 1120 daltons for the pyridine extract of the product cannot be taken seriously.

The objective of our investigations was to determine the extent to which the cross linking methylene units between aromatic systems are broken down in low-rank coals (Wyodak and Yallourn) during the phenolation reaction with p-toluenesulfonic acid and compare the results with those from the reaction with a bituminous coal. In order to determine the extent of depolymerization, the weight average molecular weight of the products were examined using Rayleigh light scattering. Thus the range of molecular weights above 6000 which were not accessible in Larsen's experiments can be accurately measured with this technique.

EXPERIMENTAL

Phenolation: Wyodak coal (C, 70.9; H, 5.2; N, 0.92; S, 0.60; O, 22.3; maf basis), Yallourn brown coal (C, 69.4; H, 4.9; N, 0.6; S, 0.3; O, 24.8), and Pittsburgh #8 coal (C, 82.0; H, 5.5; N, 2.0; S, 6.8; O, 3.7) were demineralized by heating and stirring for three hours with 1N HCl, filtered and washed with water until free of acid, and dried in vacuum at 110°C for 24 hours. Phenol and p-toluenesulfonic acid monohydrate were heated with the coals according to Ouchi's procedure (8). The reaction products were worked up by distillation in vacuo until the volume was reduced to about one-third. The product was poured into a large excess of water, stirred for 2 hours and filtered. The residue was washed with water until free of acid and steam distilled to remove residual phenol. Last traces of phenol were removed by heating the residue in vacuo at 110°C until constant weight was obtained.

The dried products were extracted with pyridine using Soxhlet extraction under dry nitrogen until there was no color observable in the solvent. The pyridine extract was concentrated to about one third its volume and added to a large excess of 1 N hydrochloric acid and stirred for 3 hours. The precipitate was filtered, washed repeatedly with 1 N hydrochloric acid and then with water until free of acid, and dried in vacuo at 110°C to a constant weight.

Reductive acetylation: The pyridine-soluble phenolation products were reductively acetylated by the method used for humic acids (9). Molecular weight determinations of the reductively acetylated products in THF were carried out as previously described with a KMX-6 low angle laser light scattering photometer (9).

RESULTS

The coals dispersed in the refluxing phenol and acid catalyst (p-toluenesulfonic acid) giving high yields of products. The weight of the product was greater than the weight of starting coal, as described in earlier papers, due to chemical combination of the phenol with the coal. The phenol uptake was inversely proportional to the coal rank. The weight increase for Yallourn brown coal was 86%, whereas the Wyodak subbituminous coal exhibited a 65% weight increase, and for the Pittsburgh #8, a 47% increase was observed.

The infrared spectra of the phenolation products were obtained by photoacoustic spectroscopy and exhibit evidence for the incorporation of phenol; that is, strong O-H, aromatic ring and ether stretching absorptions. The ether stretching absorption could be due to the formation of ethers by a dehydration reaction occurring under these conditions; however, further work is needed to establish the nature of the incorporated phenol in these products.

A large fraction of the phenolated coals became dispersible in pyridine. The phenolation product from Yallourn brown coal was 97% dispersed, the Wyodak product was 87% dispersed and the Pittsburgh #8 products was 84% dispersed. As observed

by Larsen, attempted filtration of the pyridine dispersions using a 0.5 micron Millipore filter resulted in plugging. Thus these products in pyridine should be regarded as organosols or colloids as suggested by Larsen, not as true solutions.

The objective of this study was really to determine the size of the macromolecules making up this dispersion by conversion of the coal-derived material to a soluble form so that we could apply Rayleigh light scattering techniques, which are appropriate for large macromolecules and do not rely on calibration with small molecular species. This knowledge of the molecular weight of the entire fraction of product which is dispersible in pyridine is required for the determination of the extent of depolymerization of the coal in the phenolation reaction. The pyridine dispersed materials were only slightly soluble in THF, a solvent previously used effectively in low-angle laser light scattering photometry (LALLS), and were highly colored, making observation of the Rayleigh scattering difficult.

In order to accomplish the molecular weight determination with LALLS, the pyridine-dispersed material was converted to a less polar and less colored form by reductive acetylation, as we had previously done with the humic acids from lignites. The yields of reductively-acetylated derivatives were nearly quantitative for the phenolation products from all three coals. Photoacoustic infrared spectra of these derivatives indicated complete absence of the hydroxyl stretching absorption and the presence of strong ester carbonyl absorption.

The reductively-acetylated material dissolved completely in THF and the resulting solution could be filtered through a 0.2 micron filter and did not exhibit the intense flashing (Tyndall effect) of the laser light by dispersed particulate matter. The THF solutions of the reductively-acetylated phenolation products had a lower molar absorptivity than the original phenolation products and the Rayleigh scattering could be easily observed.

Rayleigh scattering factors were measured for the dilute THF solutions of the reductively acetylated phenolation products, and corrected by means of the Cabannes factors which were determined for each of the solutions used. These corrected Rayleigh factors gave a linear reciprocal scattering plot (Kc/R_0 vs. c) with an r^2 of 0.99 for the coal derivatives. The weight average molecular weight of the reductively acetylated Wyodak product was 1.67 million daltons, as determined from the intercept of the reciprocal plot. The slope was positive ($A_2 = 3.0 \times 10^{-3}$). The reductively acetylated phenolation product from the Yallourn brown coal had a molecular weight of 2.26 million daltons ($A_2 = 1.3 \times 10^{-3}$). The weight average molecular weight of the reductively acetylated phenolation product from the Pittsburgh #8 was 2.23 million with an A_2 of 4.6×10^{-3} .

DISCUSSION

Molecular weight determinations of derivatives of the phenolation products from both high and low rank coals gave high values in the light scattering determination. These reductively acetylated derivatives of the phenolation products gave true solutions in THF as defined by their ability to pass a 0.2 micron filter and the lack of a Tyndall effect in the laser beam. Furthermore the phenolation products were completely converted to this soluble form by the reductive acetylation, so the entire sample is being examined in the light scattering experiment. This contrasts with the Larsen experiment which separated the dispersed material out by ultracentrifugation and examined the soluble material by VPO, whose limitation in determining the high molecular weight material was discussed by Larsen. Ouchi (8) defined solubility as the lack of a

residue; this does not distinguish a true solution from a colloidal dispersion, and his molecular weight measurements are subject to the same limitations as Larsen's.

Because of the high molecular weights obtained, we conclude that both the low and high rank coals were not extensively depolymerized in the phenolation reaction. The reaction serves to cleave cross-linking bonds to create some mixture of soluble and dispersed particles, probably in the submicron range as in the dispersion obtained by treating Wyodak coal with sodium hydroxide. Thus cleavage of the guaiacyl ether linkages and possibly some activated methylene bridges will accomplish this limited digestion of the coal structure which does not amount to depolymerization or solubilization. Since the coal may not consist of repeating polymer units, perhaps a better generic term for the phenolation reaction is limited digestion or degradation.

The differences in the weight average molecular weights of the three coals may not be significant with respect to the coal structures, since extensive rearrangements of bonds and chemical adduction of phenol occurred in addition to cleavage of labile benzyl ether groups and methylene bridges between the aromatic systems. This complex reaction does not really allow us to count branch points or cross-links that are broken. One must proceed to other synoptic reactions to elucidate the types of cross links or branch points in these coals.

The differences in the second virial coefficient (A_2) obtained from the slope of the reciprocal Rayleigh plot for each coal phenolation product can be attributed to the differences in the Cabannes factors for the coal derivatives. The slope of a Cabannes factor vs. concentration plot is proportional to the coal rank; that is, the Cabannes factors increase more with concentration for the Pittsburgh #8 derivative than they do for the Wyodak, which in turn increase more than the Yallourn derivative. Thus, at higher concentrations the Rayleigh factors are more corrected and therefore proportionately smaller for the Pittsburgh #8 product, and the slope of the reciprocal plot is therefore greater. The high Cabannes factors are probably due to the presence of larger polynuclear ring systems in the product from the bituminous coal which result in greater anisotropic scattering.

REFERENCES

1. Heredy, L.A. and Neuworth, M.B. *Fuel* **1962**, 41, 221-31.
2. Heredy, L.A., Kostyo, A.E. and Neuworth, M.B. *Fuel* **1965**, 44 125-33.
3. Ouchi, K., Imuta, K. and Yamashita, Y. *Fuel* **1965**, 44, 29-38.
4. Larsen, J.W. and Lee, D. *Fuel* **1983**, 62, 918-23.
5. Larsen, J.W. and Choudhury, P. *J.Org. Chem.* **1979**, 2856-9.
6. Sharma, D.K. *Fuel*, **1988**, 67, 186-190.
7. Given, P.H. in *Coal Science*, Vol 3, ed by. Gorbaty, M.L., Larsen, J.W. and Wender, I. Academic Press, Orlando Florida, **1984**, 63-252.
8. Ouchi, K., Yokoyama, Y. Katoh, T. and Itoh, H. *Fuel* **1987**, 66, 1115-7.
9. Olson, E.S., Diehl, J.W. and Froehlich, M.L. *Fuel*, **1987**, 66, 992-5.

ACKNOWLEDGEMENTS

This research was supported by Contract No. DOE-FC21-86MC10637 from the U.S. Department of Energy. References herein to any specific commercial product by trade name or manufacturer does not necessarily constitute or imply its endorsement, recommendation, or favoring by the United States Government or any agency thereof.

LIQUEFACTION KINETICS INFLUENCED BY THE AMOUNT OF DONORS AND HYDROGEN PRESSURE

Isao Mochida, Ryuji Sakata and Kinya Sakanishi

Institute of Advanced Material Study, Kyushu University
Kasuga, Fukuoka 816, JAPAN

Abstract

Influences of donor and solvent amounts, hydrogen pressure and coal deashing on the product slate as well as rates of liquid production were studied in the hydrogen donating liquefaction of an Australian brown and a Japanese subbituminous coal using tetrahydrofluoranthene(4HFL) as a donor at 450 °C. An adequate amount of donor at the fixed solvent/coal ratio provided the best yield of oil plus asphaltene. The best amount varied, depending upon the coal and liquefaction conditions. Less amount of donor at the decreasing solvent/coal ratio gave much rapid decrease of the liquid yield. Hydrogen pressure around 40 kg/cm² certainly participated favorable in the liquefaction, especially pronounced at the low donor/coal ratio as observed with pyrolyses of model substrates. Deashing to remove dominant calcium ions was generally favorable to increase the liquid yield, however some coals at the low donor/coal ratio suffered some retrogressive reaction. Such results indicate multi-fold roles of solvent and plural mechanisms of coal-macromolecular depolymerization. Different reactivities of the brown coals of different lots are briefly discussed.

Introduction

Coal liquefaction process has been investigated for quite a time by examining various ideas to improve its efficiency[1-5]. Nevertheless, the process is still far away from satisfaction about the cost of product oil. Better yield of distillate oil on the bases of reactor volume, hydrogen consumption and very severe reaction conditions as well as fed coal is desperately wanted.

The macromolecular mixtures of solid coal are digested and/or depolymerized into distillable species through solvent extraction as well as pyrolytic, hydrogen-transferring and catalytic bond dissociations[6]. Poor interaction between the solid coal grain and solid catalyst, unless the fine catalysts are highly dispersed on the coal with rather extensive cost[7,8], suggests that the first step of coal conversion to obtain liquid easily accessible to the solid catalyst is dominated by the reactions among coal molecules, the solvent and gaseous atmosphere. It has been pointed that hydrogen donor solvents derived from 3-4 ring aromatic hydrocarbons are very powerful to liquefy the coal through their proper hydrogen-donating and dissolving abilities against coal molecules[9,10]. Thus, most appropriate use of donor solvent is an approach to find better scheme of coal liquefaction. The minimum amount of donor solvent to assure the maximum yield of oil and asphaltene may increase the efficiency of hydrogen consumption and the reactor volume, and moderates the conditions[11].

In addition to a classical mechanism of stabilization of thermally produced radicals from coal molecules, it has been recognized that donor molecules directly interact with the coal macromolecules to activate via hydrogenation and hydrocracking according to the reactivity of coal molecules as well as the donor, and reaction conditions[6, 11-13]. Such bimolecular mechanisms suggest the importance of the solvent quality and quantity under reaction conditions matched to the both materials for the liquefaction efficiency.

The hydrogen transferring mechanism may also suggest the importance of hydrogen pressure when the molecular hydrogen is activated by the radical species derived from donors and coal molecules. Vernon has pointed out the participation of molecular hydrogen in the pyrolysis of dibenzyl with the existence of tetralin[14]. The radical initiator is also suggested important to initiate the chain reactions of coal and solvent molecules according to the bimolecular mechanism.

In the present report, we are going to describe the influences of donor concentration in the solvent, donor amount and hydrogen pressure in the liquefaction of an Australian brown and a Japanese subbituminous coal on the yield of oil and asphaltene which are both easily converted into distillable clean oil by the successive catalytic hydrotreating process. Influences of such reaction variables were also studied with model substrates. The reactivity of the coals is very sensitive to the coagulation of their macromolecules and maceral composition[15]. Hence, the influence of deashing on the hydrogen-donating liquefaction and microscopic coal characterization were investigated[16,17]. Morwell brown coal is found to exhibit very different reactivity according to the rot, yielding variable amounts of asphaltene and residue.

Experimental

Materials

The ultimate analyses of the sample coals are summarized in Table 1. The liquefaction(hydrogen donating) solvent was tetrahydrofluoranthene(4HFL) prepared by catalytic hydrogenation of commercial fluoranthene(FL) using a commercial Ni-Mo catalyst in an autoclave at 250 °C, and quantified by g.c. and purified by recrystallization.

Pretreatment of coal

After the coal was ground to pass 60 US mesh screen, it was kept in refluxing aq. HCl(1N) and methanol(10 vol%) under nitrogen flow to remove divalent cations such as Ca^{2+} , Mg^{2+} and Fe^{2+} . After the pretreatment, the coal was filtered, washed with water, and dried in vacuum at room temperature.

Liquefaction procedure

Liquefaction was carried out in a tube bomb(20 ml volume). The coal(2.0 g), which had been ground to less than 60 US mesh and dried at 100 °C under vacuum, and the solvent(2.0, 3.0, 4.0 or 6.0 g), after their thorough mixing, were transferred to the bomb. The bomb was then pressurized with nitrogen or hydrogen gas to 1.0 or 2.0 MPa at room temperature and immersed into a molten tin bath at the prescribed temperature, and agitated axially. The

products remaining in the bomb were extracted with THF, benzene and n-hexane. The hexane soluble(HS), hexane insoluble-benzene soluble(HI-BS), benzene insoluble-THF soluble(BI-THFS) and THF insoluble(THFI) substances were defined as oil, asphaltene, preasphaltene and residue, respectively. Gas yield was calculated by the difference between the initial and recovered weight.

Results

Influences of 4HFL concentration in the fixed solvent/coal ratio of 3/1

Influences of 4HFL concentration on the product slate in the liquefaction of Morwell-I coal at 450 °C under nitrogen were shown in Table 2. The pure 4HFL solvent liquefied the coal very rapidly, whereas a longer reaction time increased markedly the gaseous product as well as the sum yield of oil and asphaltene. Although decreasing 4HFL in the solvent reduced the rates of liquefaction as for both gas and liquefied products, the 4HFL contents of 3/4 and 2/4 in the solvent provided more favorable product slates(high yield(>80%) of oil plus asphaltene and low yields of preasphaltene and gaseous products).

Influence of 4HFL(solvent)/coal ratio

Figure 1 illustrates the oil and asphaltene yields from Morwell-I coal at 450 °C under nitrogen for the respective best residence times using variable solvent(pure 4HFL)/coal ratios. The oil and asphaltene yields were only slightly influenced by the ratios to give around 60 and 10 % yields, respectively, when the ratio ranged from 3/1 to 1.5/1, although a trend of slight decreases of both yields may be observable with decreasing the ratios. It is of value to point that the yields of preasphaltene and residue were always less than 5 %.

A drastic decrease of oil and hence the sum yield took place when the solvent/coal ratio was reduced to 1/1, while the significant increase of asphaltene with some increases of preasphaltene, residue and gas were observed at the best residence time of 10 min. The large increases of the latter three products were observed by a longer residence time at this ratio, resulting in a further marked decreases of objective products.

Influence of hydrogen pressure on coal liquefaction

Figure 2 illustrates the liquefaction yields from Morwell-I and -II coals at 450 °C and 1.5/1(4HFL/coal ratio) under nitrogen or hydrogen pressure. The conversion of asphaltene into oil was accelerated by hydrogen pressure, especially under higher pressure, where the interaction of molecular hydrogen with donor and/or coal molecules was enhanced. It should be noted that the highest oil yield from Morwell-II was achieved under higher hydrogen pressure at the reaction time of 20 min, when most of 4HFL was consumed.

Morwell-I was certainly more reactive than Morwell-II, giving higher oil yield regardless of atmosphere, although the sum yields of oil plus asphaltene were much the same. Lower reactivity of the asphaltene from Morwell-II coal is suggested.

Figure 3 illustrates the liquefaction yields from Taiheiyu

coal at 450 °C and 1.5/1(4HFL/coal ratio) under nitrogen or hydrogen pressure. Higher oil and asphaltene yield of 80 % was achieved from Taiheiyō coal than Morwell coals, reflecting much less gas yield. Pressure effect of hydrogen was marked at the reaction of 10 min, converting asphaltene into oil.

Influence of hydrogen pressure on the reaction of model compounds

Table 3 summarizes the influence of hydrogen pressure on the conversions of dibenzyl (DB) at 450 °C, 30 min and variable donor(4HFL)/substrate ratios. The conversions of DB were always higher under hydrogen pressure with less 4HFL consumption than those under nitrogen pressure. Such a tendency increases with decreasing 4HFL amount. It should be noted that hydrogen pressure enhanced the DB conversion even with a non-donor solvent.

Influence of deashing at low 4HFL/coal ratio

Figure 4 illustrates the liquefaction yields from the deashed Morwell-I and Taiheiyō coals at 450 °C-10 min and 1.5/1 (4HFL/coal ratio). The oil yield from Morwell-I coal increased to 65 % with decreasing gas, preasphaltene and residue yields. In contrast, the deashing pretreatment exhibited unfavorable effect on the liquefaction of Taiheiyō coal at low 4HFL/coal ratio, increasing the yields of gas and heavy fractions (preasphaltene and residue) with slight increase of oil yield.

Discussion

The present study revealed that the concentration and amount of donor, and hydrogen pressure are very influential on the yield of oil plus asphaltene in the hydrogen-transferring liquefaction. The volume of solvent defines the volume of reactor and its reduction can increase the productivity of the liquefaction.

The roles of solvent have been recognized multi-fold. The hydrogen donation performs the following reactions in coal liquefaction;

1. Stabilization of radicals derived thermally from the coal molecules.
2. Hydrogenation of reactive sites of coal molecules to loosen the bonds for their dissociation.
3. Cleavage of bonds in coal molecules by substitution with hydrogen atoms.

The contributions of these schemes are strongly dependent upon the reactivities of coal and solvent, and hence reaction conditions[11].

According to scheme 1, the coal liquefaction requires donor solvent over a certain quantity. Its excess amount stays unparticipated. Less amount fails to prevent the retrogressive reaction. In contrast, according to the schemes 2 and 3, the donor directly reacts with the coal molecules. Hence, its amount kinetically influences the liquefaction, more amount accelerating the rate of liquefaction. Such schemes certainly depolymerize the coal molecules into oil and asphaltene directly or indirectly through preasphaltene, but also accelerate the gas

formation through the hydrocracking of alkyl side-chains and naphthene rings. Thus, the optimum amount of donor exists to produce the maximum yield of oil plus asphaltene. The optimum amount may vary due to the coal, donor and reaction conditions which are all influential upon the participation extent of the schemes. The present study certainly indicates the optimum amount of the donor for the maximum yield. Taiheiy coal required more donor for the production of oil than Morwell-I coal. Larger extent of depolymerization is required with higher rank coal.

The solvent is expected to play roles of dissolving and dispersing agents against coal-derived molecules and donor. Their intimate contact and radical dispersion which are strongly influential on the liquefaction as well as retrogressive reactions are assured by the solvent. Hence, the amount of non-donor solvent participates the liquefaction scheme. The difference between the same amounts of the donor in the fixed amount of aromatic solvent and alone without additional solvent is thus definite, although smaller amount of solvent may be favorable when the product slate is acceptable.

The optimum amount of donor can be reduced under the hydrogen pressure if the hydrogen is transferred to the donor, coal molecules or radicals derived from donor and coal molecules. Vernon has indicated the participation of molecular hydrogens in the pyrolysis[14]. The present results indicate that it is possible with certain types of model molecules and coals. Such a participation of molecular hydrogen under some pressures may reduce the difficulty of catalytic hydrotreating process of the second stage, where the hydrocracking for more oil and hydrogenation for the solvent regeneration are both expected. The first stage requires some pressure in any case to maintain the solvent in the liquid phase and coal-derived molecules.

The deashing for some coals has been reported to increase the yield of liquid product in the hydrogen transferring liquefaction with sufficient amount of solvent through enhanced fusibility via liberation of coal macromolecules[11]. It is not always the case when less amount of solvent is applied. Larger amount of donor may be necessary at a time to match the enhanced reactivity of deashed coal. Morwell-II coal exhibited certainly less reactivity and influence of deashing. The marked difference is found in the conversion of asphaltene to oil. More unreactive asphaltene is presented in the product from Morwell-II coal. Detail structure of asphaltene is an objective of future study. Taiheiy coal exhibited little influence of deashing, especially with smaller amount of donor solvent.

The combination of deashing pretreatment and hydrogen pressure is of value for study to obtain higher yield of oil and asphaltene by reducing the preasphaltene and residue, since the deashing pretreatment is expected to simplify the liquefaction steps and solve the operational problems[18].

The amount of solvent can be hopefully reduced to the level which is necessary for coal slurry transportation, which requires a significant amount of liquid at room temperature. Such a vehicle solvent is not needed any more when a certain extent of liquefaction has proceeded to supply the solvent fraction. The

removal of such lightest portion in the solvent can economize the reactor volume.

References

1. Taunton, J.W., Trachte, K.L. and Williams, R.D., *Fuel*, 1981, 60, 788.
2. Weber, W. and Stewart, N., *EPRI Journal*, 1987, 12(1), 40.
3. Strobel, B.O. and Friedrich, F., *Proc. Int. Conf. Coal Science*, 1985, Sydney, p.7.
4. Okuma, O., Yanai, S., Mae, K., Saito, K. and Nakako, Y., *Proc. Int. Conf. Coal Science*, 1987, Maastricht, p.307.
5. Whitehurst, D.D., *Fuel Process. Technol.*, 1986, 12, 299.
6. Kamiya, Y., Ohta, H., Fukushima, A., Aizawa, M. and Mizuki, T., *Proc. Int. Conf. Coal Science*, 1983, Pittsburgh, p.195.
7. Weller, S. and Pelipetz, M.G., *I & EC Proc. Dev.*, 1951, 43(5), 1243.
8. Given, P.H. and Derbyshire, F.J., *DOE-PC-60811-7,8*, 1985, p.28.
9. Mochida, I., Otani, K., Korai, Y. and Fujitsu, H., *Chem. Lett.*, 1983, 1025.
10. Mochida, I., Yufu, A., Sakanishi, K., Korai, Y. and Shimohara, T., *J. Fuel Soc. Jpn.*, 1986, 65, 1020.
11. Mochida, I., Yufu, A., Sakanishi, K. and Korai, Y., *Fuel*, 1988, 67, 114.
12. McMillen, D.F., Ogier, W.C., Chang, S., Fleming, R.H. and Malhotra, R., *Proc. Int. Conf. Coal Science*, 1983, Pittsburgh, p.199.
13. Kamiya, Y., Futamura, S., Mizuki, T., Kajioaka, M. and Koshi, K., *Fuel Process. Technol.*, 1986, 14, 79.
14. Vernon, L.W., *Fuel*, 1980, 59, 102.
15. Mochida, I., Kishino, M., Sakanishi, K., Korai, Y. and Takahashi, R., *Energy & Fuels*, 1987, 1, 343.
16. Mochida, I., Shimohara, T., Korai, Y. and Fujitsu, H., *Fuel*, 1984, 63, 847.
17. Shimohara, T. and Mochida, I., *J. Fuel Soc. Jpn.*, 1987, 66, 134.
18. Mochida, I., Sakata, R. and Sakanishi, K., *Fuel* in press.

Table 1

Elemental analyses of sample coals

Coal name	wt% (daf)				Ash (wt%)
	C	H	N	(O+S)	
Morwell-I	60.5	5.5	0.5	33.4	2.4
Deashed-I	61.2	5.4	0.5	32.9	1.1
Morwell-II	63.7	4.9	0.6	30.8	2.3
Taiheiyo	73.5	6.3	1.2	19.0	17.3
Deashed coal	73.9	6.3	1.3	18.6	10.9

Table 2

Influences of donor(4HFL) concentration in the solvent¹⁾
on the liquefaction yields from Morwell-I coal at 450 °C

4HFL (%)	Reaction time(min)	Yield (wt%)				
		Gas	Oil	Asph.	Preasph.	Residue
100	5	19	56	13	12	0
	20	20	62	14	4	0
	30	28	53	14	5	0
75	5	13	51	15	15	6
	20	14	68	14	4	0
	30	13	68	14	5	0
50	5	6	50	23	14	7
	10	10	56	19	6	9
	30	9	60	22	6	3
25	5	8	44	21	12	15
	10	8	47	18	14	13
	30	10	48	17	7	18

1) Solvent/coal ratio = 3/1(fixed)
Solvent composition : 4HFL/(4HFL+FL)
(FL: fluoranthene, 4HFL: tetrahydro-FL)

Table 3

Influence of hydrogen pressure on dibenzyl(DB)
conversion at 450 °C-30 min

Atmosphere ¹⁾ (kg/cm ²)	Reactants (mmol)			Conversion(%)	
	DB	FL	4HFL	DB	4HFL
N ₂ (10)	2.75	14.9	0	25	-
H ₂ (20)	2.75	14.9	0	36	-
N ₂ (10)	2.75	14.6	0.24	25	100
H ₂ (20)	2.75	14.6	0.24	33	76
N ₂ (10)	2.75	14.4	0.49	32	85
H ₂ (20)	2.75	14.4	0.49	38	58

1) (): initial pressure

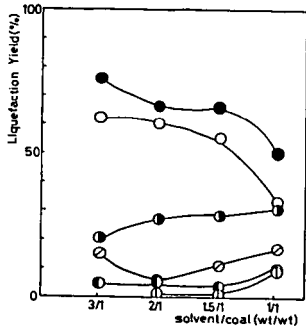


Fig. 1
Influence of solvent (4HPL)/coal ratio
on the liquefaction yields at 450°C

●: (oil+asphaltene), ○: oil, ●: gas, ○: asphaltene,
●: preasphaltene, ○: residue

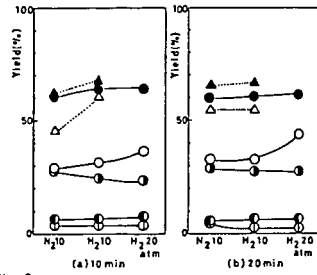


Fig. 2
Effects of hydrogen pressure on the liquefaction of
Morwell-I and -II coals at 450°C, 1.5/1 (solvent/coal)

Morwell-I ▲: O+A, △: O
Morwell-II ●: O+A, ○: O, ●: G, ○: P, ○: R

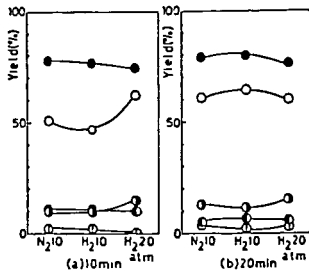


Fig. 3
Effect of hydrogen pressure on the
liquefaction of Taiheiyu coal at 450°C
and 1.5/1 (solvent/coal)

●: (O+A), ○: O, ●: G, ○: P, ○: R

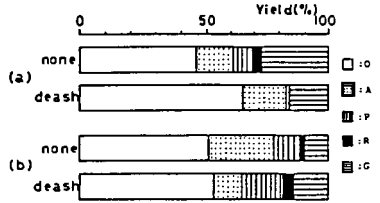


Fig. 4
Effect of deashing on the liquefaction at
450°C-10 min (solvent/coal=1.5/1, solvent:4HPL)

(a) Morwell-I (b) Taiheiyu

CATALYTIC TWO-STAGE HYDROCRACKING OF ARABIAN VACUUM RESIDUE
AT A HIGHER CONVERSION LEVEL WITHOUT SLUDGE FORMATION

Isao Mochida, Xing-zhe Zhao and Kinya Sakanishi

Institute of Advanced Material Study,
Kyushu University,
Kasuga, Fukuoka 816, JAPAN

ABSTRACT

Catalytic two-stage hydrocracking of Arabian vacuum residue was studied using commercial Ni-Mo catalysts in the autoclave to achieve a higher conversion above 50 % into 540 °C distillate without producing sludge in the product. The hydrogenation at 390 °C of the first stage was found very effective to suppress the sludge formation in the second stage of higher temperature, 430 °C, where the cracking to produce the distillate dominantly proceeded. The catalyst for the residues(KFR-10) was suitable for these purposes, while KF-842 catalyst, which exhibited excellent performance against coal liquid residues, failed to suppress the sludge formation. The shorter contact time of the second stage at a relatively higher temperature appears favorable to increase the conversion without producing the sludge. The mechanism of sludge formation in the hydrocracking process is rather comprehensibly discussed based on the previous and present results.

INTRODUCTION

Demand for clean distillate from the bottom of the barrel leads to severe hydrocracking of petroleum residues at higher temperatures[1]. The severe conditions cause problems of coke deposition on the catalyst and sludge formation in the product oil[2]. Such trouble makers of both carbonaceous materials, of which formation may be intimately related, shorten the life of the catalyst, plug transfer line and deteriorate the quality of the products[3].

Empirically, the dry sludge is believed to be produced when the conversion to the distillate is beyond a certain level(ca. 50 %) regardless of the catalyst and feedstocks[1]. Its structure, properties and formation mechanism are not fully understood yet[4].

In a previous study[5], dry sludge produced in a hydrocracked oil was analyzed chemically, and its solubility, fusibility and reactivity were studied to propose a mechanism of sludge formation in the hydrocracking process.

In the present study, catalytic two-stage hydrocracking was proposed to achieve a higher conversion into 540 °C distillate above 50 % with a minimum amount of dry sludge in the product. The idea is based on the mechanism previously proposed: the deep hydrogenation of aromatic fraction in the residue by the first stage of lower temperature may accelerate the cracking and solubility of the heaviest aromatic portion in the second stage of higher temperature, where major hydrocracking takes place.

EXPERIMENTAL

Materials

A vacuum residue (b.p. > 550 °C) of Arabian-light oil (10 g), of which properties were shown in Table 1, was hydrocracked by the single- and two-stage reactions under hydrogen pressure (15 MPa), using one of the Ni-Mo catalysts (1 g) in a batch autoclave of 100 ml capacity. The catalysts, of which properties were summarized in Table 2, were presulfided under 5 % H₂S/H₂ flow at 360 °C for 6 h.

Catalytic hydrocracking

The standard conditions were 390 °C-4 h, 420 °C-4 h for the single-stage reaction, and 390 °C-3 h (first stage) and 420 - 440 °C-1 h (second stage) for the two-stage reaction, respectively. No solvent was used except for the two-stage reaction of 390 °C-3 h and 440 °C-1 h; 10 wt% of 1-methylnaphthalene was added before the second stage for comparison with no-solvent reaction under the same conditions. After removal of the catalyst, the product was observed under a optical microscope to measure the amount of sludge in the product. The product was distilled under vacuum (5 mmHg) at 340 °C to obtain the distillate (540 °C fraction) yield.

RESULTS

Single-stage hydrocracking

Table 3 summarizes the results of single-stage hydrocracking using two Ni-Mo catalysts. The reaction at 390 °C provided the yield of 540 °C distillate below 50 %. No sludge was found with both catalysts at this temperature as shown in Figure 1a, where bluish spots of probably long-chain paraffins were observable, indicating insufficient extent of cracking. It is noted that the amount of asphaltene was unchanged after the hydrocracking at 390 °C.

Higher reaction temperature of 420 °C increased the distillate yield significantly above 70 %. However, a large amount of sludges was found with both catalysts as shown in Figures 1b and 1c. The appearances of the sludges were somewhat different with the catalysts; those with KF-842 consisted of black and rigid spheres and very fine brown oily-droplets, whereas those with KFR-10 were larger droplets which were brown and diffused. A significant amount of asphaltene was certainly converted under the conditions. It should be noted that KF-842 produced a significant amount of gaseous products at 420 °C. Thus, the catalysts, KF-842 for the distillate of coal liquid and KFR-10 for the petroleum straight residue behaved very differently against the petroleum residue.

Two-stage hydrocracking

Results of two-stage hydrocracking are summarized in Table 4. The two-stage hydrocracking using KF-842 at 390 °C-3 h and 420 °C-1 h still produced a very large amount of sludge in the product oil as shown in Figure 2a, although the distillate yield was still high. KFR-10 catalyst under the same conditions produced negligible amount of sludge as shown in Figure 2b at the distillate yield as high as 66 %. Longer reaction time of 3 h in

the second stage at 420°C increased slightly both sludge and the distillate yield(70 %).

Higher temperature of 440 °C for 1 h in the second stage increased the yield to 81 %, some sludgebeing produced as shown in Figure 2c.

Addition of 10 % 1-methylnaphthalene to the second stage at 440 °C was very effective to suppress the sludge formation (Figure 2d). The distillate yield was as high as 80 %.

Storage stability of hydrocracked product

The hydrocracked product obtained by the single stage of 420 °C-4 h using KF-842 catalyst was rather unstable. The product carried a small amount of sludge just after the reaction as shown in Figure 1b, however a much larger amount was found 150 days later in the same product(Figure 3). Insufficient hydrogenation or dehydrogenation because of high reaction temperature may leave unsaturated sites reactive for the air-oxidation. In contrast, no deterioration was observed with the products obtained by using KFR-10 catalyst under the same conditions and the two-stage reactions with either catalyst, although a large amount of sludge has been produced right after the two-stage hydrocracking with KF-842 catalyst.

DISCUSSIONS

Structure and formation mechanism of dry sludge in the hydro-cracking

The hexane-soluble fraction (HS) in the hydrocracked product consists of essentially of long-chain paraffins and long alkyl-benzenes. In contrast, the insoluble substances in the sludge are fairly aromatic with much less and shorter alkyl groups and rather polar, carrying a considerable amount of heteroatoms. The solubility decreased with increasing aromaticity and polarity, the molecular weight varying rather slightly among the fractions. Such contrast structural characteristics of HS and HI fractions may not allow their mutual miscibility, precipitating or segregating the insoluble substances from the HS matrix at room temperature.

In spite of low solubilities of the sludge components at room temperature, they melt or are dissolved in the light component at elevated temperatures above 80 °C. Thus, the sludge may disappear at elevated temperatures such as the reaction temperature, although its limited solubility in the matrix may enhance its adsorption or longer residence on the catalyst surface, leading to the severe catalyst deactivation.

Based on the analyses of the sludge, a mechanism of its formation is proposed[5]. Hydrocracking at higher temperatures to achieve a higher conversion can crack deeply the paraffinic and and alkyl aromatic hydrocarbons at a high level, however highly-condensed aromatic hydrocarbons are not fully hydrogenated at higher temperatures for their cracking because dehydrogenation is so rapid under the conditions, staying unchanged in their ring structure to be insoluble in the paraffin-rich matrix, especially at lower lower temperatures. Elimination of alkyl side-chains from aromatic hydrocarbons and severe cracking of light aromatic

hydrocarbons enhance the phase separation to lead to the sludge formation.

Such a mechanism originating from the phase separation of the fractions due to their mismatched compatibility appears to be common to bottom and shot cokes formation in the coking[6,7], and least cracking reactivity of paraffin[8-10] and sludge formation due to the slight oxidation in the coal liquid.

Effects of two-stage hydrocracking

The two-stage hydrocracking which consists of sufficient hydrogenation at a lower temperature and extensive cracking of the hydrogenated product at a higher temperature was found to allow a high yield of distillate over 60 % with a minimum amount of sludge droplets in the product at room temperature. As discussed in the mechanism section, the sludge was unhydrogenated aromatics due to high reaction temperature, which are not miscible with the paraffin-dominant matrix. The first stage of low temperature sufficiently hydrogenates the aromatic parts of the asphaltene to be easily cracked and/or to stay miscible with the matrix, increasing the yield of distillate without producing sludge in the second stage. Aromatic solvent of moderate size such as 1-methylnaphthalene is very effective in the second stage of the short reaction time to suppress the sludge by dissolving the asphaltene.

The selection of conditions for the second stage is very important because extensive cracking should take place before the dehydrogenation. Longer reaction time at higher temperature tends to produce more sludge because uncracked remaining asphaltene in the product becomes sludge. The rapid heating to the temperature of the second stage may be favorable.

The selection of the catalyst is also important. The catalyst should have strong hydrogenation activity against the asphaltene of large molecules. The large pores of the support can get access to such molecules. The catalyst of the second stage should have high cracking activity against the hydrogenated asphaltene without dehydrogenation.

Such a set of the catalysts should be designed separately to exhibit the optimum performances of the respective objectives at the respective stages.

Finally, the stability of hydrocracked product is concerned. The post-hydrogenation may be effective at a lower temperature, where sufficient hydrogenation of the whole product can proceed. Sludge can be completely removed by the steps as described in a previous paper[5]. Short reaction time of the second stage can maintain the hydrogenation level high which is achieved in the first stage, proving the stability of the product.

References

1. Saito, K. and Shimizu, S., PETROTECH, 1985, 8(1), 54.
2. Symoniak, M.F. and Frost, A.C., Oil & Gas Journal, 1971, March 15, 76.
3. McKenna, W.L., Owen, G.H. and Mettick, G.R., Oil & Gas journal, 1964, 52(20), 106.

4. Haensel, V. and Addison, G.E., Advances in Catalytic Reforming, 7th World Petroleum Congress, 1967, 4, 113.
5. Mochida, I., Zhao, X.Z. and Sakanishi, K., Ind. Eng. Chem. Res. in submission.
6. Mochida, I., Furuno, T., Korai, Y. and Fujitsu, H., Oil & Gas Journal, 1986, 3, 51.
7. Eser, S., Jenkins, R.G. and Derbyshire, F.J., Carbon, 1986, 24, 77.
8. Mochida, I., Sakanishi, K., Korai, Y. and Fujitsu, H., Proc. Int. Conf. Coal Science, 1985, Sydney, p.63.
9. Sakanishi, K., Zhao, X.Z., Fujitsu, H. and Mochida, I., Fuel Process. Technol., 1988, 18, 71.
10. Inoue, Y., Kawamoto, K., Mitarai, Y. and Takami, Y., Proc. Int. Conf. Coal Science, 1985, Sydney, p.193.

Table 1

Solubility¹⁾ of Arabian-light vacuum residue (ALVR)

	wt%		
	HS	HI-BS	BI
ALVR	91	9	0

- 1) HS: hexane soluble
 HI-BS: hexane insoluble-benzene insoluble
 BI: benzene insoluble

Table 2

Some properties of the catalysts¹⁾

Catalyst name	Support	Metal (wt%)		Surface area (m ² /g)	Pore volume (ml/g)	Mean pore diameter (Å)
		NiO	MoO ₃			
KF-842	alumina	3.1	15	273	0.52	< 100
KFR-10	silica-alumina	1.0	5.0	147	0.71	168

- 1) Supplier: Nippon Ketjen Co.

Table 3

Catalytic performances in the single-stage hydrocracking of ALVR

Catalyst	Conditions (°C- h)	Recovery (wt%)	D.Y. ¹⁾ (%)	A.S. ²⁾
KF-842	390-4	95	39	tr.
	420-4	75	72	much
KFR-10	390-4	98	41	tr.
	420-4	91	74	much

1) D.Y.: 540 °C⁻ distillate yield

2) A.S.: Amount of sludge, tr.: trace

Table 4

Catalytic performances in the two-stage hydrocracking of ALVR

Catalyst	Conditions (°C- h)	Recovery (wt%)	D.Y. ¹⁾ (%)	A.S. ²⁾
KF-842	390-3			
	420-1	94	63	much
KFR-10	390-3			
	420-1	94	66	v.tr.
	390-3			
	420-3	94	70	tr.
	390-3			
	440-1	93	81	some
	390-3			
	440-1 ³⁾	95	81	v.tr.

1) and 2): See Table 3., v.tr.: very trace

3) 10 wt% of 1-methylnaphthalene was added prior to the second stage.

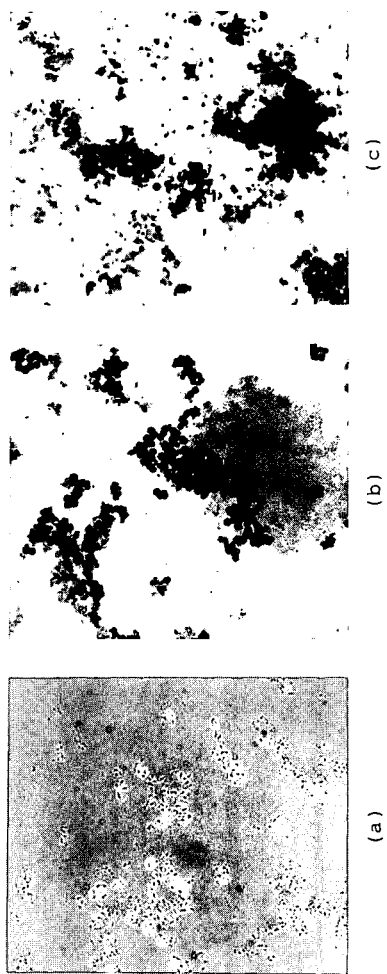


Figure 1 Microphotographs of the product oil in the single-stage reactions

- (a) 390 °C-4 h (either catalyst)
- (b) 420 °C-4 h (KF-842 catalyst)
- (c) 420 °C-4 h (KFR-10 catalyst)

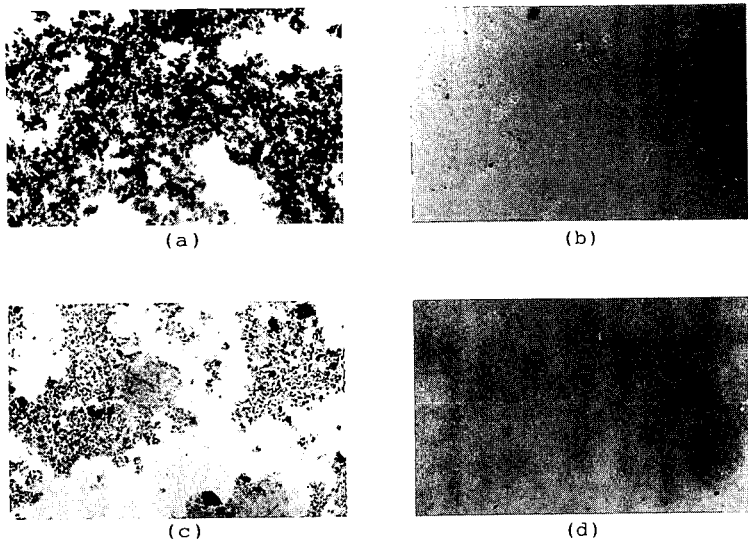


Figure 2 Microphotographs of the product oil in the two-stage reaction
 (a) 390 °C-3 h and 420 °C-1 h (KF-842 catalyst)
 (b) 390 °C-3 h and 420 °C-1 h (KFR-10 catalyst)
 (c), (d): 390 °C-3 h and 440 °C-1 h (KFR-10 catalyst)
 (c) no solvent added
 (d) 10 wt% of 1-methylnaphthalene added in the second-stage reaction

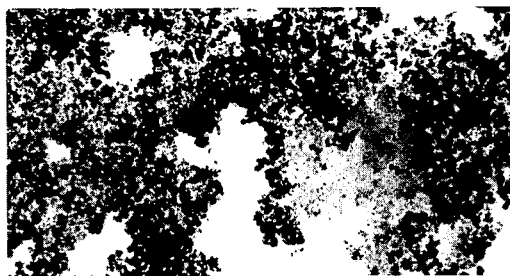


Figure 3 Microphotographs of the product of 420 °C- 4 h (KF-842) after 150 days